UNIVERSITÀ DEGLI STUDI DI NAPOLI FEDERICO II

SCUOLA DI DOTTORATO IN INGEGNERIA INDUSTRIALE

SCUOLA POLITECNICA E DELLE SCIENZE DI BASE

DOTTORATO INNOVATIVO CON CARATTERIZZAZIONE INDUSTRIALE

DIPARTIMENTO DI INGEGNERIA INDUSTRIALE

A NOISE AND VIBRATION ANALYSIS ON POSITIVE DISPLACEMENT PUMPS FOR FLUID POWER APPLICATIONS TO REDUCE FLOW PULSATION AND CAVITATION PHENOMENA

Relatori

Ch.mo Prof. Ing. Adolfo Senatore
Ch.mo Prof. Ing. Emma Frosina
Ch.mo Prof. Ing. Kim A. Stelson
Ing. Michele A. Pavanetto

Candidato

Gianluca Marinaro
matricola DR993169

XXXIII Ciclo

Table of Contents

List of Tables

List of Figures

Chapter I: **Introduction**

I.1   Background

The Fluid Power technology is handling significant changes to achieve the highest *efficiency levels* requested by the market to compete with other technologies of different fields, like hybrid and electric. One of the hydraulic application's main problems will be noise emission, especially in the next years. One need only think, for example, to all the past applications where hydraulic operating machines were powered via a very noisy diesel engine, which will be replaced by a quieter electric motor. With this configuration, the noise emitted by the hydraulic system will be more and more relevant.

Besides, scientists and health experts consider it intolerable that millions of people suffer from unacceptable noise levels; today, every environmental noise caused by traffic, industrial and recreational activities is viewed as a problem according to the EU Policy. The main focus of this policy is focused on the noise abatement of every type of equipment. For this reason, a set of directives were established in these years since they are the most important and legal tools to take a step forward in the right direction, limiting the dB emissions.

As said, the Fluid Power is affected by these regulations and, even if the world is evolving in an "electrified being", the Hydraulic is still there, and it seems that it will be there for a while longer since other technologies are still not capable of having the same power density, flexibility, and reliability of it. That is the reason why hydraulic components and systems have to be conformed to the dB limits defined by European Policy for working

environments (ref. SNSI, Horizon 2020 and Direttiva Macchine 2006/42/CE), both in mobile and industrial applications. For this reason, today and in the future, the major challenge to be achieved for Fluid Power is to reduce the acoustic emissions for all hydraulic components drastically. The primary sources of noise in hydraulic systems are pumps and motors. For this reason, over the last few years, many research activities have been focused on understanding the leading causes of the noise generated by these components.

It is acknowledged by the scientific community that there are three kinds of borne noise sources in hydraulic operating machines: structural, fluid and air-borne; as an example, in Figure 1, the distinction between the types of noise is given for a piston pump.

The air-borne noise is the noise directly detected by the human ear propagated through the air. The structural-borne noise is mainly influenced by vibrations of the mechanical components caused by an oscillating force, and it can be found in all the circuit components. The oscillating force depends on the pumping chambers' resultant instantaneous pressures, pump's inertia, and internal frictions. In addition, flow pulsation (flow ripple) is the leading cause of fluid noise. It mainly causes structural-borne noise, and its entity can be tangible under a load as a pressure ripple, which can propagate to high distances in hydraulic pipes. Thus, any reduction of the fluid-borne noise will affect the other two sources.

Theoretically, the flow pulsation can be evaluated as a function of the number of the pumping chambers, the displacement, and the shaft speed of the pump [1]. Indeed, hydraulic pumps do not produce a steady flow rate; a mean flow rate can be identified, but a periodic waveform due to a displacement pump's mechanism will be superimposed. The periodic waveform may look complicated, but a fundamental frequency can be easily identified in the frequency domain; this frequency is related to the shaft rotational frequency and the number of displacement chambers.

$$\text{Fundamental freq.} = \text{n° displ. chambers} \times \text{shaft freq.} \qquad (1)$$

Some flow ripple components can be found at shaft frequency, but usually, they are small and therefore ignored.

The flow ripple can be considered a superimposition of two different factors; a kinematic ripple due to the displacement chamber's geometries, and it is not related to the pressure. A second factor is remarkably influenced by the oil compressibility and the reverse flow rate generated by the pressure difference between the pumping chamber and the suction or delivery ports, and for this reason, it is pressure dependent.

As mentioned, the flow ripple interaction with the system characteristics causes pressure fluctuation (pressure ripple). The flow ripples can be reduced, minimizing the reverse flow rate back to the chambers. However, the rapid variation of pressure in the pumping volume contributes to the noise emission and the structure-borne noise. Also, cavitation phenomena are related to the fluid-borne noise, but no fundamental frequencies can be identified in this case [2].
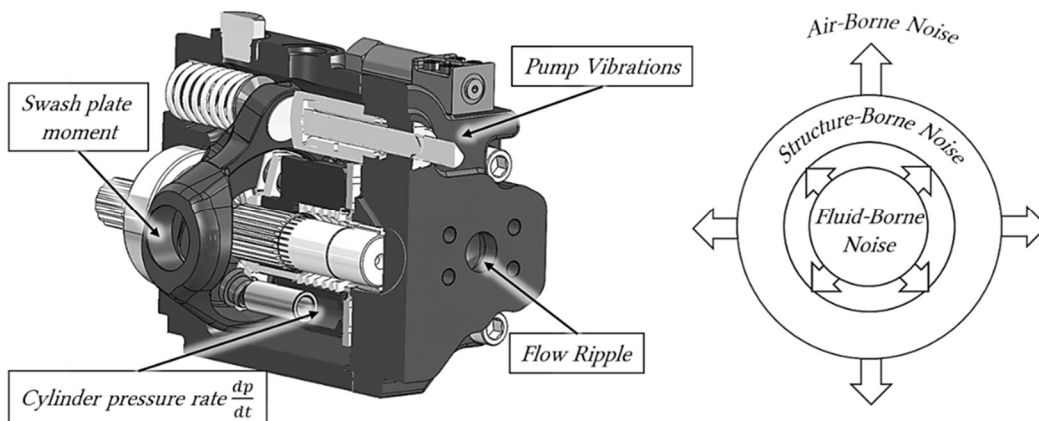
Figure 1. Fluid-, structure- and air-borne noise

Nowadays, there are many designs for positive displacement pumps, each with its booming features and weak points. Their application fields are wide, from mobile to industrial, with a very varied kind of fluids, from oil to water, passing through the water-glycol. Without even mentioning the construction materials, their applications' power can vary greatly, from a few dozen of W to hundreds of kW. One of the main aspects that all the mentioned points have in common is that, beyond everything, an engineering team has to face a pump designing process. These players' primary objective is to reduce the flow non-uniformity, created by the

3

working principle itself for a positive displacement pump. This characteristic has to be carefully studied in all its aspects (flow ripple, pressure ripple, force, and torque ripple), especially for high-pressure applications, since it represents the critical point for designing an efficient, but above all, low-noise pump. During the development of new products or the optimization of existing ones, the designers need help to understand physics and where they can act. In the past, Experimental Fluid Dynamics (EFD) was the only way to know how to improve a product with a massive prototyping effort. Today the availability of mathematical models of the involved phenomenon and the simplicity to access high computational power at reasonable costs can be the most effective method to face a prototyping process. Therefore, numerical modeling and simulation have to be considered as daily bread.

I.2   Objective

Modern fluid power systems require low-noise components to keep up with the pressing regulations about noise emission reduction for all working environments. For this reason, both industry and academia are increasing their efforts since new pump designs have high margins to improve efficiencies and reduce noise and vibrations as well. This thesis's main objective is to provide methods to analyze and comprehend the physics involved focusing the attention on flow non-uniformity and problems related to the cavitation, which is a noise and vibrations source. "Digital Twins" of hydraulic components and methods will be proposed in the next chapters. Each Chapter will present a different subject of study and the methodology applied.

All the approaches, techniques, and methodologies presented in this work of thesis are developed by the Fluid Power Research Group of the industrial engineering department at the University of Naples Federico II lead by Prof. Senatore and Prof. Frosina.

It is essential to do a clarification about the Ph.D. program before going deep into the next sections. It belongs to a particular program, established by the Italian government, called *PON Research & Innovation* (in Italian *Programma Operativo Nazionale di Ricerca ed Innovazione*) where Italian

Universities develop these Ph.D. programs in collaboration with Italian companies and foreign universities. They have a robust industrial characterization to promote and create high postgraduate formation and doctoral level specialization consistently with the Italian productive system's needs and the *Strategia Nazionale di Specializzazione Intelligente* (SNSI). For this specific program, named *"Innovative positive displacement hydraulic pumps for fluid power applications: noise and vibration reduction removing problems due to pulsation"*, the other two authorities, supporting the University of Naples Federico II, are the international company Duplomatic Motion Solution, located in the North Italian area, and the University of Minnesota (USA), in particular, with the Center for Compact and Efficient Fluid Power lead by the Prof. Kim A. Stelson.

All the presented methodologies are demonstrated to be capable of predicting the noise sources. On one side, the lumped parameter modeling demonstrated its capability to predict the flow and pressure ripples effectively but showed its limitations when complex flow fields are involved in the analysis. The 3D CFD numerical modeling, on the other side, demonstrated high capability in predicting the cavitation phenomenon and its location and evolution. As well-known in literature, each methodology has its pros and cons. Lumped parameter model needs a calibration of some parameters, and its development requires lots of effort and a good knowledge of the physics involved. Furthermore, additional efforts are necessary when the displacement chamber's volume variation is not easily parametrizable, as an example in gear machines. The CFD numerical modeling can be faster from the model developing point of view, but it is slower in computational time, and it also requires a supercomputer for high computational calculations.

However, one does not exclude the other; in particular, the CFD model can support the lamped parameter model calibration, which can be high-speed and effective for the design-of-experiment (DOE) studies, especially in prototyping phases where experimental data are not available.

Chapter II: **Piston Pumps**

II.1 Introduction

As already mentioned in Chapter I, noise reduction is increasingly significant in the fluid power field, where there is still no other technology capable of the same power density, flexibility, and reliability. Understanding fluid dynamics inside hydraulic components is fundamental, not only for optimizing component efficiencies but also for reducing noise due to the flow oscillations.

II.1.1 State-of-the-art

Several studies are available in the literature on reducing the noise in the axial piston pumps; most of them have been focused on developing numerical modeling techniques.

Xu et al. [3] showed an interesting modeling approach to reduce noise due to flow ripple. The research considered a design method focused on the valve plate's transition region for an axial piston pump. The authors demonstrated that a drastic reduction of noise could be achieved by optimizing the valve plate design.

Another interesting study aimed at noise reduction of an axial piston pump was done by Ye et al. [4]. The authors added damping holes to the valve plate to avoid air-release and cavitation. They developed a multi-objective genetic algorithm optimization method to reduce noise through variations of the valve plate dimensions. They also measured the noise emissions in a semi-anechoic chamber,

showing a correlation between outlet flow amplitude and noise sound level (dBA) [5].

Even Wang [5] analyzed axial piston pumps to avoid cavitation. The vacuum within the piston bore caused by the rising volume needs to be compensated by the flow; otherwise, the low pressure may cause cavitation and aeration. The valve plate geometry has been optimized to prevent the piston pressure below the vapor pressure. However, the paper only provides a design guide of the timings and overlap areas between valve plate ports and barrel kidneys.

Ding et al. [6] presented research numerically performed on several pumps to investigate pump performance effects from cavitation onset. In the section on axial piston pumps, the authors demonstrated that cavitation is a cause of damage on the valve plate geometry, particularly in the transition between low and high-pressure regions (or areas). Optimization of the valve plate is needed to reduce this phenomenon.

Changbin et al. [7] investigated an aviation axial-piston pump valve plate that uses a pre-pressurization fluid path (consisting of a damping hole, buffer chamber, and orifice) to reduce flow ripple. The pump models have been realized using the S-function in Matlab/Simulink® and validated with Computational Fluid Dynamic (CFD) numerical results.

Casoli et al. [8] [9] demonstrated that pressure ripple is the primary source of noise emitted by pumps in hydraulic circuits. They presented a theoretical analysis on active control of pressure ripple in an axial piston pump by adequately moving the swashplate. The reduction of pressure oscillations is studied using a mathematical model of the entire pump integrating the fluid and stable component dynamics.

Wu et al. [10] showed that ripple in the outlet flow from a high-pressure piston pump is caused by pressure pulses in the piston cavity when it rotates through the transition regions of the valve plate. This phenomenon has been studied through a parametric design approach that optimizes a piston pump valve plate's transition region structure to reduce the outlet flow's ripple.

Manring et al. [11] studied variable valve plate geometry to improve the axial piston pump's volumetric efficiency, including the fluid's compressibility losses. The author compared two valve-plate geometries showing that the valve plate

design can cause differences in the pump's operating efficiency. In particular, some valve plate designs introduce a volumetric loss, which may be accounted for by the uncontrolled expansion and compression of the fluid that occurs through the slots. However, the paper does not give a methodology to optimize the valve plate design. It only provides the theoretical reason for utilizing trapped volumes and lends general insight into the valve-plate design's overall problem.

II.1.2   The subject of the study

The research has been performed on a variable displacement axial piston pump with a maximum displacement of 65.9 cm^3/rev. The pump is a variable swashplate designed with nine-piston, suitable for open circuit application, medium-high pressure. An exploded view of the pump is visible in Figure 2. It is possible to distinguish all the main components: the swashplate, the rotating group, the valve plate, the housing, the end cover, and the pressure compensator.
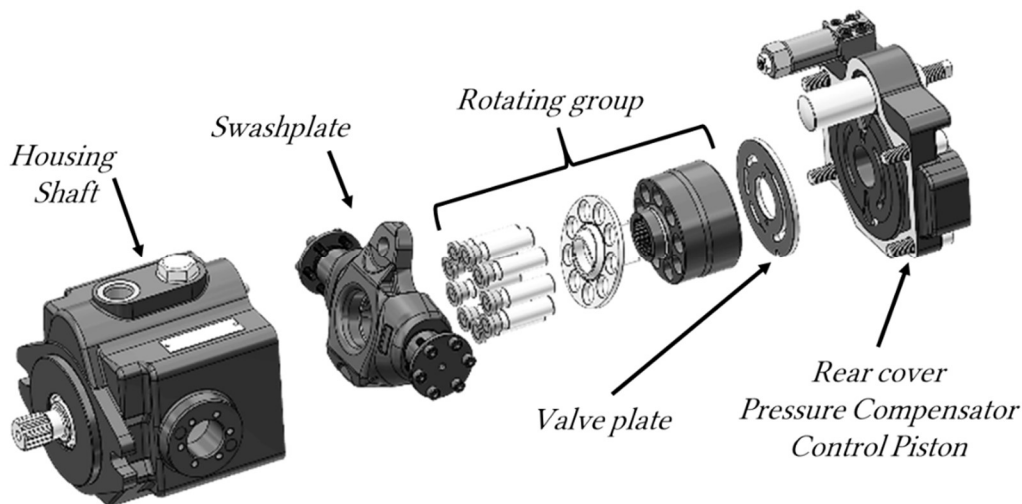
Figure 2. Exploded view of the analyzed pump

A drive shaft transmits the power from an electrical motor to the pump. The pistons are driven by the cylinder block's rotation (also called the barrel), and the swashplate inclination creates their alternating axial motion. The nine pistons' movement can be divided into rotational (around the drive shaft axis) and linear (inside the cylinder block) components. The piston motion from the top dead center (TDC) to the bottom dead center (BDC) permits the oil coming from the tank to fill the volumes generated. Later, the oil will be delivered to the pump outlet during the piston movement from the BDC to the TDC.

The basic pump's technical data are listed in Table 1.

Table 1. Pump technical data

Description	Value	Units
Maximum theoretical displacement	65.9	cm^3/rev
Speed range	500-3000	rev/min
Operating pressure (peak)	14-280 (310)	bar

This pump has been studied numerically using a lumped parameter model and a CFD approach to reduce the fluid borne noise, reducing the flow non-uniformity and avoiding an issue like cavitation.

II.2 Lumped parameter model description

II.2.1 The approach

The axial piston pump's numerical model is based on the control volume approach, where each control volume (CV) has homogeneous properties, such as pressure, temperature, etc. All the CVs are connected by resistive components (variable orifices), calculating flow rates as a function of pressure drops. The developed simulation model can predict steady-state and dynamic working conditions thanks to implementing a numerical model of the pressure compensator, which controls the pump displacement. An overview of the numerical model of the pump is shown in Figure 3.
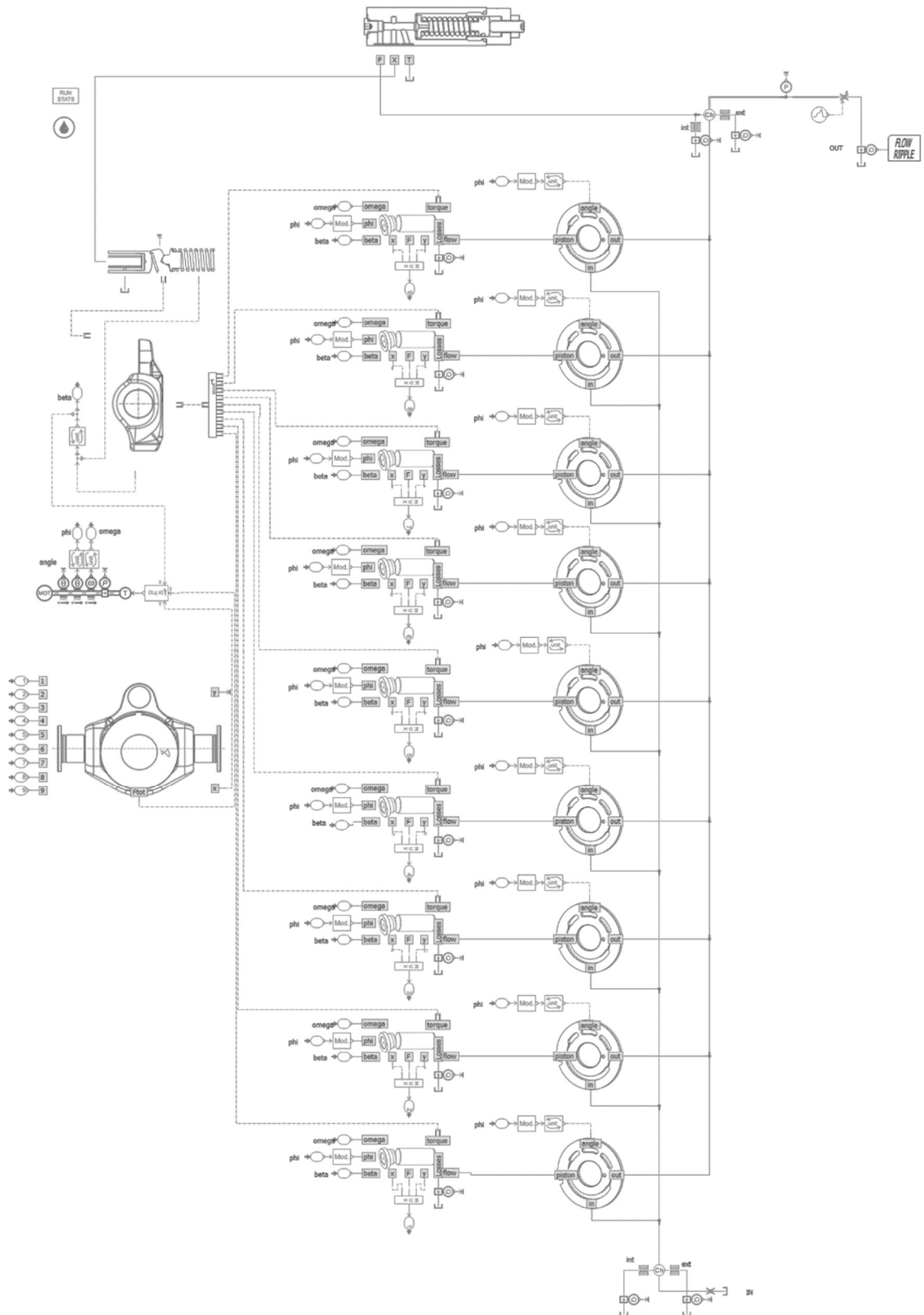
Figure 3. Overview of the lumped parameter model

The model can be split into two sub-models. The first one is related to the fluid volumes and includes the pumping volumes, the ports (both suction and

delivery), and all leakages. The second one is related to swashplate dynamics and control.

Each pumping volume has been modeled using the control volume approach. In Figure 4, the gray area represents a section view of the control volume (CV) of the *i-th* piston, which has homogeneous properties. The CV is a capacitive element, and the model calculates the pressure as a function of the net ingoing flow rate using the equation (2); CVs are connected to pressure sources through resistive components (variable orifices), calculating flow rate as a function of the pressure drop (equation (3)).
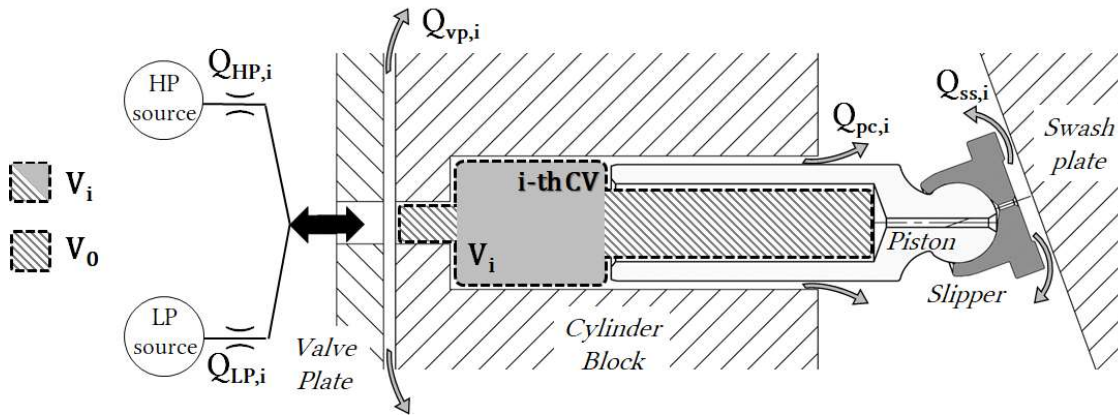
Figure 4. The net ingoing flow rate of a *i-th* control volume (CV)

$$\frac{dp_i}{dt} = \frac{B}{V_i}\left(Q_i - Q_{pc,i} - Q_{ss,i} - Q_{vp,i} - \frac{dV_i}{dt}\right) \cdot \frac{\rho_{atm}}{\rho} \qquad (2)$$

The equation of continuity (2) has been integrated to evaluate the instantaneous pressure of the *i-th* CV. Three losses, visible in Figure 4, are:

- $Q_{pc,i}$ is the leakage between the piston and the cylinder block.

- $Q_{ss,i}$ is the leakage between the slipper and the swashplate.

- $Q_{vp,i}$ is the leakage between the cylinder block and the valve plate.

B is the effective bulk modulus of the oil.

Further information can be found in the software's technical bulletin [12]. The leakage between the slipper and the piston is neglected in the model. The flow

rate $Q_i(t)$ has been modeled using the stationary equation for turbulent flow; it is the sum of the two quantities calculated by the resistive components in equation (2), using the turbulent orifice law, in equation (3):

$$Q_{HP,i} = c_d A_{HP,i} \sqrt{\frac{2|p_i - p_{HP}|}{\rho}} \times sign(p_i - p_{HP}),$$

(3)

$$Q_{LP,i} = c_d A_{LP,i} \sqrt{\frac{2|p_i - p_{LP}|}{\rho}} \times sign(p_i - p_{LP}),$$

where ρ is evaluated at the average pressure value between p_i and p_{LP} or p_i and p_{HP}. In both equations, there are two significant parameters ALP and AHP: the interface areas between the control volume and the valve plate. These areas are usually calculated with two approaches: one, CAD-based, is performed simulating through executable modules, where the components are set in motion, the geometry is analyzed, and the geometrical data is extrapolated from the CAD geometry; the other one is based on the analytical evaluation of all the geometries (analytic-based). In this work, the second approach is used since the parametrization is compatible with the next sections' optimization process. The approach will not be described in detail since it only depends on geometry. The robustness of the developed numerical method will be shown in section 3, where a comparison with experimental data is presented. Two coordinate systems, shown in Figure 5(a), have been considered in the approach; the first one *(O x y z)* is relative to the shaft, the second one *(O' x' y' z')* is relative to the swashplate. According to these systems, the volume V_i of the *i-th* piston is:

$$V_i = V_0 + \frac{\pi d_P^2}{4}\left(z_0 - z_{p,i}\right) \qquad \frac{dV_i}{dt} = -\frac{\pi d_p^2}{4}\dot{z}_{p,i} = -\frac{\pi d_p^2}{4}v_{p,i}, \qquad (4)$$

Where d_p is the piston diameter, z_0 is the variable chamber's length at zero displacement $\beta=0$, V_0 is the dead volume. Then, to find the instantaneous position of the i-th piston $z_{p,i}(t)$ in *(O x y z)*, identified by the piston head center O_i'' (in Figure 5), the angular position $\varphi_i(t)$ of the *i-th* piston has to be evaluated with equation (5):

12

$$\varphi_i = \omega\, t + \frac{2\pi}{n}(i-1)\;,$$

<div align="right">(5)</div>

$$i = 1,...,n\;,$$

Where n is the number of the pistons, ω is the shaft speed in rad/s, and t is the time.

<div align="center">(a)   (b)</div>
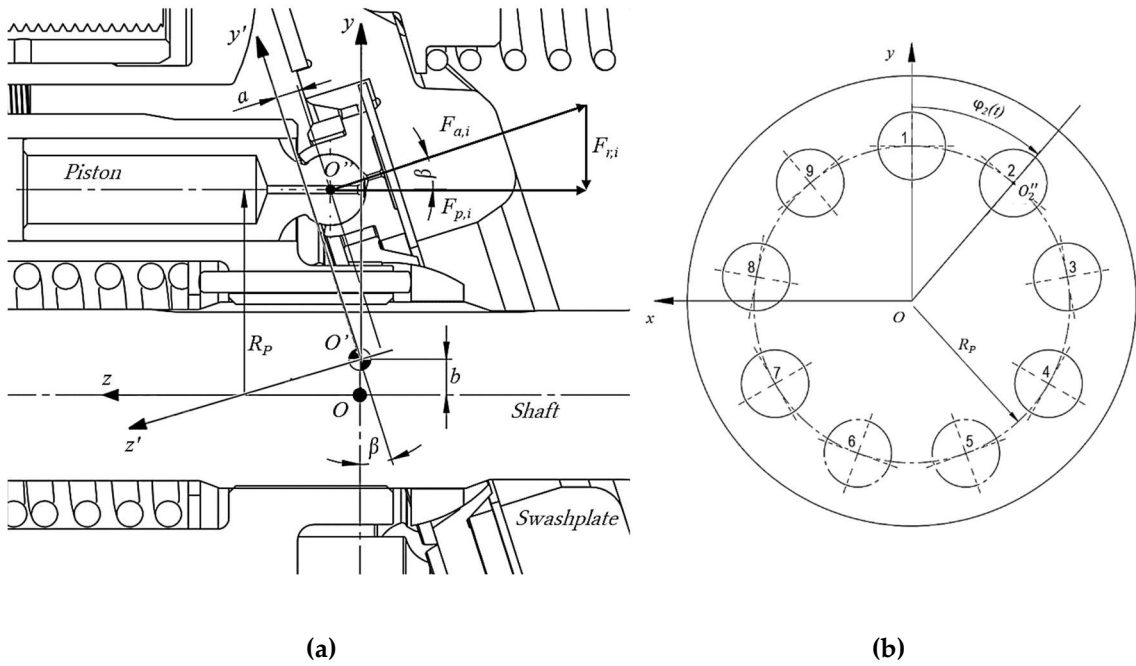
Figure 5. Pump cross-sectional view (**a**); forces and dimensions (piston at TDC). Example of the angular position of a nine-piston pump (**b**)

The term $z_{p,i}(t)$ can be calculated using equation (6). Besides the angle β, two more dimensions are needed to get the precise position of the *i-th* piston: b is the distance between the shaft rotational axis and the swashplate rotational axis, while a is the distance between the plane containing all the O_i'' centers of pistons heads and the swashplate rotational axis. Both are visible in Figure 5(a).

$$z_{p,i} = R_p \tan\beta \cos\varphi_i - b\tan\beta - a\left(\frac{1}{\cos\beta}-1\right)\;,$$

<div align="right">(6)</div>

Differentiating equation (6), it is possible to evaluate the axial velocity of the *i-th* piston:

$$\frac{dz_{p,i}}{dt} = v_{p,i} = -\dot{\varphi}_i R_p \tan \beta \sin \varphi_i = -\omega R_p \tan \beta \sin \varphi_i \tag{7}$$

II.2.2 Leakage between pistons and cylinders Q_{pc}

Leakage between the *i-th* piston and cylinder has been included in the model using equation (8), which considers both Couette and Poiseuille flows.

$$Q_{pc} = \sum_{i=1}^{n} Q_{pc,i} =$$

$$= \sum_{i=1}^{n} \left\{ -\frac{p_i - p_{case}}{12\mu l_c} \left(\frac{d_b - d_p}{2} \right)^3 \pi d_b \left[1 + 6\left(\frac{ecc}{d_b - d_p} \right)^2 \right] + \frac{v_{p,i}}{4} \left(d_b - d_p \right) \pi d_b \right\} \cdot \frac{\rho}{\rho_{atm}} \tag{8}$$

Where l_c is the contact length, μ is the fluid's dynamic viscosity taken at the mean pressure, *ecc* is the eccentricity, and v_{pi} *(t)* is the axial velocity of the *i-th* piston. The leakage between *i-th* piston and cylinder Q_{pc} is clearly shown in Figure 6.
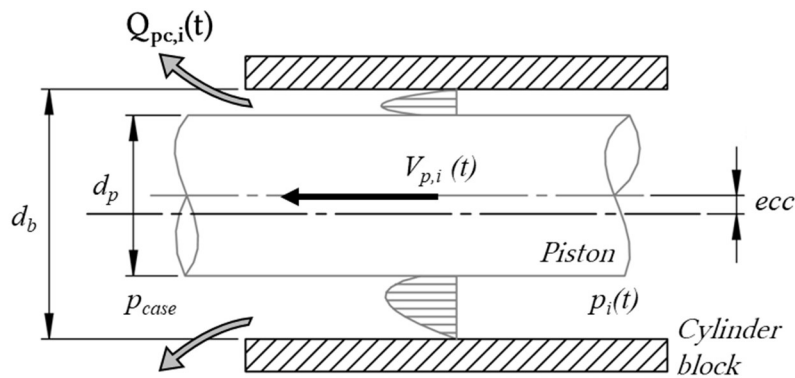
Figure 6. Leakage between piston and cylinder

II.2.3 Leakage between the slipper and the swashplate Q_{ss}

The leakage between the *i-th* slipper and swashplate has been modeled using the formula for a flow between two circular parallel surfaces with a central inflow. The equation is:

$$Q_{ss} = \sum_{i=1}^{n} Q_{ss,i} = \sum_{i=1}^{n} \frac{[p_i - p_{case}]\pi h_{ss,i}^{3}}{6\mu \ln \dfrac{r_{in}}{r_{out}}} \cdot \frac{\rho}{\rho_{atm}} \tag{9}$$

where the dynamic viscosity μ is evaluated at p_{mid}:

$$p_{mid} = \frac{[p_i - p_{case}]}{2} \tag{10}$$

In equation (9), the dimensions r_{out} and r_{in} are shown in Figure 7 and are the slipper's inner and outer radii, while h_{ss} is the height of the slipper and swashplate gap.
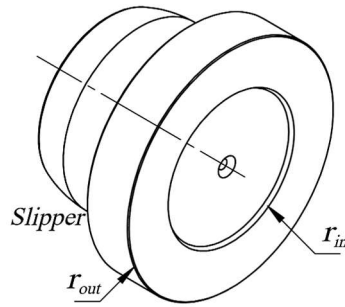
Figure 7: Design of the slipper

II.2.4 Leakage between the cylinder block and the valve plate Q_{vp}

The leakage between the cylinder block and the valve plate, shown in Figure 4, has also been included in the model. For simplification, the leakage Q_{vp} has been approximated as the sum of flows through two flat orifices since this approximation slightly influences the flow ripple and cavitation analyses. Even if the hatched areas in Figure 8(a) are curved, since the width is much greater

15

than the length, the curvature effect can be neglected. Therefore, the radial leakage between the cylinder block and the valve plate can be calculated by using the formula for a flow-through flat orifice (visible in Figure 8(b)).

The total leakage for the *i-th* CV between these two components is the sum of two radial flow.

$$Q_{vp} = Q_{vpr} + Q_{vpR} = \sum_{i=1}^{n} \left[Q_{vpr,i} + Q_{vpR,i} \right] \tag{11}$$

Two equations are implemented in the numerical model, one with the subscript *r* (related to the internal hatched area) one with the subscript *R* (associated with the external hatched area).

(a)   (b)
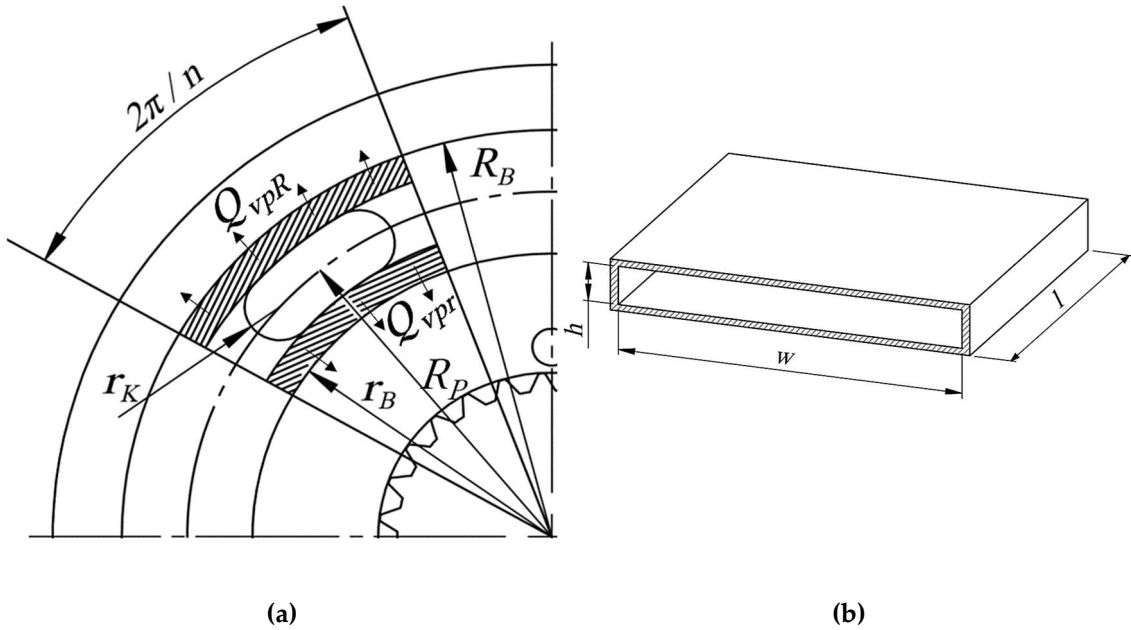
Figure 8. Areas influenced by the leakages (**a**), dimensions of the flat orifice (**b**)

From equation (11), $Q_{vpr,i}$ is evaluated using the following formula:

$$Q_{vpr,i} = \frac{\left[p_i - p_{case} \right] w_r \cdot h_{r,i}^{3}}{12 \mu l_r} \cdot \frac{\rho}{\rho_{atm}} \tag{12}$$

16

where w_r and l_r are:

$$w_r = \left(R_P - r_K - r_B \right), \qquad l_r = \left(r_B + \frac{w_r}{2} \right) \cdot \frac{2\pi}{n}, \qquad (13)$$

Instead, $Q_{vpR,i}$ is evaluated using the formula:

$$Q_{vpR,i} = \frac{\left[p_i - p_{case} \right] w_R \cdot h_{R,i}{}^3}{12 \mu l_R} \cdot \frac{\rho}{\rho_{atm}}, \qquad (14)$$

Where w_R and l_R are:

$$w_R = \left(R_B - R_P - r_K \right), \qquad l_R = \left(R_B - \frac{w_R}{2} \right) \cdot \frac{2\pi}{n}, \qquad (15)$$

Where $h_{r,i}$ $h_{R,i}$ are functions of pressure, pump speed, dynamic viscosity. The dynamic viscosity μ is evaluated at $p_{mid,}$ already presented in the equation (10).

II.2.5   Swashplate dynamics

The pump's displacement is controlled by a pressure compensator that is a simple way to control pump displacement. The pressure compensator limits the system pressure to a predetermined level, adjustable through the preload of a spring, which acts against the system pressure. This controller's task is to regulate the pump outlet flow, thanks to a piston that continuously controls the swashplate angle to the value needed to maintain the system's set pressure. The swashplate equilibrium position is determined by balancing the torques acting on it (equation 15). There are many terms to be considered: referring to Figure 5(a) the torque T_p due to the instantaneous pressure of each CV, the torque T_{sp} due to the cylinder block spring preload force F_{sp}; the torque due to the displacement controller and the bias spring T_{cp} and the friction torque T_f. Also, the mass moment of inertia of swashplate J_{sw} has been taken into account:

$$T_{CP} = -T_p - T_{sp} + T_f + K\beta + C\dot{\beta} + J_{sw}\ddot{\beta} \tag{16}$$

The torque generated by the pistons is:

$$T_p = \sum_{i=1}^{n} T_{p,i} = \sum_{i=1}^{n} \frac{F_{p,i}}{\cos\beta} \cdot y_i \tag{17}$$

where $T_{p,i}$ is a function of $F_{p,i}$ and its position on the swashplate y_i in the plane (x', y'):

$$y_i = \frac{R_P \cos\varphi_i - b - a\sin\beta}{\cos\beta} \tag{18}$$

The pressure force F_p, is (19):

$$F_{p,i} = -\left[p_i A_p - F_{frict,i} - m_p \ddot{z}_{p,i} \right] \tag{19}$$

Where F_{frict} can be evaluated using the following equation:

$$F_{frict,i} = -\pi\left(d_b - d_p\right)\left[\left(p_i - p_{case}\right)\frac{1}{4}d_b + 2\mu\frac{1}{d_b}l_C v_{p,i} \right] \tag{20}$$

In equation (19), m_p is the mass of the piston-slipper assembly. For simplification, the inertia related to this mass has not been included in the numerical model.

Taking a step back to equation (16), T_{sp} is the torque created by the cylinder block spring. It can be considered constant:

$$T_{sp} = F_{sp} \cdot b = const \tag{21}$$

F_{sp} is the precompression force of cylinder block spring; F_{sp} variation, due to the cylinder block lifting, has been neglected during the working condition.

In equation (15), the torque component T_{CP} is the Control Piston's torque (CP). It has been evaluated as a sum of two components; one is exerted by the pressure p_{cp} inside the control piston acting on area A_{cp}, the other is due to the bias spring; which holds the swashplate at its maximum allowable angle:

$$T_{CP} = \frac{\left[F_{cp} + k_{bs}(l_{0,bs} - l_{bs}) \right] \cdot l_{cp}}{\cos^2 \beta} \tag{22}$$

where l_{cp} is the distance between the control piston and the swashplate rotational axes, k_{bs} is the bias spring constant, $l_{0,bs}$ is its free length, l_{bs} is its actual working length, and F_{cp} is the force due to the pressure acting in the control piston volume, evaluated with the following equation:

$$F_{cp} = -p_{cp} \cdot A_{cp} \tag{23}$$

Where p_{cp} is the CP control pressure, and A_{cp} is the control piston area. The friction torque T_f has been evaluated through the LuGre model. The Lund – Grenoble friction model is presented in [13] [14] [15] [16] [17] by C. Canudas de Wit, H. Olsson, K.J. Astrom, and P. Lichinsky. Extensive analysis of the model and its application can also be found in [18] [19] [20] [21] [22]. The LuGre model includes viscous friction and the Stribeck effect [23]. This model has been selected since it is dynamic. One of the major disadvantages of static friction models is the limited richness of the models. It will result in inaccurate friction for some areas of interest, such as pre-sliding displacement in the stiction regime and frictional lag (hysteresis in the relationship between friction torque and rotational velocity) for some sliding regimes or stick-slip motion. The numerical model allows evaluating the total pressure force exerted by the n pistons and their position on the plane (x',y'). The equations utilized in this part of the model are:

$$F_{p,tot} = \sum_{i=1}^{n} \frac{F_{p,i}}{\cos \beta} \quad , \tag{24}$$

$$x_{F_{p,tot}} = \frac{\displaystyle\sum_{i=1}^{n} \frac{F_{p,i}}{\cos \beta} \cdot x_i}{F_{p,tot}} \quad , \qquad\qquad y_{F_{p,tot}} = \frac{\displaystyle\sum_{i=1}^{n} \frac{F_{p,i}}{\cos \beta} \cdot y_i}{F_{p,tot}} \quad , \tag{25}$$

where y_i has been already described in the eq. (18), while x_i is evaluated as:

$$x_i = R_P \sin \varphi_i \tag{26}$$

It is also significant to evaluate the torque on the pump shaft:

$$T_s = T_r + T_{vp} + T_{ss} + T_b + K\varphi + C\dot{\varphi} + J_{rg}\ddot{\varphi} \tag{27}$$

where T_b is the bearing friction torque, modeled with the Coulomb model considering viscosity and no static friction [12], J_{rg} is the mass moment of inertia of the rotating group (shaft, cylinder block, and piston-slipper assemblies), while the torque T_r, due to the pressure, is:

$$T_r = -\sum_{i=1}^{n} \left[F_{r,i} \cdot x_i \right] = -\sum_{i=1}^{n} \left[F_{p,i} \tan \beta \cdot x_i \right] \tag{28}$$

In equation (27), the torque T_{vp}, due to the viscous friction between the cylinder block and valve plate, is:

$$T_{vp} = \frac{\pi}{2h_b} \mu\omega \left[R_B^4 - 8R_p r_K \left(R_p^2 + r_K^2 \right) - r_B^4 \right] \quad \text{with} \quad h_b = \sum_{i=1}^{n} \frac{\left(h_{r,i} - h_{R,i} \right)}{2n} \tag{29}$$

20

Where μ is the dynamic viscosity estimated at an average pressure between inlet and outlet. While, T_{ss}, is the torque due to the viscous friction between slipper and swashplate, evaluated as reported below:

$$T_{ss} = \sum_{i=1}^{n} T_{ss,i} = \cos\beta \cdot R_p \cdot \sum_{i=1}^{n} F_{ss,i} = \cos\beta \cdot R_p \cdot \sum_{i=1}^{n} \left[\mu\omega \frac{R_p}{h_{ss,i}} \pi \left(r_{out}^2 - r_{in}^2 \right) \right] \qquad (30)$$

The lumped parameters model described above has been implemented using the commercial code Simcenter Amesim® developed by Siemens (5800 Granite Parkway, Suite 600, Plano, TX – 75024, USA).

II.3 Three-dimensional CFD model description

II.3.1 The approach

In industrial fields, the flows are almost always turbulent. Therefore, ideally, Direct Numerical Simulation (DNS) should be adopted to capture all the scales, but the computational time at this Reynolds number is very lengthy. Alternatively, other models can be used for the computation of turbulent flow. Large Eddy Simulation (LES) resolves the large eddies, modeling only the small-scale eddies. Still, it requires a very fine mesh and very small time-step, making it not applicable to industrial applications.

The faster and widespread way to model turbulence is to use the Reynolds-Averaged Numerical Simulation (RANS), which has been proven to predict the correct time-averaged flow field, particularly for wall-bounded flows. Simerics MP+® adopts the RANS approach to model the turbulent flow, using the standard "K-Epsilon" and the RNG "K-Epsilon" turbulence models available in the software. The standard "K-Epsilon" model has been selected for this analysis.

The pump's transient three-dimensional CFD model has been realized with the commercial code Simerics MP+®, which integrates a rotor template mesher dedicated to piston pumps with a swashplate design. This commercial software, used for years by the Fluid Power Research Group (FPRG), discretizes the governing equations, including conservation of mass (31) and momentum (32), using a finite volume method.

$$\frac{\partial}{\partial t}\int_{\Omega(t)}\rho d\Omega+\oint_\sigma \rho\vec{V}\cdot\vec{n}d\sigma=0 \tag{31}$$

$$\frac{\partial}{\partial t}\int_{\Omega(t)}\rho\vec{V}d\Omega+\oint_\sigma p\left(\vec{V}\cdot\vec{n}\right)\vec{V}d\sigma=\oint_\sigma\left(\overline{\tau}\cdot\vec{n}\right)d\sigma-\oint_\sigma p\vec{n}d\sigma \tag{32}$$

Firstly, the fluid volume domain has been extracted from the CAD 3D drawing, provided by the company's technical department in a STEP format, with the commercial software Discovery SpaceClaim®, and divided into sub-volumes which will be later interfaced during the modeling process in Simerics MP+®. Surfaces have been renamed in Discovery SpaceClaim® (through an add-in) to be later easily distinguished. Finally, the fluid domains have been exported in STL format and imported in the CFD code and then meshed with opportune grid sizes. The software includes a dedicated module for piston pumps with a swashplate design that generates a structural mesh of the displacement chambers.

(a)   **(b)**

Figure 9. Pump fluid domain (**a**) Mesh of the fluid domain (**b**)

II.3.2 *Cavitation model*

To account for cavitation phenomena, a cavitation model has been considered. Simerics MP+® includes a cavitation model based on the full cavitation model developed by Singhal et al. [24], where the working fluid in cavitating flows is always assumed to be a mixture of liquid, vapor, and some

non-condensable gases (NCG). The modeling of the non-condensable gas effects has been done with the Equilibrium Dissolved Gas Model (EDGM) available in the software [25] [18]. In the EDGM, the mass fraction of the total non-condensable gas remains as a constant, but a part of it is dissolved into the liquid to satisfy the local equilibrium condition instantly. Mathematically, in addition to the same vapor mass fraction equation and vapor mass transfer models, the EDGM model solves an additional transport equation for the mass fraction of the dissolved gas, which is assumed to be always in an equilibrium state. The modeling equations for the liquid-vapor phase change are as follows:

$$\frac{\partial(\rho f_v)}{\partial t} + \nabla \cdot \left(\rho \vec{V} f_v\right) = \nabla \cdot \left[\left(D_v + \frac{\mu_t}{\sigma_v}\right)\nabla f_v\right] + R_e - R_c \tag{33}$$

where D_v is the diffusivity of the vapor mass fraction, and σ_v is the turbulent Schmidt number. The vapor generation term, R_e, and the condensation rate, R_c, are modeled as:

$$R_e = \begin{cases} C_e \rho_l \rho_v \sqrt{\frac{2}{3}\frac{(p_v - p)}{\rho_l}}\left(1 - f_v - f_{g,f}\right) & p < p_v \\ 0 & p \geq p_v \end{cases} \tag{34}$$

$$R_c = \begin{cases} 0 & p < p_v \\ C_c \rho_l \rho_v \sqrt{\frac{2}{3}\frac{(p - p_v)}{\rho_l}}f_v & p \geq p_v \end{cases} \tag{35}$$

The free NCG mass fraction $f_{g,d}$ has not been considered constant, but its evaluation has been achieved by adding the transport equation of the dissolved gas:

$$\frac{\partial(\rho f_{g,d})}{\partial t} + \nabla \cdot (\rho \vec{V} f_{g,d}) = \nabla \cdot \left(\left(D_{g,d} + \frac{\mu_t}{\sigma_{g,d}} \right) \nabla f_{g,d} \right) +$$

$$+ \frac{\rho}{\tau} \left(\frac{p}{p_{d,equil,ref}} f_{d,equil,ref} - f_{g,d} \right) + S_{g,d}$$ (36)

$S_{g,d}$ is the user-defined law of gas dissolution or release; $f_{d,equil,ref}$ is the equilibrium mass fraction of the dissolved gas at the reference pressure $p_{d,equil,ref}$, and both parameters have user-specified values. In this equilibrium model, the time scale τ approaches zero so that the mass transfer is near-instant. The free gas has the mass fraction $f_{g,d}$, instead of f_g. The mass fraction of the free gas is obtained from the condition:

$$f_g = f_{g,f} + f_{g,d} = f_{g,specified}$$ (37)

Where $f_{g,specified}$ has a specified value.

Finally, the effective bulk modulus B is computed based on the mixture of gas and liquid, based on the Nykanen model [26] as follows:

$$B = \frac{\rho}{d\rho/dp}$$

$$\frac{d\rho}{dp} = \rho^2 \left[\frac{1}{\rho} \left(\frac{f_v}{\rho_v} + \frac{f_g}{\rho_g} \right) + \frac{1}{B_l} \frac{1 - f_g - f_l}{\rho_l} \right]$$ (38)

The subscripts l, v, and g represent the liquid, vapor, and all the non-condensable free gases in the system, respectively; f indicates the mass fraction; p is the local flow pressure, and B_l is the liquid bulk modulus.

The mixture density ρ is also referred to as an effective fluid density, calculated based on the liquid, fluid vapor, and NCG's respective mass fractions and densities. Defined in the following equation:

24

$$\frac{1}{\rho} = \frac{1}{\rho_v} + \frac{1}{\rho_g} + \frac{1 - f_v - f_l}{\rho_l} \tag{39}$$

Where ρ_v, ρ_g, ρ_l and follows their respective density laws, and f_g, f_v, and f_l are either directly specified or obtained from solving transport equations.

In particular ρ_v is evaluated as follow:

$$\rho_v = \frac{p}{p_{sat}} \rho_{sat} \tag{40}$$

Where p_{sat} and ρ_{sat} are the saturation pressure and density at the given temperature.

The model does not include heat transfer; therefore, the temperature is assumed to affect the oil kinematic viscosity and density. It is used to calculate the gas density via the Ideal-Gas Law. An exponential model for pressure and temperature dependence of dynamic viscosity has been set up in the numerical model, according to the following equation (41):

$$\mu = \mu_0 e^{\alpha p - \lambda_1 (T - T_0)} \tag{41}$$

Herein, μ_0 is the dynamic viscosity at the atmospheric pressure p_0 and oil reference temperature T_0, λ_1 and α are the temperature and pressure coefficient of viscosity. Moreover, the model contains a variable bulk modulus of the liquid, depending linearly with pressure as follow:

$$B_l = \frac{\rho_0}{d\rho / dp} = B_0 + B_1 (p - p_0) \tag{42}$$

25

B_0 is the bulk modulus at 1 bar. B_1 is the bulk modulus rising coefficient; p is the absolute liquid pressure, p_0 is the reference absolute liquid pressure, and ρ_0 is the reference liquid density.

To achieve the best output results, simulations have been run, saving solution at 0.25° shaft angle. An Intel® Core (TM) i7-7700HQ CPU 2.80 GHz, with a computational time of around 24 hours/simulation (for two pump shaft revolutions), has been used for the purpose.

II.3.3 Mesh sensitivity analysis

A mesh sensitivity analysis has been done with different mesh refinement. Different models have been studied, evincing that the best agreement with the experimental data has been achieved using around 3 million 3D cells and includes many refinement zones. In particular, a remarkable refinement zone is located in the fluid groove volume of the valve plate; indeed, the area, shown in the zoomed view of Figure 10, is susceptible to cavitation phenomena due to the reverse flow from the pump outlet to the displacement chamber.
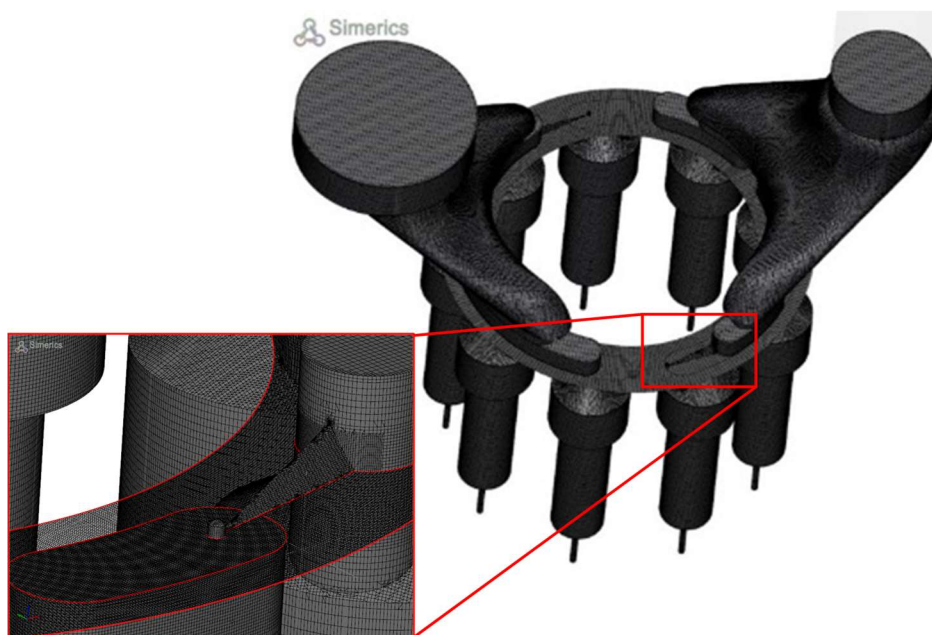
Figure 10. Mesh refinements

II.4 Numerical models comparison and validation

II.4.1 *Experimental test rig*

The experimental phase was needed to validate both numerical approaches. A preliminary pump geometry has been tested by the pump manufacturer Duplomatic Motion Solution with an oil ISO VG 46, maintained at a temperature of [50 ± 3] ° C through a heat exchanger. The hydraulic test rig schematic is visible in Figure 11.
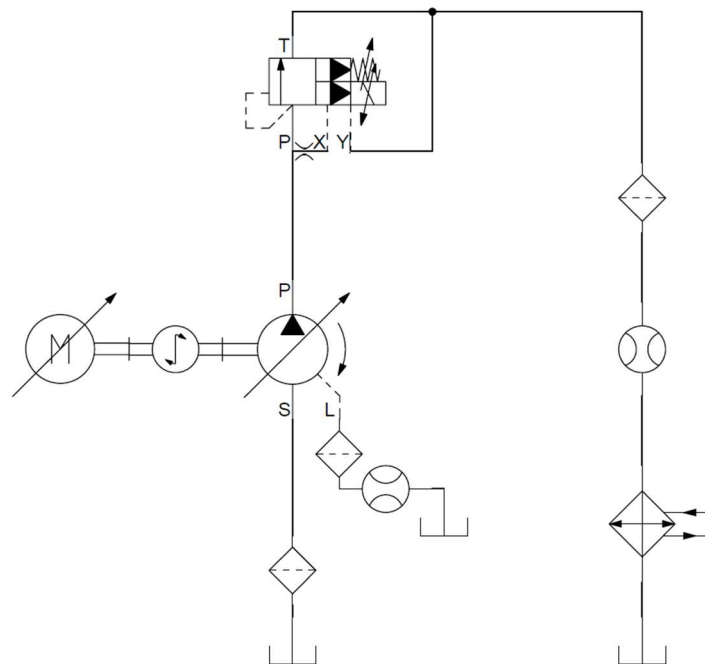
Figure 11. Hydraulic scheme of the test rig.

The Duplomatic Motion Solution test rig is visible in Figure 12. It is equipped with a VFD electrical motor, a torque meter, pressure transducers, temperature sensors, flow meters to evaluate both delivered flow and case drain, a proportional spool valve to generate the load, and all the necessary components to ensure the complete functionality of the test rig. All the signals have been acquired in LabView® and then post-processed in Matlab®.
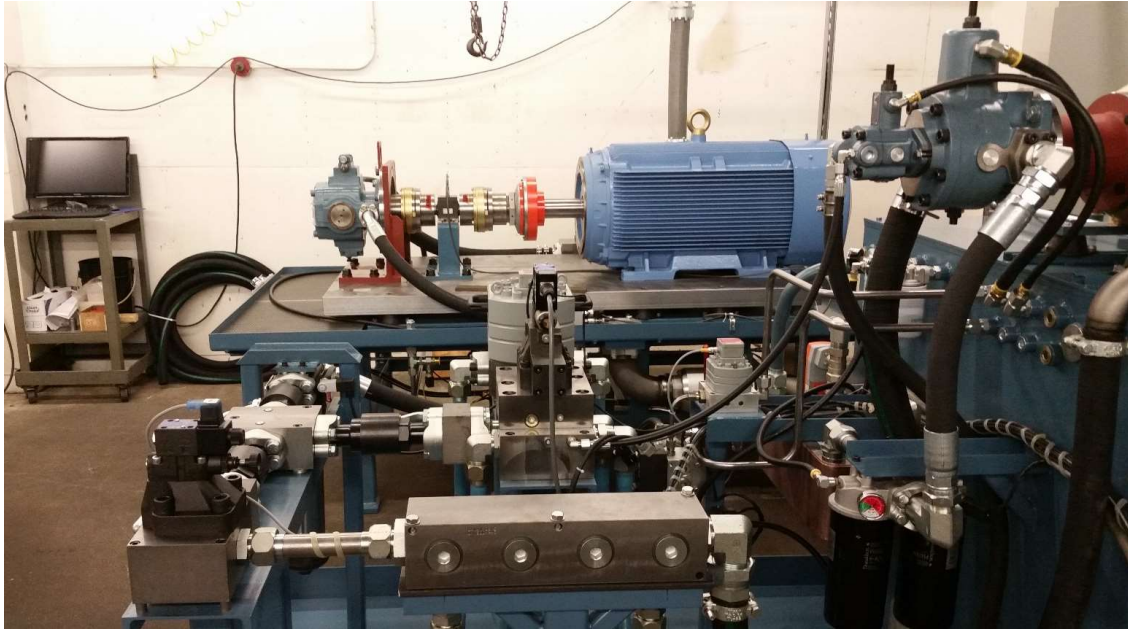
Figure 12. Test rig in Duplomatic Motion Solution's laboratory

The pump has been tested varying the shaft speed at different rotational speeds, including, in particular, 1500 rev/min and 1800 rev/min following European and American standards.

II.4.2 Three-dimensional CFD model validation in steady-state condition

The three-dimensional CFD simulation is a transient simulation done in a steady-state condition. In particular, the model has been set at the same working condition as the experimental tests. The boundary conditions are listed below:

- Inlet Pressure: 0 bar;

- Outlet pressure variable in the range [25÷280] bar;

- Pump speed of 1500 rpm and 1800 rpm;

- Maximum displacement (swashplate angle: 17.5°);

- Oil temperature of 50 °C.

A comparison between tests and numerical data (shown in Figure 13) has demonstrated an error percentage of less than 2% (flow meter accuracy is 0.3% FS, pressure transducer accuracy is 0.5% FS). Numerical models with a finer mesh provided more precise results, but the additional computational time did not justify the extra time required by a more refined mesh for reaching a stable

28

solution. Models with less dense mesh required lower computational time, but the error was not acceptable.
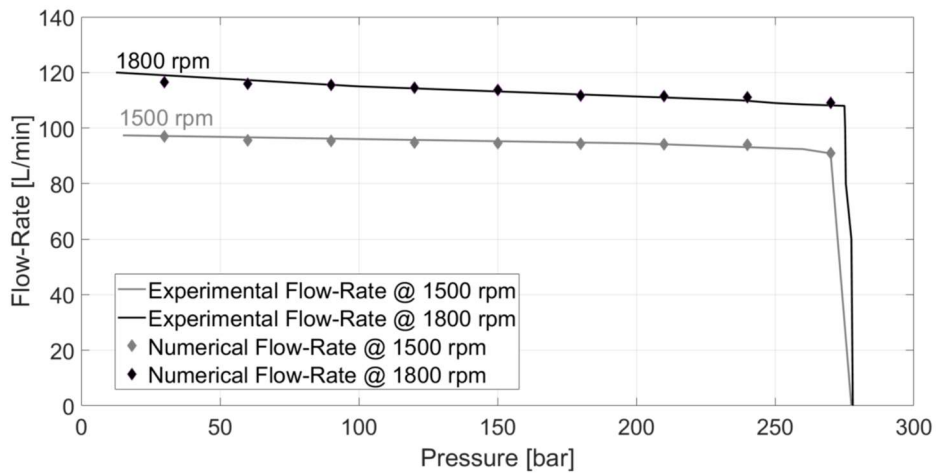
Figure 13. Average numerical CFD/measured flow-rates at the full displacement

As said, particular attention has been reserved for the flow losses due to cavitation using the equilibrium dissolved gas model (EDGM) already described in a previous paragrapher. From the numerical simulation, it has been noted a cavitation occurrence during the transition between suction to delivery when the pump runs at 1800 rev/min and maximum pressure. The volume of the gas fraction is visible in Figure 14.
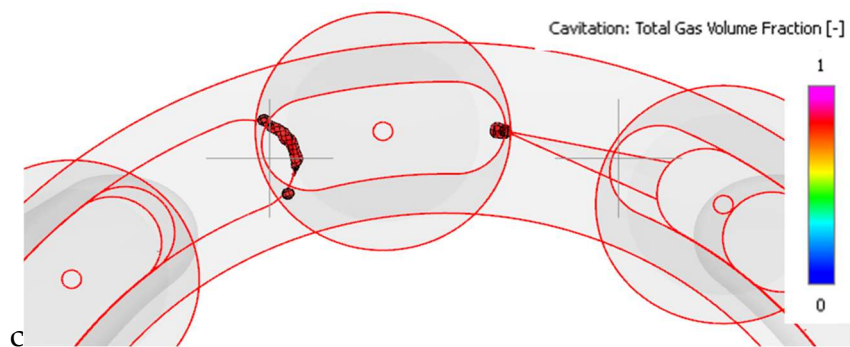
Figure 14. Total volume fraction iso-surface

An endurance test has been performed at maximum power to validate the EDGM model:

- shaft speed: 1800 rev/min;

- delivery pressure (generated by the load valve): 275 bar.

29

The pump has been tested for 500 hours to create cavitation damage, then disassembled. The analysis confirmed cavitation in the transition area from suction to the pre-compression delivery groove, as visible in Figure 15.
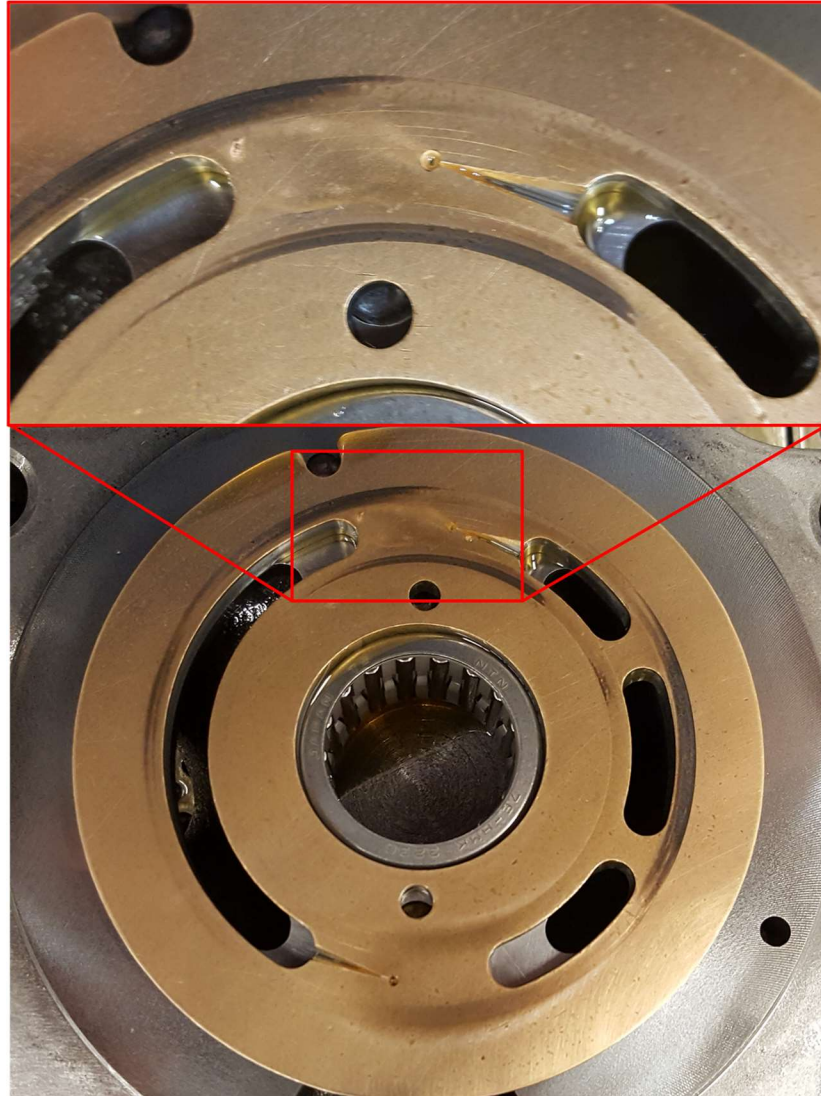
Figure 15. Cavitation erosion damage after 500 hours running at maximum power

The comparison confirms that the adopted numerical approach permits a high level of understanding of the unit's operation, finding the critical aspects and giving important information to the designer to improve the pump performance.

II.4.3   Lumped parameter model validation in dynamic condition

The lumped parameter model, as presented previously, is also capable of simulating the dynamic behavior of the pump since also the pressure compensator (PC) has been included in the numerical model using the same

approach. In particular, the swashplate dynamics have been investigated experimentally, measuring the dynamic pressure which controls the pump displacement. The pressure that controls the piston that regulates the pump displacement and the load (system) pressure has been acquired using a subplate with two fast pressure transducers located under the PC valve's mounting interface, as shown in Figure 16.
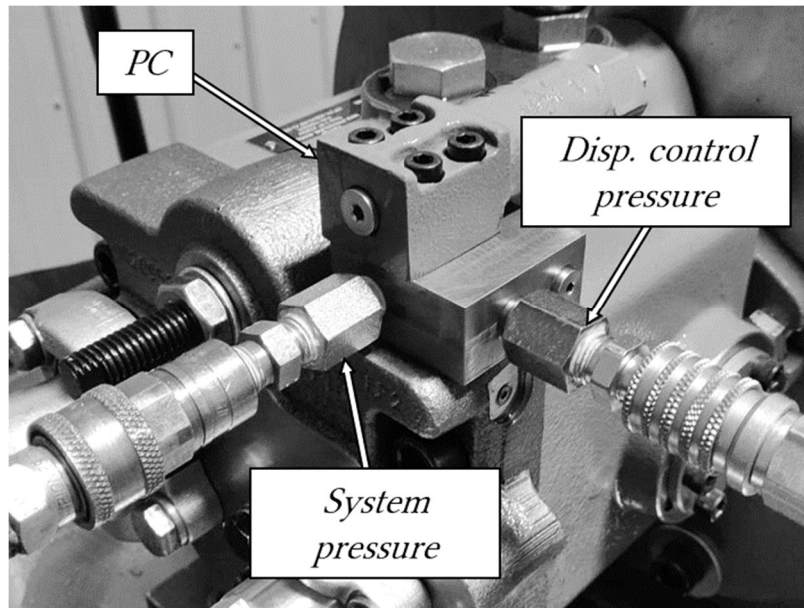
Figure 16. Experimental set-up used for the piston control pressure acquisition

Figure 17 and Figure 18 show two diagrams, where to check pump's performance, a comparison between an experimental test and the numerical simulation has been presented.

The load valve, a Duplomatic DSPE7 directional closed center valve with proportional control, has been used for this typical test. The valve has been gradually opened at 1800 rev/min from a closed condition to achieve a minimum pressure in the system. It has been closed in the same way to achieve the initial state. The simulation has been conducted similarly, where a valve with the same characteristics as the DSPE7 valve has been modeled. The comparison in Figure 17 presents a good overlapping of the numerical and experimental delivered flows as a function of the system pressure. To reduce the computational time, only the high-pressure side of the curve has been simulated. Figure 18 presents the control pressure p_{CP} as a function of the system pressure for the same test. The control limits the maximum system pressure set in the pressure compensator (PC). For this example, maximum pressure of 240 bar has been set for the PC. As

visible from both figures, the numerical model, including the PC valve, has the same experimental data behavior.
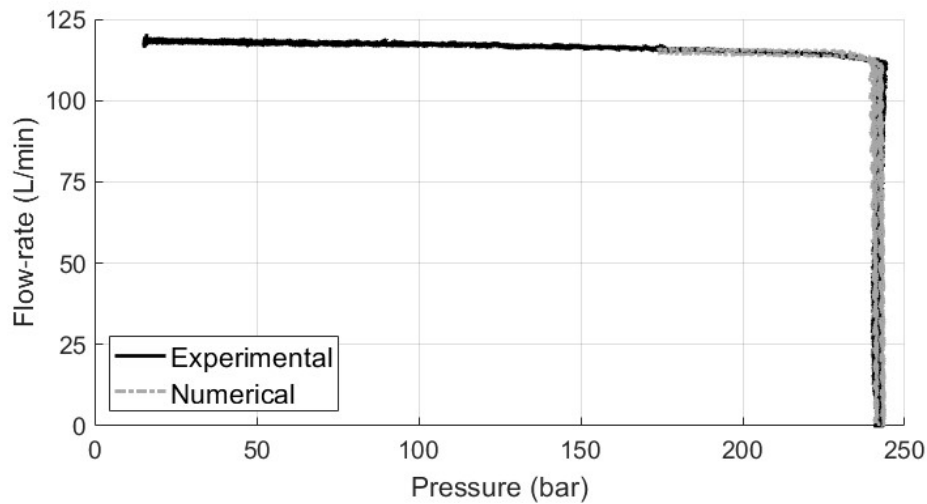
Figure 17. Comparison between an experimental performance test and the numerical model: pump flow-rate vs. system pressure
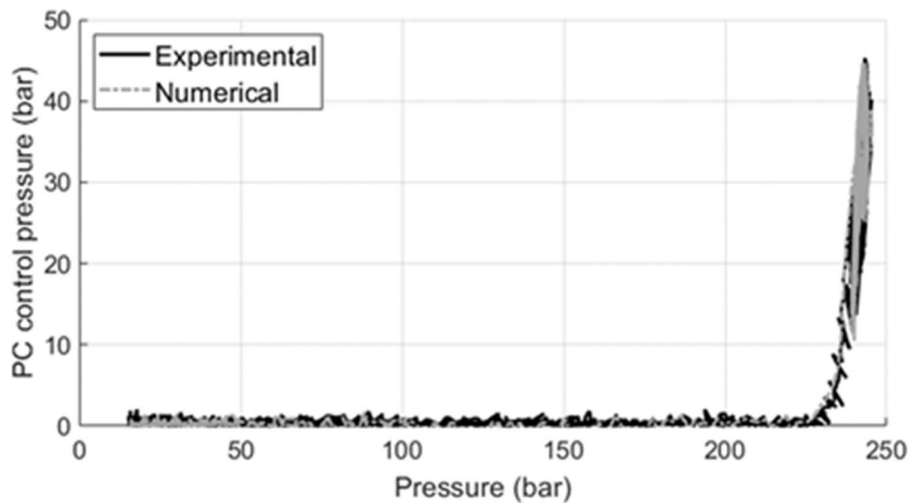
Figure 18. Comparison between an experimental performance test and the numerical model: PC pressure vs. system pressure

The same set-up has been used to run an additional test, different from the typical one showed in the two previous figures (from no flow – maximum pressure to maximum flow – minimum pressure and vice versa). This well-known test is made to check the pump's dynamic response and consists of a sudden closure of the load valve. A comparison between the numerical data and the experimental results has been done with the acquired data and presented in Figure 19 and Figure 20.
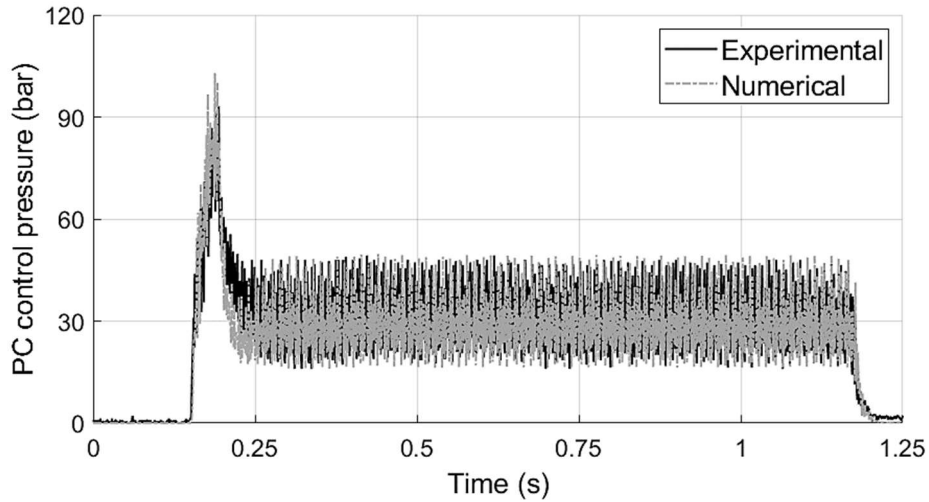
Figure 19. Comparison between an experimental dynamic response test and the numerical model: PC pressure vs. time
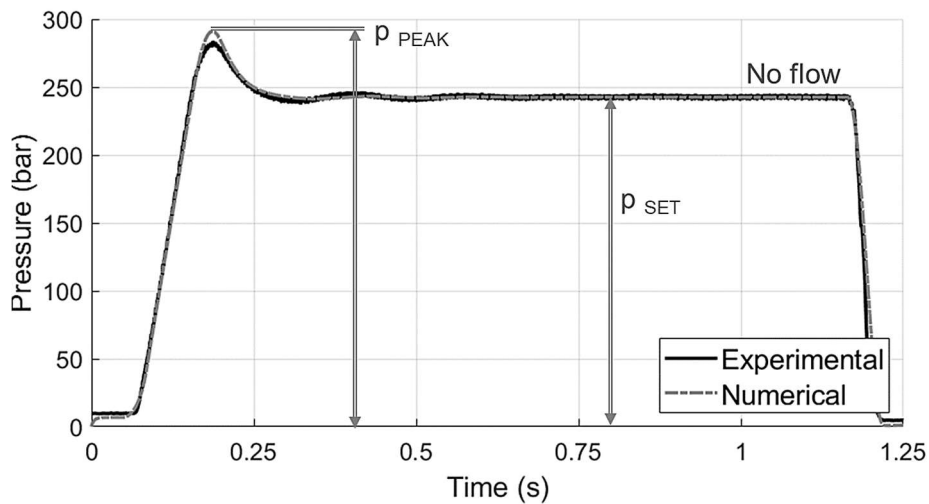
Figure 20. Comparison between an experimental dynamic response test and the numerical model: system pressure vs. time

The system layout has been integrated into the numerical model to better match the experimental setup, particularly the pipe dimensions, stiffness, and bulk modulus. With this consideration, the numerical model can predict the pump step response with a high agreement.

Another significative numerical result is presented in Figure 21 with the swashplate angle as a function of time.
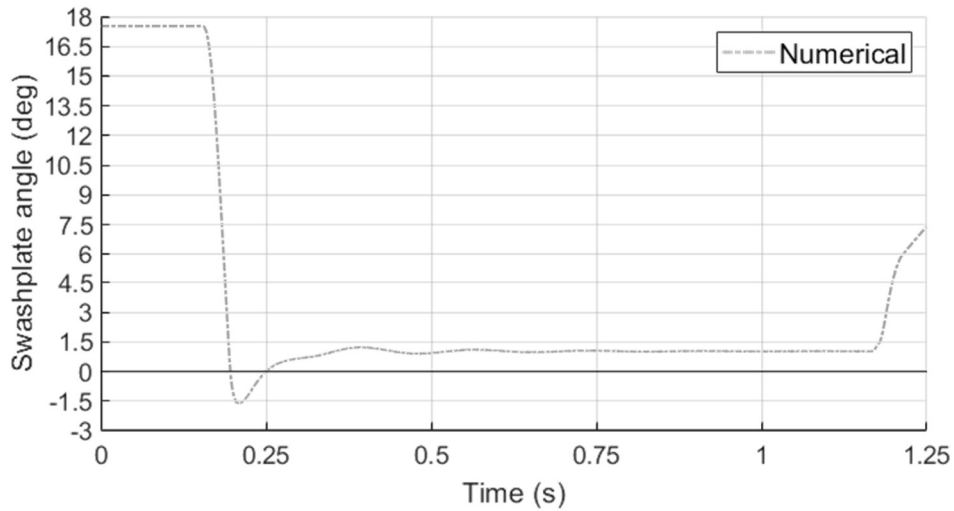
Figure 21. Numerical result: pump swashplate angular position

As already seen in Figure 20, during the first phase (0 - 0.16 s), the system pressure increases since the load valve suddenly closes (it takes around 0.08 s to switch from fully open to fully closed). When the system pressure achieves the maximum allowed pressure, set by the PC p_{SET}, the PC valve starts working and meters some oil to the control piston chamber so that its stroke reduces the pump displacement. At 0.20 s the system's dynamic response causes a peak of pressure, generating, as a consequence, a negative displacement of the pump (0.21-0.25 s). The pump then achieves a stable value of β around 1 degree necessary to hold the system pressure and compensate for the leakages. In Figure 22, the numerical torque T_{CP}, evaluated with equations (16) and (22), is presented. This torque is the sum of two components; one is exerted by the control piston itself, while the other, due to the bias spring, opposes.
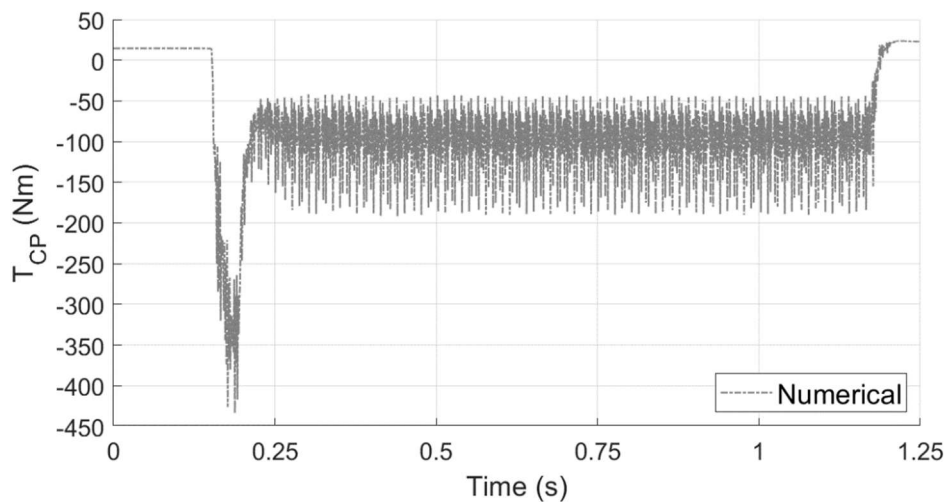
Figure 22. Numerical result: torque acting on the swashplate

34

The trend in Figure 22 starts from a constant value from the bias spring. In the time interval (0.21-0.25 s), when the displacement of the pump is negative, the torque decreases, achieving the value of 425 Nm and, at that point, increases, starting to oscillate around an average value of 100 Nm.

Other relevant quantities, useful for the design and displacement control of an axial piston pump, are calculated with equations (24) and (25). The results for one revolution at 1800 rev/min and 280 bar, as a pressure boundary condition, are shown in Figure 23 and Figure 24.
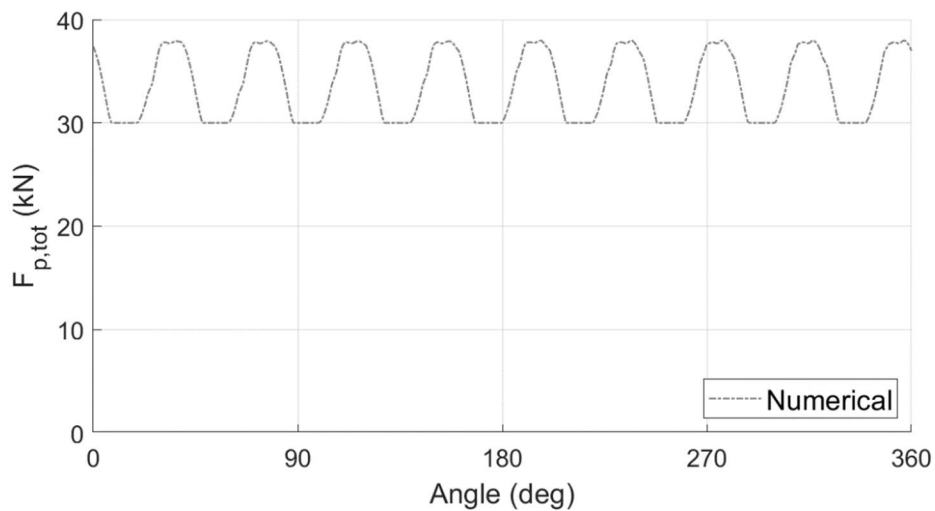
Figure 23. Numerical result: total force on the swashplate

The first one shows the total pressure force exerted by the nine pistons on the swashplate ($F_{p,tot}$), while the next one shows the position of $F_{p,tot}$ on the plane ($x'y'$). This figure shows the typical butterfly pattern characteristic of a pump with an odd number of pistons.
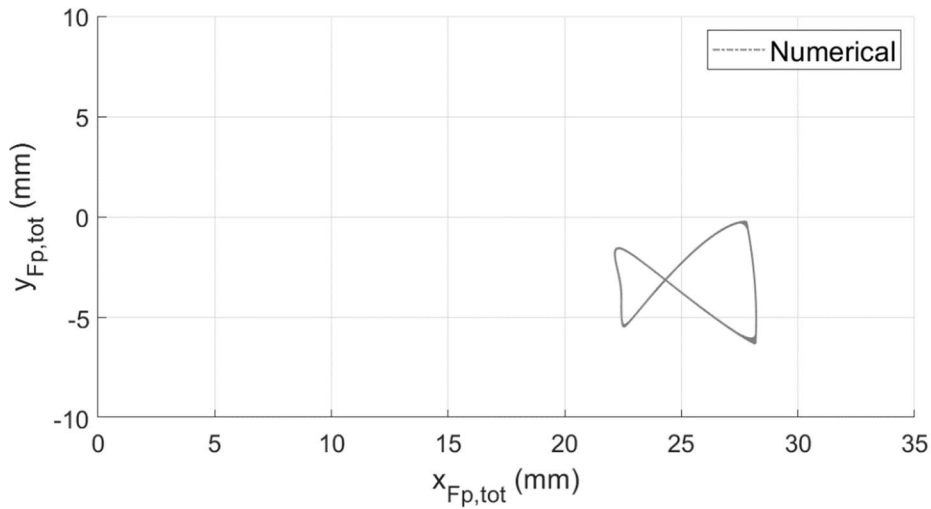
Figure 24. Numerical result: the position of the total force on the swashplate

II.4.4 Validation on pressure ripple

As a further analysis, both numerical models (3D CFD and lumped parameter) have been validated for pressure ripple, measured in different steady-state conditions.
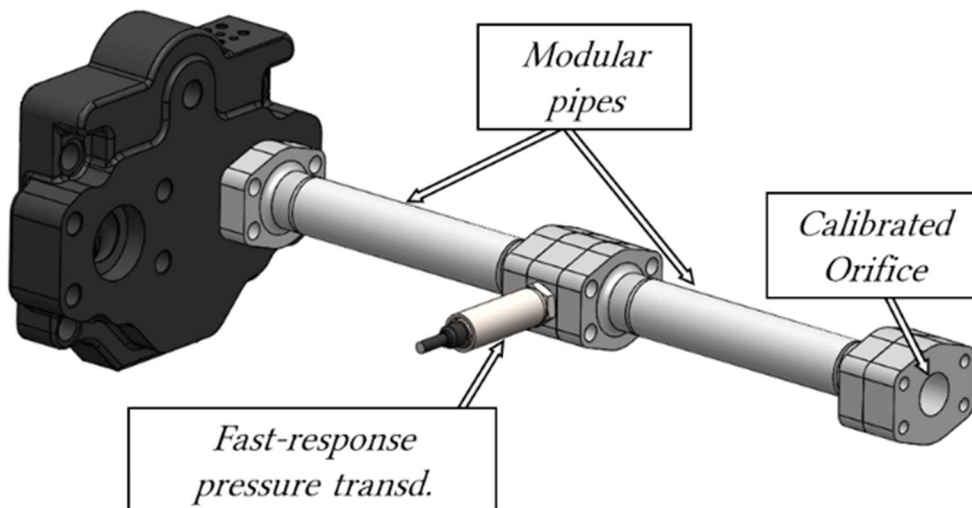
Figure 25. Set-up to measure pressure ripple: CAD model

For this purpose, the pump delivery port has been connected through two modular pipes (see Figure 25 and Figure 26) to calibrated orifices, generating different loads.

Figure 26. Set-up to measure pressure ripple: Test rig

This simple configuration allows the reduction of system reflection and can be easily implemented in both numerical models. Particular attention has been reserved for selecting the fast-response pressure transducer used to measure the pressure ripple. Model PD 4000, manufactured by Parker-Hannifin, has been chosen for the purpose, with a measuring range of 0-400 bar, a response time lower than 1 ms, and an accuracy of 0.5% FS. The modular pipe has a length of 482.6 mm and an internal diameter of 24.3 mm. The transducer is held by special support and located between the two pipes (Figure 25).

In Figure 27, Figure 28, Figure 29, and Figure 30, some comparisons, in both time and frequency domains, of the measured and simulated pressure ripples are presented. The acquired pressure ripple has been filtered with a low-pass filter with a cutoff frequency of 3000 Hz to remove signal noise. For completeness, both signals (filtered and unfiltered) are presented. Figure 27 shows results obtained at 2000 rev/min with a calibrated orifice diameter of 5 mm.
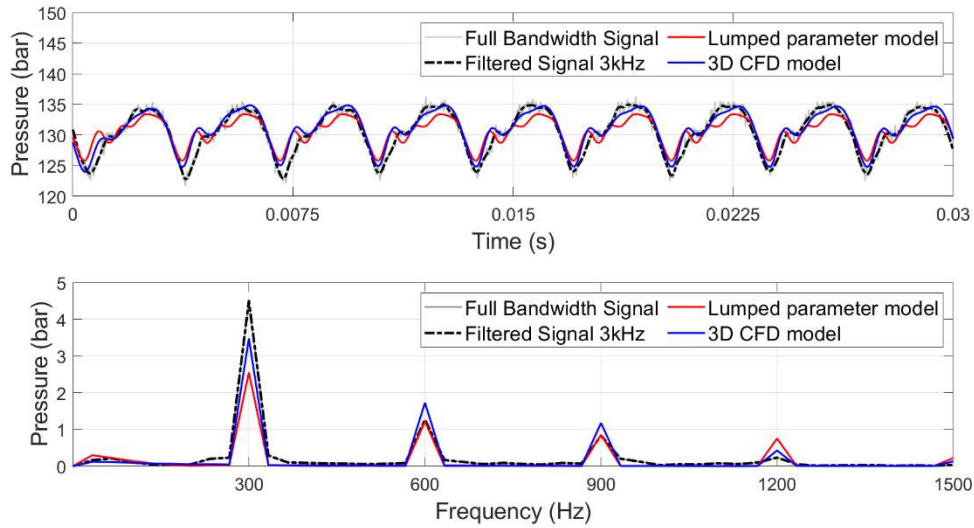
Figure 27. Model validation: 2000 rev/min, 5 mm orifice diameter.
Pressure ripple (time and frequency domains)

Figure 28, instead, shows the pressure ripple comparison for a pump shaft rotational speed of 1800 rev/min with the same calibrated orifice diameter of 4 mm.
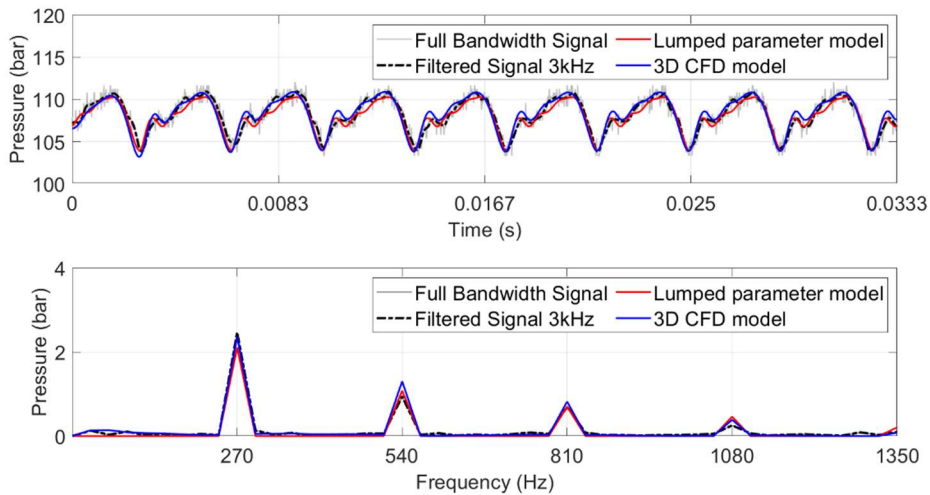
Figure 28. Model validation: 1800 rev/min, 5 mm orifice diameter.
Pressure ripple (time and frequency domains)

The same plots have been shown for 1500 rev/min and 1300 rev/min in Figure 29 and Figure 30.
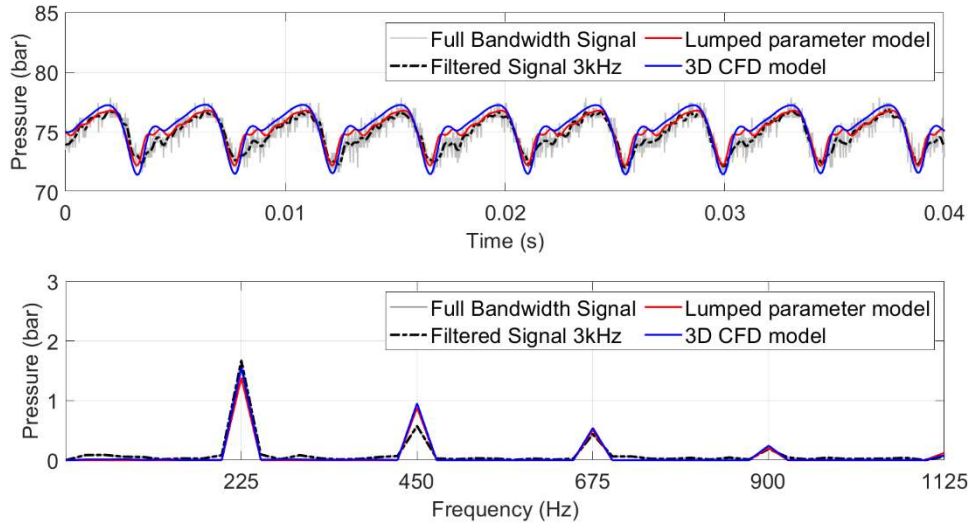
Figure 29. Model validation: 1500 rev/min, 5 mm orifice diameter.
Pressure ripple (time and frequency domains)
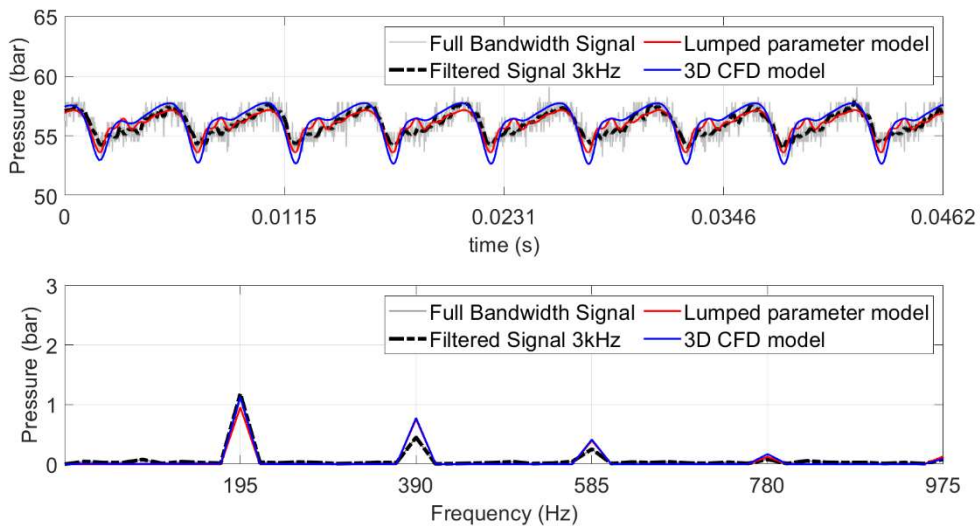
Figure 30. Model validation: 1300 rev/min, 5 mm orifice diameter.
Pressure ripple (time and frequency domains)

From the comparison of the presented results, it is visible the robustness of both approaches. It is important to remark how the model predicts mean values, amplitudes, and trends accurately in the time domain. The first fundamental has the highest value for both figures as expected.

Thanks to these in-depth validations, the two methodologies have been used for optimizations.

II.5 Numerical optimization with the lumped parameter model

Because of complete parametrization, the model can be used in an optimization process for designing a new valve plate geometry (later called optimized timing) to achieve a reduction of the flow ripple to lower the pump noise.

II.5.1 Optimization process: the NLPQL algorithm

An optimization process aims to find the best design (parameter settings) that matches a given objective (minimize a value) and does not violate the constraints.

$$
\begin{aligned}
&\min f(x) \\
x \in \mathbb{R}^n \quad &g_j(x) \geq 0 \quad j = 1,...,m \\
&x_l \leq x \leq x_u
\end{aligned}
\tag{43}
$$

f is the objective function, and the g_j (j=1,...,m) functions represent the constraints. Constraints are different from bounds. Indeed, bounds are known a priori and are never violated, whereas constraints are known as a posteriori and are something that the algorithm tries not to violate.

The Non-Linear Programming by Quadratic Lagrangian (NLPQL) algorithm is based on gradients and is an iterative process. It tries to decrease the objective function to zero. For this, it computes the gradients of the objective function and constraints in all directions available in the design space (each input parameter involved in the optimization process is a direction).

II.5.2 Optimization process: the objective function

In this study, the target is to find an appropriate set of parameters (valve plate geometries) to minimize the "Non-Uniformity Grade" (NUG) [1] and to keep the constraints not violated. The optimization process to reduce the fluid-borne noise has been done on the valve plate geometry using an NLPQL method, where the selected objective function is the NUG (44).

$$NUG = \frac{\Delta Q}{Q_{AVG}} = \frac{Q_{MAX} - Q_{MIN}}{Q_{AVG}} \qquad (44)$$

The definition of the objective function is given in equation (45).

$$Objective\ Function : \ min\ \left(NUG \right) \qquad (45)$$

This objective function has a simple interpretation: it tends to minimize the "Non-Uniformity Grade".

II.5.3 Optimization process: the input parameters and constraints

The optimization's input is the valve plate design (Figure 31), while the maximum pressure of 280 bar has been used as an assumption for the simulation's boundary condition. Optimization constraints were put on the pump's initial volumetric efficiency so that the algorithm will automatically exclude all the designs that excessively reduce this volumetric efficiency.
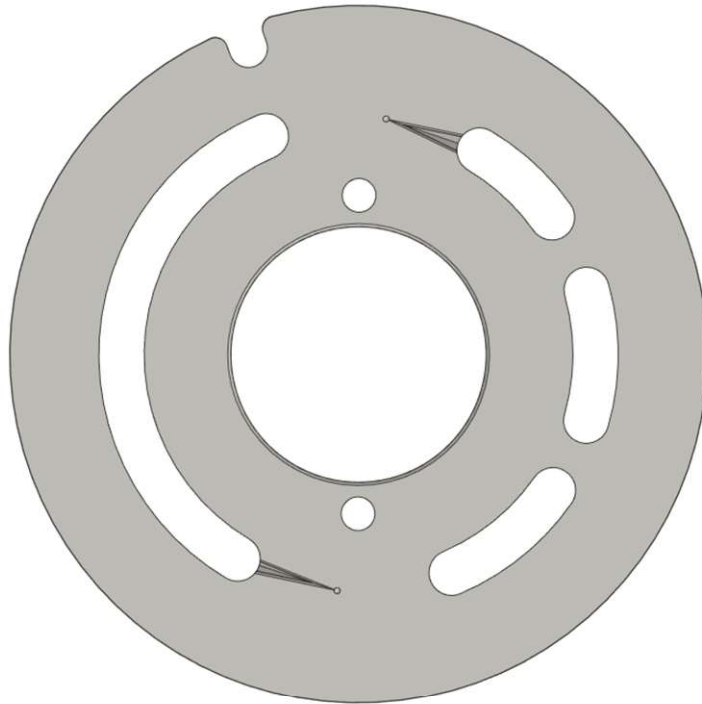
Figure 31. Valve plate not optimized geometry

II.5.4   Optimization process: the best design

Thanks to the NLPQL algorithm, a set of parameters resulting in the NUG reduction has been found. This algorithm presents the advantage of performing a few runs that give precise results. Note that the algorithm can stop at a local minimum. The success depends on the starting point's choice, and it is up to the user to be careful.

The optimization process took 148 iterations to be completed successfully, as shown in Figure 32.
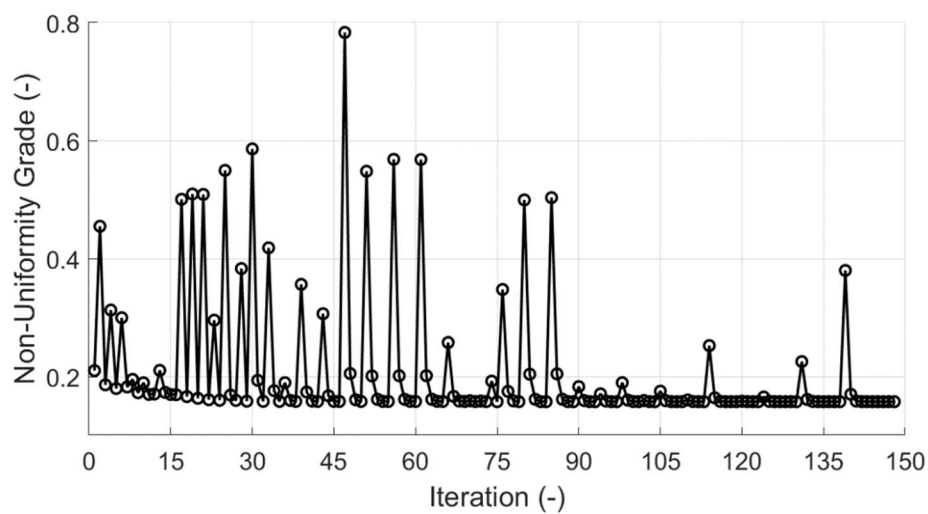
Figure 32. Value of the NUG during the optimization process

The best design parameters resulting from the process have been presented in Table 2.

Table 2. Optimization results

INPUTS	Units	Initial Design	Best Design
Starting angle suction kidney	(deg)	25.44	25.55
Closing angle suction kidney	(deg)	164.79	166.35
Starting angle of decompression groove	(deg)	4.26	4.21
Height of decompression groove	(mm)	0.076	0.077
Slope of the decompression groove	(deg)	8.40	8.46
Starting angle delivery kidney	(deg)	25.44	24.20
Closing angle delivery kidney	(deg)	161.70	165.25
Starting angle of compression groove	(deg)	5.73	5.66
Height of compression groove	(mm)	0.102	0.103
Slope of the compression groove	(deg)	12.12	8.94
OUTPUT	Units	Initial Design	Best Design
Non-Uniformity Grade	(-)	0.210	0.159

As shown in Table 2, a 24.30% effective reduction of the NUG has been achieved with the optimization process. Flow ripple at pump outlet and A_{HP}-A_{LP}, used in equations (3) interface areas for the CV_1, is presented in Figure 33 and Figure 34.
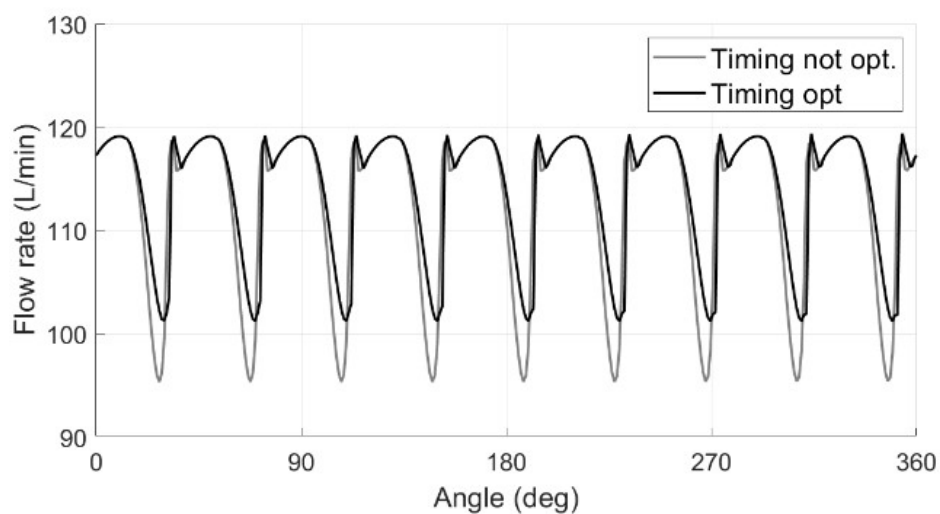
Figure 33. Results before and after the optimization process: flow ripple
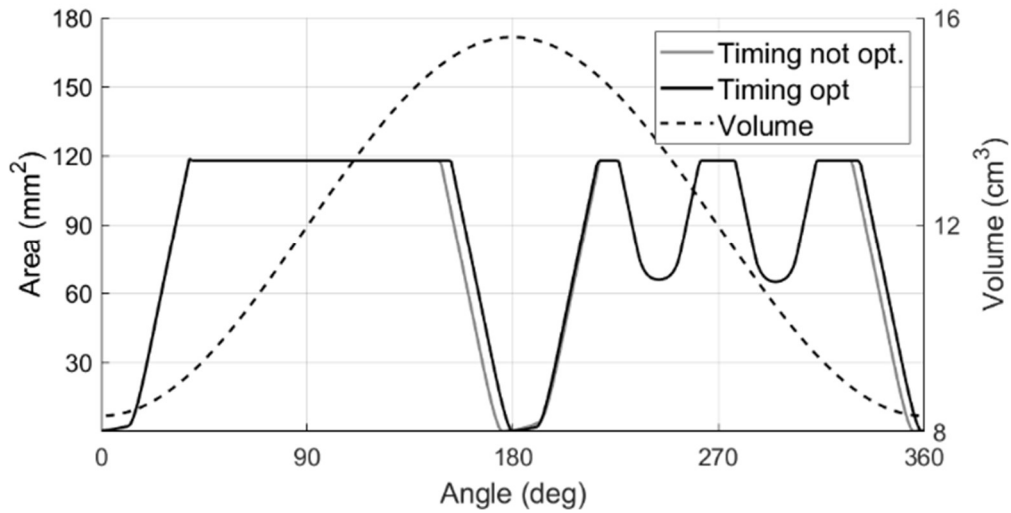
Figure 34. Results before and after the optimization process: interface areas of the CV1

Figure 33 shows that the flow ripple amplitude has been reduced, and, at the same time, the volumetric efficiency is improved around 1% at maximum pressure since the average outlet flow increased. A prototype based on the best design, presented in Table 2, has been manufactured. The pressure ripple has been measured with the same approach already shown in section 2.4.4. Figure 35 compares the measured pressure ripple of the initial and the best design for the same working condition. It is evident in the figure a significant reduction of oscillation amplitude, around 18.5%. From the plot of the pressure ripple in the frequency domain, it is notable a reduction mainly on the first two fundamental frequencies.
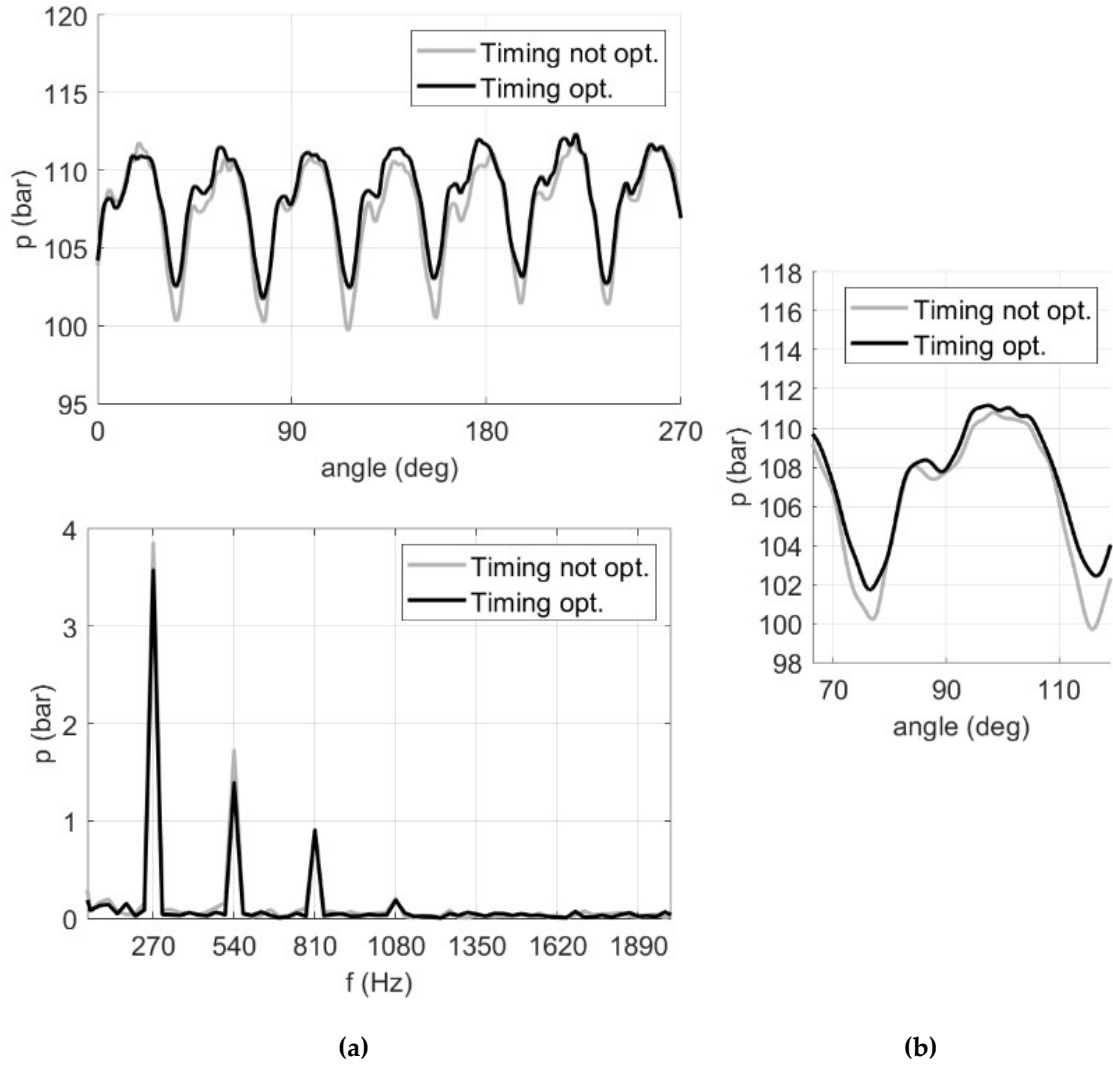
Figure 35. Initial and best design comparison: 1800 rev/min, 5 mm orifice diameter. Pressure ripple (time and frequency domains) (**a**), single pressure ripple (**b**)

Figure 36 shows an interesting result obtained from the numerical model; the best design also reduces the void fraction during the transition from suction to delivery (when the CV_1 is at BDC) after the optimization process. The void fraction is defined as:

$$Void\_Fraction = \frac{V_{air} + V_{vap}}{V_{liq} + V_{air} + V_{vap}} \cdot 100\% \tag{46}$$

Where V_{air} is the volume of undissolved air/gas, V_{vap} is the vapor volume, and V_{liq} is the volume of pure liquid inside the CV.
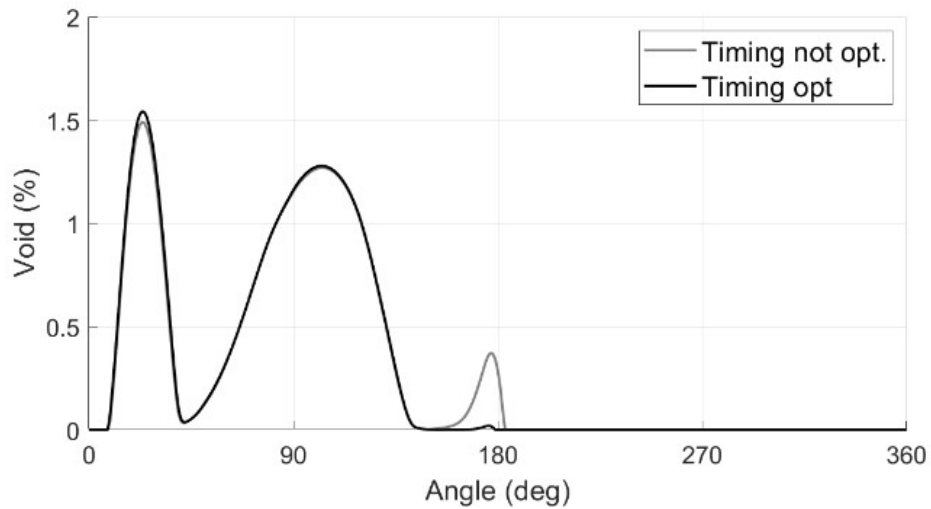
Figure 36. Results before and after the optimization process: the void fraction of the CV_1

This transition has particular importance since it is located in a valve plate area, where gas bubbles, released from the solution, could collapse during pre-compression, producing high cavitation erosion. For completeness, also, the CV_1 pressure during one revolution is presented in Figure 37.
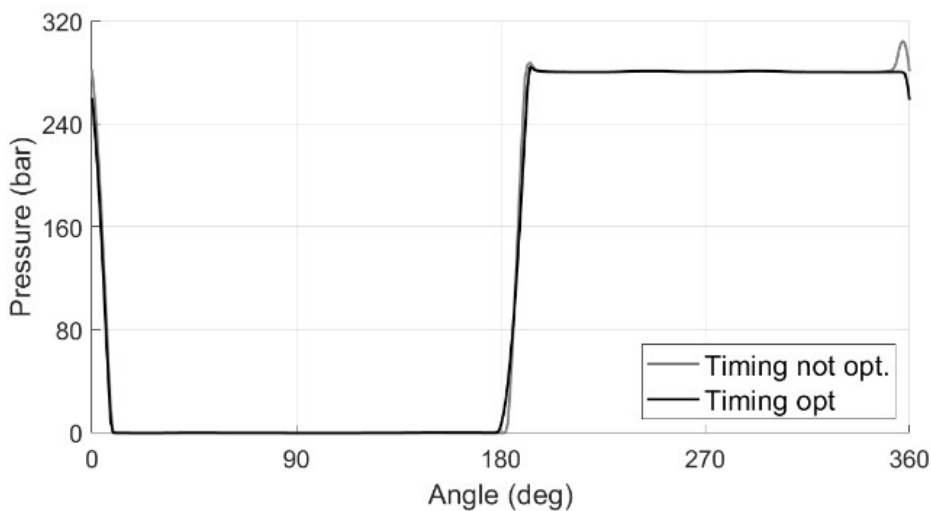
Figure 37. Results before and after the optimization process: the pressure of the CV_1

The erosion reduction has been proved by prototyping the best design and running an endurance test of 500 hours at maximum power (1800 rev/min at 280 bar). Figure 38 shows a comparison of the damage caused by the cavitation erosion on both valve plates (initial design and optimized best design).

(a) **(b)**

Figure 38. Cavitation erosion damages after the maximum power test: initial design inspection after 150h (**a**), best design inspection after 500h (**b**)

The tests have been done with programmed inspections every 50 hours. The picture in Figure 38(a) shows the valve plate (initial design) damage status after the third inspection (150 hours), capturing the transition areas of the valve plates from suction to delivery. At that point, the test has been suspended since the volumetric efficiency dropped as a consequence of the valve plate erosion due to the cavitation. The second picture (b), instead, shows the valve plate (best design) status after the last inspection (500 hours). In this test, no appreciable variations have been observed in the volumetric efficiency. Therefore, it is notable how the erosion has been substantially reduced, as predicted by the model in Figure 36.
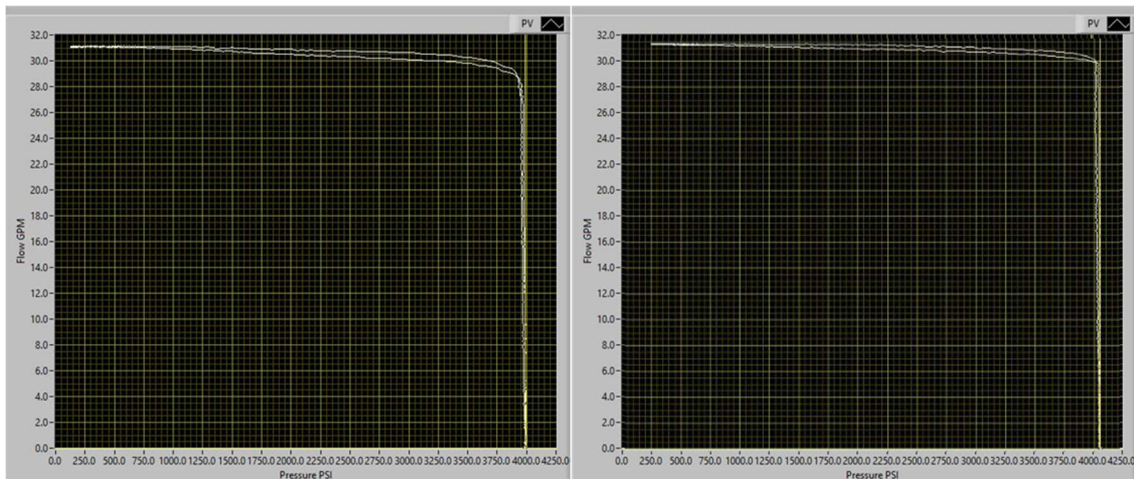
(a) **(b)**

Figure 39. P-Q curve before inspection: Initial design after 150h (**a**), best design after 150h (**b**)

Finally, in Figure 39, the standard performance curves for a pressure compensated pump have been reported. The increment of volumetric efficiency

with the new design of the valve plate at maximum power is notable. The x-axis reports the pressure (in psi) while flow-rate (in USgal/min) on the y-axis.

II.6 Pressure ripple reduction with a PCFV: a 3D CFD analysis

II.6.1 Pre-compression Filter Volume (PCFV) and pre-compression relief groove introduction

Diffusion of pressure relief grooves and pre-compression filter volume (PCFV), also known as pre-compression volume (PCV), in an axial piston pump permits to reduce flow ripple compared to a traditional design. As said, the flow ripple is the main cause of the fluid borne noise. The flow ripples can be reduced by minimizing the reverse flow rate back to the cylinder [27], acting as said on the valve plate design. PCFV has been studied for years, and it has been demonstrated to help with the reduction of flow ripple. For this reason, an analysis has been done, introducing this idea to the studied pump. The PCFV has been implemented in the axial piston pump to reduce the sensitivity to variations in operational conditions, as shown in Figure 40.
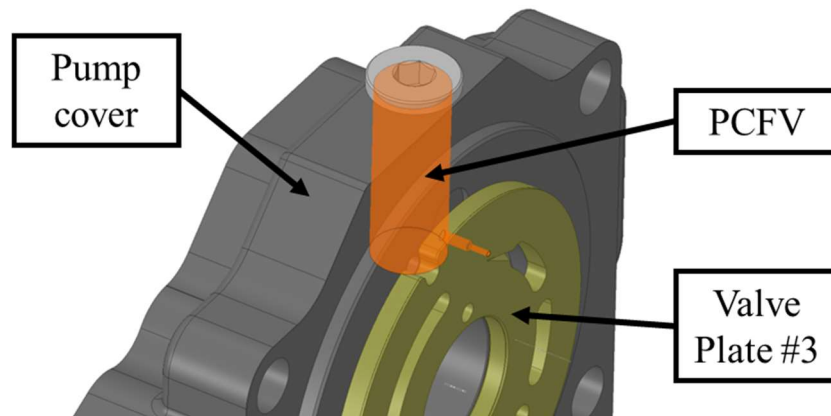
Figure 40. The PCFV highlighted in the pump cover

(a)   **(b)**
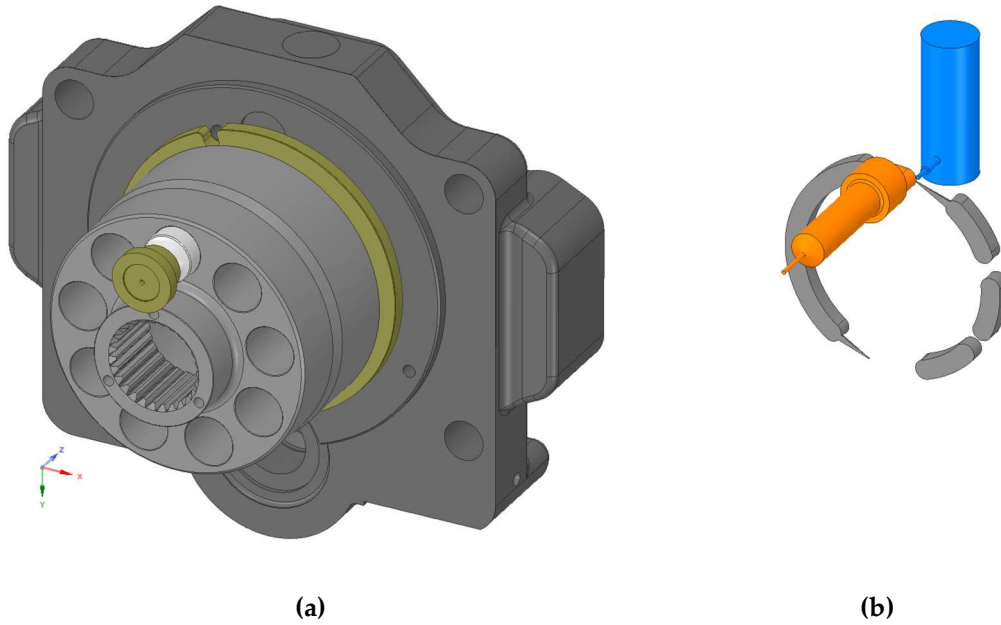
Figure 41. PCFV: CAD model (**a**), extracted fluid volume (**b**)

Concerning the images in Figure 42, the working principle of the PCFV has been explained. The pressurized fluid volume of the PCFV gives a small amount of discharge flow to the cylinder at low pressure before connecting to the delivery port.
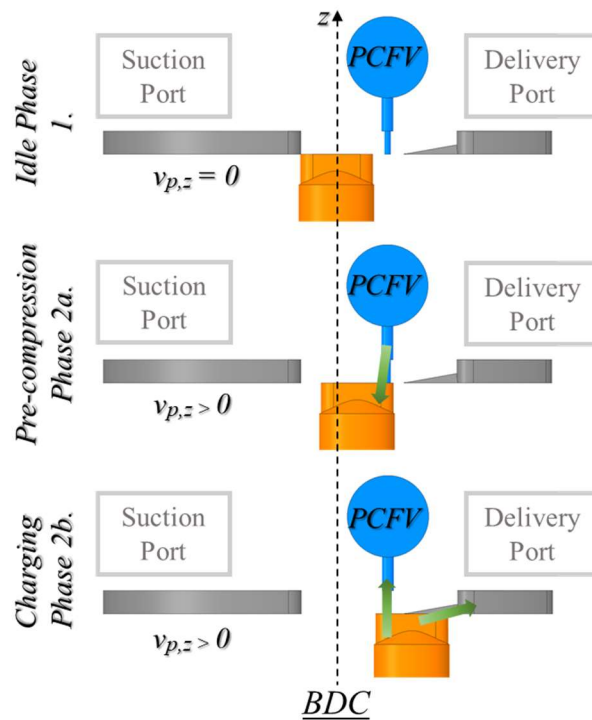
Figure 42. PCFV: working phases

This pressurized fluid is not taken directly from the delivery port but through an auxiliary volume (the PCFV), reducing, in this way, the reverse flow from the delivery port. The pre-compression through the PCFV can be divided into two phases. In the first one, the PCFV quickly pressurizes the linked cylinder while, in the second phase, the cylinder is connected to delivery and PCFV. After the pressure equalization among the volumes, a small amount of fluid flows from the cylinder to the PCFV. In this way, the pre-compression volume is recharged, becoming ready to pre-pressurize the next cylinder.

The model used for this study is the already presented one in the previous paragraph 2.3. The analysis of the PCFV has been done only numerically. Two new configurations have been studied; the first one is optimizing the valve plate's pre-compression groove geometry. The second configuration uses the same valve plate, but the PCFV has been added. In particular, the analyzed designs are the following:

- Valve plate #1: which is the preliminary design of the valve plate;

- Valve plate #2: which is the first new design with the optimized pre-compression relief groove and the timing;

- Valve plate #3: which has the same geometries as Valve plate #2 with the PCFV implementation.

Numerical simulations have shown a drastic reduction of the discharge ripples from the initial geometry of almost 40% by adding the pre-compression filter volume.

II.6.2   Valve plate designs

The first proposed design has been obtained, modifying the pressure relief groove to reduce flow ripple and improve the volumetric efficiency. Improvement of the efficiency can be ensured if the relief groove (on the delivery side) is not reached before the cylinder port (in black in Figure 43) is disconnected from the inlet kidney.
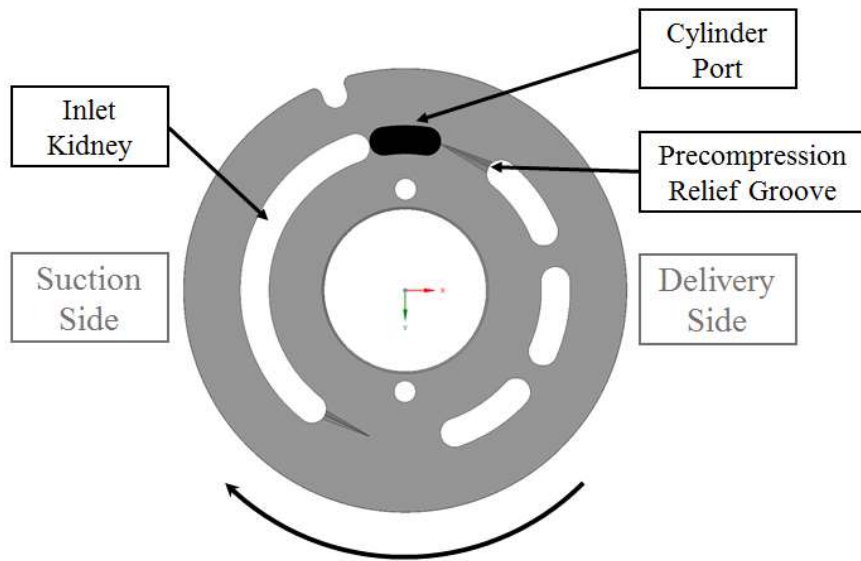
Figure 43. Valve plate #2 with precompression relief groove optimized

The second proposed design has been developed based on Valve Plate #2. The valve plate has been modified, adding a PCFV (in blue in Figure 41(b)) as suggested by Petterson [27], where the ratio between the PCFV volume and the cylinder volume (dead volume included) is 3.
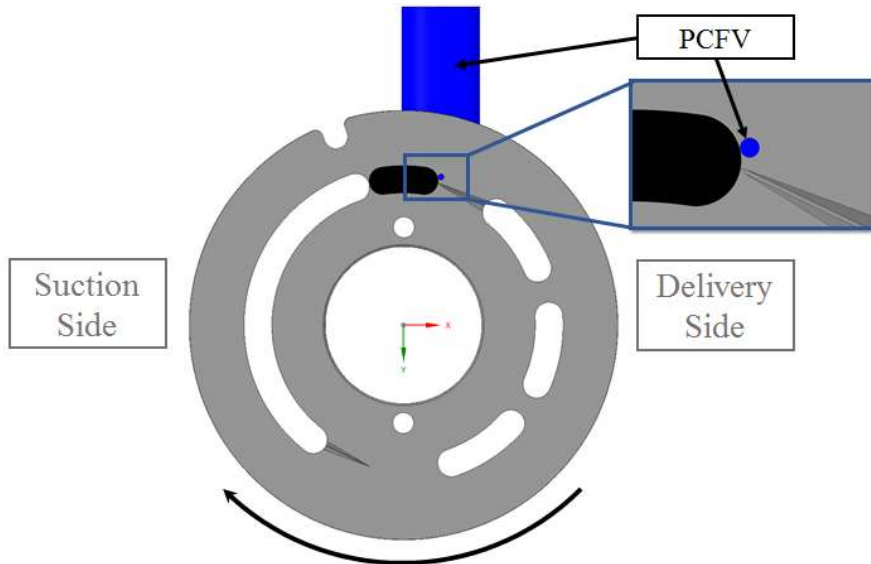
Figure 44. Valve plate #3 with Pre-Compression Filter Volume (PCFV)

II.6.3   Numerical results

Three numerical models, each for every valve plate, have been made to study the fluid-borne noise. All the simulations have been run under the

following operating condition: pump at maximum displacement (swashplate angle 17.5 deg), pump shaft speed of 1500 rev/min, delivery pressure of 280 bar. The pressure boundary condition has been realized through a calibrated orifice implemented at the end of the delivery tube, as visible in Figure 45.
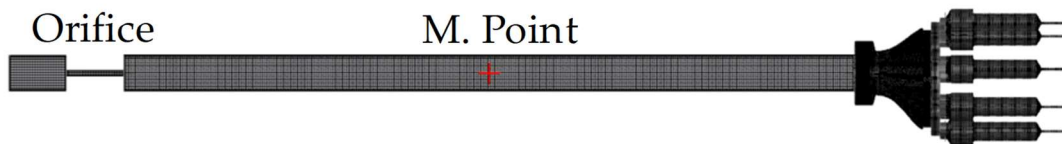
Figure 45. Mesh of the delivery tube

The pressure ripple has been measured through the monitoring point visible in red in Figure 45, in a central section of the delivery tubing.

The reduction of flow ripple achieved by introducing the PCFV is clear from Figure 46 and Figure 47, where the flow ripple and a zoomed view of a single flow ripple have been presented, respectively.
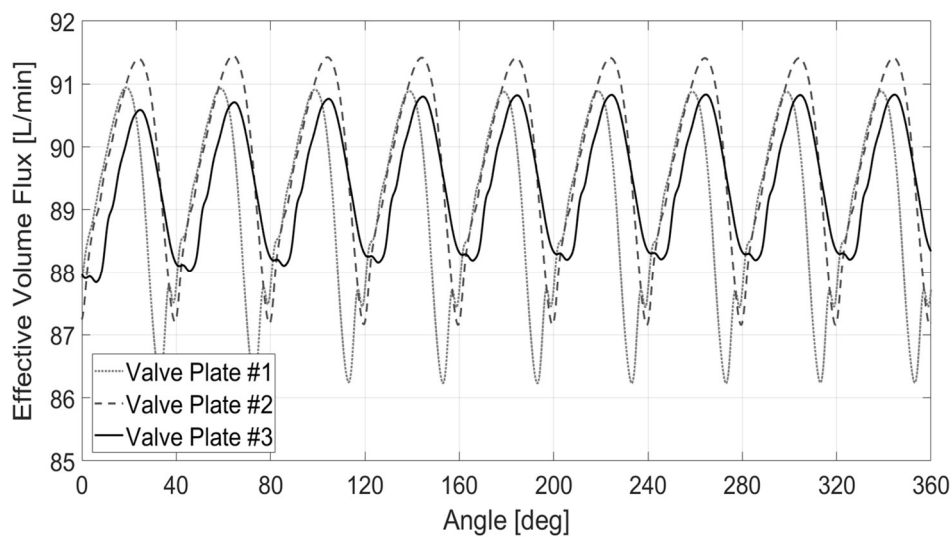
Figure 46. Numerical flow ripple at full displacement (1500 rev/min and 280 bar)

The reduction of the internal volumetric losses achieved by implementing the well-designed relief grooves is evident from Figure 46 and Figure 47. Valve plate #2 shows a small decrease of the flow ripple of around 7%, confirming an average delivery flow rate increment.
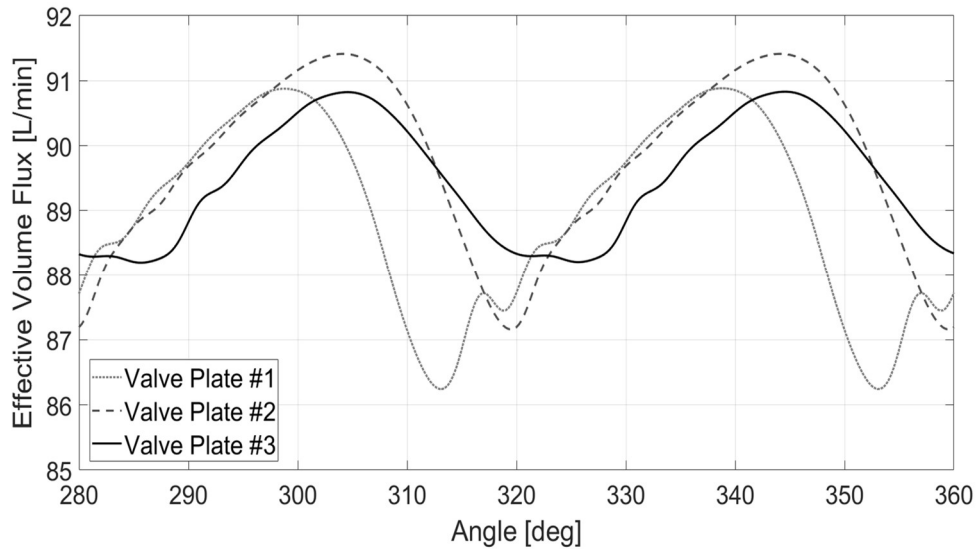
Figure 47. Numerical single flow ripple at full displacement (1500 rev/min and 280 bar)

The further reduction of flow ripple with Valve Plate #3 has been only obtained with the introduction of the PCFV (since both share the same geometries), attesting the flow ripple reduction around 40%, if compared to the Valve Plate #1. The same percentage reductions are notable on the pressure ripple from Figure 48 and Figure 49.
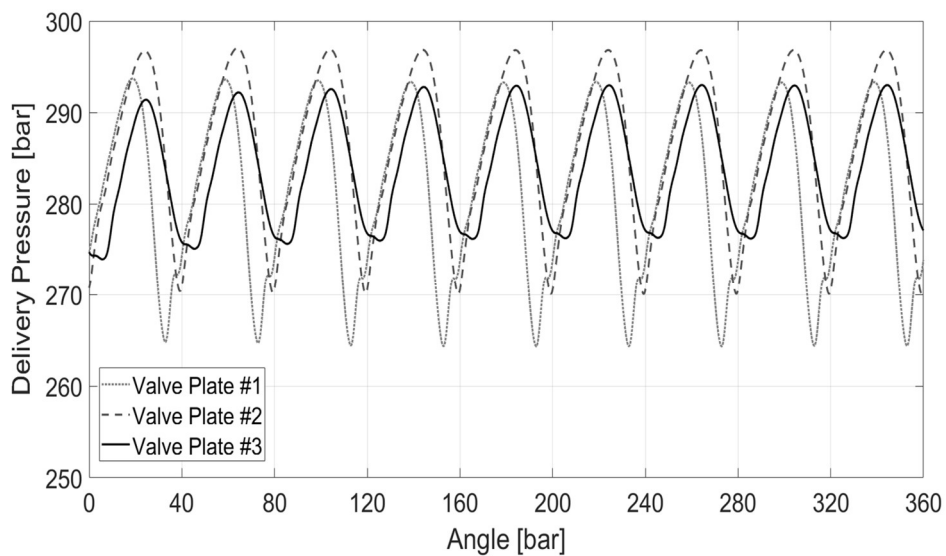
Figure 48. Numerical pressure ripple at full displacement (1500 rev/min and 280 bar)
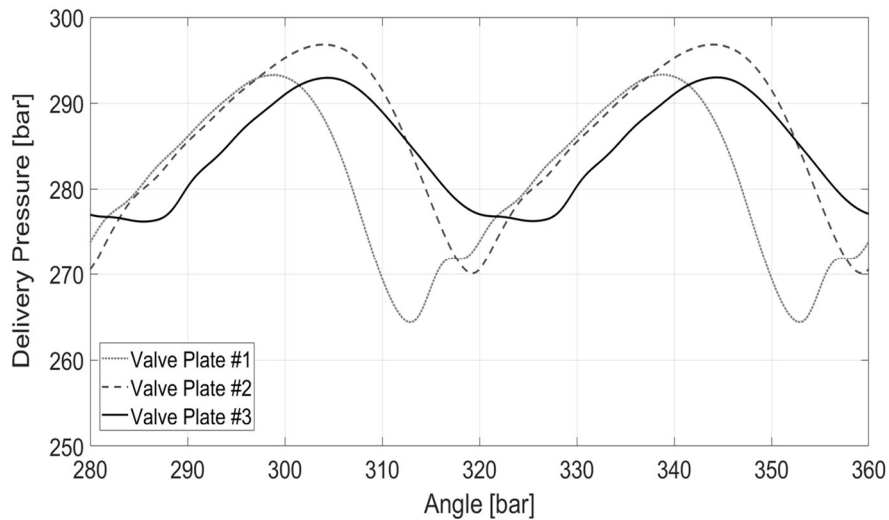
Figure 49. Numerical single pressure ripple at full displacement (1500 rev/min and 280 bar)

Figure 50 shows another crucial effect produced by introducing a PCFV; the cylinder pressurization with Valve plate #3 starts earlier (5÷6 degrees at these operating conditions) than Valve plate #2.
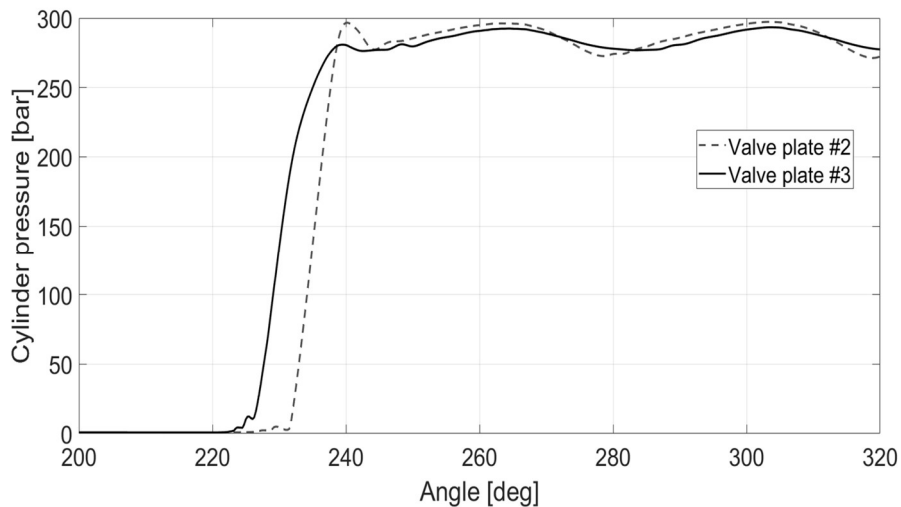
Figure 50. Numerical cylinder pressure at full displacement (1500 rev/min and 280 bar):
Comparison of valve plates #2 and #3

The early pressurization of the cylinder (in Figure 50) permits a reduction of the flow-rate from the delivery side back to the cylinder. This effect is also visible in Figure 51, where the reverse flow-rate from the delivery port to the cylinder is shown for each analyzed valve plate. The dotted line in the graph represents the reverse flow of the "Valve plate #1". The "Valve plate #1" timing is entirely different from the two optimized new valve plates, as is known from the figure

below. Looking at Figure 51, it is also evident that the "Valve plate #1" acts as a cross-flow, indeed during the first phase (around the angle 295 deg.), the port flow-rate does not reach the null value. Instead, trends of "Valve plates #2 and #3" go to a zero flow around the angle of 300 deg. It happens because, as said, "Valve plates #2 and #3" have the same timing. The dashed and the solid lines, relative to the "Valve plate #2" and the "Valve plate #3", respectively, reduce the reverse flow drastically; areas subtended to both curves are significantly less than the case with the "Valve plate #1". However, "Valve plate #3" achieves a reduction of the reverse flow higher than "Valve plate #2". This reduction depends only on the introduction of the PCFV, where, as said, the timing is the same. Therefore, the supplementary volume of the PCFV can influence the flow ripple, as shown in Figure 46. The flow ripple is remarkably related to the reduction of the reverse flow.
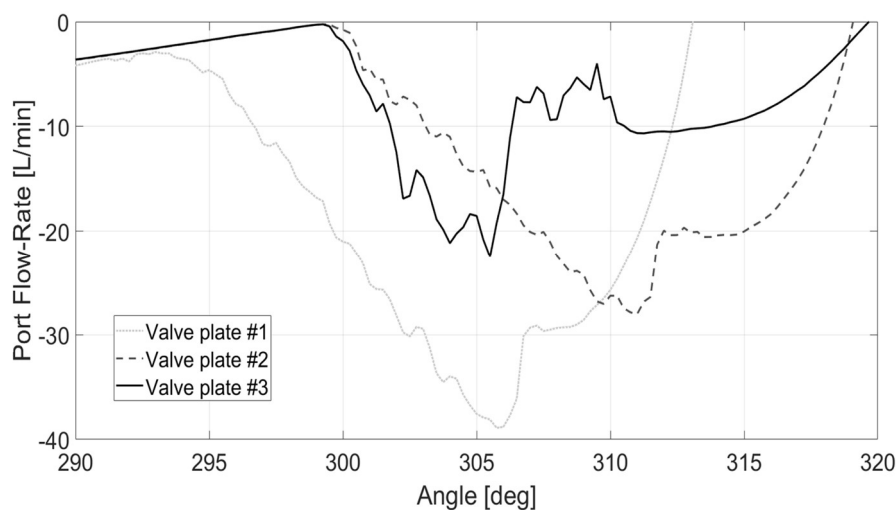
Figure 51. Numerical cylinder port reverse flow at full displacement (1500 rev/min and 280 bar)

The numerical analysis presented in this subparagraph demonstrates the effective reduction of the fluid-borne noise achieved with the optimization of the pre-compression groove and the introduction of the PCFV.

II.7 Conclusions

In this Chapter, two different numerical approaches have been deeply presented for studying axial piston pumps. Their development has been crucial for understanding how the fluid-borne noise can be analyzed and subsequently

reduced, working on the flow ripple reduction and avoiding cavitation occurrence, which is recognized as a very noisy phenomenon.

The first presented approach is based on the control volume approach, where each CV has homogeneous properties, such as pressure, temperature, etc. All the CVs are connected by variable orifices, calculating the flow rate as a pressure drop function. The developed numerical model has been validated comparing results with experimental data supplied by Duplomatic MS, the pump manufacturer, showing a high agreement for both steady-state and dynamic working conditions.

By means of the validated model, optimization of valve plate geometry has been conducted using a Non-Linear Programming by Quadratic Lagrangian (NLPQL) method to reduce the fluid borne noise. The well-known "Non-Uniformity Grade" has been chosen as the objective function. The algorithm has reduced the NUG by 24.30% after 148 iterations.

Based on the best design, the new valve plate prototype has been tested; a comparison between the acquired pressure ripples of the initial and the best design valve plates has been presented, showing a reduction of 18.5% on the amplitude for the presented working condition. In particular, a significative reduction has been seen in the frequency domain on the first two fundamental frequencies. Side benefits have been found on the volumetric efficiency and the cavitation erosion. The volumetric efficiency has been increased by 1%, and the flow ripple has also been reduced. Cavitation damage has been removed during the transition from suction to delivery (at BDC). The model's high capacity in predicting the pump behavior has been confirmed by tests done on the prototype, which demonstrated the significant reduction of erosion damage caused by cavitation.

Therefore, the first numerical approach presented in this Thesis constitutes a useful tool to design and optimize a positive-displacement piston pump. From an industrial point of view, it drastically reduces the prototyping and development cost and time. The optimized pump will be tested in an anechoic chamber, comparing the reference and the optimized pumps' noise.

The optimization process creates the best design for a single working condition, giving the user no guide about how to act on the valve plate geometries. To

discover the influence of single geometries changes, the pump's full working map should be optimized.

The second approach is based on a three-dimensional CFD methodology, which discretizes the governing equations, including conservation of mass and momentum, using a finite volume method. The used software (Simerics MP+) adopts the RANS approach to model the turbulent flow, using the standard "K-Epsilon" turbulence models. A cavitation module is needed for the pump model since a not-optimized pump can create circumstances where a pressure drop can cause a release of the dissolved air in the liquid out of the solution.

The model has been used mainly to study the effects of the reverse flow on the flow ripple. In particular, three valve plates have been analyzed for understanding the impacts of pre-compression grooves and pre-compression filter volume on the flow ripple; analysis that can be done only using a 3D CFD approach. Pressure relief grooves have been completely re-designed to improve the volumetric efficiency of the pump. Simultaneously, the introduction of the PCFV determined a surprising reduction of the flow ripple of almost 40%. This reduction also depends on the reverse flow's reduction from the delivery port to the cylinder.

This Chapter has also been shown a comparison of the two described approaches with the experimental data on the pressure ripple prediction. The comparison showed a perfect overlapping of numerical models in both time and frequency domain and for many working conditions.

Therefore, for investigating axial piston pumps, the three-dimensional CFD model is still vital for the lumped parameter model calibration. However, after a good calibration, the lumped parameter model can be used for the optimization processes, which are the most effective methodology for prototyping in the industry.

II.8 Nomenclature

Acronyms

Name	Descriptions
BDC	Bottom dead center
CAD	Computer-Aided Design
CFD	Computational Fluid Dynamic
CPU	Central Processing Unit
CV	Control volume internal
EDGM	Equilibrium Dissolved Gas Model
ISO	International Organization for Standardization
NCG	Non-Condensable Gas
NLPQL	Non-Linear Programming by Quadratic Lagrangian
NSGA-II	Non-dominated Sorting Genetic Algorithm II
NUG	Non-Uniformity Grade
RANS	Reynolds Average Navier-Stokes
TDC	Top dead center

Symbols

Name	Descriptions
a	Distance between the plane containing all the O_i'' centres of pistons heads (m)
A_{cp}	Control piston area (m²)
A_{HP}	Interface area at the delivery side (m²)
A_{LP}	Interface area at the suction side (m²)
A_p	Piston area (m²)
b	Distance between the shaft rotational axis and the swashplate rotational axis (m)
B	Effective bulk modulus (bar)
B_0	Liquid bulk modulus at 0 bar
B_1	Bulk modulus rising coefficient
B_L	Liquid bulk modulus
C	Camping coefficient
C_c	Cavitation condensation coefficient
c_d	Discharge coefficient
C_e	Cavitation evaporation coefficient
d_b	Cylinder diameter (m)
d_c	External piston diameter (m)
$D_{g,d}$	Diffusivity of the dissolved NCG (m²/s)
d_p	Piston diameter (m)
D_v	Diffusivity of the vapor mass fraction (m²/s)
ecc	Piston eccentricity (m)

F_{cp}	Force due the pressure acting in the control piston volume
$f_{d,equil,ref}$	Equilibrium mass fraction of the dissolved gas at the reference pressure
$F_{frict,i}$	Friction between piston and cylinder block
f_g	Mass fraction of free NCG
$f_{g,d}$	Free NCG mass fraction
$f_{g,f}$	Mass fraction of dissolved NCG
$f_{g,specified}$	User-specified value
$F_{p,i}$	Pressure force of the i-th piston (Pa)
$F_{p,tot}$	Pressure force (Pa)
F_{sp}	Cylinder block spring preload force (N)
F_{ss}	Viscous friction between slipper and swashplate
f_v	Mass fraction of the vapor
h_b	Average height (m)
$h_{ss,i}$	Height of the gap between slipper and swashplate (m)
$h_{r,i}$	Internal height of the flat orifice (m)
$h_{R,i}$	External height of the flat orifice (m)
J_{rg}	Inertia moment – rotating group
J_{sw}	Inertia moment – swashplate
K	Stiffness coefficient
k_{bs}	Spring constant
$l_{0,bs}$	Free length of the bias spring (m)
l_{bs}	Bias spring working length (m)
l_c	Contact length (m)
l_{cp}	Distance between control piston and swashplate rotational axes (m)
l_r	Internal length of the flat orifice (m)
l_R	External length of the flat orifice (m)
m_p	Mass of the piston – slipper assembly (g)
n	Number of pistons
$\vec{n}$	Surface normal of the surface σ
O	Pump shaft rotation center
O'	Swashplate center
O''	Piston head center
p	Pressure (Pa)
p_{case}	Pressure in the pump case (Pa)
p_{cp}	PC control pressure (Pa)
$p_{d,equil,ref}$	Reference pressure for the dissolved gas equilibrium mass fraction (Pa)
p_{HP}	High pressure (Pa)
p_i	Pressure of the i-th piston (Pa)
p_{LP}	Low pressure (Pa)
p_{mid}	Average pressure (Pa)

p_v	Phase-change threshold pressure (Pa)
Q	Flowrate (L/min)
Q_{avg}	Average value of the flow ripple (L/min)
$Q_{HP,i}$	Flow rate delivered by the i-th piston to the outlet port (L/min)
Q_i	Flow rate of the i-th piston (L/min)
$Q_{LP,i}$	Flow rate coming from the suction port that entering into the i-th piston (L/min)
Q_{max}	Maximum value of the flow ripple (L/min)
Q_{min}	Minimum value of the flow ripple (L/min)
$Q_{pc,i}$	Leakage between piston and cylinder of the i-th piston (L/min)
$Q_{ss,i}$	Leakage between slipper and swashplate of the i-th piston (L/min)
$Q_{vp,i}$	Leakage between cylinder block and valveplate of the i-th piston (L/min)
$Q_{vpr,i}$	Leakage between cylinder block and valveplate of the i-th piston related to r (L/min)
$Q_{vpR,i}$	Leakage between cylinder block and valveplate of the i-th piston related to R (L/min)
R_B	Radius of the external sealing land (m)
r_B	Radius of the internal sealing land (m)
R_c	Vapor condensation rate
R_e	Vapor generation rate
r_{in}	Slipper internal radius (m)
r_K	Internal cylinder block slot radius (m)
R_K	External cylinder block slot radius (m)
r_{out}	Slipper external radius (m)
R_p	Pitch radius of the pistons (m)
$S_{g,d}$	Source of dissolved NCG (kg/m³)
t	Time (s)
T_b	Bearing friction torque (Nm)
T_{CP}	Torque due to the displacement controller and the bias spring (Nm)
T_f	Friction torque (Nm)
$T_{p,i}$	Torque of the i-th piston on the swashplate (Nm)
T_r	Torque due to pressure (Nm)
T_s	Torque on the pump shaft (Nm)
T_{sp}	Cylinder block spring torque (Nm)
T_{ss}	Torque due to the viscous friction between slipper and swashplate (Nm)
$T_{ss,i}$	Torque due to the viscous friction between slipper and swashplate of the i-th piston (Nm)
T_{vp}	Viscous friction between cylinder block and valveplate (Nm)
V_0	Piston dead volume
V_{air}	Volume of undissolved air/gas inside the CV (m³)

V_i	Volume of the i-th piston (m³)
V_{liq}	Volume of pure liquid inside the CV (m³)
v_{pi}	Axial velocity of the i-th piston (m/s)
V_{vap}	Vapor volume inside the CV
w_r	Width of the flat orifices (m)
w_R	Width of the flat orifices (m)
$x_{Fp,tot}$	Position of the $F_{p,i}$ along the x axis
x_i	Position on the swashplate along the x axis
$y_{Fp,tot}$	Position of the $F_{p,i}$ along the y axis
y_i	Position on the swashplate along the y axis
z_0	Length of the variable chamber at zero displacement β=0 (m)
$z_{p,i}$	Position of the i-th piston

Greek letters

Name	Descriptions
α	Viscosity pressure coefficient
β	Swashplate angle (deg)
β_{eff}	Effective fluid bulk modulus
φ_i	Angular position of the i-th piston
λ_1	Viscosity temperature coefficient
μ	Fluid dynamic viscosity (Pa*s)
μ_0	Fluid dynamic viscosity at reference pressure (Pa*s)
μ_t	Turbulent viscosity (Pa·s)
Ω	Control volume (m³)
ω	Angular velocity (rad/s)
ρ	Density of mixture (kg/m³)
ρ_0	Fluid density at reference pressure (kg/ m³)
ρ_{atm}	Fluid density at atmospheric pressure (kg/ m³)
ρ_g	Density of gas (kg/m³)
ρ_l	Density of liquid (kg/m³)
σ	Surface of the control volume (m²)
$\sigma_{g,d}$	Dissolved gas Schmidt number
σ_v	Vapor Schmidt number
τ	Time scale (s)
$\vec{\tau}$	Stress tensor

Chapter III: **External Gear Pumps**

III.1 Introduction

Chapter III is focused on the study of the external gear machines (EGMs); machines characterized by low-cost, manufacturing simplicity, and their broad applicability in many fields, such as automotive (low/medium-pressure application), fluid transportation (low-pressure), heavy industry (high-pressure), and food industry (low-pressure). However, both mobile and industrial fields are desiring low-noise machines; for this reason, particular care has to be given to the gear meshing.

III.1.1 State-of-the-art

Even if the working principle of the external gear pumps (EGPs) is elementary, many studies are available in the literature, focusing on their performance improvement. An external gear pump (EGP) consists of driving gear connected to the pump's shaft and driven gear (Figure 52) [1] [28]. The displacement chambers, generated by the gears meshing, are connected to the ports through two wear-plates.

The request for low noise EGPs has pushed research towards developing innovative design solutions capable of minimizing the kinematic flow ripple. Among them, many solutions improve the standard involute gear design concept done using numerical and experimental techniques.

Numerical models can be an efficient way to analyze the operation of EGPs and predict their performance, to center this target. Several authors studied the ideal

flow behavior of those machines using theoretical models (Ivantysyn et al. [1] and Manring et al. [29]). In contrast, others adopted numerical modeling, both with lumped parameter and CFD approaches.

Vacca et al. [30] [31] [32] [33] [34] developed a numerical tool for the understanding of EGPs also with asymmetric tooth profiles; in [31] they optimized an EGP using an NSGA-II algorithm to reduce the flow ripple and, as a consequence, the emitted fluid-borne noise. The same authors in a recent study [33] implement a thermal model improving the pump operation's prediction on the already developed lumped parameter tool.

Borghi et al. [35] [36], studying the EGPs, developed through the years lumped parameter numerical models to predict both the volumetric and hydro-mechanical efficiencies and all significant losses.

Mancò et al. [37] studied an EGPusing a lumped parameter approach compared with experimental data with high accuracy.

Zhou et al. [38] developed a lumped parameter approach to consider the dynamic nature of the gas cavitation process in External Gear Machines (EGMs).

Lumped parameter-based models have many advantages; one of them is that they can also be integrated with mechanical models for the evaluation of gear micromotion like proposed models by Zardin et al. [39], Falfari et al. [40], Mucchi et al. [41] and by Vacca et al. [30].

Other studies present in the literature analyzed EGPs using 2D modeling approaches with deforming mesh and volume re-meshing. However, even if the 2D modeling approaches give interesting results, they cannot predict the internal flow behavior like 3D models [42]. It depends on the fact that flow is complex during the operation of those machines because of the rotational speed (typically in the range of 500–3000 rpm) and the high pressure.

Besides, three-dimensional CFD methods are widely used for studying EGPs [43]. Corvaglia et al. [44] showed a new application of a 3D CDF algorithm to predict the unsteady flow rate in hydraulic pipes placed after the pump's delivery port. The authors compared experimental data and numerical results with excellent agreement.

Castilla et al. [45] presented a numerical technique applied on an EGP to predict vortexes' general shape generated in the meshing zone and distribution. The

same authors in [46] introduced a decompression slot in the plates located in the meshing zone using the same tool previously described in [45] for the analysis.

Other researchers modified the design of the plates adding grooves with the aim of noise reduction. However, even if those grooves can reduce the pump's fluid-borne noise, they can significantly affect the volumetric efficiency of the EGP if not well designed because they connect volumes at different pressures [35]. Grooves' effects inside the plates have been widely numerically studied by Borghi et al. [47], looking at the reverse flow in the transition area between high and low-pressure volumes.

III.1.2 The subject of the study

In this paragraph, a Hydreco prototype pump for industrial applications (theoretical displacement of 53 cm³/rev), with a pressure rated up to 350 bar and a speed range of 450-3500 rev/min, has been studied to minimize noise emission, acting on the flow ripple.
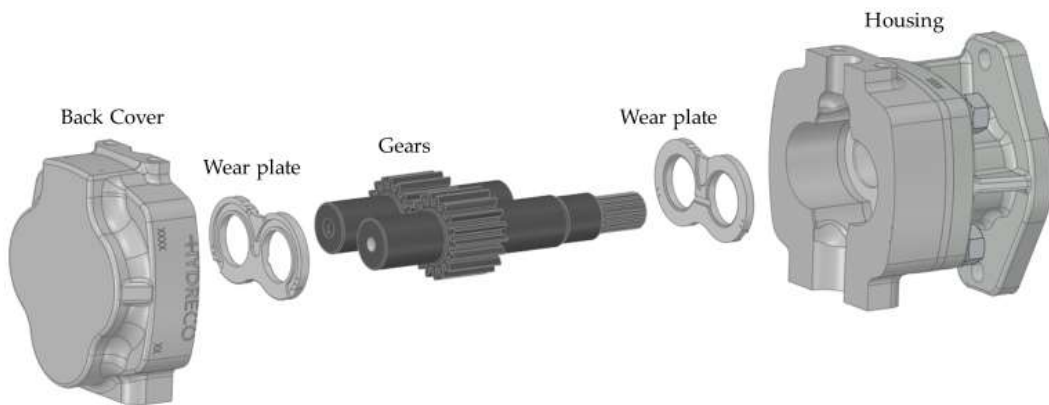
Figure 52. Reference external gear pump

More data are available in the following table:

Table 3. Prototype technical specification

Description	Value	Units
Displacement	53.0	cm³/rev
Maximum rated pressure	350	bar
Maximum peak pressure	360	bar
Speed range	450-3500	rev/min

The next section has been reported for a better understanding of all the phases of the presented study.

III.1.3 Inherited project

With the recent acquisition of Hydreco company by Duplomatic Group, the research and development department of Duplomatic MS has inherited some projects of this new English company. In particular, one is very interesting for the Group market, and it is related to a very efficient external gear pump for a wide range of applications. The inherited project has delivered to the research department, which immediately glimpsed its potential. During earlier tests at Duplomatic labs, the pump resulted very efficiently from the volumetric point of view, but the emission had not convinced the research and development department. At that time, Duplomatic MS asked for support from the University of Naples. The support was mainly based on numerical modeling and opportunely testing the pump to understand if there is a noise source and how it eventually acts.

III.2 Experimental noise measurement

An experimental noise measurement campaign was needed to prove the effective feeling of Duplomatic engineers. Therefore, the author carried a batch of similar pumps at the University of Dresden at the Institute for Mechatronic Engineering for further analysis with Ph.D. candidates' support of the german university. The batch of pumps selected for this analysis is composed as follows:

Table 4. Pump analyzed

Pump	number of teeth/gear	Type of gear	Manufacturer
1	10	Spur (S)	Competitor 1
2	12	Spur (S)	Competitor 2
3	**18**	**Spur (S)**	**Hydreco**
4	18	Helical (H)	Hydreco
5	18	Helical (H)	Hydreco
6	11	Spur (S)	Hydreco

In particular, besides the prototype pump, identified by pump number 3 in Table 4. The pumps listed in the table are similar for characteristics, even if they have particular advantages in some applications. Two of the studied pumps are

manufactured by two different competitors; their noise emissions have been measured to compare the Hydreco product to what is available on the market.

III.2.1 The semi-anechoic room at the University of Dresden

The noise measurement setup visible in Figure 53, available at Technische Universität (TU) Dresden has been designed according to DIN ISO 3745 standard; it has an accuracy level of class 1.

Figure 53. Measurement setup at TU of Dresden

According to the standard used in this field, this setup permits to acquire sound pressure level and sound power level in steady-state conditions. The pump noise emissions have been obtained for different working conditions. The test bench is also able to acquire inlet and outlet pressures and temperatures. It has provided a torque meter and can control the oil temperature and pressure at the pump inlet.

III.2.2 Results from measurement

Sound pressure levels (A-weighted) $L_{p,A}$ have been reported in the next figures. The $L_{p,A}$ has been plotted as a function of the outlet pressure; different figures have been presented for different operational speeds. The company requested not to show the measured sound pressure level in the figures, but it is possible to say that the y-grid size is 5 dBA.

In particular, Figure 54 presents the $L_{p,A}$ at a lower rotational speed of 1000 rev/min.
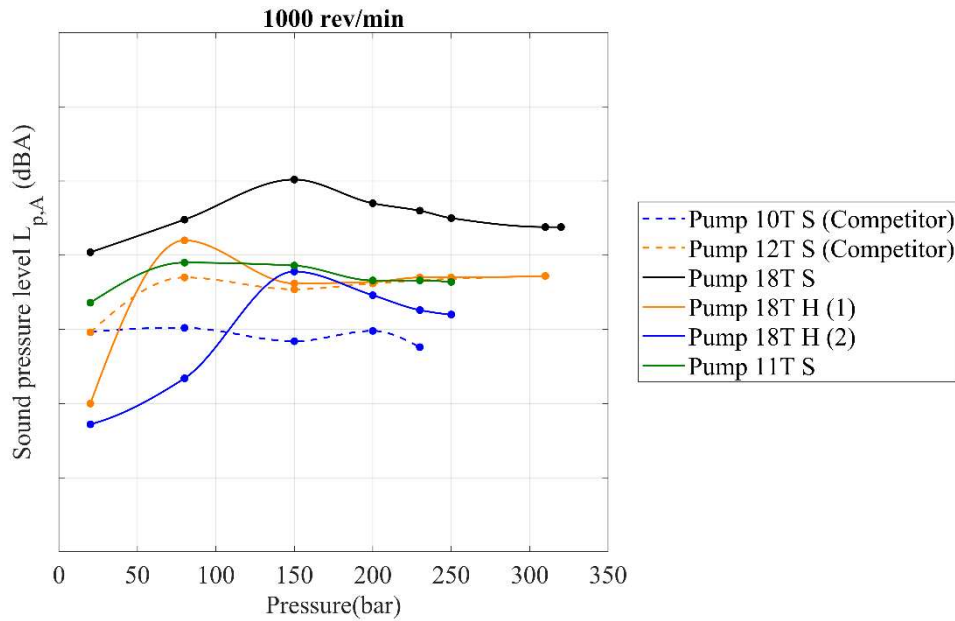
Figure 54. Sound pressure level acquisition campaign at 1000 rev/min

This figure shows that the subject of the study suffers from higher noise emissions, not comparable with other products.
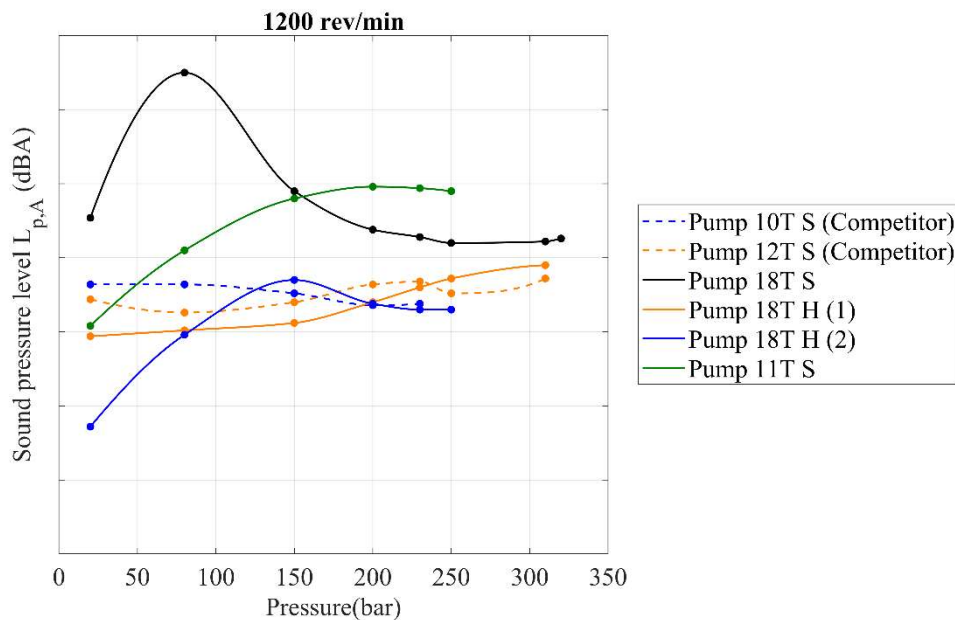
Figure 55. Sound pressure level acquisition campaign at 1200 rev/min

In Figure 55, where the operational speed is 1200 rev/min, the difference looks higher in low-pressure zones, while it reduces at higher pressures.
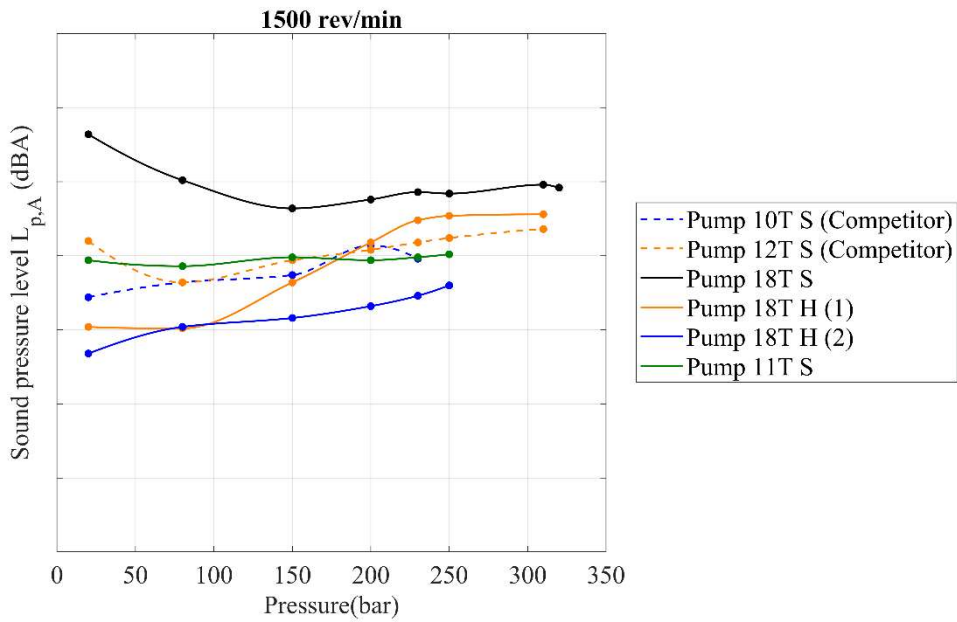
Figure 56. Sound pressure level acquisition campaign at 1500 rev/min

Figure 56 confirms the same trends in the two previous figures. Here, the operational speed is 1500 rev/min.
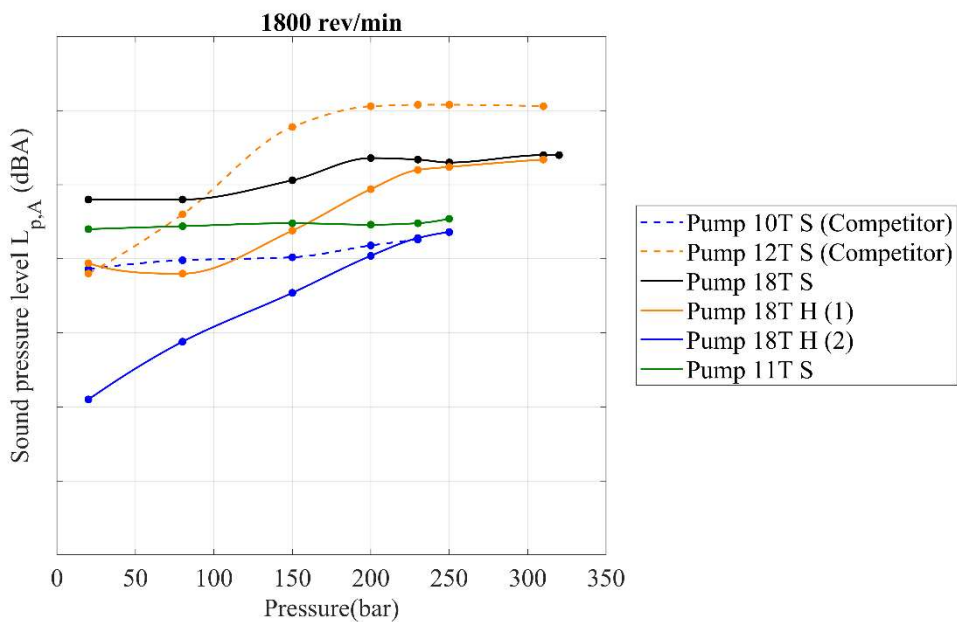
Figure 57. Sound pressure level acquisition campaign at 1800 rev/min

The last figure, Figure 57, shows the results for an operational speed of 1800 rev/min. Here the $L_{p,A}$ difference is reduced, but the performance is not in line with other Hydreco products, even if it is better than the competitor number 2, especially at high pressures.

This analysis has confirmed the first tests' feeling, where the prototype appeared noisier than other pumps.

III.3 The EgeMATor: a tool for EGMs numerical analysis

When Duplomatic MS asked for support from the University of Naples, it soon appeared that a tool for the EGPs simulation was needed. Something was happening in the pump, creating higher noise emissions than expected.

A tool has been developed for the machines' hydro-mechanical numerical simulation as a parallel process to the noise measurement. Its support will be fundamental during the re-prototyping phase.

III.3.1 Description of the tool: EgeMATor

EgeMATor (**E**xternal **Ge**ar **Ma**chine Multi **T**ool Simulat**or**) is a tool entirely developed from zero for the numerical simulations of external gear machines. The tool is composed of different subroutines designed in different environments, interconnected, as visible from its workflow in Figure 58 to deeply study the EGMs.
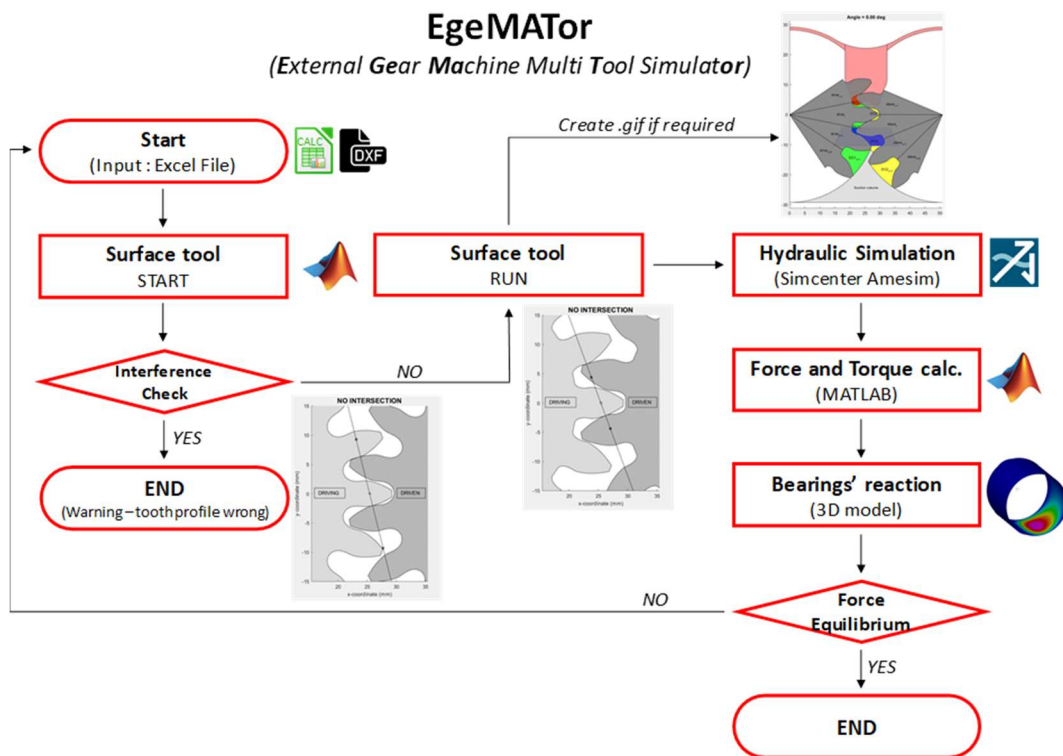
Figure 58. The EgeMATor's workflow

The hydraulic simulation main subroutine, visible in the previous figure, runs a numerical simulation of the pump in Simcenter Amesim®, using a lumped parameter method based on the control volume approach. This step is preceded by a code written in MATLAB®, called Surface Tool©, that provides all the information needed by the hydraulic simulation subroutine concerning displacement volumes, how the gears rotate, and their connection with the contiguous elements. After the hydraulic simulation, it is possible to activate a subroutine that calculates gears' forces and torques. Next, another subroutine can evaluate bearings' reaction; then, results are compared and, if a different gear positioning is necessary, the Surface Tool© starts the process again. Further information will be provided in the next section.

III.3.2 The Surface Tool©: gears meshing

The Surface Tool©, the hearth of EgeMATor, needs for its calculation, an excel file with all the pump parameters, and drawings of the components to start. An example of this excel file has been shown in Figure 59, where the pump parameters are defined (such as the number of teeth, gears center to center distance, axial dimension, gear micromotion, etc.). The folder path containing DXF files (Drawing Exchange Format) of tooth profile and wear-plates relief groove geometries is linked as well. The DXF files, used as input, can be saved directly from a CAD model (only exporting a sketch) or from experimental measurement like a non-contact 3D laser scan arm. The code, written in MATLAB®, locates the right cell of the excel file and uses the relative value during the script running. Firstly, the Surface Tool© runs control on the gear engagement with these inputs, checking any interference in the meshing zone. In case of interference, the tool provides a warning; otherwise, it continues its subroutine, generating all the required data files needed by the lumped parameter model.

PARAMETER	VALUE	UNITS	NOTE
pitch diameter	46.9	[mm]	center to center distance
y micromotion	-0.027	[mm]	vertical value for gear micromotion
z	10	[-]	number of teeth
alfa	0.3	[deg]	rotation of slave gear to achieve tee
base pitch	9.373	[mm]	
major diameter	56.965	[mm]	
root_diameter	35.589	[mm]	
case angle	78	[deg]	sealing angle for sealing (considered
tw	1.052	[mm]	tip width
b	22	[mm]	gear axial dimension
ANGULAR STEP			
dt	0.25	[deg]	saving delta angle
IMAGE OUTPUT			
save gif	1	[-]	1 yes 0 no
gif name			DUPLO_00_0.25.gif
DXF			
general path			E:\OneDrive - UniNA\UniNA\egeMA
tooth profile name			dente_punti.dxf
inlet 1 groove profile			inlet 1_punti.dxf
outlet groove profile			outlet 1_punti.dxf
backflow drive profile			bf drive_01_punti.dxf
backflow slave profile			bf slave_01_punti.dxf
inlet 2 groove profile			inlet 2_punti.dxf
OD1			OD1_punti.dxf
OS1			OS1_punti.dxf

Figure 59. Excel sheet input sample for the Surface Tool© input

When the gears provided by a supplier of the prototype pump have been deeply controlled in terms of quality, something looked different as per drawing from the Hydreco gear standard. The root zone of the teeth appeared to be quite different from the standard. An analysis was needed to understand the effects of dissimilar geometries during the gear meshing.

For this reason, starting from reverse engineering of the hob's geometries that realized the component, it has been found a not perfect geometry in the tooth's not-functional profile (root area). A foul in the mating root has been detected, using the gear check subroutine of the Surface Tool©.

In Table 5, figures of the gears meshing have been reported every 2 degrees of rotation. It can be noted how the subroutine finds teeth intersection in the root areas (red highlighted).

Table 5. Gear meshing figures (images every 2 deg of rotation)

ANGLE 8.0 deg — NO INTERSECTION

ANGLE 10.0 deg — NO INTERSECTION

ANGLE 12.0 deg — INTERSECTION

ANGLE 14.0 deg — INTERSECTION
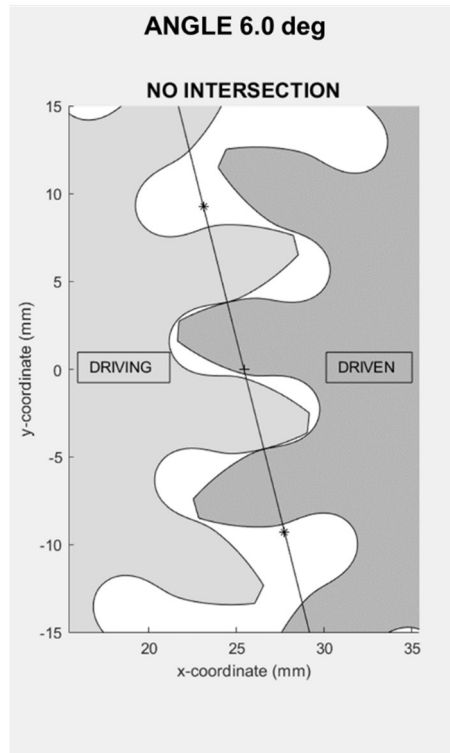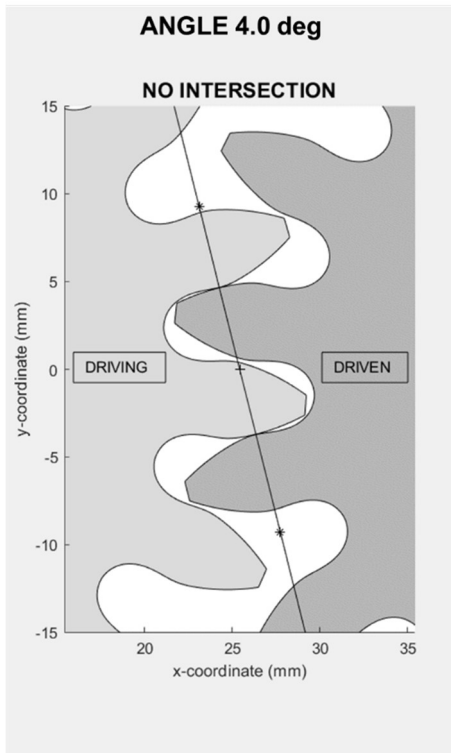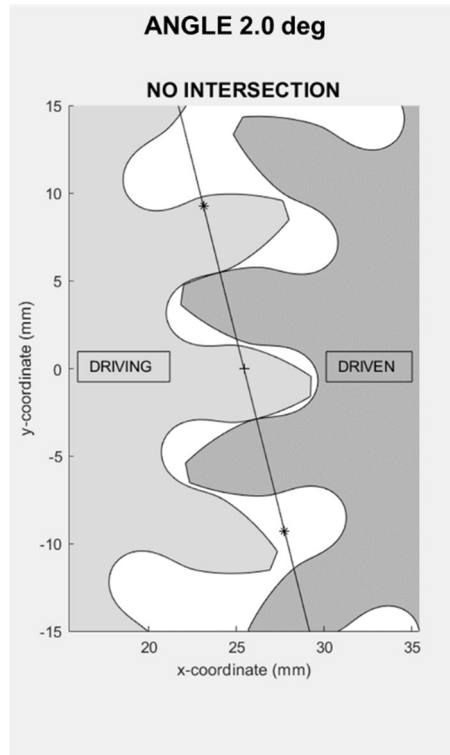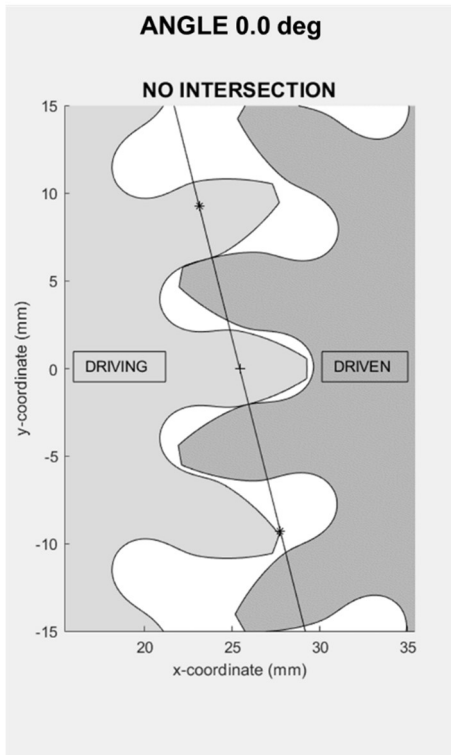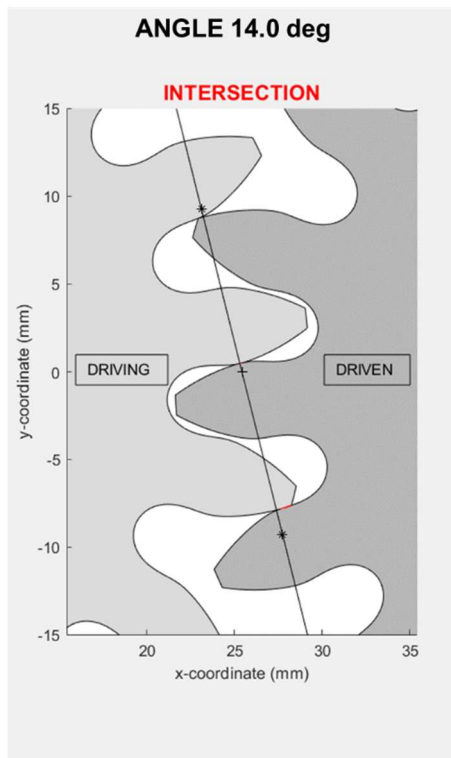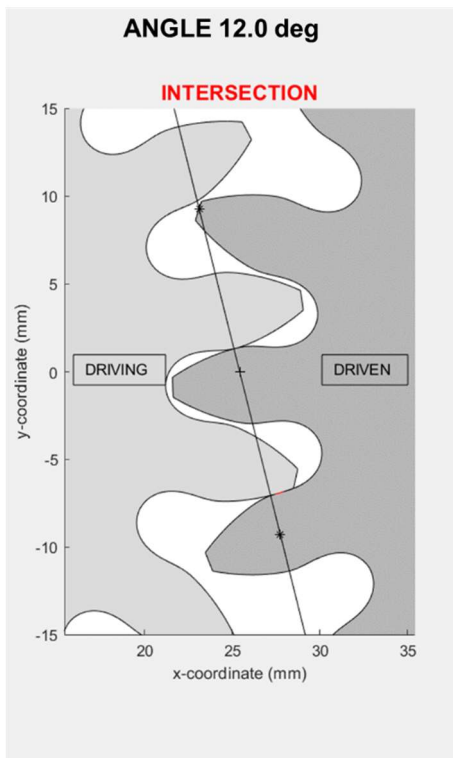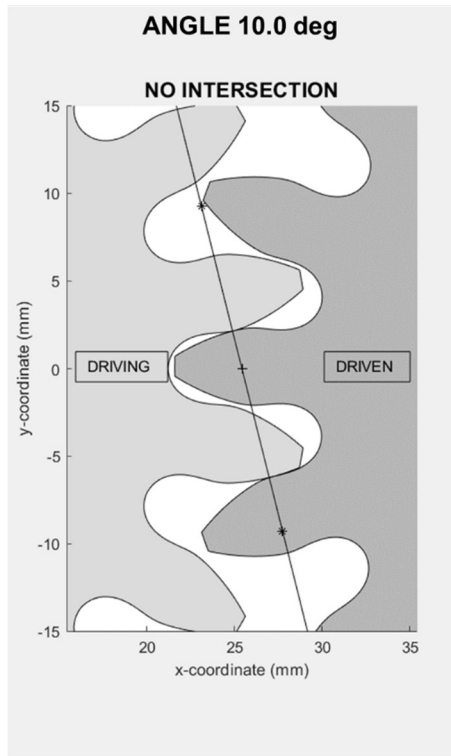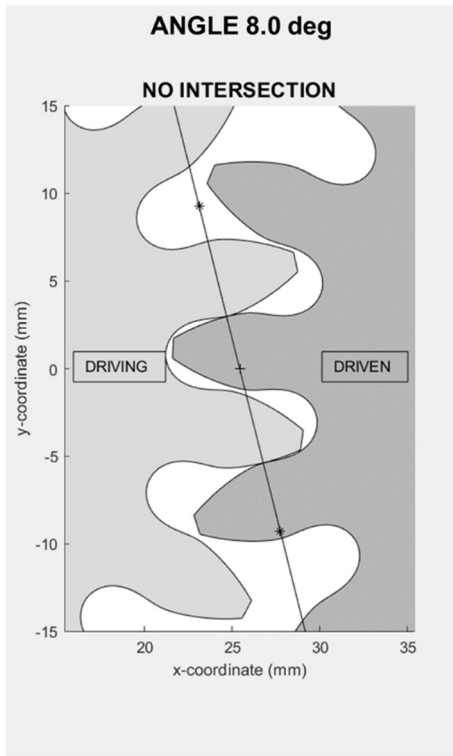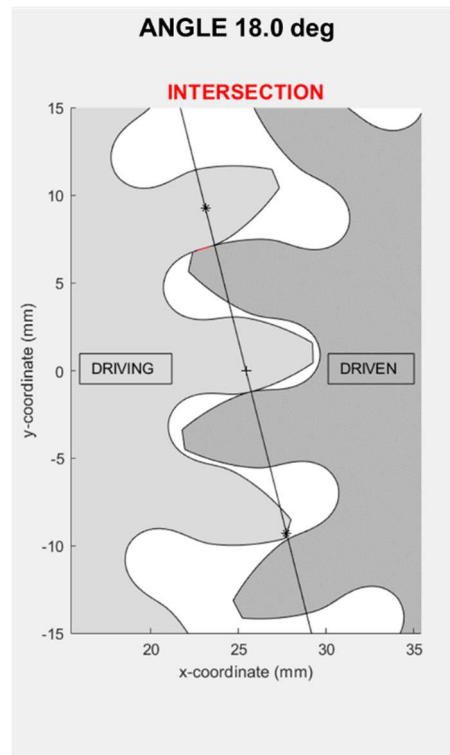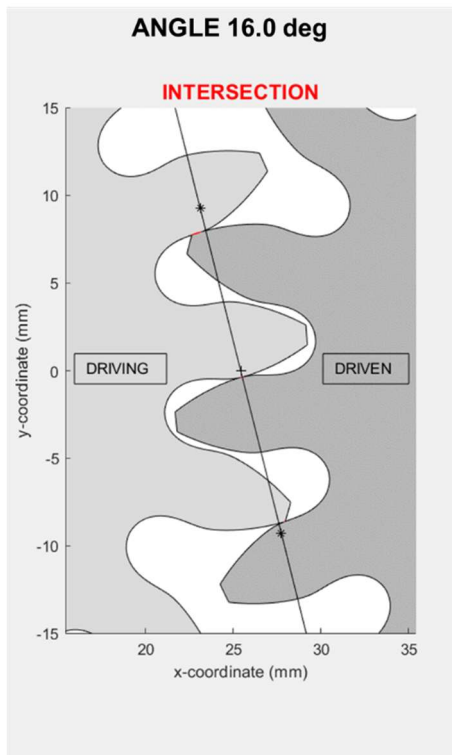
At this point, it was clear that the Hydreco project needed some modifications.

For a simplification perspective of the project, the Duplomatic's R&D technical department, with the University of Naples' support, decided to project a new, more straightforward gear profile with a standard module for the re-design of the pump. This novel design, presented in Figure 60, consists of a number of teeth reduction per gear, from 18 to 16, to accommodate the rotating group in the same pump housing.

(a)   **(b)**
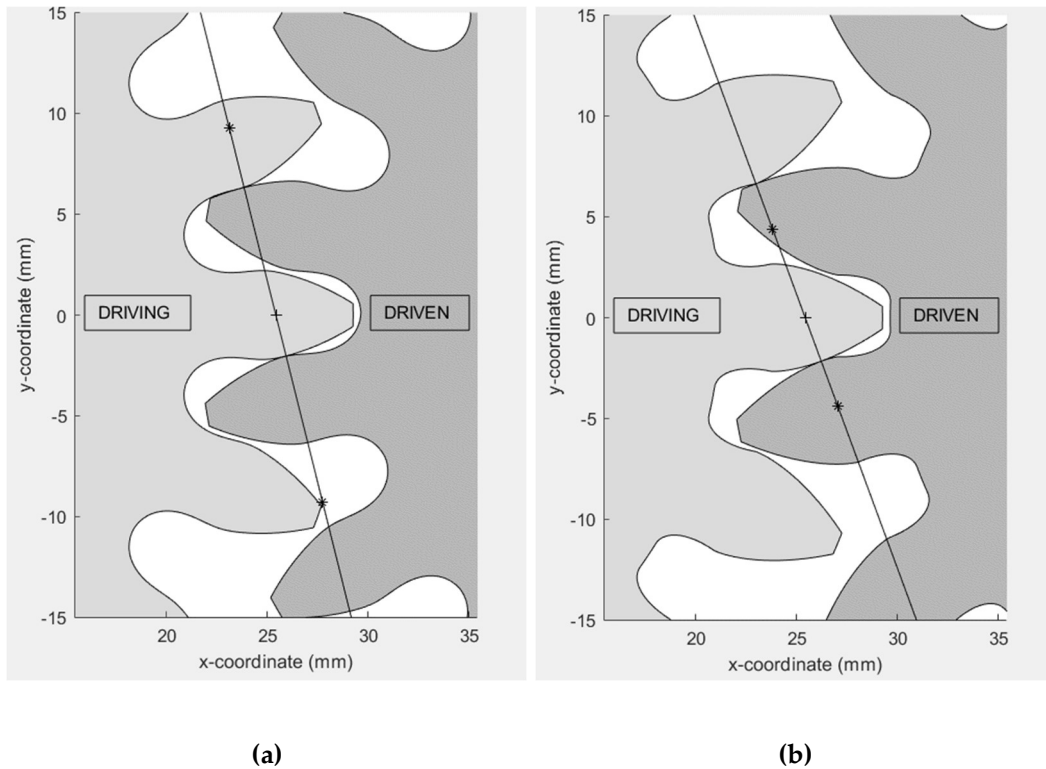
Figure 60. Gear meshing: old prototype pump with 18 teeth/gear (a), new design with 16 teeth/gear (b)

From this point, the analysis has been focused on the new design with 16 teeth. For this reason, everything that is going to be presented will be referred to gears in Figure 60(b).

III.3.3 The Surface Tool©: output files

When the Surface Tool© subroutine has been run, no warnings on gears meshing have been reported. The tool continued its subroutines, generating all the required data files needed by the lumped parameter model. In particular, it saves around 100 data files, where every calculated dimension, such as the volumes of the displacement chambers G_i (driving gear) and N_i (driven gear), are tabled as a function of the angular position (Figure 61).
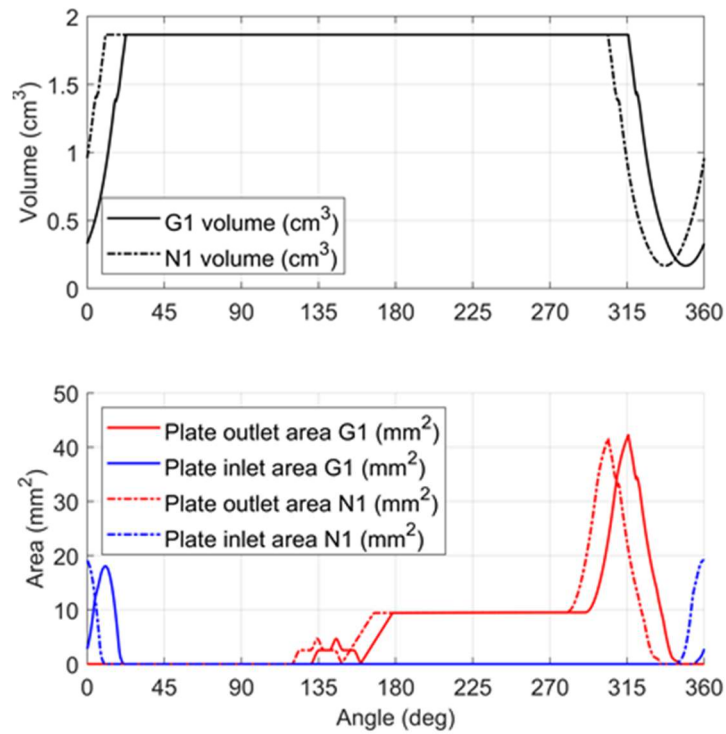
Figure 61. Samples of output data

To provide support for the user, helping to visualize the displacement chambers' morphology and their connections with the wear-plates, the Surface Tool© can optionally generate a GIF (Graphics Interchange Format) animation of gear meshing. The GIF animation frames have been presented in Figure 62 and Figure 63 for two different angular positions, where the *i-th* displacement chambers are visible. In the figure, the G_i and N_i volumes with their previous and following chambers are notable. The wear-plate relief grooves and suction/delivery volume have been added in the background as well.
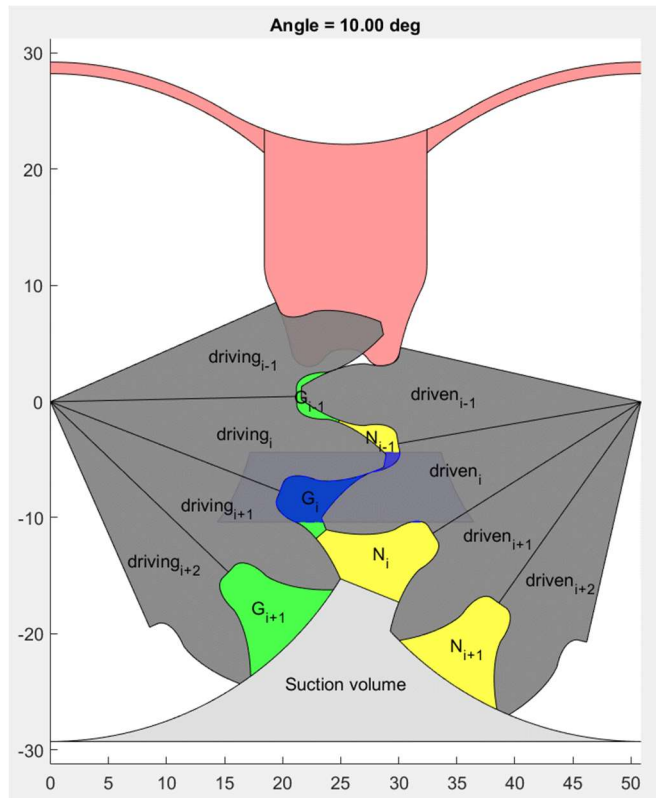
Figure 62. Extracted frames from the GIF animation, in particular at 10 deg of rotation

Figure 63. Extracted frames from the GIF animation, in particular at 320 deg of rotation

According to the following formulation, the tool also estimates the pump displacement VE; for the analyzed pump, the calculated displacement is 52.72 cm³/rev.

$$V_E = z_T \cdot [\max(V_{G_i} + V_{N_i}) - \min(V_{G_i} + V_{N_i})] \, , \tag{47}$$

Where z_T is the number of teeth, V_{G_i} is the volume of the displacement chamber G_i and V_{N_i} is the volume of the displacement chamber N_i.

Doing a step back to the EgeMATor workflow in Figure 58, the tool is now ready to simulate the hydraulic behavior with a model created in the Simcenter Amesim® environment. The modeling is based on a control volume approach, well-known in the literature.

In Figure 64, an overview of the lumped parameter model has been presented to understand better its functional approach and how volumes are connected.
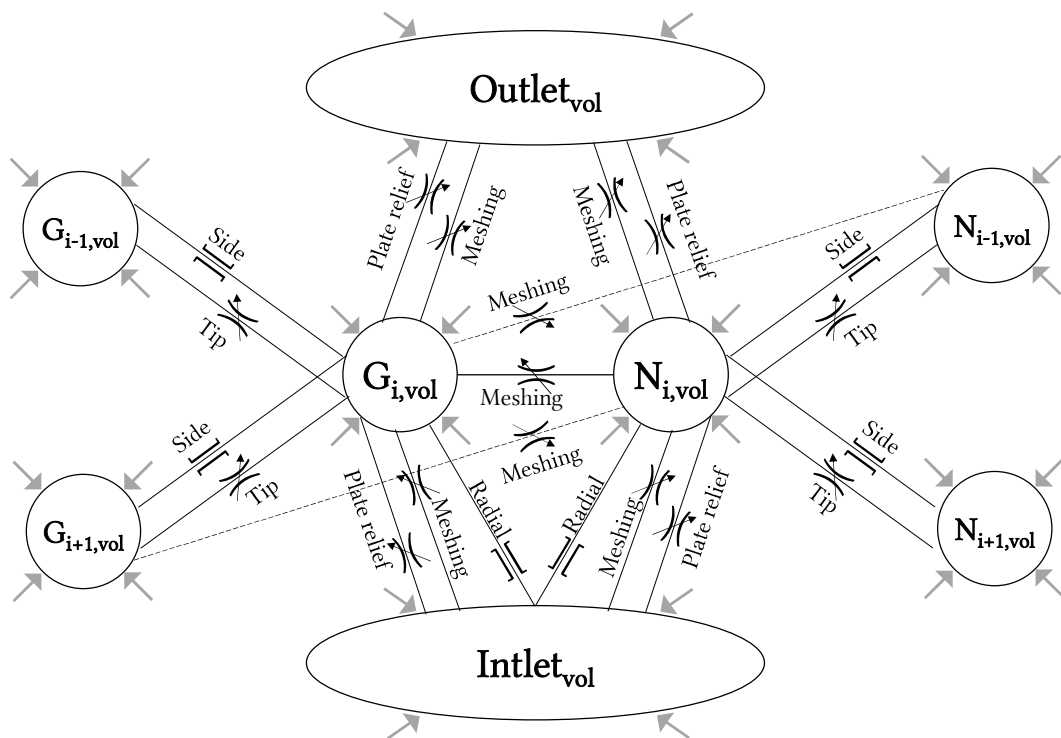
Figure 64. Overview of the lumped parameter model

III.3.4 The hydraulic model

Concerning Figure 62, Figure 63, and Figure 64, it is important to underline how the control volumes approach works. For the control volume approach, every G_i and N_i volume has homogeneous properties, and they are modeled as capacitive elements, whose pressure is calculated as follows:

$$\frac{dp}{dt} = \frac{\beta_k}{V}\left(\sum Q - \frac{dV}{dt}\right)\frac{\rho_{atm}}{\rho}\, ,$$

(48)

Where volumetric fluxes Q are evaluated for every connection presented in Figure 64. The equation to evaluate the flux depends on the physic of the connection.

Fluxes relative to meshing areas and wear plate relief grooves have been modeled as a turbulent non-circular orifice:

$$Q = c_d A\sqrt{\frac{2\,|\Delta p|}{\rho}} \times sign\left(\Delta p\right)$$

(49)

Where c_d is the flow coefficient, A is the cross-sectional area of the orifice (constant or variable), Δp is the pressure difference between the displacement chamber and the preceding/following one, and ρ is the average working fluid density between the two chambers. The value of the orifice's cross-sectional area is read from tables generated by the Surface Tool© as a function of the rotation angle, as already mentioned.

The flow coefficient c_d in equation (49) is a parameter that characterizes the orifice behavior, and the following equation regulates its value:

$$c_d = c_{d,\max} \cdot \tanh\left(\frac{2 \cdot \lambda}{\lambda_{crit}}\right)$$

(50)

Where $c_{d,max}$ is the maximum flow coefficient (defined by the user), λ is the flow number, and λ_{crit} is the critical flow number (defined by the user). The values of $c_{d,max,}$ and λ_{crit} present in equation (50) are parameters that can be changed to tune up the orifice's behavior.

Therefore, the value of c_d depends on the flow number as follows:

$$\lambda = \frac{D_h}{\nu} \cdot \sqrt{\frac{2 \cdot |\Delta p|}{\rho}} \quad \text{where} \quad D_h = \frac{4 \cdot Area}{perimeter} \tag{51}$$

D_h is the orifice's hydraulic diameter, ν is the kinematic viscosity evaluated at the average pressure. The hydraulic diameter of the non-circular orifice has been calculated as a function of the orifice area and its wet perimeter.

Meanwhile, tip (Figure 65) and side (Figure 66)fluxes have been modeled considering both Couette and Poiseuille flow contributions.
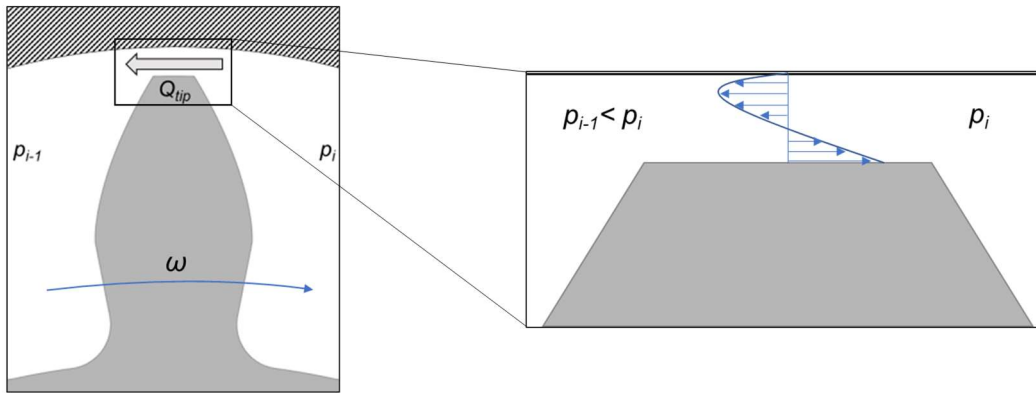
Figure 65. Tooth tip flux

More precisely, for the tip flux, the following formulation has been considered:

$$Q_{tip} = \frac{bh_{tip}^{3}}{12\mu l_{tip}} \Delta p - \frac{bh_{tip} \omega R_{tip}}{2} \tag{52}$$

Where ω is the rotational speed in rad/s, R_{tip} is the tip radius, h_{tip} is the height of tip gap calculated by the Surface Tool© according to the gear micromotion, and l_{tip} is the tooth tip's width. b is the gear's axial dimension, and μ is the dynamic viscosity calculated at an average pressure.

For what concerns the tooth side flux, n slices have been obtained from the tooth profile for the leakage approximation.
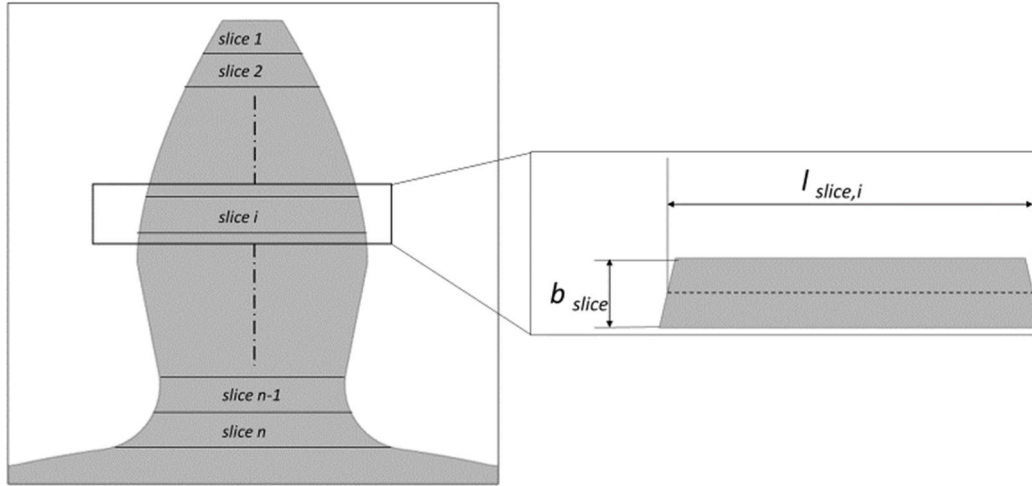
Figure 66. Tooth side flux

The equation used for the flux calculation is the following:

$$Q_{side} = 2 \cdot \sum_{i=1}^{n} \left(\frac{b_{slice} h_{gap}^3}{12 \mu l_{slice,i}} \Delta p - \frac{b_{slice} h_{gap} \omega R_{slice,i}}{2} \right) \tag{53}$$

Where b_{slice} represents the width of the n slices, $l_{slice,i}$ is the average length of the i-th slice, and $R_{slice,i}$ is the average radius that individuates the i-th slice, h_{gap} has been maintained as a constant during the simulation since it slightly interferes with the flow ripple. A factor of two is included in the equation to consider the flux of both tooth sides. Usually, for teeth similar to what has been analyzed here, an n value between 6 and 10 is adequate for the approximation.

Radial flux, from the displacement chamber to pump housing (inlet), has been modeled as a flat orifice.

The Surface Tool© requires a vital parameter to complete its subroutine; it is the "saving delta angle" $\Delta\varphi$, which is crucial for a robust hydraulic simulation. As said, the tool creates a batch of data files, where a collection of (φ,y) couple is stored. Each couple represents a dimension (y) as a function of the rotational angle (φ). For this reason, it is significant to define the table "saving delta angle" ($\Delta\varphi = \varphi_{i+1} - \varphi_i$). With a bigger $\Delta\varphi$ the Surface Tool© subroutine will be faster, but some information could be lost, while lower $\Delta\varphi$ will provide more than necessaries information, consuming CPU resources with consequently more computational times. An analysis of the numerical flow ripple has been done to find the hydraulic simulation independence from the parameter $\Delta\varphi$. Results, presented in Figure 67, show a single flow ripple of the analyzed pump, simulated with the hydraulic model in Simcenter Amesim® (an overview has been shown in Figure 68) at 1500 rev/min with an imposed outlet pressure of 230 bar. It is visible that the instantaneous flow at pump delivery becomes independent for $\Delta\varphi \leq 0.50$ deg.
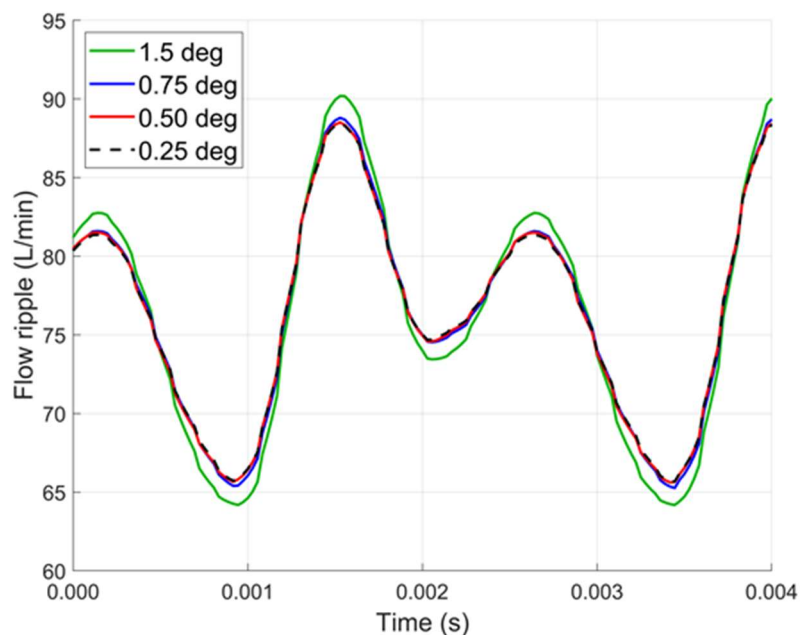
Figure 67. Effects of the table "saving delta angle" ($\Delta\varphi$) on the numerical flow ripple

In Table 6, the CPU time required by an Intel® Core™ i7-7700HQ CPU 2.80 GHz to complete the subroutines have been presented as well. The same independence has been observed on the G_i and N_i pressurizations. A fair tradeoff for the $\Delta\varphi$ as input in the Surface Tool© is 0.50 deg, but since both subroutines (Surface Tool© and hydraulic simulation) require around 10 minutes to complete, a value of 0.25 deg has been set for the presented study.

Table 6. The computational time for different "saving delta angle" (Δφ)

Δφ	Surface Tool© CPU time	Hydraulic simulation CPU time
1.5 deg	98 sec	7 min
0.75 deg	206 sec	8 min
0.50 deg	302 sec	9 min
0.25 deg	572 sec	11 min
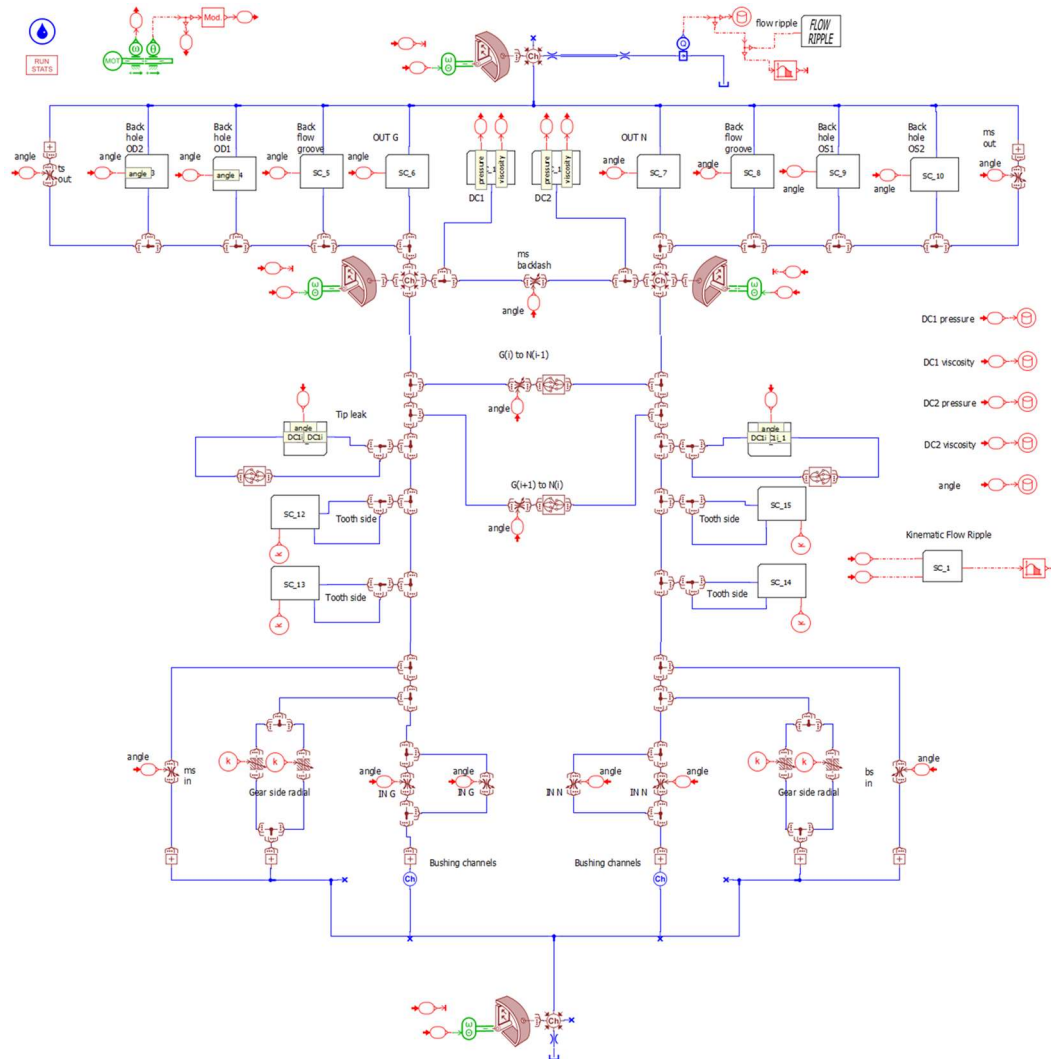
Figure 68 . Hydraulic Simulation model overview

III.3.5 Torques calculation

In EgeMATor, a calculation of forces and torques acting on gears has been implemented through a MATLAB® subroutine.

The total torque required by the pump shaft is the sum of different factors:

$$M_{tot} = M_G + M_N + M_{f,teeth} + M_{housing} + M_{bearings} + M_{churning\ losses} \qquad (54)$$

Where:

- M_G and M_N are the moments acting on driving and driven gears due to pressure and friction;

- $M_{f,teeth}$ is the friction moment due to the teeth contact;

- $M_{housing}$ is the moment of friction due to the contact between gears and housing;

- $M_{bearing}$ is the moment of viscous friction in the bearings;

- $M_{churning\ losses}$ is the moment due to the churning losses;

The moments' M_G and M_N on gears have been evaluated as follow:

$$M_G = M_{p,G} + M_{tip,G} + M_{side,G} + M_{drain,G}$$

$$(55)$$

$$M_N = M_{p,N} + M_{tip,N} + M_{side,N} + M_{drain,N}$$

M_p is the moment of the pressure forces, M_{tip} and M_{side} are the moments of the viscous forces on the tooth tip and sides, and M_{drain} is the moment due to the drain flow's viscous friction.

III.3.5.1 Evaluation of the moment due to pressure forces: M_p

The pressure force's moment of a displacement chamber is generated in the meshing zone, where deformed chambers create pressure force not directed towards the gear center.

In the meshing zone, the surface between two consecutive teeth is influenced by three different pressures, as visible from Figure 69 and Figure 70, where the three pressure forces for each teeth cavity have been presented for the driving and

driven gears. Even the three zones red, blue, and green (later called *R*, *B*, and *G)* are visible and used as a reference.
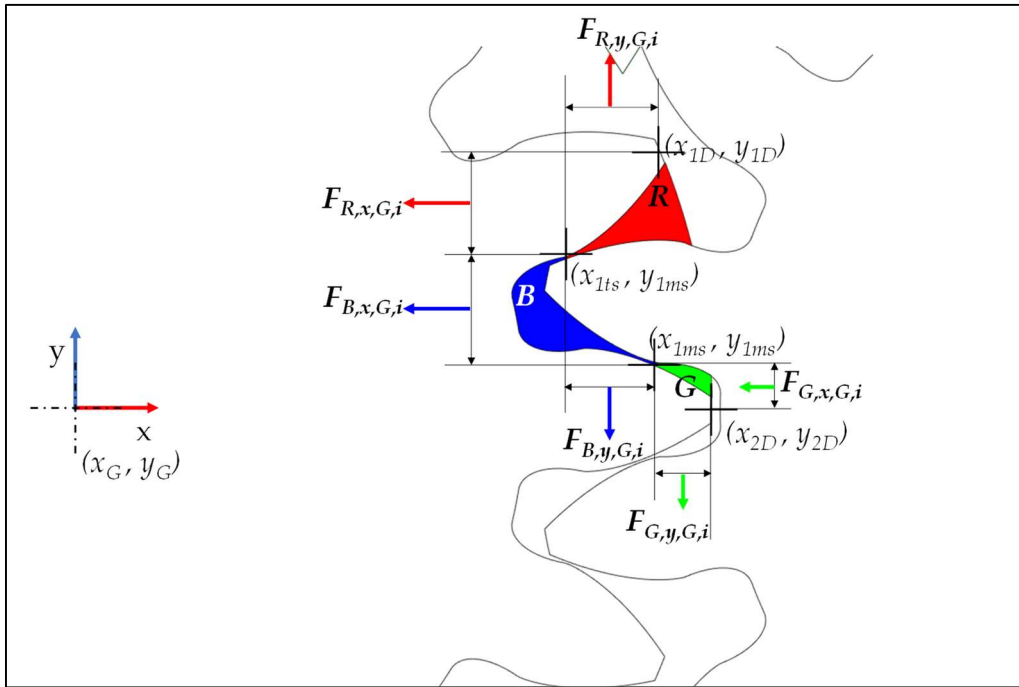
Figure 69. Pressure Force Driving Gear Meshing Zone
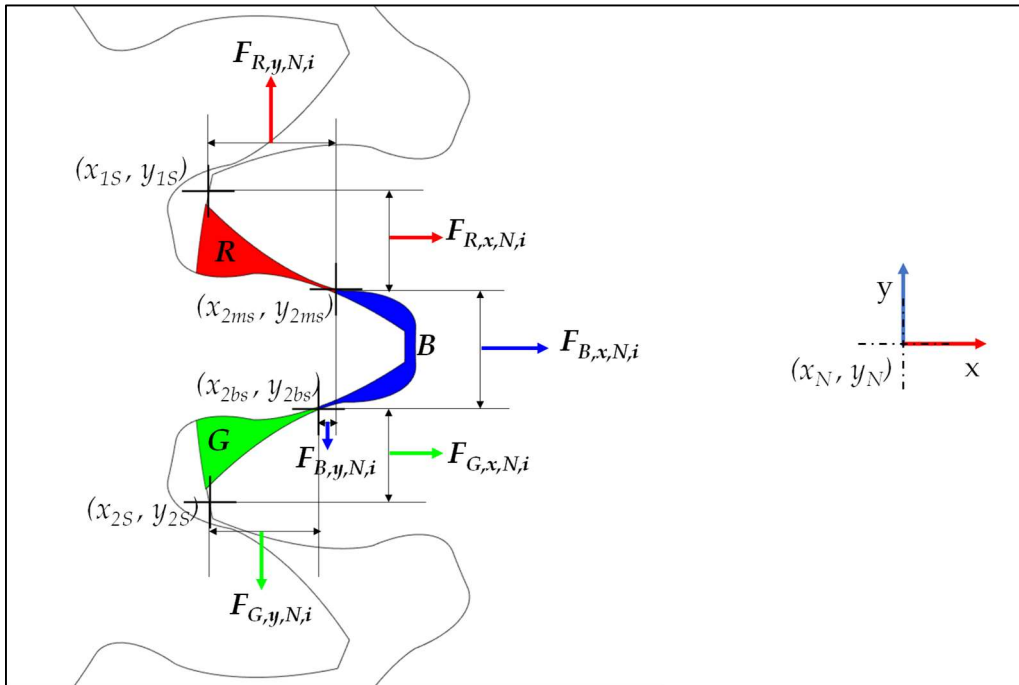
Figure 70. Pressure Force Driven Gear Meshing Zone

Therefore, the surface corresponding to each area's tooth profile has also been projected on planes parallel to the reference system's axes. In the first

approximation, the pressure forces are supposed to be applied to the profile projections' center. In this way, the evaluation of these moments has been obtained through linear equations that require, besides the pressure forces' values, distance values easily obtainable by the Surface Tool©. Thus, the moment generated by the pressure is the sum of the following components for the driving and driven gears.

$$M_{p,G} = \sum_{Z_t} \left(M_{Rx,G,i} + M_{Bx,G,i} + M_{Gx,G,i} + M_{Ry,G,i} + M_{By,G,i} + M_{Gy,G,i} \right)$$

(56)

$$M_{p,N} = \sum_{Z_t} \left(M_{Rx,N,i} + M_{Bx,N,i} + M_{Gx,N,i} + M_{Ry,N,i} + M_{By,N,i} + M_{Gy,N,i} \right)$$

Where the moments of each zone for the driving gear have been evaluated using the equations reported as follow:

$$M_{Rx,G,i} = -F_{Rx,G,i} \cdot \left[\frac{\left| y_{1D} + y_{1ts} \right|}{2} - y_G \right] \cdot sign \left[\frac{\left(y_{1D} + y_{1ts} \right)}{2} - y_G \right]$$

(57)

$$M_{Ry,G,i} = F_{Ry,G,i} \cdot \left[\frac{\left| x_{1D} + x_{1ts} \right|}{2} - x_G \right] \cdot sign \left[\frac{\left(x_{1D} + x_{1ts} \right)}{2} - x_G \right]$$

Equation (57) is referred to as the red zone (R zone), while for the B zone:

$$M_{Bx,G,i} = -F_{Bx,G,i} \cdot \left[\frac{\left| y_{1ts} + y_{1ms} \right|}{2} - y_G \right] \cdot sign \left[\frac{\left(y_{1ts} + y_{1ms} \right)}{2} - y_G \right]$$

(58)

$$M_{By,G,i} = F_{By,G,i} \cdot \left[\frac{\left| x_{1ts} + x_{1ms} \right|}{2} - x_G \right]$$

Finally, for the G zone:

$$M_{Gx,G,i} = -F_{Gx,G,i} \cdot \left[\frac{|y_{1ms} + y_{2D}|}{2} - y_G \right] \cdot sign\left[\frac{(y_{1ms} + y_{2D})}{2} - y_G \right]$$

<div align="right">(59)</div>

$$M_{Gy,G,i} = F_{Gy,G,i} \cdot \left[\frac{|x_{2D} + x_{1ms}|}{2} - x_G \right]$$

The same approach has been used for the driven gear; the equations to consider are the following:

$$M_{Rx,N,i} = -F_{Rx,N,i} \cdot \left[\frac{|y_{1S} + y_{2ms}|}{2} - y_N \right] \cdot sign\left[\frac{(y_{1S} + y_{2ms})}{2} - y_N \right]$$

<div align="right">(60)</div>

$$M_{Ry,N,i} = F_{Ry,N,i} \cdot \left[\frac{|x_{1S} + x_{2ms}|}{2} - x_N \right]$$

For what concern the R zone; while for the B zone:

$$M_{Bx,N,i} = -F_{Bx,N,i} \cdot \left[\frac{|y_{2ms} + y_{2bs}|}{2} - y_N \right] \cdot sign\left[\frac{(y_{2ms} + y_{2bs})}{2} - y_N \right]$$

<div align="right">(61)</div>

$$M_{By,N,i} = F_{By,N,i} \cdot \left[\frac{|x_{2ms} + x_{2bs}|}{2} - x_N \right]$$

And for the G zone:

$$M_{Gx,N,i} = -F_{Gx,N,i} \cdot \left[\frac{|y_{2S} + y_{2bs}|}{2} - y_N \right] \cdot sign \left[\frac{(y_{2S} + y_{2bs})}{2} - y_N \right]$$

(62)

$$M_{Gy,N,i} = F_{Gy,N,i} \cdot \left[\frac{|x_{2S} + x_{2bs}|}{2} - x_N \right]$$

Where x_G, y_G, x_N and y_N are the x and y coordinates of the center of rotation of the driving gear and the driven gear. The other coordinates are relative to points indicated in Figure 69 and Figure 70.

III.3.5.2 Evaluation of the pressure forces for the three zones

The evaluation of the instantaneous pressure forces utilized in the equations (57)-(62) has been obtained through linear equations that require, besides the values of instantaneous pressure, distance values that have been calculated by the Surface Tool©. With reference to Figure 69 and Figure 70, the forces have been calculated as follow:

$$F_{Rx,G,i} = -p_{N,i-1} \cdot \left[b \cdot |y_{1D} - y_{1ts}| \right]$$

(63)

$$F_{Ry,G,i} = p_{N,i-1} \cdot \left[b \cdot |x_{1D} - x_{1ts}| \right]$$

$$F_{Gx,G,i} = -p_{N,i} \cdot \left[b \cdot |y_{1ms} - y_{2D}| \right]$$

(64)

$$F_{Gy,G,i} = -p_{N,i} \cdot \left[b \cdot |x_{2D} - x_{1ms}| \right]$$

For what concerns the driving gear. For the driven, the equations are:

$$F_{Rx,N,i} = p_{G,i} \cdot \left[b \cdot \left| y_{1S} - y_{2ms} \right| \right]$$

$$F_{Ry,N,i} = p_{G,i} \cdot \left[b \cdot \left| x_{1S} - x_{2ms} \right| \right]$$

(65)

$$F_{Bx,N,i} = p_{N,i} \cdot \left[b \cdot \left| y_{2ms} - y_{2bs} \right| \right]$$

$$F_{By,N,i} = p_{N,i} \cdot \left[b \cdot \left| x_{2ms} - x_{2bs} \right| \right] \cdot sign\left(x_{2bs} - x_{2ms} \right)$$

(66)

$$F_{Gx,N,i} = p_{G,i+1} \cdot \left[b \cdot \left| y_{2bs} - y_{2S} \right| \right]$$

$$F_{Gy,N,i} = - p_{G,i+1} \cdot \left[b \cdot \left| x_{2bs} - x_{2S} \right| \right]$$

(67)

III.3.5.3 Evaluation of the moment due to tooth tip leakage: M_tip

Viscous friction forces on the tooth tip have been evaluated with the leakage's shear stress integration on the tip's surface. Since the flow is considered as a sum of the Couette and Poiseuille effects, the shear stress has been evaluated as follows:

$$\tau_{tip,i} = -\frac{\mu\omega R_{tip}}{h} + \frac{h}{2}\frac{\left(p_i - p_{i-1} \right)}{l_{tip}}$$

(68)

Where h and l_{tip} are the tooth's height gap and width, the dynamic viscosity μ has been evaluated at the average pressure.
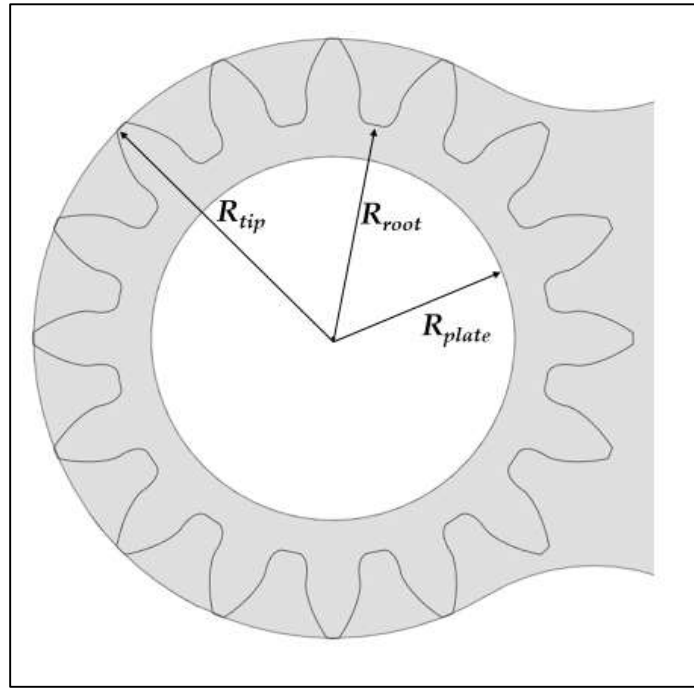
Figure 71. Definition of R_{tip}, R_{root} and R_{plate}

Thus, the friction forces due to the Couette-Poiseuille flow over the tooth tip is:

$$F_{tip,G,i} = \tau_{tip,G,i} \cdot b \cdot l_{tip}$$

$$F_{tip,N,i} = \tau_{tip,N,i} \cdot b \cdot l_{tip}$$

(69)

For the driving and driven gear, respectively. The moment generated by the above forces on each gear can be expressed as follows:

$$M_{tip,G} = \sum_{Z_t} F_{tip,G,i} R_{tip}$$

$$M_{tip,N} = -\sum_{Z_t} F_{tip,N,i} R_{tip}$$

(70)

III.3.5.4 Evaluation of the moment due to tooth side leakage: M_{side}

Since the contributions of Couette and Poiseuille have been considered in the tooth side leakages, the shear stress to evaluate the friction moment due to this leakage has the following formulation for the *n-th* slice (Figure 66):

$$\tau_{side,i,n} = -\frac{\mu \omega R_n}{h} + \frac{h}{2}\frac{(p_i - p_{i-1})}{l_n}$$

(71)

Where the l_n and R_n the length and the radius of the *n-th* slice. Therefore, the friction force for each tooth is:

$$F_{side,n,G,i} = \int_{R_n - \frac{b_{slice}}{2}}^{R_n + \frac{b_{slice}}{2}} \left(\tau_{side,n,G,i} \cdot l_{n,G}\right) dR$$

(72)

$$F_{side,n,N,i} = \int_{R_n - \frac{b_{slice}}{2}}^{R_n + \frac{b_{slice}}{2}} \left(\tau_{side,n,N,i} \cdot l_{n,N}\right) dR$$

Where b_{slice} is the slice's width, as defined in Figure 66.

The friction moment due to the shear stress on a single tooth is:

$$M_{side,n,G,i} = F_{side,n,G,i} \cdot R_{n,G}$$

(73)

$$M_{side,n,N,i} = F_{side,n,N,i} \cdot R_{n,N}$$

The friction moment of each tooth side is:

$$M_{side,G,i} = \sum_n M_{side,n,G,i}$$

(74)

$$M_{side,N,i} = \sum_n M_{side,n,N,i}$$

The total friction moment acting on the two lateral clearances for each gear is:

$$M_{side,G} = 2\sum_{Z_t} M_{side,G,i}$$

$$M_{side,N} = 2\sum_{Z_t} M_{side,N,i}$$

(75)

III.3.5.5 Evaluation of the moment due to drain leakage: M_{drain}

The pressure-driven leakage flow (Poiseuille type) along the radial direction generates shear stress, which does not create any friction moment. The friction moment is only due to the Couette effect, and its shear stress can be calculated as follows:

$$\tau_{drain,t} = \frac{\mu\omega r}{h}$$

(76)
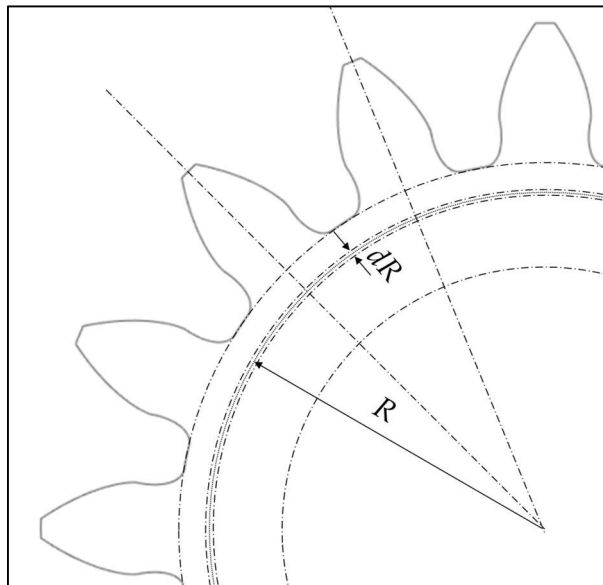
Figure 72. Dimensions for the drain shear stress

The friction forces have been calculated as follow:

$$F_{drain,t,G,i} = \int_{R_{plate}}^{R_{root}} \left(\tau_{drain,t,G,i} \cdot \frac{2\pi R}{Z_t} \right) dR$$

$$F_{drain,t,N,i} = \int_{R_{plate}}^{R_{root}} \left(\tau_{drain,t,N,i} \cdot \frac{2\pi R}{Z_t} \right) dR$$

(77)

The friction moment for the shear stress is:

$$M_{drain,t,G,i} = F_{drain,t,G,i} \cdot \left(\frac{R_{root} + R_{plate}}{2} \right)$$

$$M_{drain,t,N,i} = F_{drain,t,N,i} \cdot \left(\frac{R_{root} + R_{plate}}{2} \right)$$

(78)

Therefore, for the total moment for the two gears:

$$M_{drain,G} = 2\sum_{Z_t} M_{drain,t,G,i}$$

$$M_{drain,N} = 2\sum_{Z_t} M_{drain,t,N,i}$$

(79)

The moments $M_{housing}$, $M_{bearing}$, $M_{churning\ losses,}$ and $M_{f.teeth}$ have been neglected in this study.

III.3.6 Force calculation

An analysis of each gear's forces during the rotation has also been carried out. On each gear, the resultant force applied is the sum of different type of forces:

$$F_{tot,G} = F_{p,tot,G} + F_{tip,G} + F_{side,G} + F_{drain,r,G} + F_{contact,G}$$

(80)

$$F_{tot,N} = F_{p,tot,N} + F_{tip,N} + F_{side,N} + F_{drain,r,N} + F_{contact,N}$$

$F_{drain,t}$ and $F_{contact}$ are the force of the pressure-driven leakage to the drain and the contact force between gears, while $F_{p,tot}$ is the total pressure force, also considering pressure contributes F_{pn} outside the meshing zone. The other quantities have already been presented.

$$F_{p,tot,G} = \sum_{Z_t} \left(F_{pn,G,i} + F_{R,G,i} + F_{B,G,i} + F_{G,G,i} \right)$$

(81)

$$F_{p,tot,N} = \sum_{Z_t} \left(F_{pn,N,i} + F_{R,N,i} + F_{B,N,i} + F_{G,N,i} \right)$$

The pressure force outside the meshing zone is visible in Figure 73 and Figure 74 for the driving and driven gear.
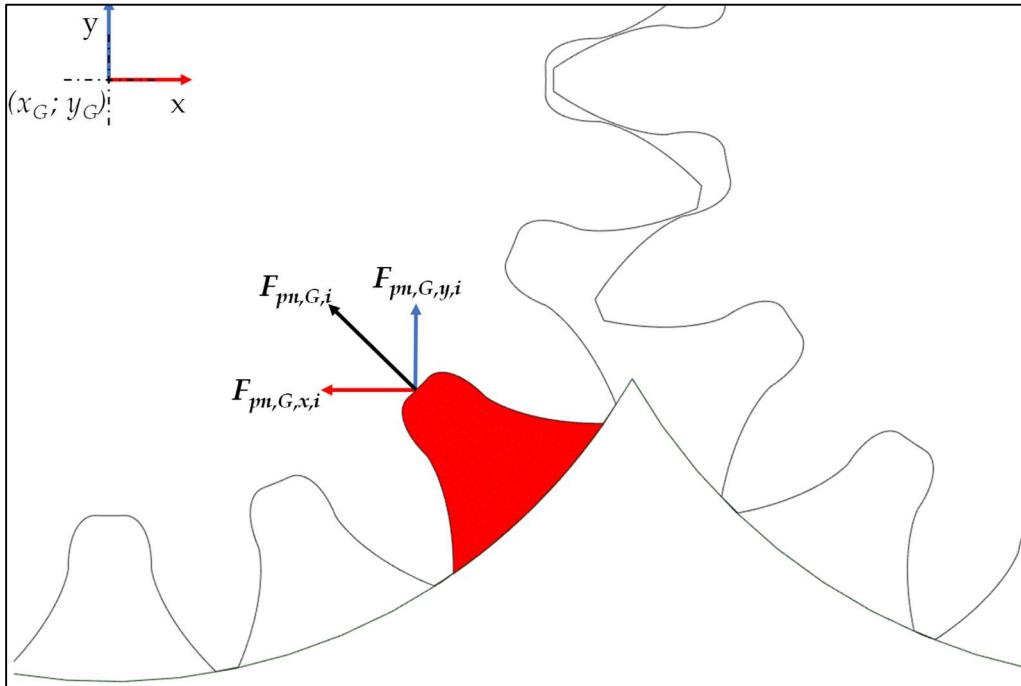
Figure 73. Pressure force in the non-meshing zone (driving gear)

In particular, for the driving gear:

$$F_{pn,G,x,i} = -F_{pn,G,i} \cdot \cos\left(\varphi + \frac{\pi}{Z_t}\right) = -p_{G,i} \cdot b \cdot \frac{2\pi}{Z_t} \cdot \cos\left(\varphi + \frac{\pi}{Z_t}\right)$$

$$(82)$$

$$F_{pn,G,y,i} = F_{pn,G,i} \cdot \sin\left(\varphi + \frac{\pi}{Z_t}\right) = p_{G,i} \cdot b \cdot \frac{2\pi}{Z_t} \cdot \sin\left(\varphi + \frac{\pi}{Z_t}\right)$$
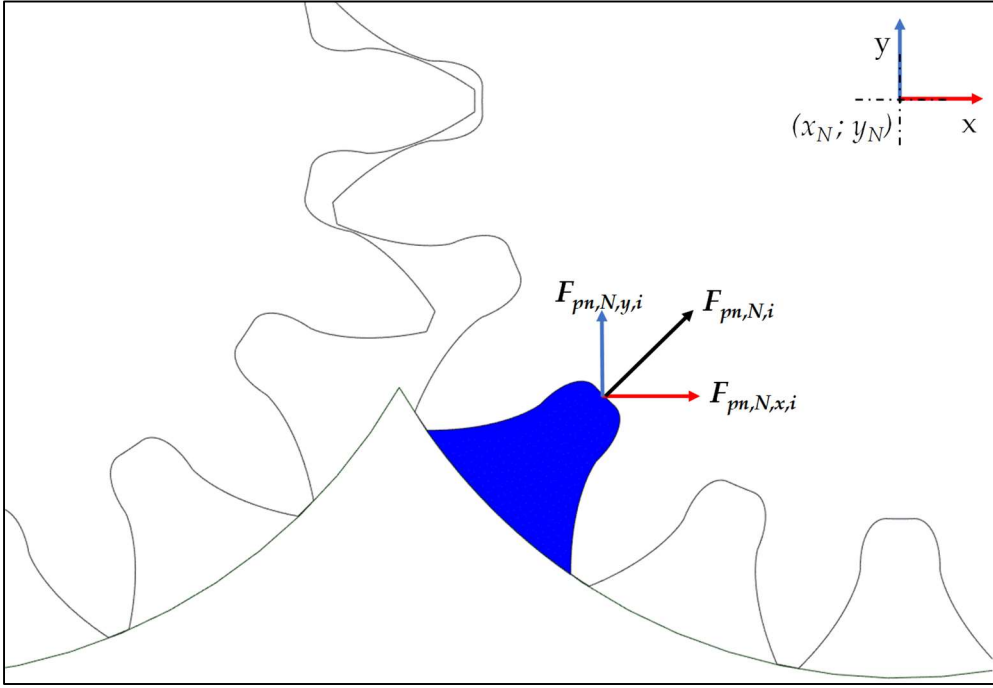
Figure 74. Pressure force in the non-meshing zone (driven gear)

In contrast, for the driven gear:

$$F_{pn,N,x,i} = -F_{pn,N,i} \cdot \cos\left(\varphi + \frac{2\pi}{Z_t} - \xi\right) = -p_{N,i} \cdot b \cdot \frac{2\pi}{Z_t} \cdot \cos\left(\varphi + \frac{2\pi}{Z_t} - \xi\right)$$

$$(83)$$

$$F_{pn,N,y,i} = -F_{pn,N,i} \cdot \sin\left(\varphi + \frac{2\pi}{Z_t} - \xi\right) = -p_{N,i} \cdot b \cdot \frac{2\pi}{Z_t} \cdot \sin\left(\varphi + \frac{2\pi}{Z_t} - \xi\right)$$

Where ξ is the angle to achieve a contact configuration between teeth of both gears.

Finally, the component of the total pressure force can be evaluated as follows:

$$F_{p,tot,G,x} = \sum\nolimits_{Z_t} \left(F_{pn,G,x,i} + F_{R,G,x,i} + F_{B,G,x,i} + F_{G,G,x,i} \right)$$

$$F_{p,tot,G,y} = \sum\nolimits_{Z_t} \left(F_{pn,G,y,i} + F_{R,G,y,i} + F_{B,G,y,i} + F_{G,G,y,i} \right)$$

$$F_{p,tot,N,x} = \sum\nolimits_{Z_t} \left(F_{pn,N,x,i} + F_{R,N,x,i} + F_{B,N,x,i} + F_{G,N,x,i} \right)$$ (84)

$$F_{p,tot,N,y} = \sum\nolimits_{Z_t} \left(F_{pn,N,y,i} + F_{R,N,y,i} + F_{B,N,y,i} + F_{G,N,y,i} \right)$$

The force components for the tooth tip leakage are:

$$F_{tip,G,x} = \sum\nolimits_{Z_t} \left(F_{tip,G,i} \cdot \sin \varphi \right)$$

$$F_{tip,G,y} = \sum\nolimits_{Z_t} \left(F_{tip,G,i} \cdot \cos \varphi \right)$$

$$F_{tip,N,x} = -\sum\nolimits_{Z_t} \left(F_{tip,N,i} \cdot \sin \left(\varphi + \frac{2\pi}{Z_t} - \xi \right) \right)$$ (85)

$$F_{tip,N,y} = \sum\nolimits_{Z_t} \left(F_{tip,N,i} \cdot \cos \left(\varphi + \frac{2\pi}{Z_t} - \xi \right) \right)$$

The force components for the side tip leakage are:

$$F_{side,G,x} = 2 \cdot \sum\nolimits_{Z_t} \left(F_{side,G,i} \cdot \sin \varphi \right)$$

$$F_{side,G,y} = 2 \cdot \sum\nolimits_{Z_t} \left(F_{side,G,i} \cdot \cos \varphi \right)$$ (86)

$$F_{side,N,x} = -2 \cdot \sum_{Z_t} \left(F_{side,N,i} \cdot \sin\left(\varphi + \frac{2\pi}{Z_t} - \xi \right) \right)$$

$$F_{side,N,y} = 2 \cdot \sum_{Z_t} \left(F_{side,N,i} \cdot \cos\left(\varphi + \frac{2\pi}{Z_t} - \xi \right) \right)$$

As said, the shear stress due to Poiseuille effects does not generate a moment for what concerns the drain leakage. In contrast, it generates a force acting on the gear. Instead, although it generates a moment on the gear, the Couette effect does not create a force for its symmetrical behavior. The shear stress in the radial direction for the drain leakage can be evaluated:

$$\tau_{drain,r,i} = \frac{h}{2} \cdot \frac{\left(p_i - p_{housing} \right)}{l} \quad \text{where} \quad l = \frac{\pi \left(R_{root} + R_{plate} \right)}{Z_t} \tag{87}$$

Where h is the height of the axial gap and $p_{housing}$ is the housing pressure.

$$F_{drain,r,G,i} = \int_{R_{plate}}^{R_{root}} \tau_{drain,r,G,i} \cdot l \cdot \frac{2\pi}{Z_t} dR$$

$$F_{drain,r,N,i} = \int_{R_{plate}}^{R_{root}} \tau_{drain,r,N,i} \cdot l \cdot \frac{2\pi}{Z_t} dR \tag{88}$$

Therefore:

$$F_{drain,r,G,x} = -2 \cdot \sum_{Z_t} \left(F_{drain,r,G,i} \cdot \sin\left(\varphi + \frac{\pi}{Z_t} \right) \right) \tag{89}$$

97

$$F_{drain,r,G,y} = 2 \cdot \sum_{Z_t} \left(F_{drain,r,G,i} \cdot \cos\left(\varphi + \frac{\pi}{Z_t} \right) \right)$$

$$F_{drain,r,N,x} = 2 \cdot \sum_{Z_t} \left(F_{drain,r,N,i} \cdot \sin\left(\varphi + \frac{2\pi}{Z_t} - \xi \right) \right)$$

$$F_{drain,r,N,y} = 2 \cdot \sum_{Z_t} \left(F_{drain,r,N,i} \cdot \cos\left(\varphi + \frac{2\pi}{Z_t} - \xi \right) \right)$$

III.3.6.1 Teeth contact force

The contact force $F_{contact}$, visible in Figure 75, is the force due to the contact between the gears, and it is responsible for balancing the moment on the driven gear acting along the line of contact of the coupled gears' teeth.
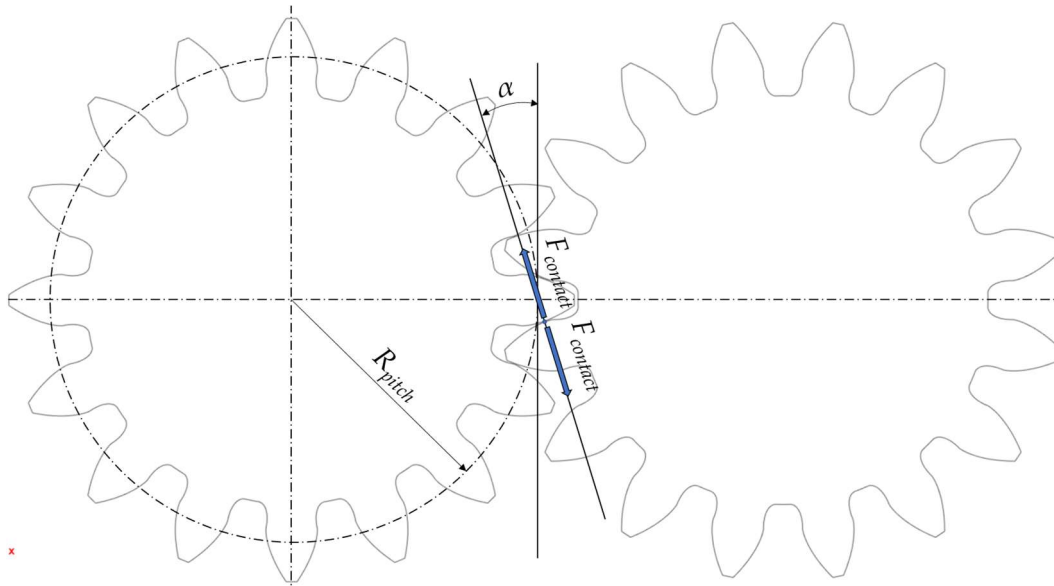
Figure 75. Teeth contact force

The equation expresses its value:

$$F_{contact} = \frac{M_N}{R_{pitch} \cdot \cos \alpha} \tag{90}$$

Where R_{pitch} is the radius of the pitch circle, and α is the pressure angle of the coupled gears.

This force acts along the contact line, creating a couple of equal value forces but with the opposite direction, as shown in Figure 75. Its components are the following:

$$F_{contact,G,x} = -F_{contact} \sin \alpha$$

$$F_{contact,G,y} = F_{contact} \cos \alpha$$

(91)

$$F_{contact,N,x} = F_{contact} \sin \alpha$$

$$F_{contact,N,y} = -F_{contact} \cos \alpha$$

III.3.6.2 The overall force acting on each gear

The overall force value along the x and y-axis of the reference system acting on each gear is:

$$F_{tot,G,x} = F_{p,G,x} + F_{tip,G,x} + F_{side,G,x} + F_{drain,r,G,x} + F_{contact,G,x}$$

$$F_{tot,G,y} = F_{p,G,y} + F_{tip,G,y} + F_{side,G,y} + F_{drain,r,G,y} + F_{contact,G,y}$$

(92)

$$F_{tot,N,x} = F_{p,N,x} + F_{tip,N,x} + F_{side,N,x} + F_{drain,r,N,x} + F_{contact,N,x}$$

$$F_{tot,N,y} = F_{p,N,y} + F_{tip,N,y} + F_{side,N,y} + F_{drain,r,N,y} + F_{contact,N,y}$$

Finally, the overall force value and the angle of its line of direction acting on each gear are:

$$F_{tot,G} = \sqrt{F_{tot,G,x}^2 + F_{tot,G,y}^2}$$

$$\alpha_G = \arctan\left(\frac{F_{tot,G,y}}{F_{tot,G,x}}\right)$$

(93)

$$F_{tot,N} = \sqrt{F_{tot,N,x}^2 + F_{tot,N,y}^2}$$

$$\alpha_N = \arctan\left(\frac{F_{tot,N,y}}{F_{tot,N,x}}\right)$$

(94)

III.4 The three-dimensional CFD numerical model

III.4.1 The approach

A transient three-dimensional CFD model of the external gear pump has been built up only to validate results obtained with EgeMATor in the absence of experimental data. The model has been developed with the commercial software Simerics MP+®, which perfectly fits this kind of analysis. It discretizes the conservation of mass and momentum equations using a finite volume method. The CFD code uses a template mesher for EGPs, which creates a structural mesh for the two gears. The model accounts for cavitation phenomena using the same approach presented in paragraph II.3.1.

In the absence of experimental data, a mesh sensitivity analysis has been done, increasing or decreasing the cell number of the displacement chambers and wear-plates to achieve a stable solution of the monitored model's outputs. The model requires a computational time of around one day for each pump revolution on an Intel® Xeon® CPU E5-2640v2 @ 2.00 GHz (two processors) and consists of about 554000 3D cells (Figure 76). Heat transfer is not included in the modeling, and temperature affects only fluid viscosity and density. To solve the turbulent flow, Simerics MP+® adopts a RANS approach, with the standard "K-Epsilon" turbulence model, which has been proved to be capable of predicting the correct time-averaged flow field, in particular for wall-bounded flows.
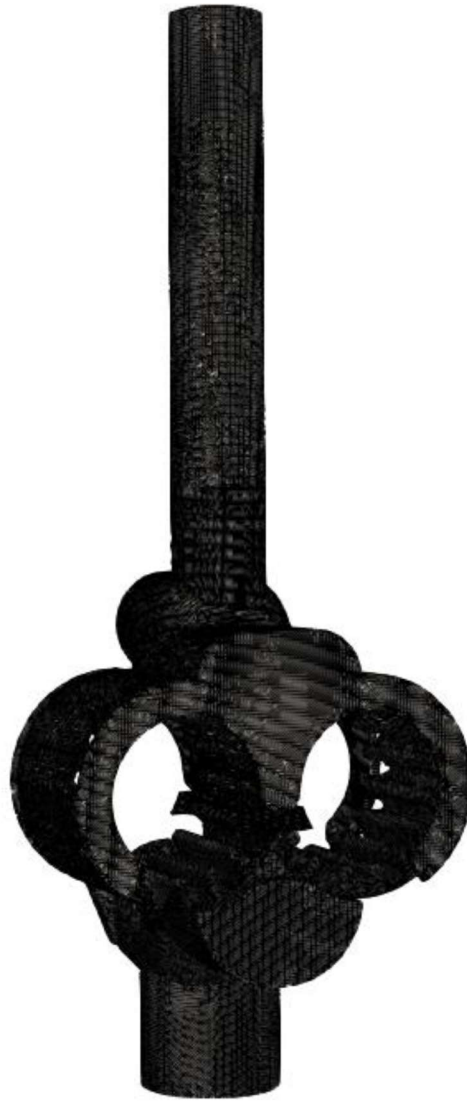
Figure 76. The mesh of the pump's fluid domain

III.4.2 Gears micromotion

For the three-dimensional CAD model, the theoretical radial clearance between the tooth tip and the internal housing is 36 μm. However, to reproduce the gear micromotion due to the pressure toward the inlet side, both gears have been offset by 30 μm to create a micro-gap of fluid to respect a non-zero volume cell required by Simerics MP+®. This micromotion makes eccentricity for the housing, increasing the gap over the tip at the pump's high-pressure side. Another small clearance is needed between the driving and driven gears' teeth to reproduce the contact. In particular, a relative rotation of 0.21° has been set to get a 5 μm gap, as shown in Figure 77.
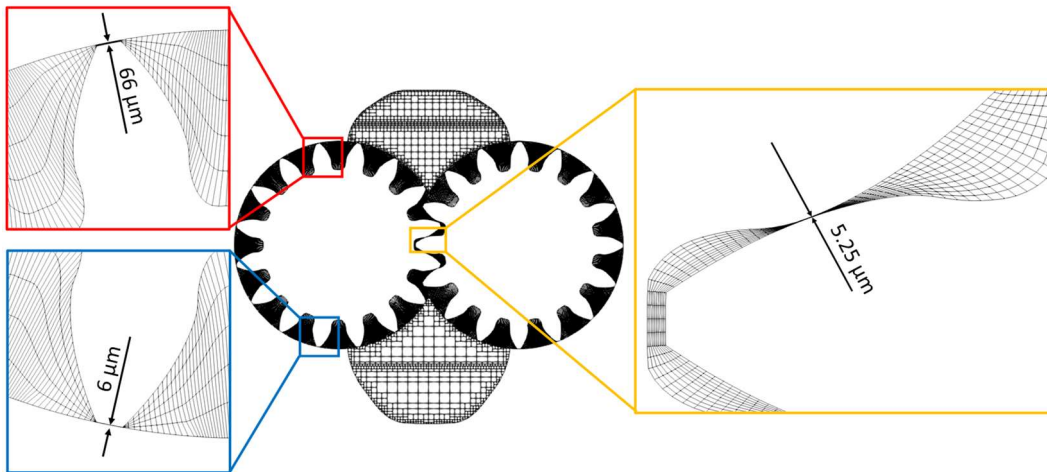
Figure 77. Section of the domain mesh - Teeth gap in the zoomed view

The numerical 3D CFD model has been run at the same boundary conditions and fluid properties simulated with EgeMATor:

- The pressure at inlet port: 0 bar;

- The pressure at outlet port: 230, 350 bar;

- The fluid is a hydraulic oil ISO VG46;

- Variable dynamic viscosity;

- Variable liquid bulk modulus (linearly dependent with pressure);

- Oil Temperature: 313K.

III.5 EgeMATor validation and 3D CFD comparison

In this paragraph, a comparison between the presented methods has been shown. The accuracy of the three-dimensional CFD approach, used in this work to validate EgeMATor tool, is already present in the literature in previous studies done by the same research group [48].

Outlet flow ripple and displacement chambers (G_i and N_i) pressures have been compared. The next graphs will show results from three different models, where each item has particular significate:

1. *EgeMATor (STD)* are the results of the lumped parameter model in standard condition, where sealing conditions (gears teeth contact, gears-housing micromotion) are strictly respected;

2. *EgeMATor (3D CFD)* are the results of the lumped parameter model with imposed clearances to match the 3D CFD simulating conditions (no perfect sealing);

3. *3D CFD* is data referred to as the three-dimensional CFD numerical model with minimum clearance to respect a CFD simulation context.

All the following results have been referred to a rotational speed of 1500 rev/min and 350 bar of the outlet pressure (maximum pressure).

III.5.1 Outlet flow ripple

In Figure 78, the outlet flow ripple has been presented in both time and frequency domains. It is notable a similar prediction of both approaches. As expected, the *EgeMATor (STD)* model, identified with the blue line in the figure, provides an average outlet flow higher than the *EgeMATor (3D CFD)* model (black line) for its better sealing conditions. As predictable, the *3D CFD* model (red line) provides an average outlet flow closer to the lumped parameter model with imposed clearances (*EgeMATor 3D CFD*).
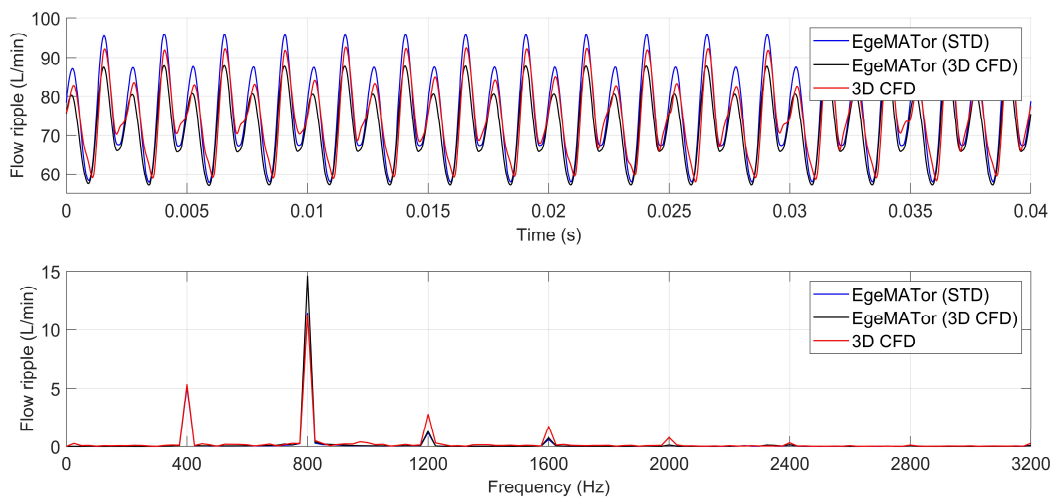
Figure 78. Outlet flow ripple at 1500 rev/min and 350 bar

III.5.2 Gi and Ni pressure distributions

The effects of the clearances imposed in the EgeMATor (3D CFD) model are better visible in Figure 79, where the pressure distributions of the displacement chambers G_1 and N_1 have been presented. Indeed, for the two models: EgeMATor (3D CFD) and 3D CFD, the chambers' pressurization phase has a similar prediction. In contrast, the EgeMATor (STD) shows different pressurization starting angle. This delay is related to the reduced tip clearance in this model during the pressurization phase transition.
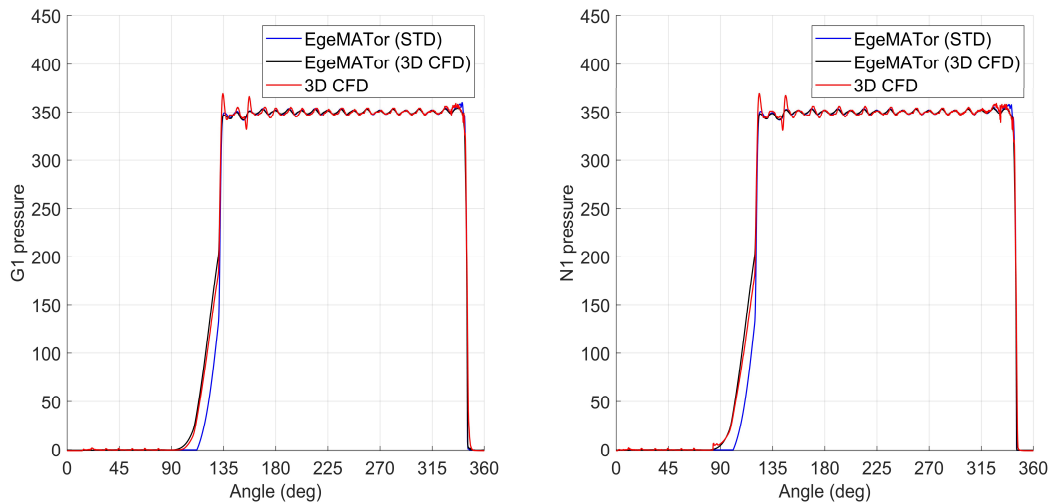
Figure 79. Gi and Ni pressure distributions

Even in these plots, the comparison shows a good agreement among the numerical simulations, confirming the adopted methodology's robustness. Considering the leakage flux across the driving tooth number 2 (ref. to Figure 62 and Figure 63), it is visible the effects of the different radial clearance between the two lumped parameter models in Figure 80. Moreover, it is also visible that the 3D CFD results are more similar to the EgeMATor (3D CFD) model, especially during the pressurization phase (around 85-130 deg of the figure). Negative values represent a flux exiting the control volume G_2.
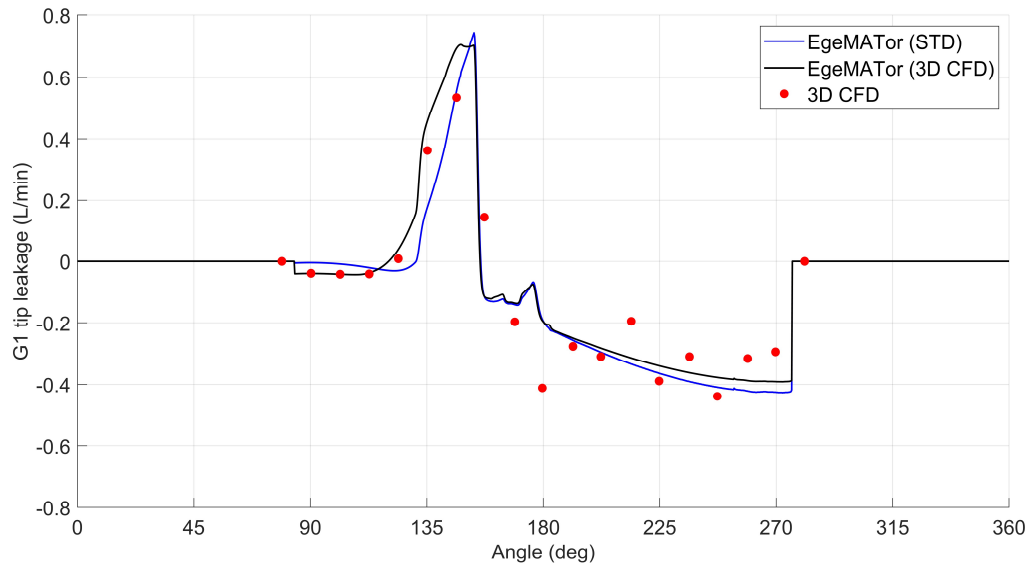
Figure 80. Tip leakage across driving tooth n°2 at 1500 rev/min and 350 bar

A secondary study on a different pump, which has a lower number of teeth per gear (ten instead of sixteen), has been presented in the next figure to prove the proposed tool's effectiveness and robustness.
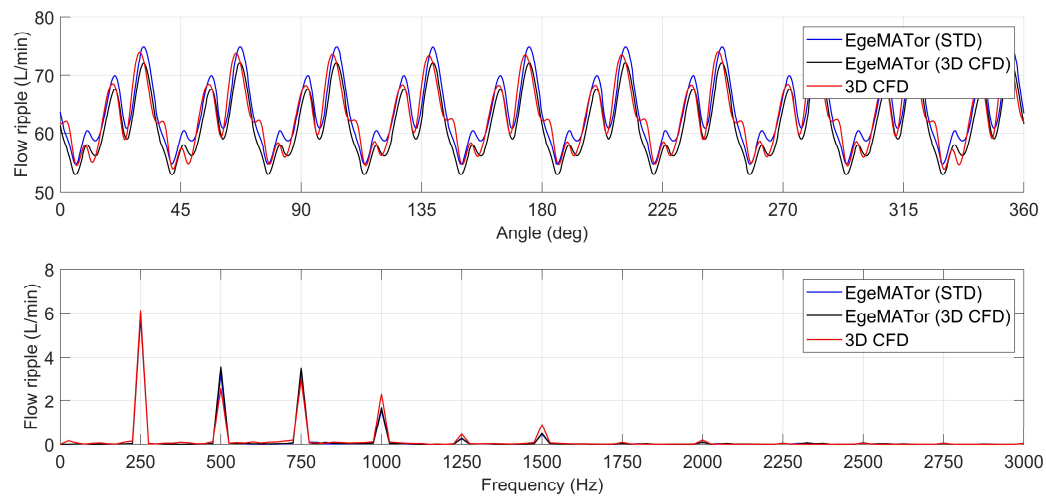
Figure 81. Flow ripple comparison in both time (angle) and frequency domains at 260 bar, 1500 rpm for a ten teeth EGP

It can be seen from Figure 81 and Figure 82, where flow ripple and displacement chambers pressure distributions, a good agreement between the 3D CFD approach and the EgeMATor model.
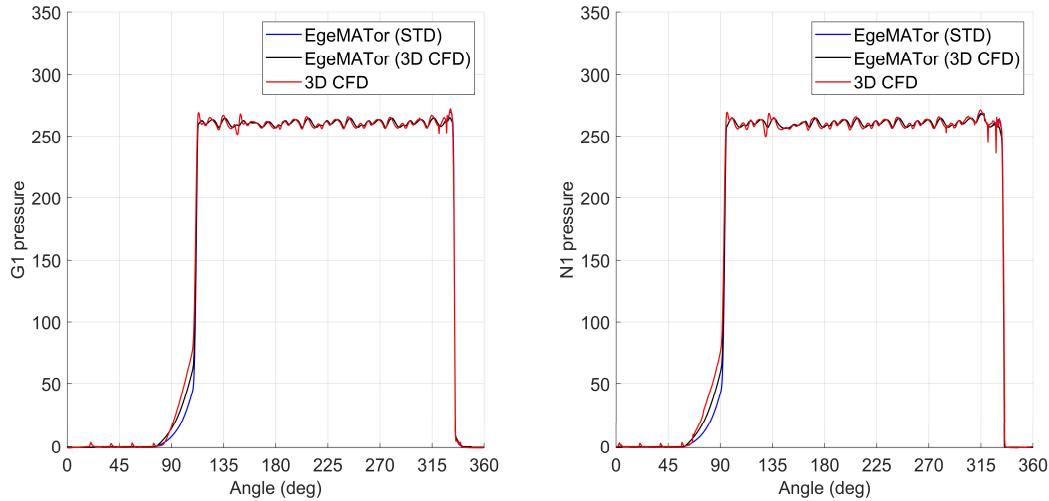
Figure 82. Gi and Ni pressure distributions for a ten teeth EGP

In this case, experimental results (P-Q curve) were available (reported in Table 7 for 1500 rev/min), and models have been validated on the average outlet flow, confirming the proposed methodologies' robustness.

Table 7. Experimental vs. Numerical average outlet flow at 1500 rev/min

| Pressure (bar) | Average outlet flow (L/min) | | Variation |
	Experimental	Numerical	
20	65.9	65.95	+0.1%
100	64.0	64.51	+0.8%
260	63.0	63.70	+1%

For this reason, EgeMATor has been used to design a wear plate geometry to reduce the flow ripple and increase volumetric efficiency.
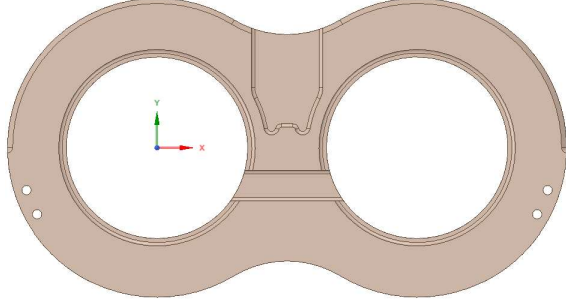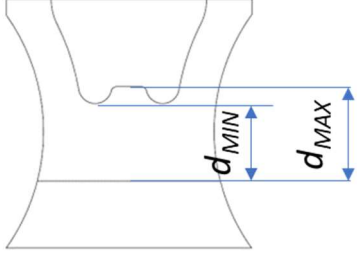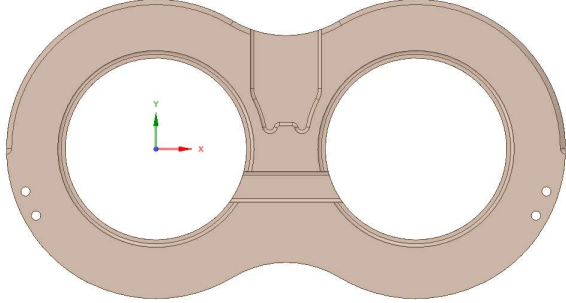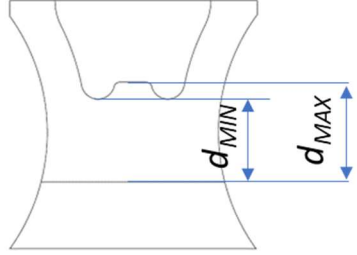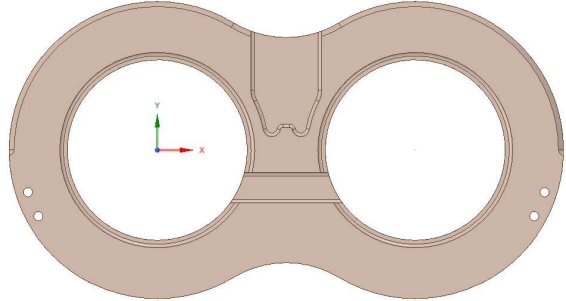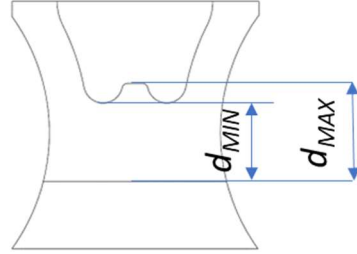
III.6 Flow ripple analysis on different wear plate designs

In this paragraph, three different wear plates have been designed to act on the outlet pressure relief groove's geometries, changing its distance from the inlet relief groove. Two different lengths have been identified; d_{min} is the minimum distance from the inlet and outlet grooves, while d_{max} determines the same length without considering the two little "fingers" of the outlet relief groove.

III.6.1 Wear-plate outlet groove geometry for flow ripple reduction

The three different versions have been presented in Table 8. In this table, 3D model and grooves sketch have been shown.

Table 8. Wear plate designs

Version	3D model	2D sketch
v1		
v2		
v3		

The geometries have been designed as a function of two ratios, which consider the gear base pitch and the two lengths presented above, as visible in Table 9.

Table 9. Wear plate ratios

Wear plate	$r_{MIN} = (\pi \cdot m \cos \alpha_t) \cos \alpha_{wt} / d_{MIN}$	$r_{MAX} = (\pi \cdot m \cos \alpha_t) \cos \alpha_{wt} / d_{MAX}$
v1	1.275	1.048
v2	1.189	0.989
v3	1.248	1.000

Where m is the gear module, α_t and α_{wt} are the pressure angle and the working pressure angle.

107

The three geometries have been numerically simulated in EgeMATor (STD, with a perfect sealing) in standard working conditions. The flow ripple is visible in Figure 83.
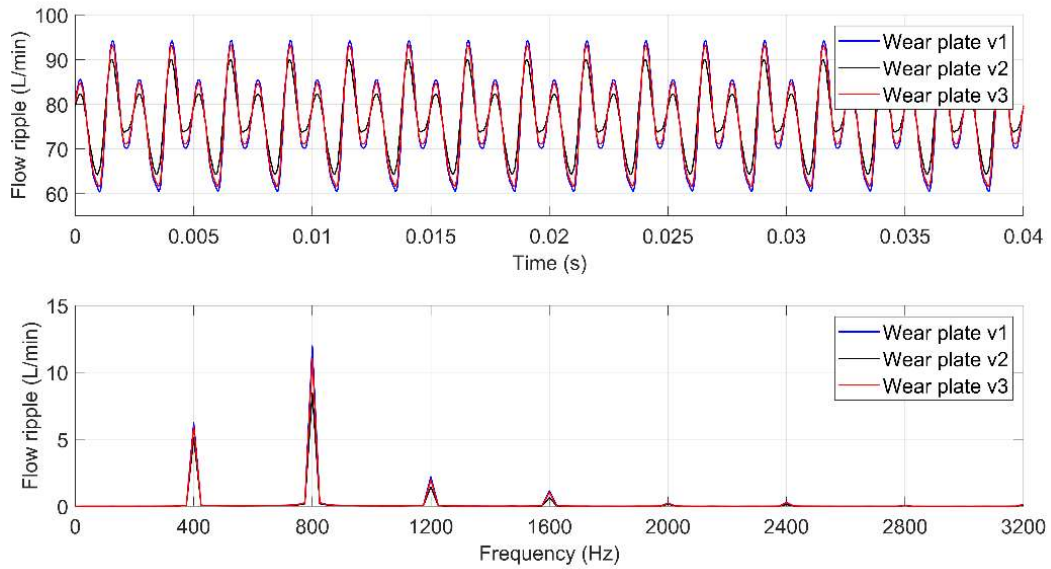
Figure 83. Outlet flow ripple at 1500 rev/min and 230 bar

The flow ripple amplitude is visibly lower in the wear plate version 2 in these working conditions. Even the average delivered flow rate is slightly higher with this design.

Table 10. Average flow-rate for the three proposed geometries

Wear plate	Average Delivered Flow (L/min)
v1	76.3575
v2	76.9238
v3	76.5156

No significant variations have been appreciated in the displacement chambers distribution. In particular, no pressure spikes have been observed at the end of the pressure transition zone.
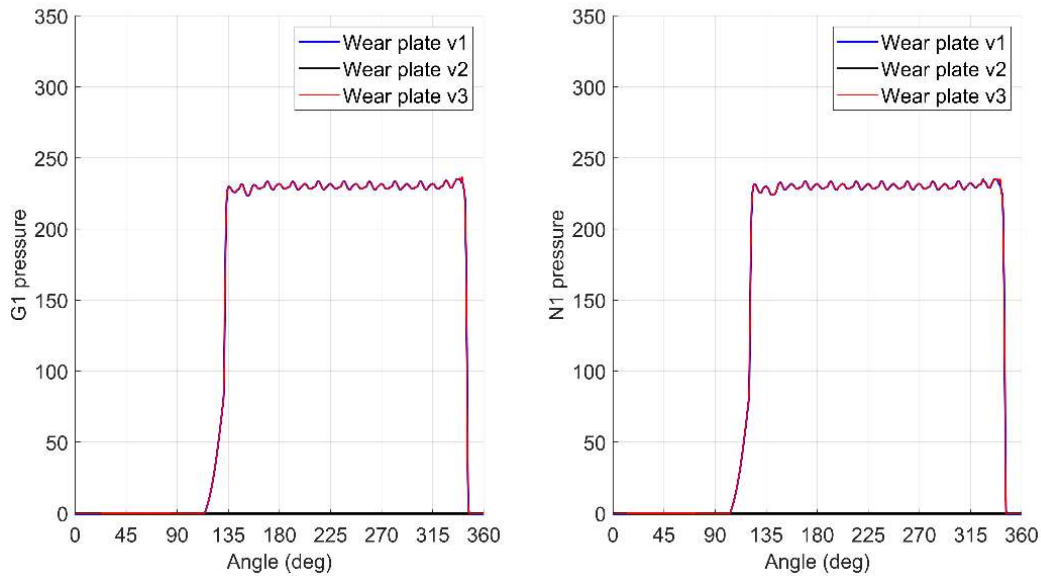
Figure 84. G1 and N1 pressure distributions for the three different wear plates

Looking at Table 9, values of r_{MAX} around 1 (±1%) and r_{MIN} around 1.19 fit to reduce the flow amplitude, keeping high volumetric efficiency. Indeed, the volumetric efficiency with the wear plate number version 2 is about 97.3% (at a medium-high pressure).

The next section presents an analysis of noise and vibration on the initial prototype pump with 18 teeth tested in Dresden and the new design with 16 teeth and the v2 wear-plate.

III.7 Noise and Vibrations analyses on *v2* pump version

III.7.1 Introduction

Due to the pandemic that affected the entire Earth in 2020, no more analyses could be done in Dresden to compare the new pump designs. For this reason, noise and vibrations analyses have been done in Duplomatic MS's lab to compare the prototype pump (18 teeth, spur gear) with the new version (16 teeth, spur gear with the v2 wear-plate).

Noise measurements have been taken with 1/2" pre-polarized free-field condenser microphone with a sensitivity of 50 mV/Pa (+/-1.5 dB), and a frequency range of 3.75 Hz - 20 kHz (+/-2 dB) with 1/2" ICP® preamplifier (426E01) and TEDS located at 1 m from the pump. Vibrations have been measured through three high sensitivity, ceramic shear ICP® accelerometers, with a sensitivity of 100 mV/g,

and a frequency range of 0.5 Hz to 10k Hz, mounted on the top, back, and outlet port of the pump.

III.7.2 Noise and vibration analyses

Different working points have been studied for both pumps and three operating speeds have been presented in the next figures. Even in this case, the company requested not to show the measured sound pressure level values, but it is possible to say that, also for these diagrams, the y-grid size is 5 dBA. The maximum pressure has been set at 250 bar due to the electric motor torque limits. Therefore, Figure 85, Figure 86, and Figure 87 show that the A-weighted sound pressure level, as a function of the pump outlet pressure at different shaft speed (1000, 1500, 1800 rev/min), has been highly reduced.
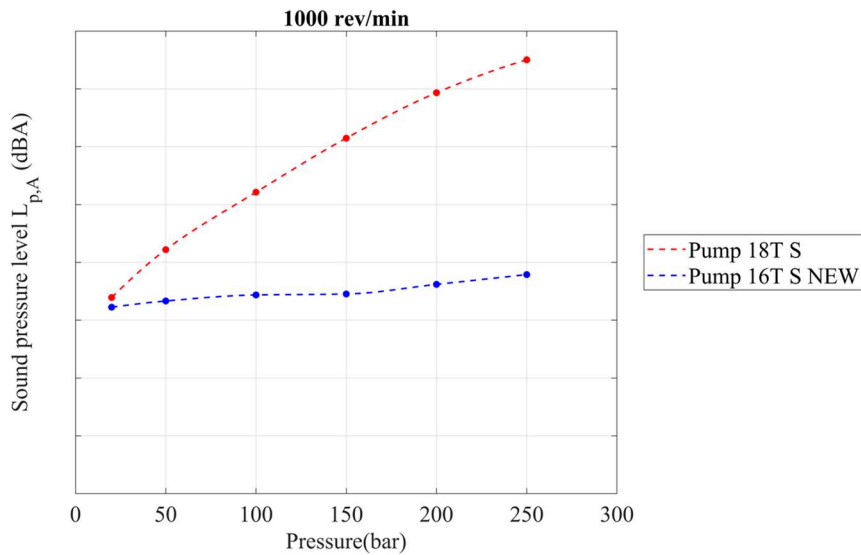
Figure 85. Sound pressure level measured at 1 m from the pump at 1000 rev/min
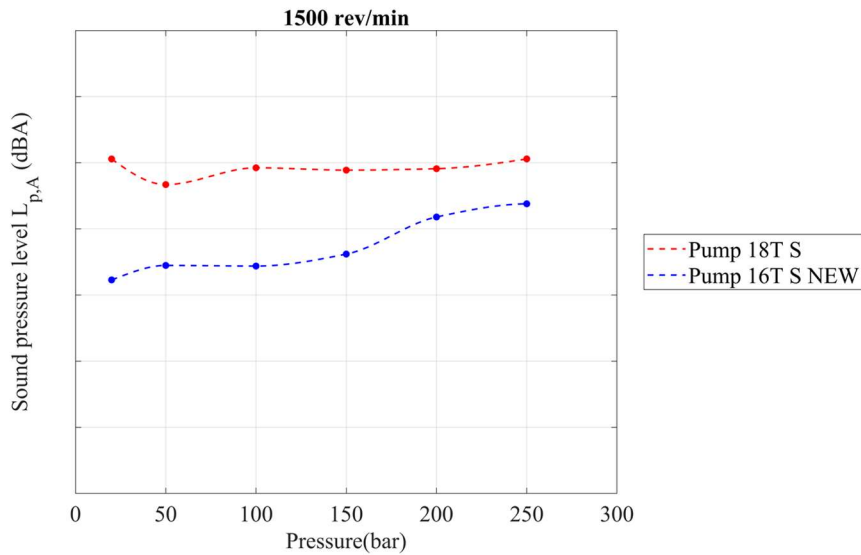
Figure 86. Sound pressure level measured at 1 m from the pump at 1500 rev/min
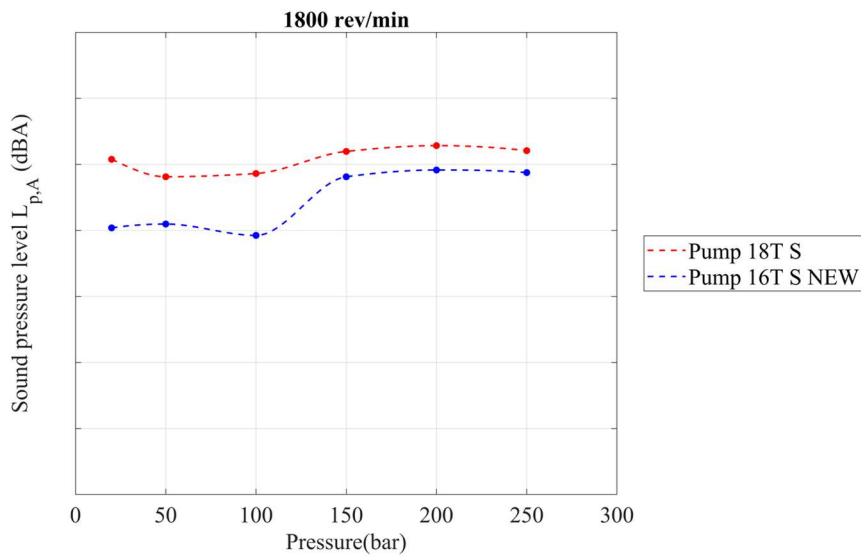
Figure 87. Sound pressure level measured at 1 m from the pump at 1800 rev/min

Further analyses have been presented for the 1000 rev/min working points. In particular, a third-octave acoustic noise spectrum analysis has been reported in this thesis for both pumps at 20 and 250 bar where the noise difference emitted by both pumps is minimum and maximum, respectively. With equation (1), the first fundamental frequency can be evaluated; in particular, for the 18 teeth pump, the first fundamental frequency is 600Hz, while for the new pump, it is 533Hz. In the next figures, the y-grid size different from the previous.
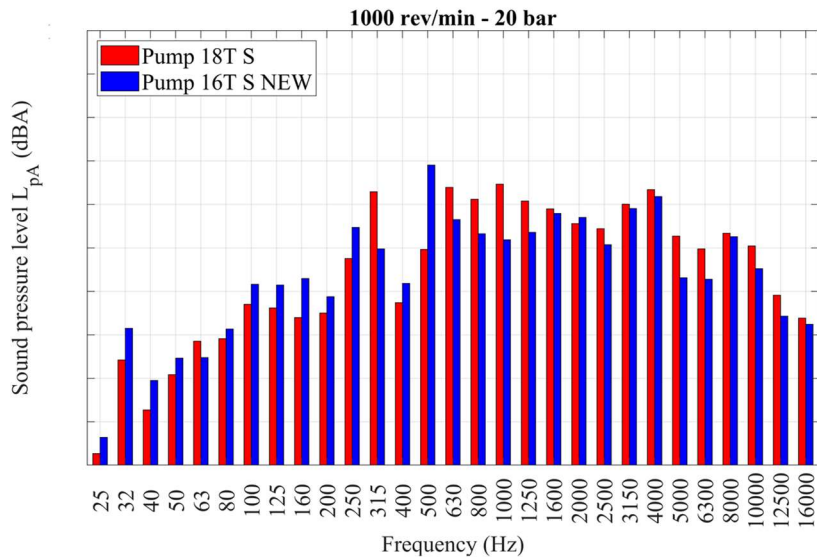
Figure 88. Noise spectrum for both pumps at 1000 rev/min and 20 bar

Figure 88 shows that only the 16 teeth pump has the first fundamental preponderant (500 Hz band). Instead, for the 18 teeth pump, the first fundamental is not preponderant, while a 315 Hz band shows higher values. It is due to the small gear intersection detected by the Surface Tool© in the meshing zone, already presented in Table 5, since the 315 Hz band includes the frequency of the 18 teeth at 1000 rev/min (300 Hz).
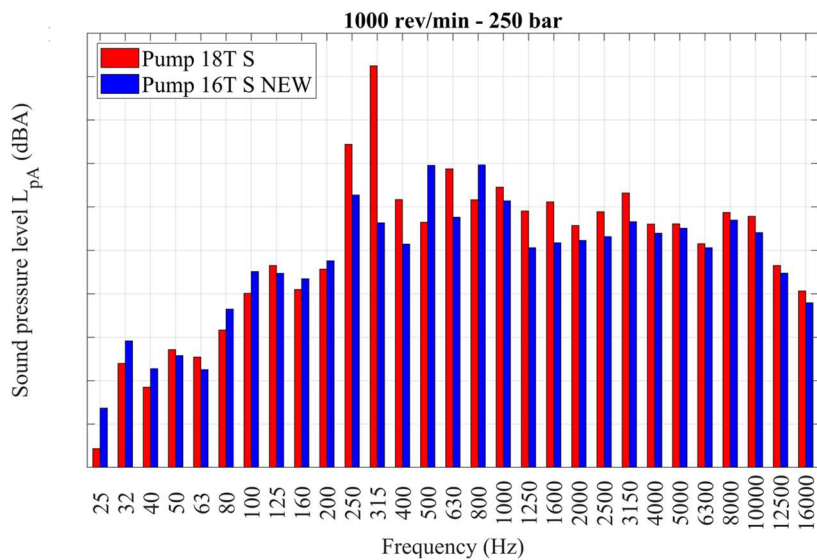
Figure 89. Noise spectrum for both pumps at 1000 rev/min and 250 bar

The same considerations can be done in Figure 89, where the 315 Hz band increases drastically due to the pump outlet pressure, which reduces the gears' center-to-center distance.

The FFT acceleration spectra presented in Figure 90 and Figure 91 is in line with the previous third-octave acoustic noise spectrum analysis.
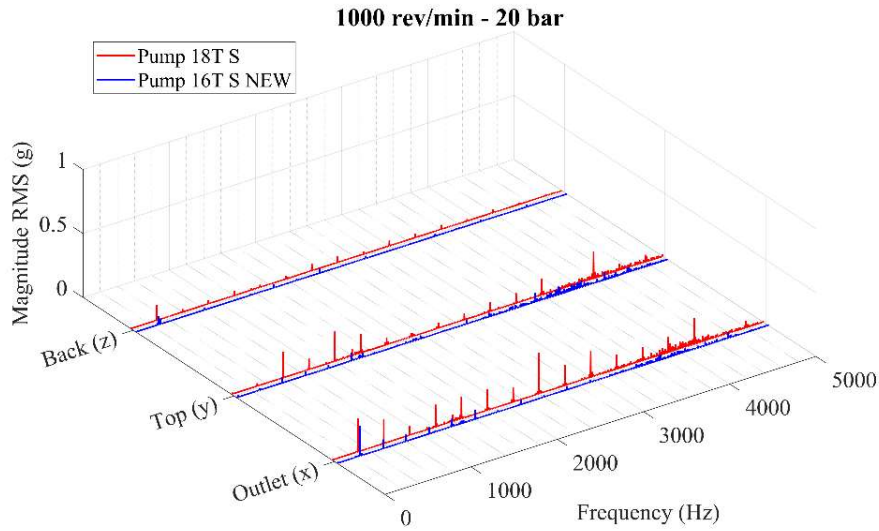
Figure 90. FFT vibrations spectrum for both pumps at 1000 rev/min and 20 bar

In particular, at 250 bar the spectrum confirmed the 300 Hz predominant frequency for the 18 teeth pump, which results much higher than the 16 teeth pump spectrum.
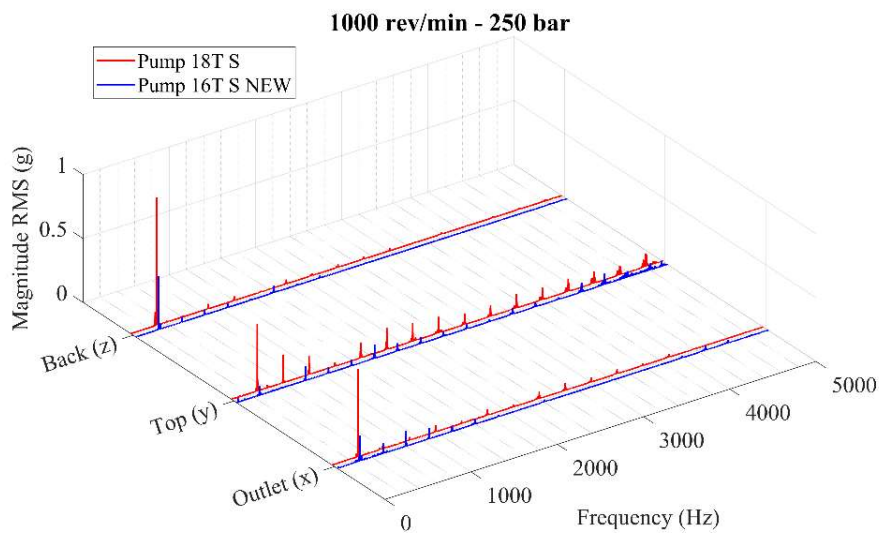
Figure 91. FFT vibrations spectrum for both pumps at 1000 rev/min and 250 bar

The presented results have been shown how EgeMATor tool created is capable of supporting EGP development and optimization.

The next paragraph focuses on optimizing the pump performance, looking, in particular, to reduce the flow ripple further. For this purpose, an innovative solution called ACV is introduced in EgeMATor, providing interesting results.

III.8 The Alternative Capacitive Volume technology

III.8.1 Idea

The main idea behind introducing the Alternative Capacitive Volumes (ACV) is to act on the reverse flow from the delivery volume to the displacement chambers during the pressurization (Figure 92 and Figure 93). Usually, the displacement chamber's pressurization happens through a reverse flow coming directly from the outlet volume, creating a drop clearly visible on the flow ripple. With the introduction of the ACV, a volume of oil trapped between two small orifices (around 4 cm^3 for the presented case) is used for the chamber pressurization. Thus, the reverse flow is controlled and uniformized. The first orifice is a threaded orifice inserted to connect the ACV with the delivery volume (Figure 92 and Figure 93), while the second one is directly machined in the wear-plate connecting the displacement volume to the ACV, highlighted in Figure 95. Every visible external access will be opportunely sealed, as well as the wear-plate back.
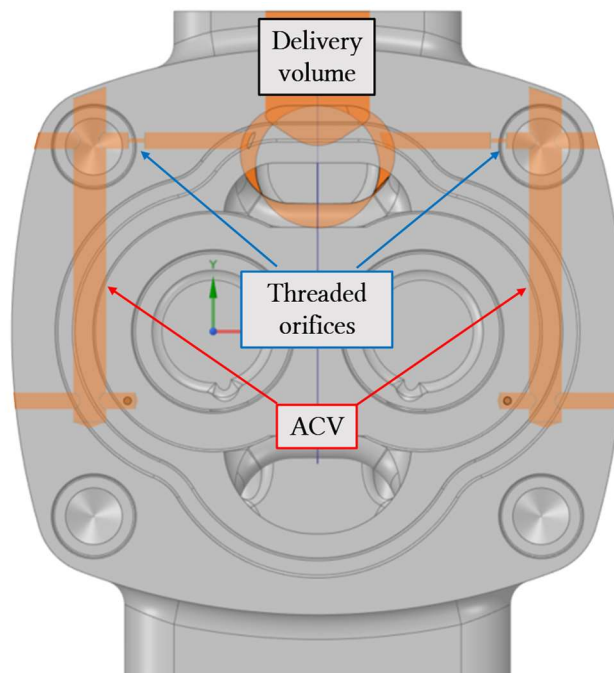
Figure 92. Pump housing views with highlighted ACV surfaces: Front view.
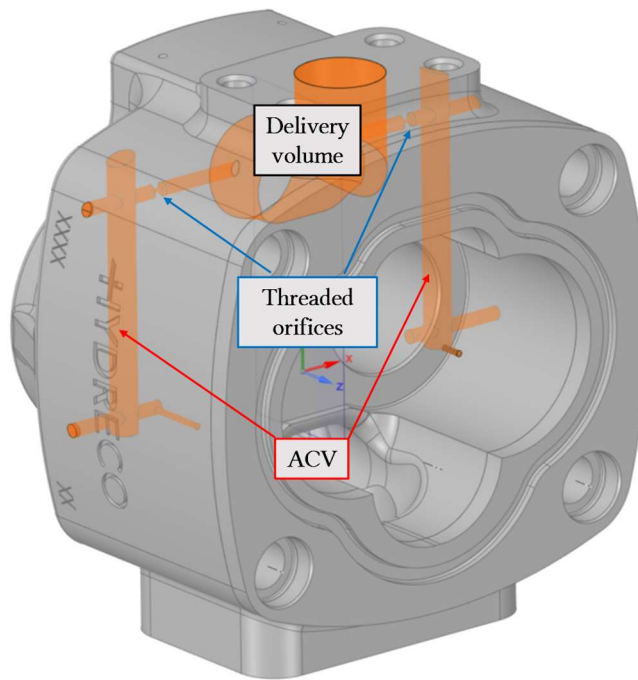
Figure 93. Pump housing views with highlighted ACV surfaces: Prospective view.

A standard 1 mm threaded orifice has been selected for the ACV connection with the delivery port to make the system industrially reliable. A volume of the ACV that could easily fit in the pump housing through additional machining has been designed. Then, numerical simulations have been run to prove the idea.
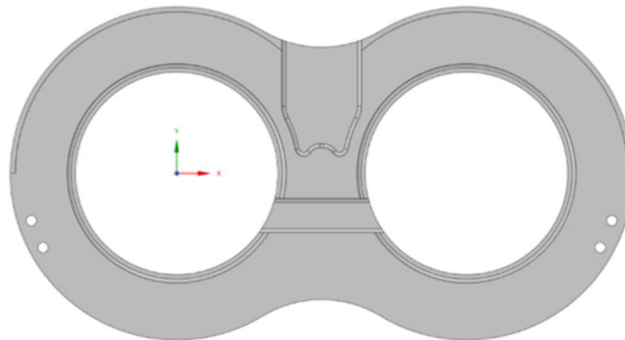
Figure 94. Wear-plate design: Standard configuration
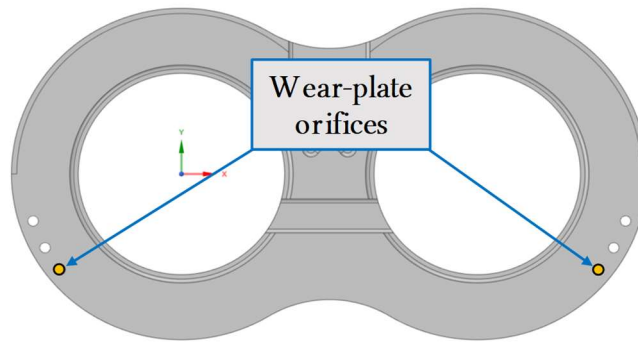
Figure 95. Wear-plate design: Configuration with orifice connection to the ACV.

The first set of simulations has been run to compare results from 3D CFD (ACV) model with EgeMATor (3D CFD ACV), validating the lumped parameter approach and the ACV introduction. The simulation constraints are 1500 rev/min (average working speed) and 230 bar (average working pressure). This analysis has been presented in Figure 96, where the EgeMATor (3D CFD), identified with a blue line, shows a higher numerical flow non-uniformity amplitude than the pump model with the ACV (black line). The same results are visible for the 3D CFD model, which is very similar in the flow ripple prediction. The same figure, looking at the frequency domain, shows a reduction of the flow ripple on the second fundamental frequency (800 Hz). It is due to the reduction of the reverse flow for each displacement chamber (at 1500 rev/min the shaft frequency is 25 Hz, value that if it is multiplied by the number of 32 displacement chambers gives 800 Hz).
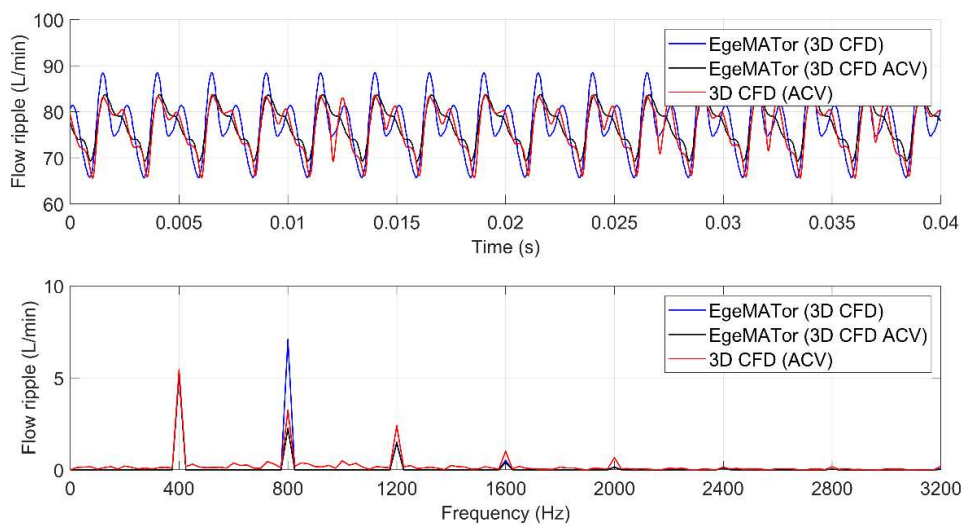
Figure 96. Outlet flow ripple at 1500 rev/min and 230 bar in time and frequency domains.

After this validation, the second set of simulations has been run only in the EgeMATor environment, with perfect sealing, not reliable in the 3D CFD model. The mentioned analysis has been presented in Figure 97, where the flow ripple amplitude reduction is still effective.
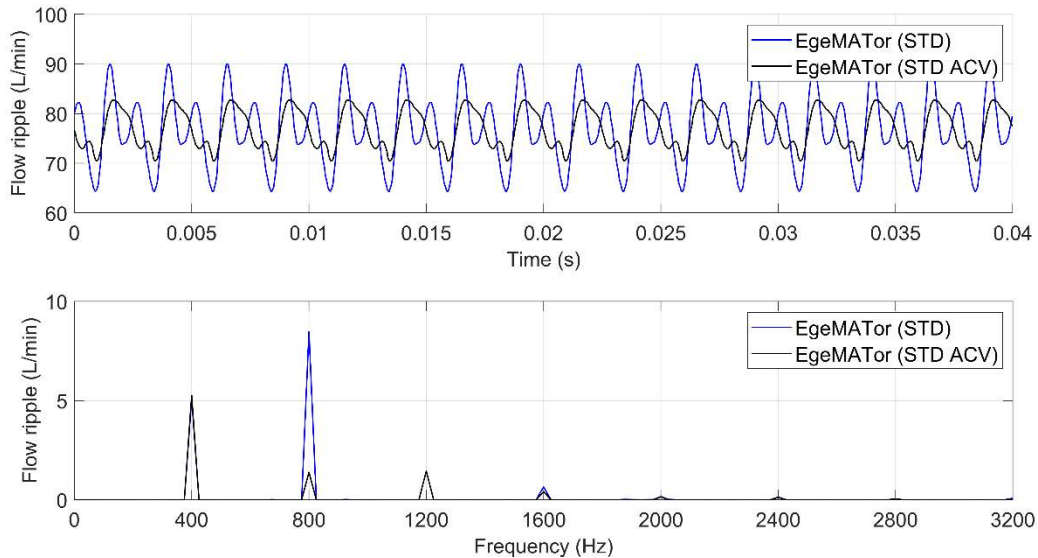
Figure 97. Standard vs. ACV (no gap), Outlet flow ripple at 1500 rev/min and 230 bar in time and frequency domains.

As visible, the second fundamental frequency of the flow ripple, visible in the frequency domain, is highly reduced. No relevant differences have been observed on the other frequencies.

III.8.2 The ACV's β Angle Optimization

Since the dumper functionality of the ACV has been proved, an optimization process has been run to get the best design's benefits. The optimization process has been performed directly in EgeMATor since Simcenter Amesim® permits this kind of study. The process has been performed directly in Simcenter Amesim® for its speed of calculation. It has been decided to run an optimization to reduce the flow ripple simply modulating the angle β visible in Figure 98 since the Surface Tool© does not allow parametrization of the plate's geometries. In this way, the Non-Uniformity Grade (NUG) [1] can be minimized, reducing the fluid-borne noise. The optimization process aimed at the fluid-borne noise reduction has been done using a Non-Linear Programming by Quadratic Lagrangian (NLPQL) method, which particularly fits this kind of study, where a single objective function has to be minimized.
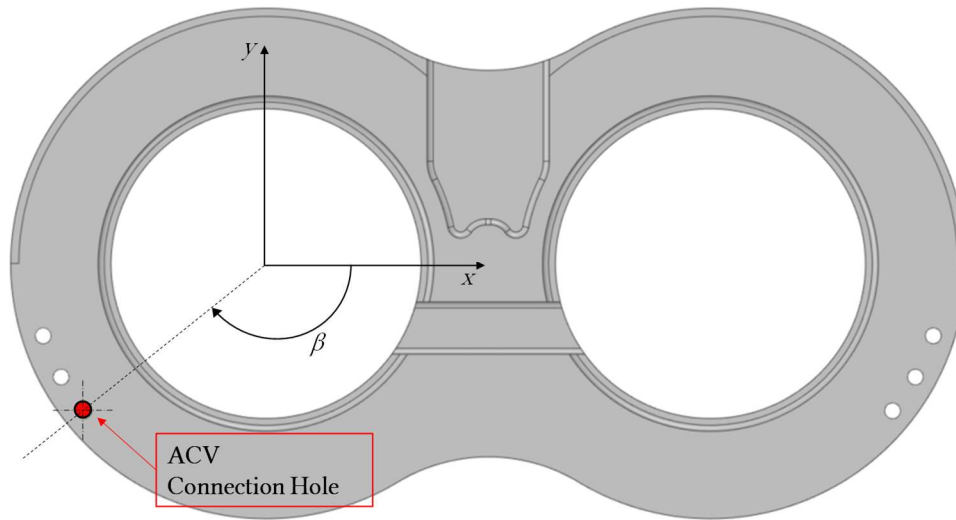
Figure 98. Definition of the Angle β.

The optimization process's input is the parameter Δβ, which shifts the hole's angular position that connects the displacement chamber to the ACV. Analysis of ACV volume influence has been conducted; its minimum volume to achieve flow ripple reduction has been found around two times the displacement chamber maximum's volume, smaller volumes have been investigated, showing no sensible improvements. The selected volume is the maximum obtainable not to affect the structural strength of the housing. The effects of gears' micromotions have been neglected since they lie in the drawings' tolerance range. The definition of the objective function is given in the following equation:

$$Objective\ Function: \ min(NUG) \tag{95}$$

This *Objective Function* has a simple interpretation: it tends to minimize the "Non-Uniformity Grade". Parameters set for the optimization study are the following:

- Optimization technique: NLPQL;

- Relative gradient step: 0.0001;

- Desired final accuracy: 0.001.

The optimization process took nine iterations to complete the algorithm, as shown in Figure 99. It can be noted from the figure that the NUG has been further reduced from the initial value of 0.160 to 0.131, with a reduction of 18.1%. The

corresponding $\Delta\beta$ variation from the initial value is −0.51 deg. The working condition constraints are 1500 rev/min (average working speed) and 230 bar (average working pressure).
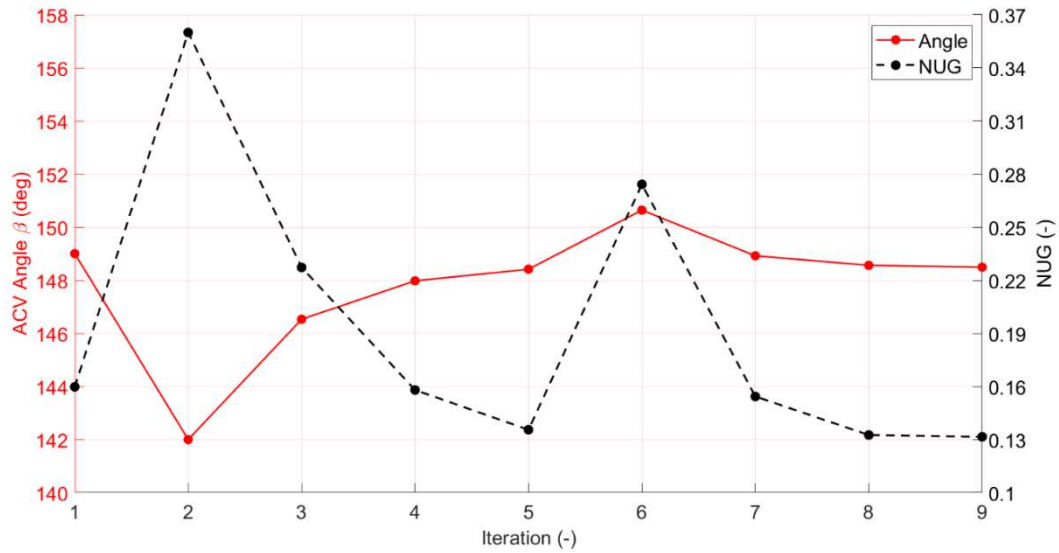
Figure 99. Optimization process trend.

III.8.3 Results from optimization

Using EgeMATor, further analysis has been presented in Figure 100. Here, the numerical flow ripple comparison has been reported, for both time and frequency domains, among the initial standard pump (blue line), the pump with the ACV (black line), and the pump with the ACV angle optimized (red line). A further reduction in the flow ripple amplitude using the optimized angle is visible from the figure's top plot. The same results are evident in the frequency domain, again on the second fundamental frequency (800 Hz).
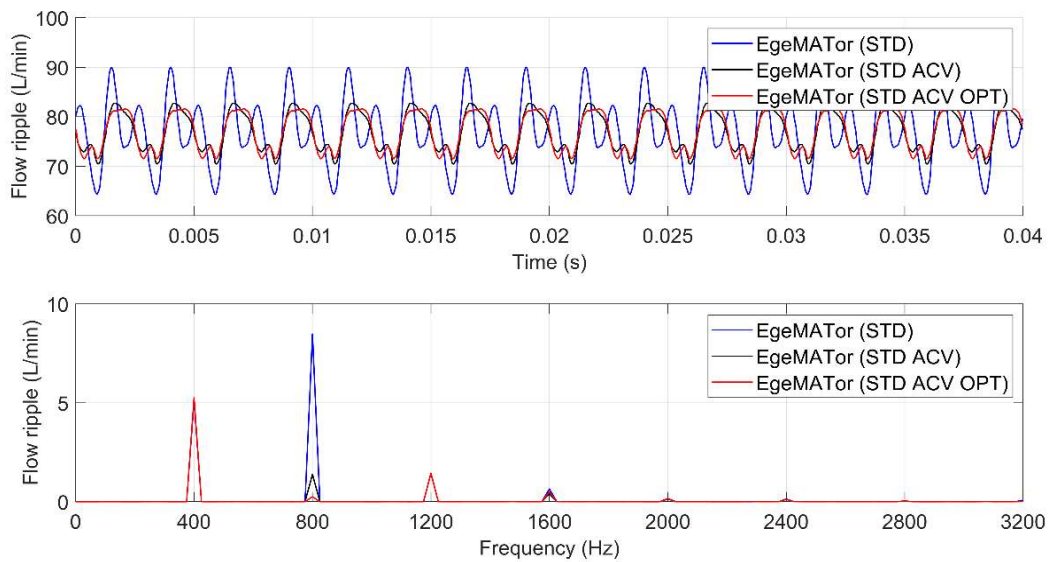
Figure 100. Flow ripple comparison in both time and frequency domains at 230 bar, 1500 rev/min.

Table 11 presents a summary of the NUG reduction achieved with the optimization process.

Table 11. Results summary at 1500 rev/min and 230 bar.

EgeMATor Model	NUG	Reduction from STD Model
Standard (STD)	0.334	/
with ACV (STD ACV)	0.160	−52.1%
with ACV optimized (STD ACV OPT)	0.131	−60.8%

About the G_i and N_i pressure distributions visible in Figure 101, the effects of the ACV introduction are also evident. The pressurization, due to the tip leakage, becomes shorter in terms of angular extension.
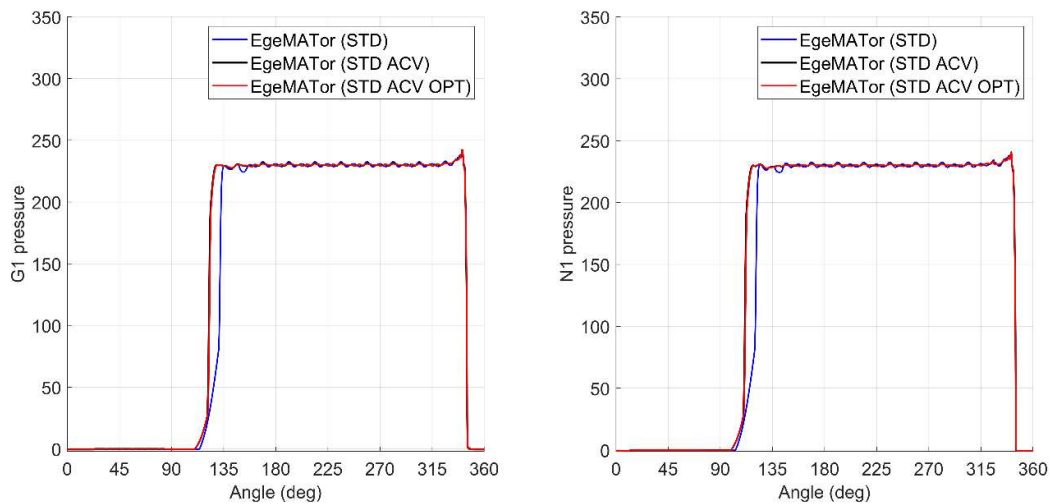
Figure 101. Gi and Ni pressure distributions.

Since EgeMATor can also evaluate force and torque on the gears through a subroutine developed in MATLAB®, the following figures have been presented to compare the three different pumps, showing the effects of the ACV introduction on the forces and torques ripples.

As shown in Figure 102 and Figure 103, only a slight variation on the gears' forces has been observed. Not relevant variations have been appreciated on the torque acting on the shaft.
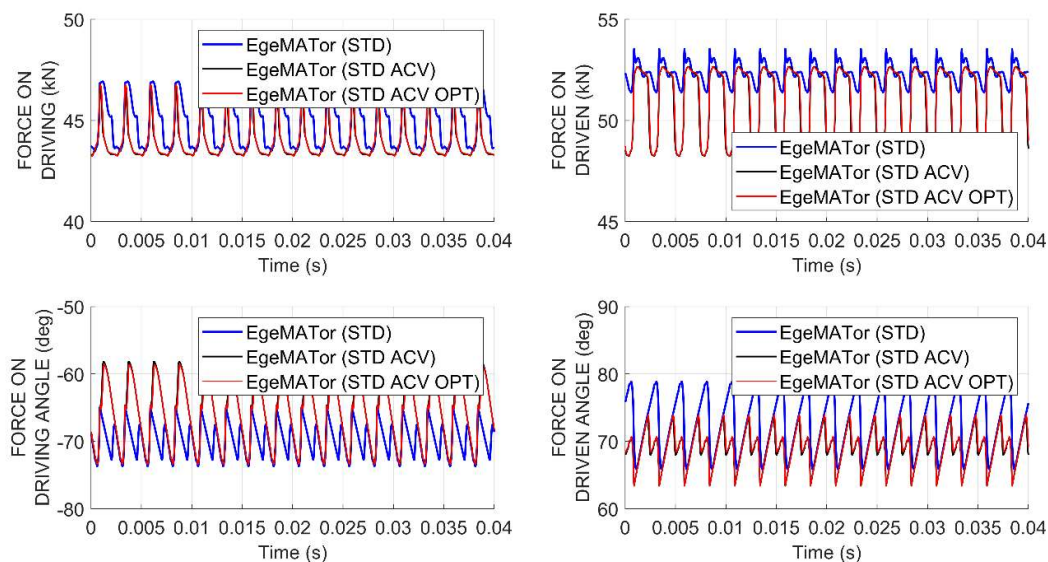
Figure 102. Numerical forces and their directions, acting on driving and driven gears.
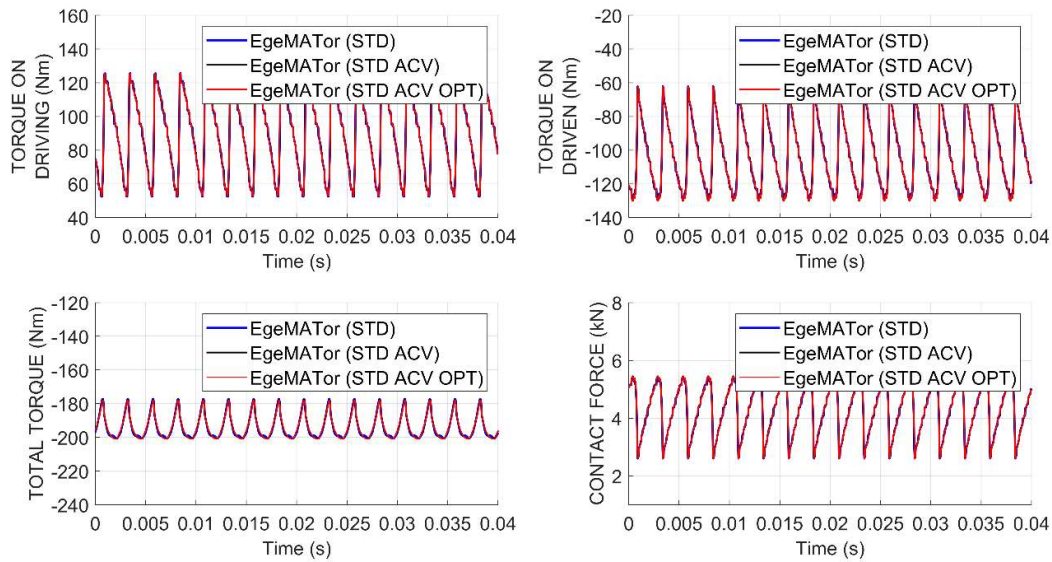
Figure 103. Contact force and numerical torques, acting on driving and driven gears.

This analysis confirms that the ACV system can reduce the pump's fluid-borne noise, without increasing the structural borne-noise, which is mainly influenced by oscillating forces and torques.

Other six working conditions have been analyzed to understand the effects of the ACV at different speeds and pressures. A summary of this analysis has been reported in Table 12, where it is evident that, at the same speed used as a boundary condition for the optimization process, the flow ripple reduction (in terms of NUG) is still very interesting also varying the pump outlet pressure (studies n° 1 and 2). In other cases, particularly for the studies n° 3 and 4 at lower speeds, the improvements are less relevant but still consistent. At higher speeds (studies n° 5 and 6), the benefits disappeared; indeed, the NUG gets slightly worse.

Table 12. Analysis of different working conditions.

Study Number	Pump Speed (rev/min)	Outlet Pressure (bar)	NUG STD (/-)	NUG STD ACV OPT (/)	Variation (%)
1	1500	350	0.403	0.170	−57.82%
2	1500	120	0.269	0.159	−40.89%
3	800	350	0.482	0.392	−18.67%
4	800	120	0.308	0.234	−24.03%
5	3000	350	0.340	0.363	+6.76%
6	3000	120	0.317	0.345	+8.83%

Finally, an additional optimization process has been run. In this case, the input parameter $\Delta\beta$, which shifts the ACV's connection hole, has been differentiated for the driving and the driven gears. The optimization process trend for this

analysis has been shown in Figure 104, where it can be noted that after twenty-four iterations, even if the NUG has been further reduced, the improvement achieved differentiating the two angles is irrelevant. Indeed, the optimized NUG is now equal to 0.129, which means a further reduction of 1.5%, a value not relevant if it is considered that the wear-plate will lose its symmetry (that simplifies the meshing and the assembly processes).
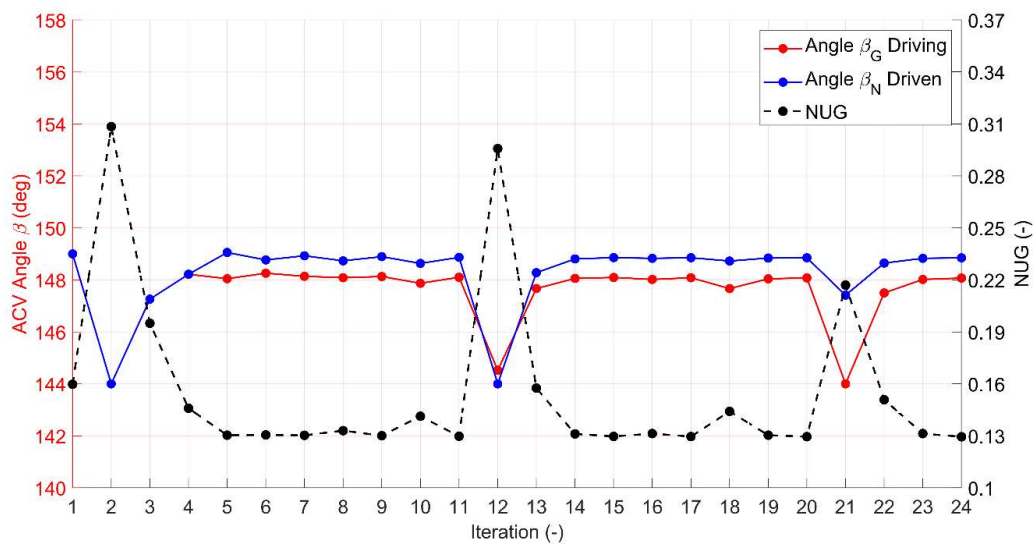
Figure 104. Second optimization process trend.

III.9 Conclusion

In this chapter, an analysis of an external gear pump has been conducted. The subject of the study was a pump that showed noisy behaviors. A series of noise measurements have been done on the subject. A re-prototyping process has been done using two different approaches to simulate the fluid dynamic. The first methodology uses a lumped parameter method, it is based on the control volume approach, and it has been simulated through a tool (EgeMATor). The second methodology uses a three-dimensional CFD commercial software that includes a specific template mesher for EGPs. Since no experimental data were available during the analysis, because the pump was still in a prototyping phase, results from both methodologies have been compared; in particular, the three-dimensional CFD simulation has also been used to validate the EgeMATor results deeply. Due to the nature itself of the CFD simulation, where contact between pump elements cannot be realized since a minimum fluid gap is always required (to avoid zero volume cells), two models have been realized with

EgeMATor. The first one (called STD) replicates a perfect sealing during the simulation; a second model, instead, uses the minimum gaps as imposed in the three-dimensional CFD model. Obtained results have permitted validation of the EgeMATor approach, so the tool has been used to run further analyses. Two volumes have been accommodated in the pump housing, and they have been used to connect the delivery volume and the displacement chambers cyclically through two opportune orifices. The new system, called ACV, has been used to control the reverse flow coming from the pump outlet that pressurizes the displacement chamber. In this way, the reverse flow has been controlled and uniformized. The wear-plate geometries have been then optimized with an NLPQL algorithm, showing a reduction of the flow ripple (NUG) by 61%, reducing the fluid-borne noise substantially. Analysis of force and torque that could create structural vibrations has been done as well. Results obtained with EgeMATor showed no significant variation on gears forces and torques. Further optimization will be done on orifices dimensions and ACV volumes, but the actual best design will be firstly manufactured and tested to measure the noise emissions again.

Noise and vibration analyses have been conducted on the initial prototype pump and the optimized one, confirming that the vibrational analysis can be used to predict the structural-borne noise in the absence of anechoic room.

The developed methodology demonstrates to be usefully used in optimizing the fluid-borne noise of EGPs. However, with the subroutine's introduction to evaluate forces and torques, also gives interesting information because it can easily predict if the design's modification for optimizing the fluid dynamic gives unwanted effects on the structural vibration.

III.10 Nomenclature

Acronyms

Name	Descriptions
ACV	Alternative Capacitive Volumes
CAD	Computer-Aided Design
CFD	Computational Fluid Dynamic
CPU	Central Processing Unit
DXF	Drawing Exchange Format
EDGM	Equilibrium Dissolved Gas Model
EgeMATor	External Gear Machine Multi Tool Simulator
EGMs	External Gear Machines
EGP	External Gear Pump
GIF	Graphical Interchange Format
ISO	International Organization for Standardization
NCG	Non-Condensable Gas
NLPQL	Non-Linear Programming by Quadratic Lagrangian
NSGA-II	Non-dominated Sorting Genetic Algorithm II
NUG	Non-Uniformity Grade
RANS	Reynolds Average Navier-Stokes

Symbols

Name	Descriptions
A	Generic orifice area (m^2)
b	Gear axial dimension (m)
b_{slice}	Width of tooth side slice (m)
c_d	Flow coefficient
$c_{d,max}$	Maximum flow coefficient
D_h	Hydraulic diameter (m)
F_B	Pressure forces in the B-zone (N)
F_{drain}	Friction force due to drain flow (N)
F_G	Pressure forces in the G-zone (N)
F_R	Pressure forces in the R-zone (N)
F_{side}	Friction force on tooth side (N)
F_{tip}	Tip flux friction force (N)
F_{tot}	Total force acting on the gear (N)
h_{tip}	Tip gap dimension (m)
h_{gep}	Axial gap dimension (m)
l_{slice}	Length of tooth side slice (m)
l_{tip}	Tip length dimension (m)
M_B	Moment due to pressure forces in the B-zone (Nm)
$M_{bearings}$	Moment of viscous friction in the bearings (Nm)
$M_{churning\ losses}$	Moment due to churning losses (Nm)

$M_{drain,G}$	Moment of viscous forces drain flow on driving gear (Nm)
$M_{drain,N}$	Moment of viscous forces drain flow on driven gear (Nm)
$M_{f,teeth}$	Moment of friction teeth contact (Nm)
M_G	Moment on driving gear (Nm)
M_G	Moment due to pressure forces in the G-zone (Nm)
$M_{housing}$	Moment of friction due to gear housing contact (Nm)
M_N	Moment on driven gear (Nm)
$M_{p,G}$	Moment of pressure forces on driving gear (Nm)
$M_{p,N}$	Moment of pressure forces on driven gear (Nm)
M_R	Moment due to pressure forces in the R-zone (Nm)
$M_{side,G}$	Moment of viscous forces on driving gear tooth side (Nm)
$M_{side,N}$	Moment of viscous forces on driven gear tooth side (Nm)
$M_{tip,G}$	Moment of viscous forces on driving gear tooth tip (Nm)
$M_{tip,N}$	Moment of viscous forces on driven gear tooth tip (Nm)
M_{tot}	Total moment on pump shaft (Nm)
p	Pressure (Pa)
Q	Flow (m³/s)
Q_{tip}	Tip tooth flux (m³/s)
Q_{side}	Side tooth flux (m³/s)
R_{plate}	Wear plate minimum radius (m)
R_{root}	Gear root radius (m)
R_{tip}	Tip radius (m)
$R_{slice,i}$	Average radius of the i-th slice for side flux (m)
V	Volume (m³)
V_E	Estimated pump displacement (m³/rev)
V_{Gi}	i-th volume of the driving gear (m³)
V_{Ni}	i-th volume of the driven gear (cm³)
t	Time (s)
x	X-coordinate (m)
y	Y-coordinate
Z_t	Number of teeth

Greek Symbols

α	Angle of the total force (deg)
β	Angle on the ACV
β_k	Fluid bulk modulus
λ	Flow number
λ_{crit}	Critical flow number
μ	Dynamic viscosity (Pas)
υ	Kinematic viscosity (m²/s)
ω	Rotational speed (rad/s)
ρ	Fluid density (kg/m³)
ρ_{atm}	Fluid density at atmospheric pressure (kg/m³)
τ	Shear stress (N/mm²)

126

| φ | Angle (deg) |
| $\varDelta\varphi$ | Saving delta angle (deg) |

Chapter IV: **Vane Pumps**

IV.1 Introduction

A numerical three-dimensional CFD analysis of an unbalanced variable displacement vane pump has been conducted in this chapter. The study falls within the scope of this thesis because it aims to investigate fluid-borne noise that means the analysis of the pressure ripple. A previous CFD numerical model developed by the FPRG of UniNA was not capable of predict with reasonable accuracy the pressure ripple. In particular, the model overestimated those ripples. In this chapter, a new feature of the model has been implemented considering the effects on the pressure ripple's behavior caused by the vanes detaching from the pressure ring. To perform this analysis, a Duplomatic MS's pump already available on the market has been modeled. The numerical model includes the variation of the fluid volume over the vane tip due to pressure balances. Therefore, the fluid in those areas is re-meshed at every time step as a function of the forces acting on the bottom and the top of each vane. The numerical model has been developed using the commercial tool, Simerics MP+®, including turbulence and cavitation models already presented in previous chapters. The validation of the model has been done comparing numerical and experimental data. It has been observed that the detachment of the vane occurs during the transition zones when unwanted pressure spikes are generated by a non-optimized valve plate design. The prediction of vane detachment is crucial for designing a quieter and more durable pump. Vane collision on the stator ring can be a noise source, producing both components' premature wear. Vane detachment from the stator ring directly affects the pressure ripple even if the volumetric efficiency is only slightly influenced.

Variable displacement vane pumps are widely used in industrial applications. There are many reasons for their spread; they are very compact, especially axially, and have very low flow pulsation [1]. They have desirable characteristics, including variable sealing between the vanes and stator ring that can self-compensate for wear through additional vane extension without losing volumetric efficiency. However, if the wear of the vane's tip becomes excessive, the vanes can easily be replaced.

To better understand and optimize the fluid dynamics, numerical models can help reduce the number of prototype iterations for this pump's typology. As detailed below, several numerical studies are available in the literature to understand the operation of vane pumps in a wide variety of applications.

Geist et al. [49] analyzed a vane pump used to lubricate an internal combustion engine. An accurate numerical model has been built to account for the effect of the eccentricity rate of change on the internal forces and torques acting on the variable displacement mechanism within a pivoting vane pump.

Sullivan et al. [50] focused attention on the internal forces of a variable displacement vane pump. A CFD numerical model has been developed, showing that the pump speed has a more significant influence than eccentricity on internal forces. The maximum value of the internal moment occurs at high speeds and maximum eccentricity.

Other interesting investigations have been done by Rundo et al. [51] [52] using both lumped and three-dimensional numerical approaches. In particular, Rundo in [51] shown a customized lumped model implemented in the LMS Amesim® environment able to predict the filling capability, leakage, and pressure ripple of a vane pump. While in [52], using the same approach, the authors optimized a pump analyzing the effect of the geometry, the position of the silencing grooves, the shape of the vane tip, the clearances, and the precision on the stability of the displacement.

With a similar approach, Fornarelli et al. [53] also studied a vane pump using a lumped parameter approach to estimate friction forces' effect on volumetric efficiency loss but without supporting experimental tests.

There is only a paper available in the literature written by the UniNA's FPRG [53] where a preliminary CFD model has been introduced about the vane detachment from the stator ring. This model had many disadvantages, and it had a high computational time. For this reason, this previous model has been completely modified, adding a subroutine written in the local expression editor able to predict the vane detachment. With this implementation, feature optimization of vane pumps could be done since the vane detachment from the stator ring directly affects the pressure ripple even if the volumetric efficiency is only slightly influenced.

IV.1.2 The subject of the Study
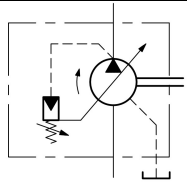
The research presented in this chapter results from a collaboration between three universities: the University of Naples, the University of Sannio, and the University of Minnesota. Their researchers have been working on this topic for many years, looking, as said, at predicting the vane detachment due to fluid-dynamic effects and the resulting high-pressure ripple [54] [55]. This feature is of particular interest to the scientific community.

In an unbalanced variable displacement vane pump, an individual displacement chamber is bounded by the rotor and the stator ring in the radial direction and by two consecutive vanes in the circumferential direction. An unbalanced vane pump has an eccentricity between the rotor and stator, which creates the displacement volume. The sliding of the vanes in the rotor slots creates extra displacement volumes (usually called under-vane), and, for this reason, vanes are considered active elements in the pumping mechanism.

The study's subject is a prototype vane pump supplied by the Italian company Duplomatic MS; the main technical specifications are listed in Table 13.

Table 13. Technical specifications

Description	Value	Units
Geometrical displacement (±3%)	63	cm^3/rev
Theoretical flow rate at 1500 rev/min	94.5	L/min
Maximum continuous pressure	250	bar
Pressure adjustment range	20 ÷ 250	bar
Rotation speed range	800 ÷ 1500	rev/min

Rotation type	CCW	-
Number of vanes (z)	11	-

Hydraulic symbol

The pump is a variable displacement vane pump with a hydraulic operated pressure compensator, which permits instantaneous adjustment of the flow rate to match the application requirements. The pressure compensator operates to keep the stator ring in the required eccentric position actuated by a piston hydraulically controlled by a pressure pilot stage. When the delivery pressure equals the pressure corresponding to the pilot stage setting, the stator ring is moved toward the center, adjusting the flow rate to the system requirements. At zero flow demand conditions, the pump delivers oil only to compensate for leaking and piloting, keeping the circuit pressure constant.

The geometrical displacement presented in Table 13 is slightly variable for any particular pump because of production and assembly variations. This type of positive displacement pump is frequently used for industrial applications at medium- or high-pressure levels. The clearance around the stator ring depends on manufacturing tolerances. A screw alters the thrust block position to remove this clearance, creating an offset perpendicular to the pump eccentricity (later called Y-offset). This procedure is performed during pump calibration and breaking-in, assuring a working condition with no clearances. The Y-offset can be positive or negative, affecting the maximum and minimum volumes angular position of the displacement between vanes and shifting the valve plate timing. In fact, it can cause an unwanted premature closing of the delivery kidney, reducing the effective pump displacement below the manufacturer's nominal geometrical displacement. To create a more accurate numerical model, the Y-offset has been measured before the pump tests and considered in the numerical model.

IV.2 The experimental set-up at the University of Minnesota

Experimental tests have been performed on a test rig at the Mechanical Engineering Department of the University of Minnesota. The schematic and the test rig are shown in Figure 105. A three-phase, 150HP motor (1) is used to drive the hydraulic pump (2) test; it has been connected to a variable-frequency drive (VFD) (8). The motor has been linked to the hydraulic pump through a torque transducer (Lebow 1225), with its speed controlled by the VFD model ABB ACH550-UH-180A-4. The load valve (3) is an Eaton CMA200 that is an advanced CAN-Enabled electrohydraulic sectional mobile valve with independent metering that utilizes pressure and position sensors, onboard electronics, and advanced software control algorithms. The test rig is equipped with a water-oil heat exchanger (6), a filter (5), a tank (7), and a manifold (4) housing a turbine type flow meter, a thermocouple, and a fast response pressure transducer. The oil used is ISO VG46. The fluid temperature is controlled to 313 K.

(a)   (b)
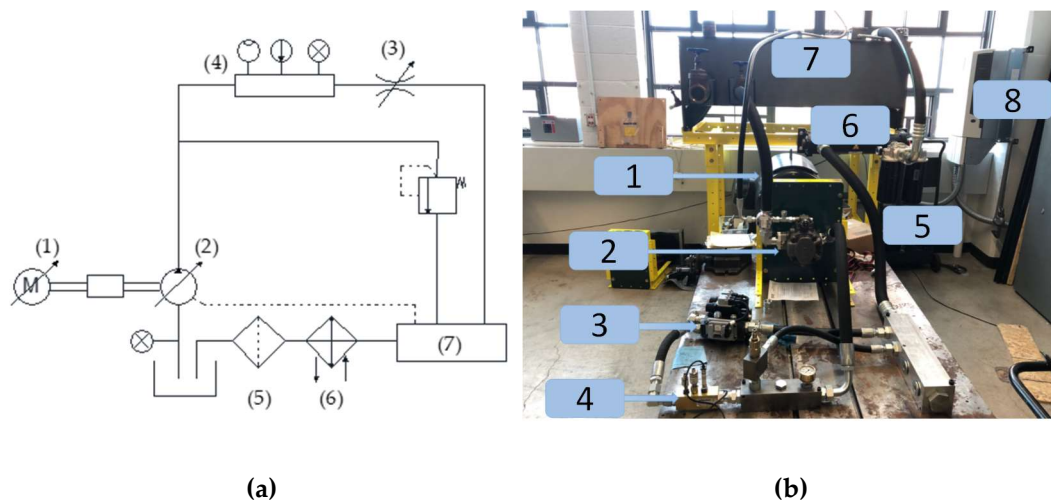
Figure 105. Test rig of the University of Minnesota; Schematic of the test stand (a), Set of the hydraulic pump test stand (b)

IV.3 Three-dimensional CFD model

IV.3.1 The approach

The pump has been modeled with the commercial code Simerics MP+®, which integrates a rotor template mesher dedicated for vane pumps. The approach has already been well described in II.3.1. Here, a script has been integrated for the vane tip volume's re-meshing every time-step to

132

simulate vane detachment from the stator ring, explained later. As said in previous chapters, the commercial software discretizes the governing equations, including conservation of mass and momentum, using a finite volume method. Therefore, the fluid volume domain has been extracted from the CAD 3D drawing provided by the company in a STEP format, with the commercial software Discovery SpaceClaim®, and divided into sub-volumes, which will be interfaced during modeling in Simerics MP+®. To help the interfacing process, surfaces have been renamed in Discovery SpaceClaim® to be easily distinguished. Finally, the fluid domains have been exported in STL format, imported in the CFD code, and then meshed with suitable grid sizes. The numerical model does not include heat transfer. The temperature is constant and affects oil viscosity and density; the dynamic viscosity and liquid bulk modulus are exponentially and linearly pressure dependent.

A cavitation module is needed for the vane pump model. Since pump timing is relatively variable, conditions can create circumstances where a pressure drop can cause a release of the dissolved air in the liquid out of the solution. In particular, since the local pressure affects the vane balance, a cavitation model is needed; otherwise, the pressure force evaluation on the vane will be inaccurate if the pressure is negative. The model used for cavitation is based on the advanced cavitation model proposed by Singhal et al. [24], where non-condensable gas (NCG) in both dissolved and undissolved states are considered. In this analysis, the "equilibrium dissolved gas model", integrated into Simerics MP+® has been used for this purpose. Here the sum of the dissolved and undissolved mass fraction is constant.

IV.3.2 Mesh sensitivity analysis

A mesh sensitivity analysis has been conducted to obtain the outlet volumetric flow-rate independence from cell size. As visible in Figure 106, this condition has been achieved with a model of around 1M cells. In particular, the rotor mesher for the structured vane volumes has been set as follows: 440 cells in the circumferential direction, 8 in the radial direction, 46 in the axial direction, and 5 x 10 in the tip gap. A model with finer mesh has been investigated, but the results did not justify the increment in the computational time, as visible from the following figure.
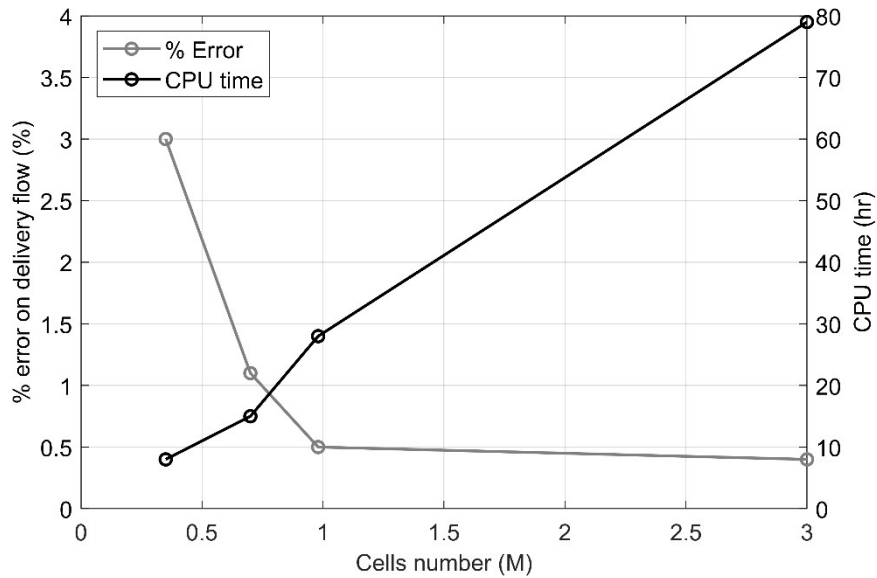
Figure 106. Mesh sensitivity analysis

An opportune convergence criterion has been set to assure mass flow conservation between inlet and outlet. The number of the time step, $\varDelta t$, per rotation is 880, corresponding to an angular step of 0.4 deg. The conditions for the simulation are the following:

- Inlet and case pressure: 0 bar;

- Outlet pressure in the range: 20 ÷ 250 bar;

- Oil type: commercial ISO VG46;

- Temperature: 313 K.

The two axial gaps between rotating elements and valve plates have been considered a function of the outlet pressure to simulate the "clamping" force exerted by the two valve plates due to the pressure balance on their surfaces. It is designed to maintain high volumetric efficiency at higher pressures.

IV.3.3 The script for the vane detachment

The script introduced models of the vane detachment from the stator ring, following equation (96). A force balance between two terms evaluates the occurrence of detachment; one includes the effect of the pressure force coming from the under-vane added to the centrifugal force, while the other

considers the radial pressure force acting on each vane (equation (96)). The forces are shown in Figure 107.
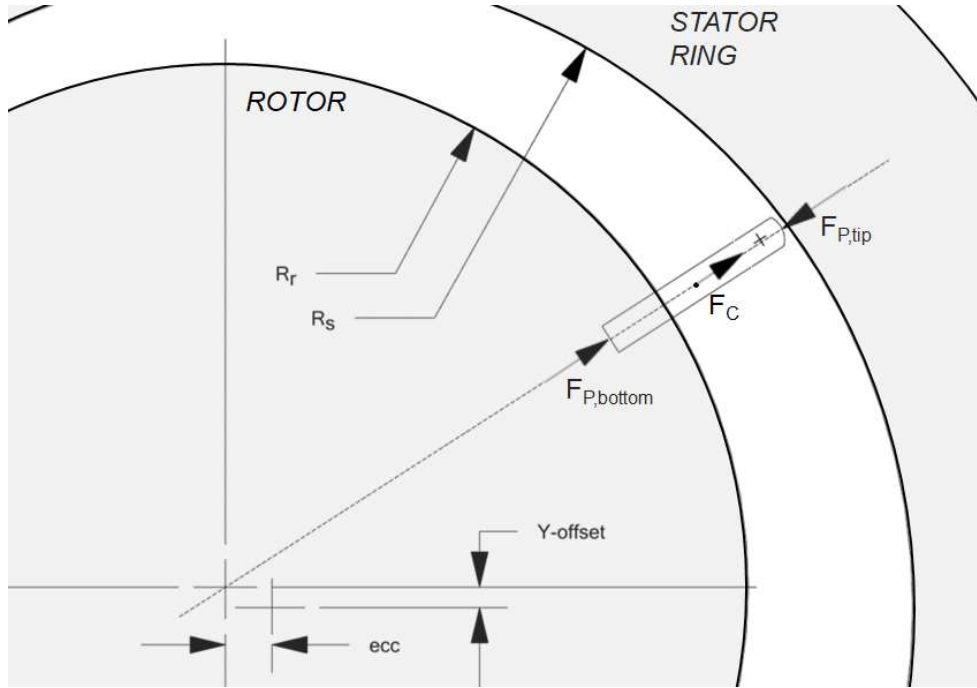
Figure 107. Force considered for the vane balance

$$F_{contact}(t) = \left(F_{p,bottom}(t) + F_C(t) \right) - F_{p,tip}(t) \tag{96}$$

Where $F_{contact}$ is the contact force between the vane and the stator ring, $F_{p,bottom}$, and $F_{p,tip}$ are the pressure forces acting on the bottom and top of the vane, F_C is the centrifugal force on the vane; friction forces are neglected. If the value $F_{contact}$ at the time t is not negative, the tip gap remains constant and equal to the minimum value at the time $(t+\Delta t)$, otherwise the script re-mesh the vane tip gap h_{tip} according to a scaling factor α, as described in the equation below:

$$\begin{cases} h_{tip}(t + \Delta t) = h_{tip,MIN}, & F_{contact}(t) \geq 0 \\ h_{tip}(t + \Delta t) = -\alpha (F_{contact}(t)) \cdot h_{tip,MIN}, & F_{contact}(t) < 0 \end{cases} \tag{97}$$

In equation (97), the scaling factor α has been tuned to reach a smooth detachment avoiding an unrealistic gradient on the vane displacement. Its value is a function of the ratio between the maximum $F_{contact}$ and the

135

maximum allowable vane displacement. This calculation has been done for each of the eleven vanes.

<p style="text-align:center;">(a)   (b)</p>
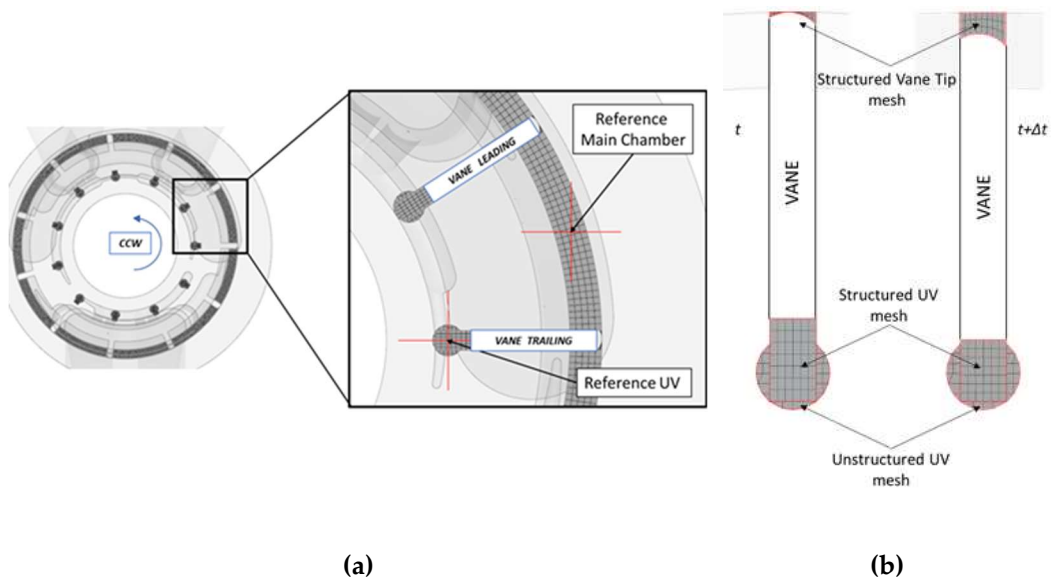
Figure 108. Mesh of the fluid domain at zero displacement with nomenclatures in the zoomed view (**a**); an example of the vane re-mesh from time t to time $t+\Delta t$ if the contact force is negative (**b**)

In Figure 108(a), the mesh of the pump fluid domain is visible. The reference under-vane and main chamber volumes at the starting angle (0 rad) have been shown in the zoomed view. The figure will be helpful for the understanding of the polar plots presented later. The nomenclature for the two vanes is also shown. Figure 108(b) shows an exaggerated view of how the script integrated works to simulate the vane detachment.

Regarding Figure 108(b), two volumes at the vane top and bottom can be seen. Both volumes have been modeled with a structured mesh, which helps re-meshing, especially when cells need to be stretched along an orthogonal direction. If the quantity evaluated by equation (96) becomes negative, the two volumes are re-meshed to simulate vane detachment from the stator ring. The structured mesh of the under-vane (UV) is re-meshed every time step to follow the stator ring's eccentricity.

IV.4 Model validation and results

IV.4.1 Effects of Y-offset

Once the mesh sensitivity analysis has been completed, the model and the script can be validated on experimental data. Simulations have been conducted on a desktop workstation equipped with an Intel® Xeon® CPU E5-2640 v2, 16 cores, where each run took around seven hours for a pump revolution. In Figure 109, experimental and numerical results have been presented on a flow-pressure diagram; three rotational speeds have been analyzed (1000, 1200, 1500 rev/min). Only for the rotational speed of 1500 rev/min, the simulations have been run considering and not the Y-offset. The imposed Y-offset has been measured on the test rig before testing.
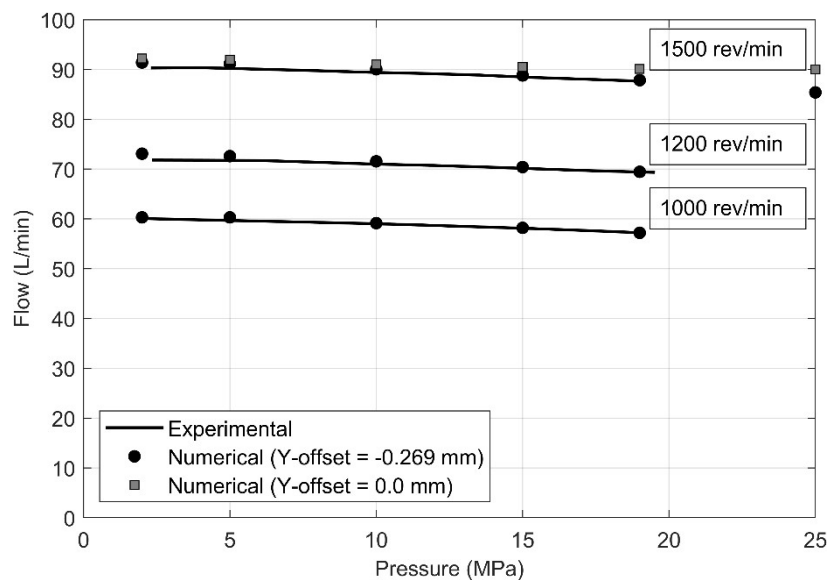
Figure 109. Numerical model validation

The importance of considering the Y-offset is visible in Figure 109 for the 1500 rev/min curve. Since it acts on the valve plate timing, the offset reduces the effective pump displacement. Considering the measured Y-offset and the tuned scaling factor, useful for the vane detachment re-meshing, the errors are within 1% of the experimental data for all rotational speeds.

IV.4.2 Script effects on the numerical pressure ripple

The primary evidence of the effects of the introduction of the vane detachment is pressure ripple, which is the primary purpose of this study. Experimental data have been acquired using a calibrated orifice. This

methodology creates a system load that can be easily implemented in the numerical model.
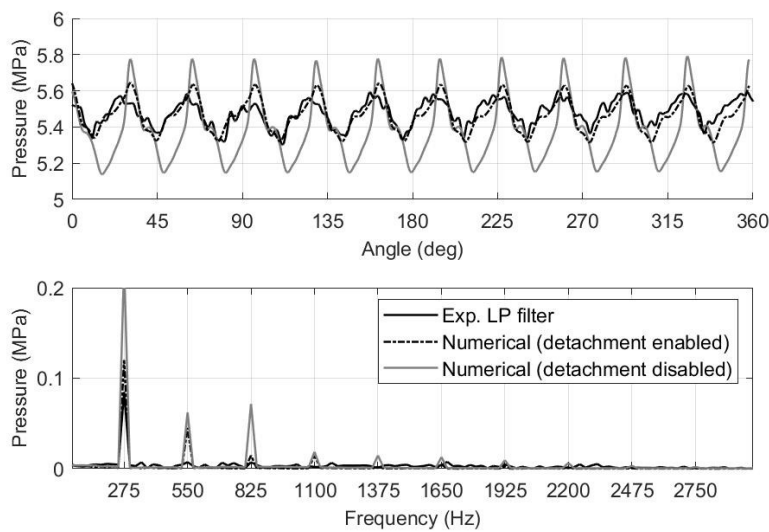
Figure 110. Experimental/Numerical pressure ripple

Figure 110 shows the experimental pressure ripple acquired at 50 kHz, filtered with a 70th order lowpass FIR with a cutoff frequency of 3 kHz, and numerical pressure ripples, with and without the vane detachment script. Results in the figure have been presented in both time (angle) and frequency domains. Figure 110 clearly reveals the importance of considering vane detachment for an accurate analysis. The amplitude of the pressure ripple oscillation (visible on the 1st fundamental frequency) is quite different from experimental data if the script is not enabled. Vane detachment has to be considered when pressure/flow ripples are analyzed; otherwise, an overestimation will result.

IV.4.3 Model significative results

Polar diagrams have been generated using the interesting numerical simulation results; in particular, in those plots, the valve plate shadow has been added as a background to understand the pump behavior better. Looking at the valve-plate, the internal smaller kidneys are related to the under-vane timing while the external bigger ones to the main chamber. The upper side is connected to the pump outlet for all the following figures, while the lower side is linked to the pump inlet.

In Figure 111, the displacement volumes have been plotted as a function of angle. As expected, the under-vane maximum and minimum volumes occur at 0 and π radians. In contrast, the main chamber's maximum volume is not aligned to -π/z because it is shifted by a value of around π/36 (5 deg) caused by a not-null Y-offset.
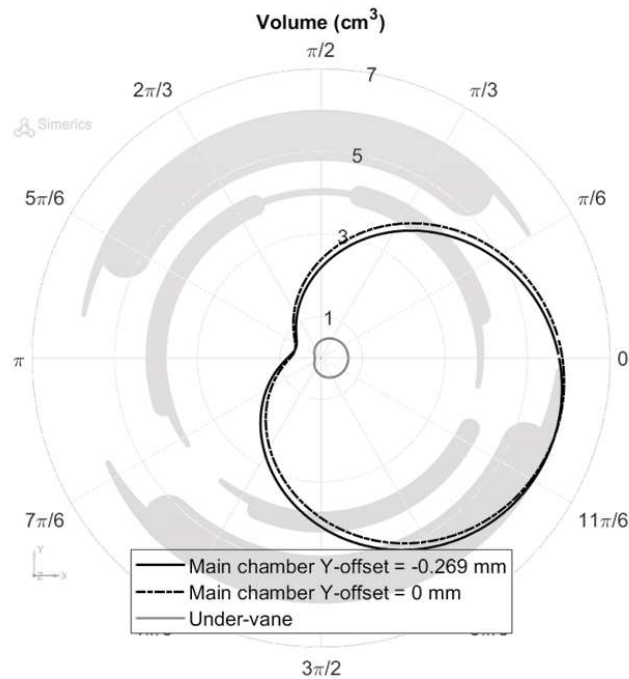
Figure 111. Polar plot: Displacement chambers volume

In Figure 111, both main chamber volumes, with and without the Y-offset, have been shown. Since this dimension highly influences the pump fluid dynamics, all the following results consider the Y-offset's measured value of 0.269 mm.
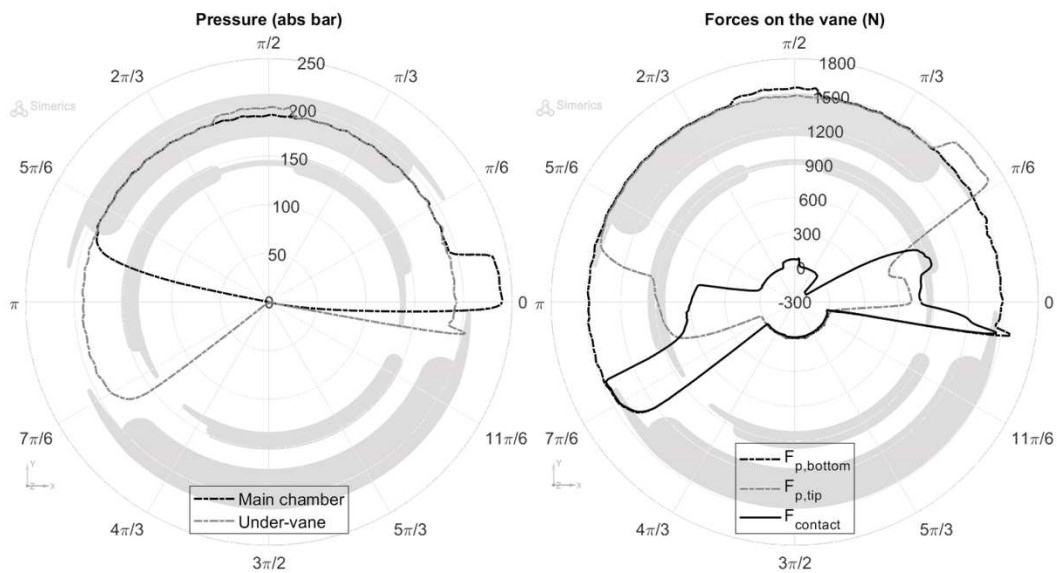
(a)   **(b)**

Figure 112. Polar plots: Displacement volumes pressure (a), forces on the vane (b)

In Figure 112(a) the pressure trends of the main chamber and under-vane volumes have been presented. It is visible how the under-vane chamber pressure builds up before the initial angle (0 rad), and it is still in pressure after π rad to create a proper sealing between the pump inlet and outlet. In Figure 112(b) $F_{contact}$ is shown. It achieves a maximum value of around 1500 N while it becomes negative in the angular region between $\pi/6$ and $\pi/3$. The effect of the reference main chamber's pressure spike is a leading vane detachment. This effect has been diagrammed in Figure 113(a).
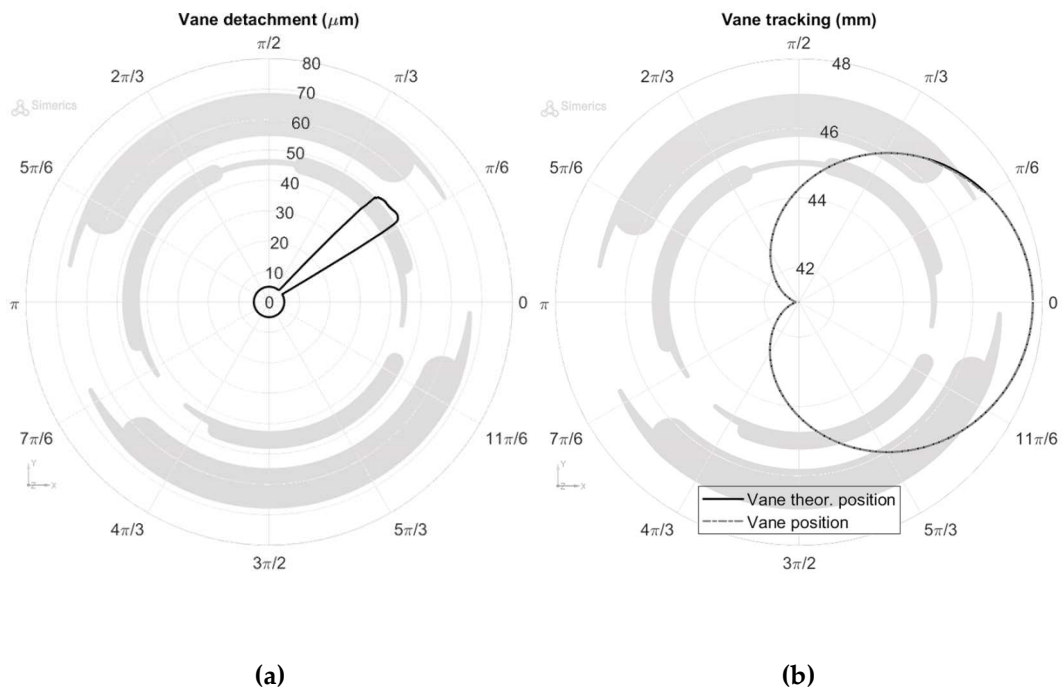
Figure 113. Detachment (a), tracking for the trailing vane (b)

Figure 113(a) shows the calculated vane detachment from the stator ring estimated in about 50 μm occurring in the same angular region where $F_{contact}$ becomes negative. In Figure 113(b), the instantaneous and theoretical vane position tracking is visible, including with or without the vane detachment script.

IV.4.4 Stator ring wear prediction

The predicted detachment effect is investigated in this section, where the pump's stator ring is presented in three views (Figure 114). The pictures have been taken during a preliminary disassembly, coincident with the Y-offset acquisition, so at that time, the pump only did the running in; for this motivation, the signs can be more accentuated after some hour in working condition. In the middle picture of Figure 114, the contact force polar plot has been inserted. Looking at the same colors' squares, signs of the contact between vane and stator ring can be noted. The left view picture identifies the transition region from delivery to suction; in the blue square, the ring area where there is a partial contact force (around 600N) has been evidenced; scratches are evident in this area. In the same view, the red square area presents significant signs, more than the previous blue area; here the contact force achieves maximum values (almost 1500N). On the other side, during suction to delivery transition, the same signs are evident in the green highlighted region, where the contact force achieves the

141

maximum value for a moment. Just before the vane detachment, it is visible densification in a well-identified angular strip in the yellow area. Here the force increases to a value of 900N. This qualitative observation further confirms the predictive ability of the methodology.
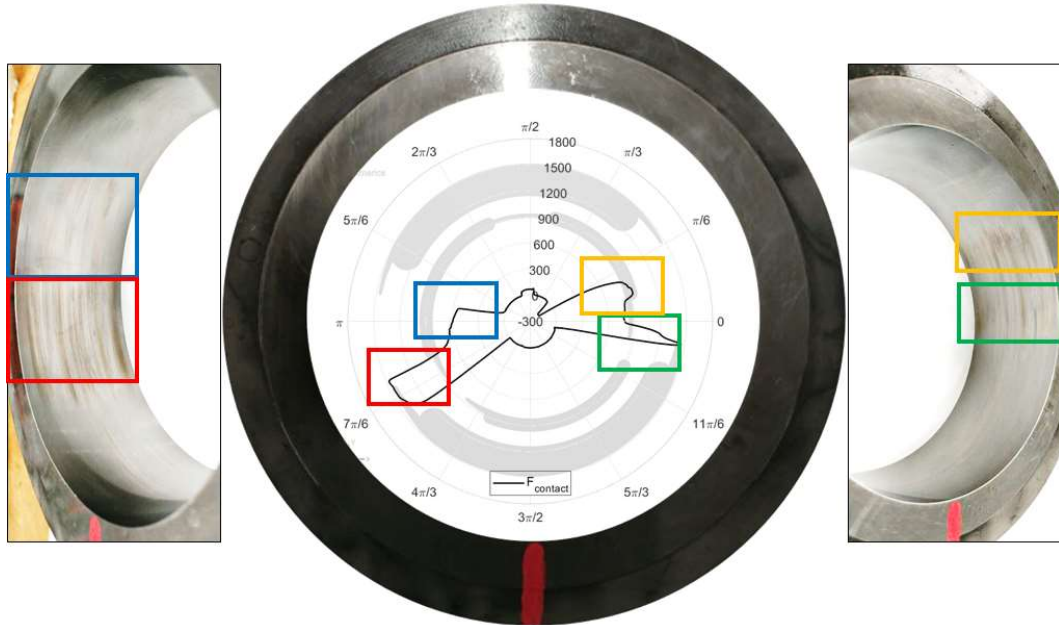
Figure 114. Stator ring projections with an integrated plot for contact force

IV.5 Conclusion

A study on an unbalanced variable displacement vane pump for industrial application has been presented in this chapter. The pump has been supplied by the Duplomatic MS company and tested at the University of Minnesota since both of them are part of this Ph.D. program. Numerical analysis has been conducted in a three-dimensional CFD environment with the commercial software Simerics MP+® at the University of Naples "Federico II" and the University of Sannio. Effects of vane detachment and Y-offset presence have been investigated. The mesh built by the rotor template mesher, included in the commercial code, has been modified at every time step with an integrated script.

The presented results confirmed the methodology's accuracy, which can be used during the design process to control the contact force to increase component lifetimes. An overestimation of the pressure ripple has been found if detachment is ignored in the pump. For the analyzed design, no

problems of vane collision on the stator ring have been found. Detachment has been observed in the numerical model; after that, the contact force became very small. The Y-offset has to be considered during valve plate timing design since this value can be variable because of dimensional component variations. This timing change can dangerously change pump behavior. The Y-offset lies in a particular range, a function of exact dimensions for an individual pump. For this reason, the pump timing has to be designed to compensate for production dimensional variations on the final parts. Like the one presented in this study, methodologies can be beneficial during the design process, cost-effective, and reduce prototyping time.

IV.6 Nomenclature

Acronyms

Name	Descriptions
CAD	Computer-aided design
CCW	Counterclockwise
CFD	Computational fluid dynamics
FIR	Finite impulse response
STEP	Standard for the Exchange of Product Data
STL	Standard Triangle Language
UV	Under-vane

Symbols

Name	Descriptions
F_C	Vane centrifugal force (N)
$F_{contact}$	Contact force between vane and stator ring (N)
$F_{p,bottom}$	Pressure force acting on vane bottom radially (Pa)
$F_{p,tip}$	Pressure force acting on vane tip radially (Pa)
h_{tip}	Vane tip gap dimension (m)
$h_{tip,MIN}$	Vane tip gap minimum dimension (m)

Greek Symbols

α	Scaling factor

Chapter V: **Cavitation study on a PMMA spool valve**

V.1 Introduction

V.1.1 The objective

Fluid-borne noise can also be found in valves; poppets or spool oscillation can generate noise related to the fluids. Also, cavitation phenomena are relevant for the fluid-borne noise; some applications require attention to noise generation in valves since, at low frequency, the noise can travel great distances via a different medium like air, water, and solids. Even these subjects can be studied with a numerical approach. In particular, the presented 3D CFD numerical model has been tested to prove its robustness also in this field.

V.1.2 The subject of the study

Spool valves are subject to deteriorated performance and noise due to the occurrence of a phenomenon called cavitation. Cavitation affects every component's performance and causes unwanted noise; noise sound levels are influenced by many parameters, but mainly by a not optimized geometry. In this paper, a 2 way – 2 position directional control valve has been studied using experimental and numerical approaches. Tests have been performed on a plexiglass body, and a steel spool opportunely ground to have sharp edges analyzing the cavitating area that arises and develops in U-notches. A dedicated test rig has been equipped with a high-speed

camera placed directly in front of the area of interest, where the phenomenon occurs. Different working conditions have been tested, varying the upstream pressure to encourage the development of cavitation. Images have been acquired and subsequently post-processed, focusing the contour extraction between liquid and gas phases. Subsequently, these images have been compared with results from three-dimensional CFD numerical simulations performed using a commercial code. The numerical estimation of the flow characteristics was in good agreement with the investigations carried out using a fast camera, including periodic cavitation structures. The study demonstrates the criticality and usefulness of using a three-dimensional CFD approach during a prototyping phase to create a quieter design.

V.1.3 State-of-the-art

Nowadays, different kinds of directional control valves are widely used in hydraulic systems for many applications [56]. The majority of them can be recognized by different metering elements, usually a spool or a poppet; its position is determined by an electronic, hydraulic, or manual controller. The valve's final application critically influences its oil flow characteristic, electronic complexity, and valve cost. Many studies have been completed and documented in the literature, where techniques to detect fault behaviors have been presented [57]. Other studies have been conducted to improve the proportional valve performance in terms of fluid dynamic optimization. Usually, spools of proportional valves are machined with U-notches or V-notches to create a proportional command. There could be some working conditions where the spool could be in an opening position with only the notches opened, creating conditions that the flow accelerates uncontrollably, generating cavitation phenomena with a subsequent unwanted noise emission and performance reduction and damage. As known, the pressure plays an essential role in cavitation occurrence, where severe flow acceleration can release the dissolved gas out of the solution [1]. The cavitation inception is judged from the overall sound noise levels; it is known from the literature that the cavitation occurrence for defined working conditions depends on the spool's notch geometry [56].

Martin et al. [58] presented research on spool valves with an experimental investigation to look at the cavitation damage mechanisms in aircraft hydraulic systems. The used test facility allowed the measurement of

hydraulic parameters under both no-cavitating and cavitating conditions. Finally, the authors developed a diagnostic technique to detect the onset of cavitation.

Oshima et al. [59] [60] [61] [62] studied the cavitation phenomenon experimentally in two water hydraulic poppet valves; one had a sharp-edged seat while the other one had a chamfered edge of the seat. The authors found that the geometry affects the cavitation occurrence, noise loudness, and induced choking phenomenon in the observed flow rate characteristics.

Liu et al. [63] carried out an experimental investigation on a water two-step throttle valve. Experiments were done investigating the flow-pressure and cavitation characteristics of throttles with different shapes.

Lu et al. [64] analyzed U-notches' influence on the cavitation phenomenon in a spool valve experimentally. The authors created a plexiglass valve equipped with an accelerometer to measure the vibration induced by the cavitation frequency peaks. A cavitation number has been correlated to the measured frequency peak, the consecutive bubbles collapsing produced frequency peaks in the spectra, which decreased with the cavitation number.

Yinshui et al. [65] also performed tests on a multi-stage throttle valve, studying cavitation damages. All the experiments were carried out with and without back-pressure, showing that the multi-stage throttle and operating conditions' shape has remarkable effects on the flow and cavitation characteristics. Other authors studied the cavitation phenomenon on valves also using numerical techniques.

Lui et al. [66] analyzed a biofluid flow through a throttle valve. Firstly, the pressure drop across the throttle valve, and the formation of vortex flow downstream has been numerically evaluated. Then, experimental analysis on the flow visualization has been conducted to capture images of the cavitation near the orifice using a high-speed camera. The results allowed the authors to observe, understand, and manage the cavitation phenomenon for these kinds of valves.

He et al. [67] also studied experimentally and numerically the cavitation flow in a throttle valve. The authors analyzed the cavitation flow capturing

147

images using a high-speed camera. Some parameters mainly affecting the cavitation were identified, providing the basis for a better understanding of the cavitation phenomenon in this kind of valves. From a physical point of view, the cavitation phenomenon's first event is a sudden formation of gas bubbles. The formation and growth of the bubbles is a well-known phenomenon in literature; however, the cavitation inception in proportional valves needs to be further investigated.

The analysis of the behavior of bubbles has been studied in several fields by using a fast image acquisition [68] [69] [70]. Furthermore, due to high-quality image resolution, CMOS sensors' advent provides advanced solutions to study the cavitation phenomenon. The uses of the fast-cam technique permit analyses of the cavitation phenomenon and the behavior of its dynamic evolution.

Osterman et al. [71], using an imaging approach, defined an incipient cavitation status in an axial valve. Payri et al. [72] defined the thickness of a contract vein of a nozzle by using a fast-cam with CMOS sensor, optimizing the image to distinguish better the gas phase from the liquid one, while Wu et al. [73] used the fast image technique to analyze the development of a sheet of cavitation in a cloud of bubbles.

V.1.4 The study

In this work, a directional control spool valve with a U-notches machining has been studied to understand better the growth, development, and collapse of bubbles varying the U-notches opening. For this purpose, a plexiglass valve body has been realized starting from a raw bar, and it has been installed on a dedicated test rig, equipped with pressure transducers, while a high-resolution, high-speed camera has been placed directly in front of the defined Area of Interest (called AOI), to record a sequence of images for capturing the cavitation. Images of the AOI have been post-processed with an algorithm developed using a neural network method [74]. In MATLAB, this code focuses on contour extraction between the liquid and the gas phases creating new optimized images where the contours are more perceptible than the originals. Optimized images are used to determine the gas phase thickness and define the dynamics of the valve operation. The valve has also been numerically modeled using a three-dimensional CFD

approach, showing a good prediction of the phenomenon under the same working conditions [75] [76].

V.2 The experimental setup

A dedicated test rig, located in the Fluid Power Lab of the University of Naples Federico II, has been used to investigate gaseous cavitation in the spool valve under study (visible in the dashed red rectangle in Figure 115. The flow, generated by the power supply group, can be delivered to the valve understudy or through a bypass 3-way valve, sent to the tank. Since the pump has no variable displacement, the flow is controlled by a flow control valve; also, a max pressure relief valve is installed to control the desired pressure. A flow meter, placed after a shuttle valve (used for safety purposes) and digital pressure transducers, completes the circuit. An accumulator has also been installed in the circuit to reduce flow oscillation, but it has not been used in this study.
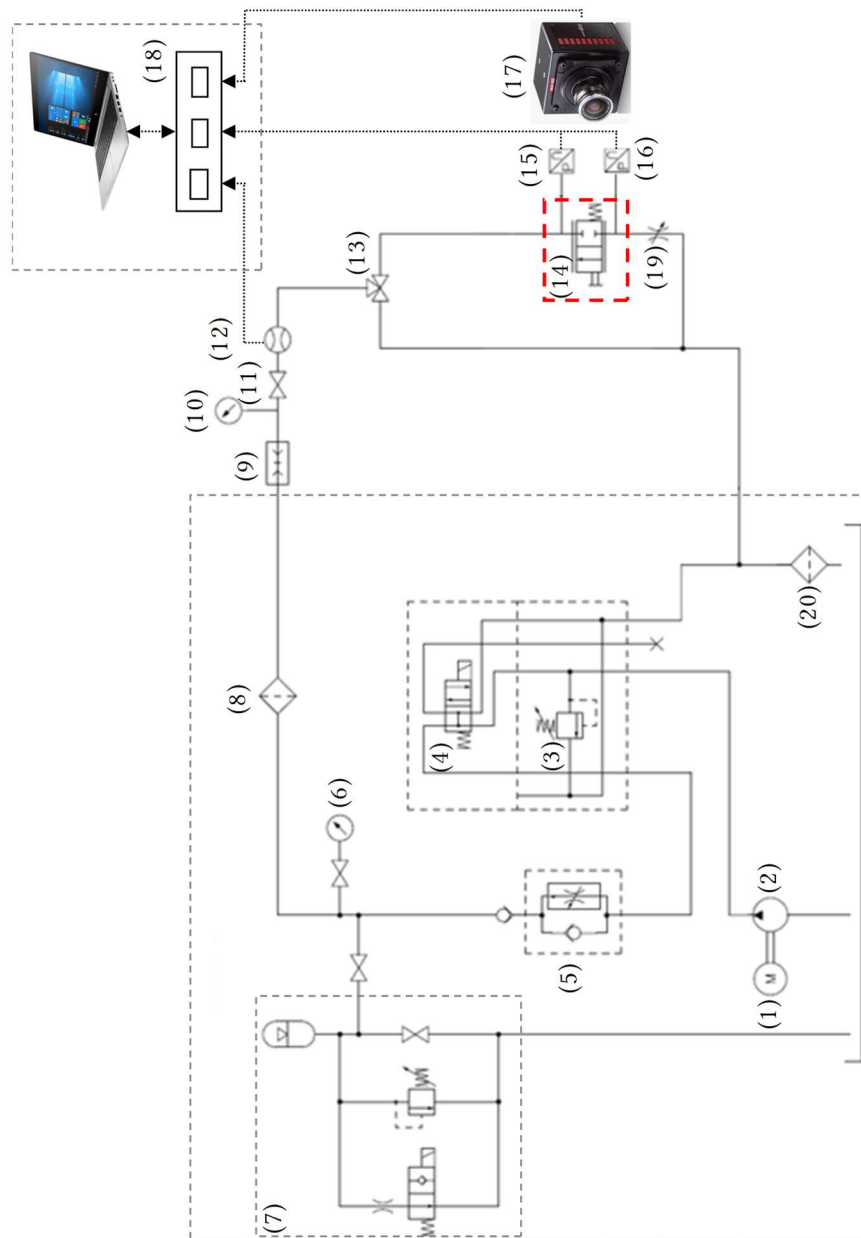
(1)	Electic motor 4 kW	(11)	In line two-way valve
(2)	Hydraulic pump EGP	(12)	Flow meter Endress Proline 33F
(3)	Pressure relief valve, Duplomatic MS, model PRM5	(13)	3-way plug valve
(4)	Solenoid actuated directional control valve, Duplomatic MS, model DL5B	(14)	Plexiglass valve
(5)	Flow control valve, Duplomatic MS, model RPC2	(15)	Upstream pressure transducer, AVL, model AVLLP11DA
(6)	Pressure gauge	(16)	Downstream pressure transducer, AVL, AVLLP11DA
(7)	Damper group	(17)	Fastcam AX100
(8)	Oil filter	(18)	NI data acquisition system
(9)	Fast coupling	(19)	Flow control valve
(10)	Pressure gauge	(20)	Oil filter

Figure 115. Test rig layout

An Endress Proline 33F flow meter with a range of 0-6500 kg/h has been used to acquire the fluid temperature and density; thanks to the direct measuring of those variables, the volumetric flow can be acquired. Two AVL LP11DA pressure transducers, installed in a manifold right below the valve body, were used for acquiring the valve upstream and downstream pressure. The pressure transducer, located at the inlet port, has a measuring range of 0-30 bar(a), while the second, installed at the valve outlet, has a measuring range 0-5 bar(a). The main characteristics of the test bench's transducers are listed in Table 14. A National Instruments® hardware/software system has been implemented (the data acquisition system in Figure 115); the hardware system is based on a data acquisition board NI PCI16-E1-MIO (12-bit ADC converter resolution, 16 single-ended or 8 differential input channels, 68 pins shielded desktop connector block NI SCB-68). The software to acquire the data has been developed with NI LabVIEW® 2015. The valve has been tested according to a suitable pressure to avoid material failure; the fluid used is a hydraulic oil ISO VG46.

Table 14. Transducers characteristics

	Measure	*Precision*	*Frequency Response*	*Linearity*	*Repeatability*
Flow Meter	Coriolis	±0,1% [AV]	/	/	±0.05% [AV]
p_{in}	Piezo resistive	/	>50kHz	<±0,1 [%FS]	/
P_{out}	Piezo resistive	≤0,3[%FS]	/	<±0,1 [%FS]	/

The spool that slides inside the valve plexiglass body has been shown in Figure 116. It can be moved through a micrometer to measure its position with reasonable accuracy and, consequently, set the desired opening. An instantaneous cavitation structure has been observed for small spool openings (1 mm and 2 mm); tests have been done varying the flow in the range 1 – 10 L/min and measuring the pressure drop across the valve. The high-speed camera has been installed on the test rig to acquire an instantaneous cavitation morphology. The camera is a fastcam Mini AX100 placed directly in front of the valve, looking at the AOI limited by the dashed red rectangle in Figure 117. The camera delivers images with a 1-megapixel resolution (1024 x 1024 pixels) at frame rates of 4,000 fps.
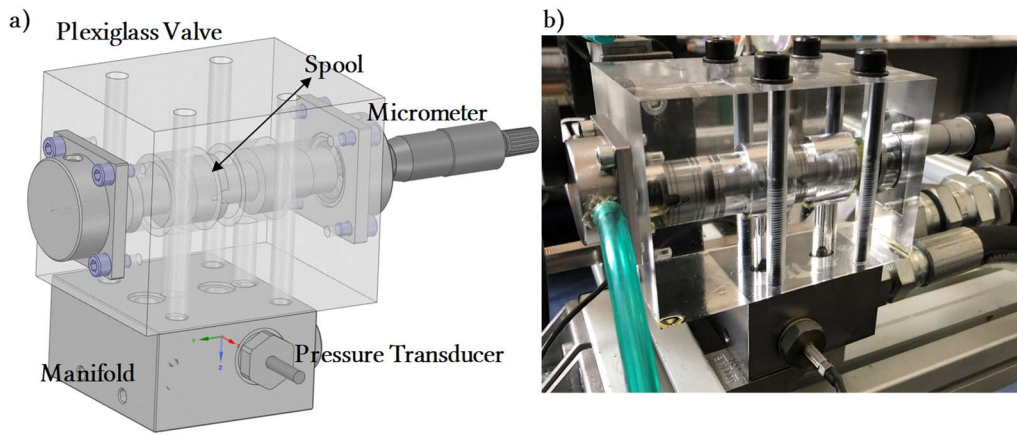
Figure 116. Valve in Plexiglass under study; a) CAD model, b) The tested valve

Each acquired image has been post-processed to isolate the bubbles contouring. The analysis of the captured images will be better described in the next section.

Figure 117. Particular of the AOI varying the valve opening

Before looking at the post-processed images, in Figure 118, the experimental flow rate through the valve for different pressure drops has been shown for both valve openings.

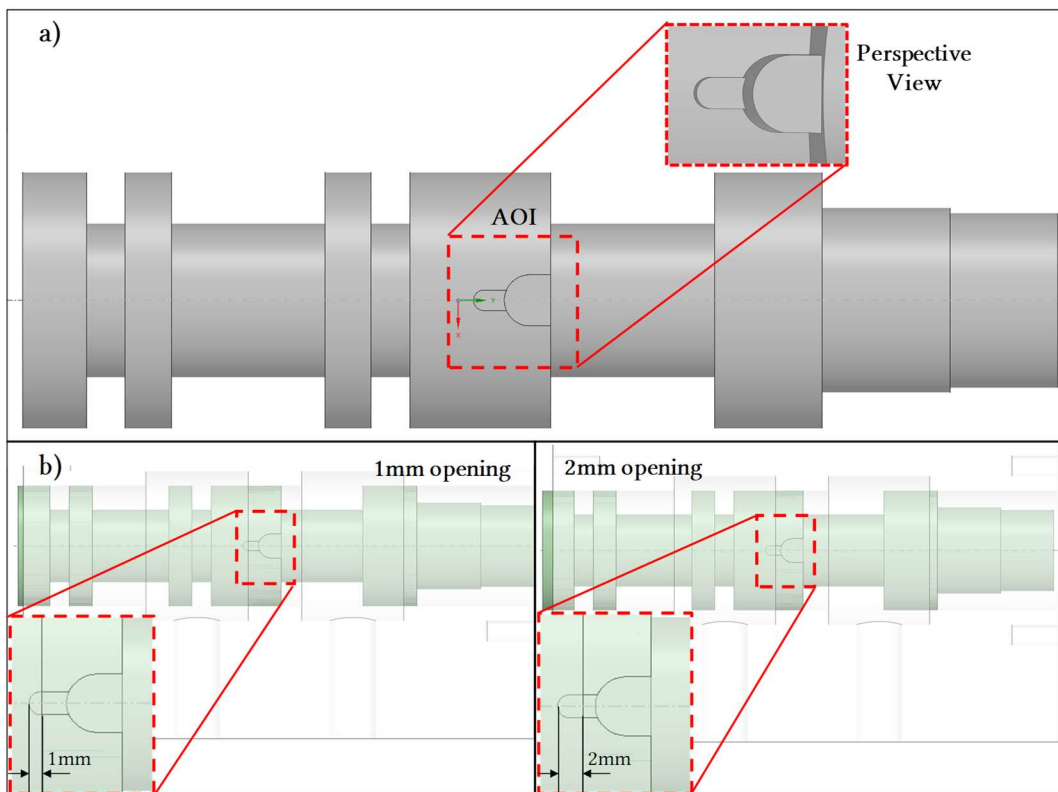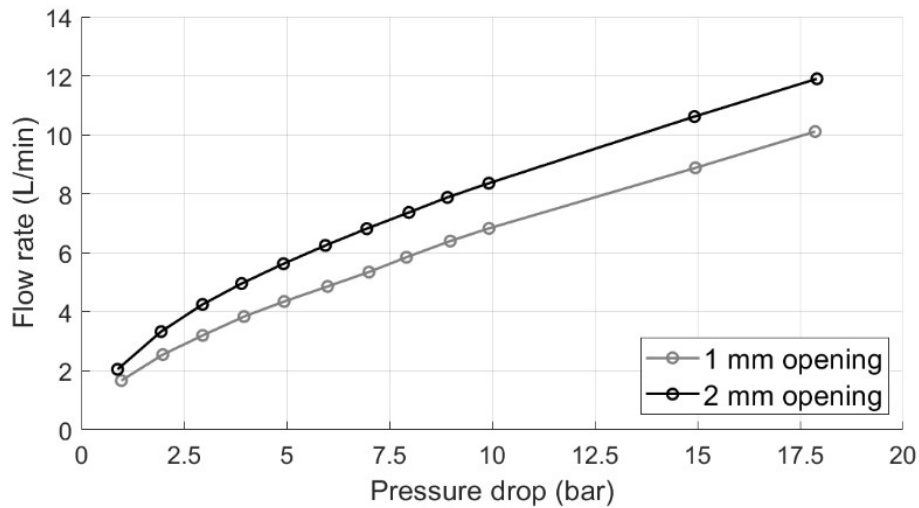**Figure 118. An experimental test for two different spool openings**

The acquired images showing the cavitation phenomenon will be shown for different working conditions in the next sections. It has been observed that for these smaller openings, an upstream pressure of 6 bar is enough to initiate the bubbles growing; the phenomenon become gradually bigger until it achieves complete atomization. A comparison of some acquired images for a spool opening of 1mm has been shown in Figure 119. In particular, the first image (Figure 119(a)) has been obtained imposing a flow-rate of 5.35 L/min corresponding to an upstream pressure of 7.04 bar and a downstream pressure of 0.038 bar, while in Figure 119(b)) a flow-rate of 8.88 L/min has been imposed to obtain an upstream pressure of 15.00 bar and a downstream pressure of 0.050 bar.
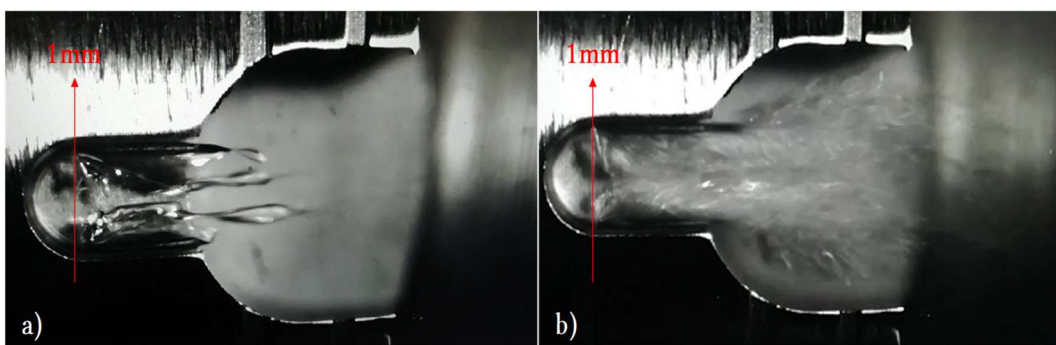

Figure 119. Captured images: comparison between two working condition for a 1 mm opening

V.3 Images post-processing

The first step of the image analysis starts from a well-defined frame acquisition. The AOI has been highlighted by using an HLX 64627 - halogen Lamp 12 DCV 100 W OSRAM to create the right brightness needed for high-frequency image acquisition. In particular, the used lamp is filled with Xenon gas, which provides light with a preponderant wavelength of around 650 nm, where the fastcam Photron AX100 sensor is susceptible. In this work, a standard 50mm Canon objective has been used to facilitate the post-processing procedure. This choice does not permit a good magnification but provides a stable and sharp image even with a shallow depth of field. Furthermore, this optical setup permits a good range of the focus, and all the recorded objects will have a good definition, as shown in Figure 120.
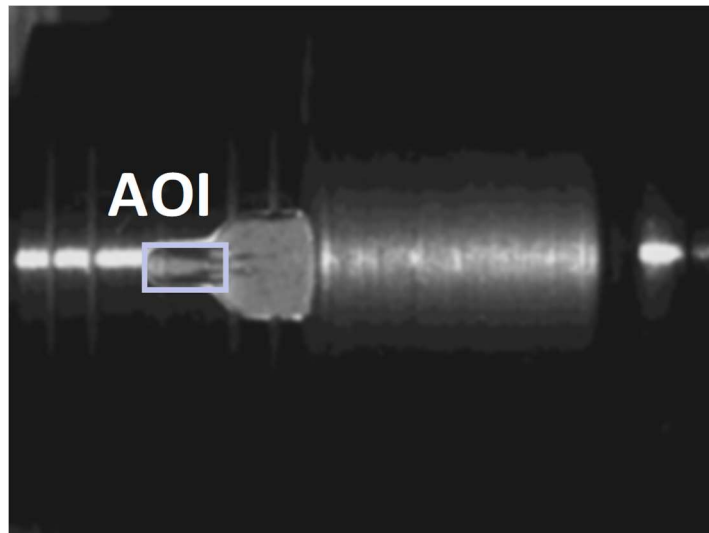
Figure 120. A single frame of a recorded sequence

The post-processing performed has been focused on the contour extraction between the liquid and the gas phases. Concerning Figure 121, the AOI is the region inside the rectangle with dimensions 5.5 x 2 mm. The main dimensions DT and D, visible in Figure 121, of the U-notch, are 2 mm and 5 mm respectively, while DG is the dimension of the contract vena due to the onset of the cavitation phenomenon, which will be measured according to the number of pixels.
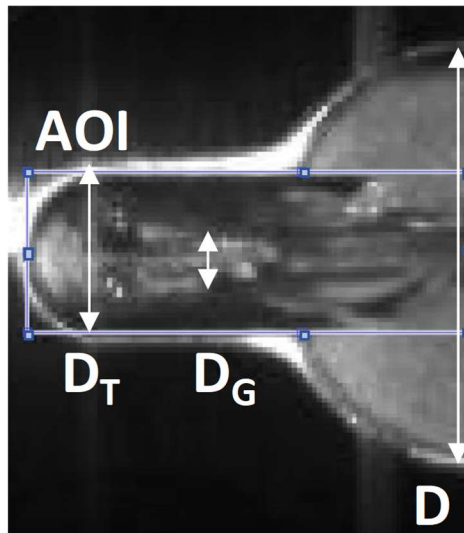
Figure 121. The box defines the AOI of a single frame

The AOI, in Figure 121, put in evidence both the liquid and the gas phases. Using a post-processing tool built up using Matlab®, the contours dividing the two phases can be observed. The AOI image is a matrix of known dimension, and this keeps easy to extend the procedure to the whole sequence of images. The used technique starts from the original frame and adopts the neural network (Multilayer Perceptron, MLP) [77] [78]. The application of this method optimizes the pixel choice after the definition of a threshold: it permits to obtain the division of the light gray and dark gray pixels through a non-linear threshold function. The function separates the pixels of the different layers of the neural network with the results shown in Figure 122.

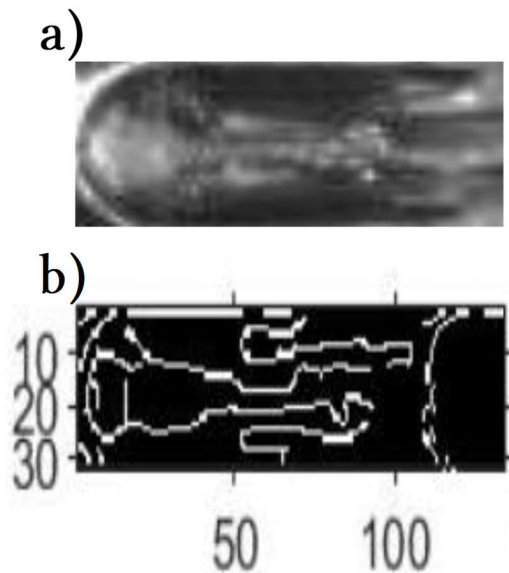**Figure 122.** Spool opening 1mm: a) Recorded image; b) Post-processed image (axes in pixels)

The carried-out image represents the contours between the liquid phase and the gas phase in white color and permits to elaborate the content information numerically. The recorded image verifies how the flow's behavior follows the geometry of the valve notches. Figure 123 represents the overlap of images in Figure 122 and better highlights the different regions; those regions have been called A, B, and C; A is the laminar region, B is the reduced section, and C is the expansion section. The region B is of particular interest because it is the area where the gas phase's growth almost throttles the liquid fluid. The width of the throttle of the liquid phase, changing the valve opening, and the upstream pressure has been measured to follow this event. The AOI is a rectangle of 30x200 pixels, and each pixel is equivalent to 0.13 mm, so the AOI is about 1.20mmx8mm.
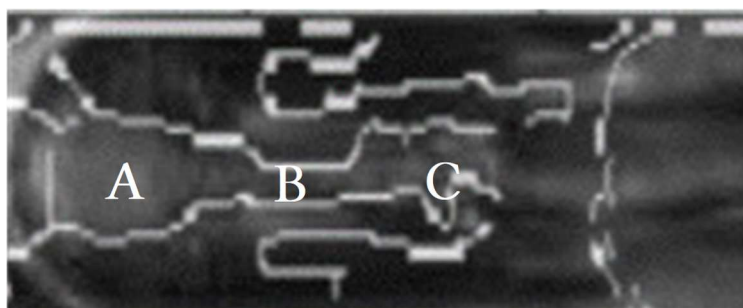

Figure 123. The overlap of the acquired image and the contour image and the developed region

As shown in Figure 123, region A is determined by the upstream pressure immediate drop area opening's variation and the flow's discontinuity due to a sharp-edge. Due to the sudden pressure drop, the air dissolved inside the oil comes out from the solution. For the system's symmetry, due to the valve body's geometry, in region A, the liquid phase remains at the center of the valve notch and is surrounded by the gas phase. The gas phase's growth increases along with the notch to a point where the liquid passage section becomes minimal (region B shows the restricted area in Figure 123). After the restricted region B, which shows almost a constant dimension DG, the U-notch increases its dimension, identified in Figure 121 with the parameter D. The more significant dimension of this section modifies the structure of the two-phase flow (region C), creating a flow enlargement able to recover a static pressure with a reduction of the gas phase. Furthermore, the elongation of the air bubbles tends to create a gas phase instability at the end of region C. In particular, at this point, the Rayleigh-Taylor instability begins [79], and some little bubbles detach from the gas phase at great speed.

As shown in the paragraph regarding the experimental setup, the spool inside the valve body can be moved using a micrometer. The tests have been carried out for openings of 1 and 2 mm, respectively; the valve has been tested according to the maximum reachable pressure of the body material, which was around 20 bar, using a safety factor of 0.5. The following tables (Table 15 and Table 16) summarize the results obtained during the tests; those tables are fundamental for understanding effects on the behavior of the gas and the liquid phases for upstream pressure and valve opening variations. Interesting considerations regarding bubble growth and increase are described in the "annotations" column. In both tables, the Euler number Eu and the cavitation number σ have been calculated; those parameters can help understand the presented cavitation process. The Eu has been evaluated using the following equation:

$$Eu = \frac{p_u - p_d}{\rho v_B^2} \tag{98}$$

Where p_u and p_d are the measured upstream and downstream pressures, ρ is the fluid density, and v_B is the velocity of the fluid in section B (section

already shown in Figure 123) evaluated, including the cavitation effect, by applying the equation of continuity for incompressible fluids from the section 1 to the section B (Figure 124). As said in the previous section, vB is calculated considering the contract vena's dimension obtained from the post-processed images by measuring the pixels' number.

From the acquired pressures, the cavitation number has been evaluated using the equation reported below [64] where p_v is the oil vapor pressure equal to zero for the hydraulic oils:

$$\sigma = \frac{p_d - p_v}{p_u - p_d} \qquad (99)$$

σ has been used through the years to characterize the cavitation; it has been demonstrated that the reduction of the cavitation number indicates a greater probability of the phenomenon occurring [58].

Table 15. Trial conditions for a valve opening of 1mm

Test	Flow rate	p_u	p_d	Eu	σ	
Nr.	L/min	bar(g)	bar(g)	-	-	Annotations
1	1.67	1.01	0.037	0.539	1.06	No bubbles
2	2.55	2.02	0.037	0.471	0.52	No bubbles
3	3.20	2.99	0.038	0.445	0.35	No bubbles
4	3.84	4.00	0.040	0.4148	0.26	No bubbles
5	4.35	4.97	0.034	0.178	0.21	Small bubbles growth
6	4.86	6.03	0.036	0.027	0.17	Instantaneous bubbles growth
Test	Flow rate	p_u	p_d	Eu	σ	Annotation
Nr.	L/min	bar(g)	bar(g)	-	-	
7	5.35	7.04	0.038	0.040	0.15	Instantaneous bubbles growth
8	5.85	7.95	0.036	0.026	0.13	Noise starts and bubbles
9	6.40	9.02	0.038	0.027	0.12	Noise-Bubbles
10	6.83	9.96	0.035	0.023	0.10	Increasing Noise-Bubbles
11	8.88	15.00	0.050	0.020	0.07	Instability and atomization
12	10.11	17.92	0.055	0.010	0.06	Instability and atomization

Table 16. Trial conditions for a valve opening of 2mm

| Test Nr.	Flow rate L/min	p_u bar(g)	p_d bar(g)	Eu -	σ -	Annotation
13	2.05	0.93	0.050	0.321	1.19	No bubbles
14	3.33	2.00	0.060	0.268	0.55	No bubbles
15	4.25	3.01	0.060	0.251	0.36	No bubbles
16	4.96	3.96	0.060	0.095	0.27	No bubbles
17	5.63	4.99	0.070	0.073	0.22	Small bubbles growth
<u>18</u>	<u>6.25</u>	<u>6.01</u>	<u>0.070</u>	<u>0.032</u>	<u>0.18</u>	<u>Noise start and bubbles</u>
19	6.82	7.02	0.070	0.024	0.15	Noise and bubbles
20	7.37	8.05	0.075	0.014	0.13	Noise and bubbles
21	7.88	8.99	0.077	0.009	0.12	Increasing Noise-Bubbles
22	8.36	10.00	0.080	0.004	0.10	Increasing Noise-Bubbles
23	10.62	15.03	0.103	0.001	0.07	Instability and atomization
24	11.90	18.03	0.120	0.0002	0.06	Instability and atomization
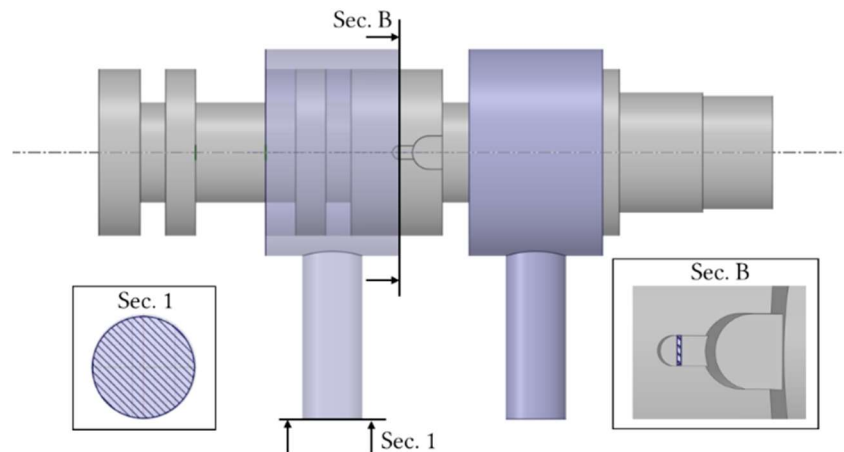
Figure 124. Sections of application of equation of continuity for incompressible fluids

As said, the acquired images have been post-processed, using the technique already described, identifying three particular regions called *A*, *B*, and *C* in Figure 123. For each image, the throttle zone's length and how it varies with the time has been calculated. A first result has been shown in Figure 125;

159

where the flow coefficient C_d is expressed as a function of the lost energy ratio evaluated using the following equation:

$$Lost\ Energy\ Ratio = \frac{\Delta p}{\gamma} = \frac{(p_u - p_d)}{\rho g} \qquad (100)$$

$$C_d = \frac{D_G}{D_T} \qquad (101)$$

The following figures presented in Table 15 and Table 16 will clearly illustrate the transition from no cavitation to cavitation using parameters in equation (100). In particular, the transition happens, for both analyzed openings, at the same value of the energy lost ratio (70m). The value of 70m has been achieved in tests number 6 (1mm opening) and 18 (2mm opening).
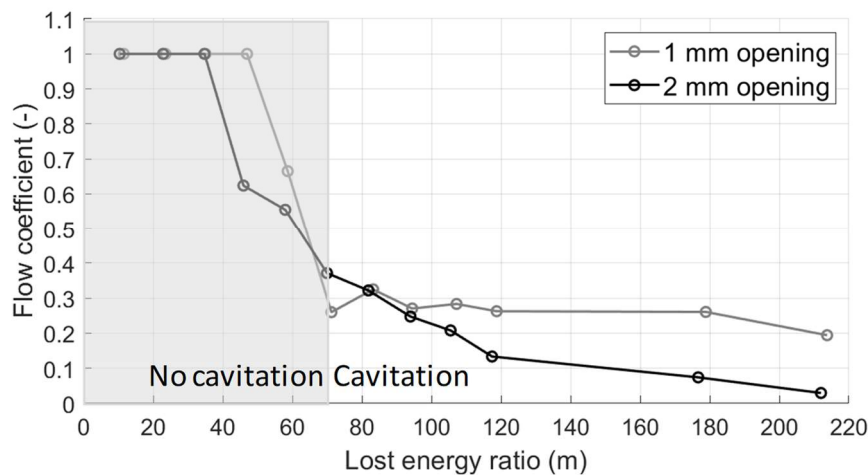

Figure 125. The trend of the flow coefficient Cd versus the lost energy ratio Δp/γ

It is evident from Figure 125 how the transition from no-cavitation to cavitation condition creates a drop in the calculated flow coefficients, highlighting the bubble growth. Until a value of 40 – 60 m the regime in the U-notches is laminar (C_d = 1), then it rapidly becomes turbulent, and the flow coefficient suddenly drops to a value around 0.3 with small increases in the lost energy ratio; the turbulent regime should stay in higher value, to

160

remove instability from the hydraulic caused by the cavitation phenomenon and improve the valve performance and control.

The same consideration can be done for Figure 126, where the Euler number has been presented as a function of the lost energy ratio. The transition from no cavitation to a cavitating flow, already identified with a value of $\Delta p/\gamma=70$ m for both considered openings, occurs when Eu drops below 0.1. It means that the inertial forces are one order of magnitude more than the pressure forces.
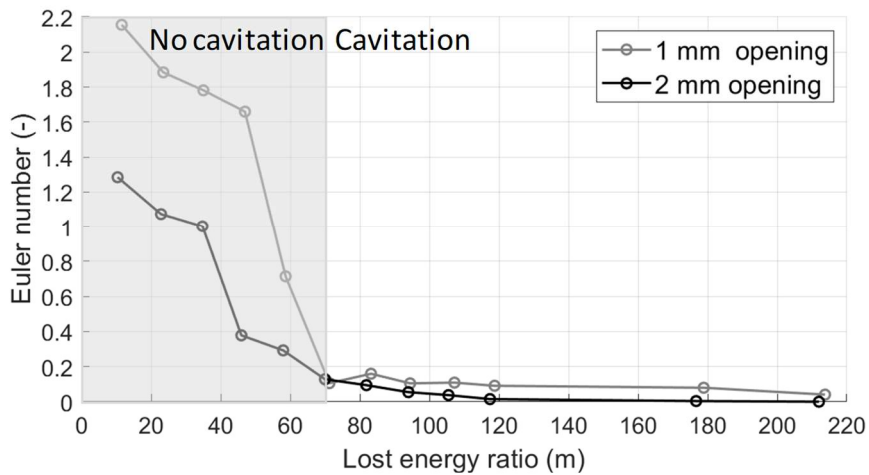

Figure 126. The trend line of the Euler number versus the lost energy ratio $\Delta p/\gamma$

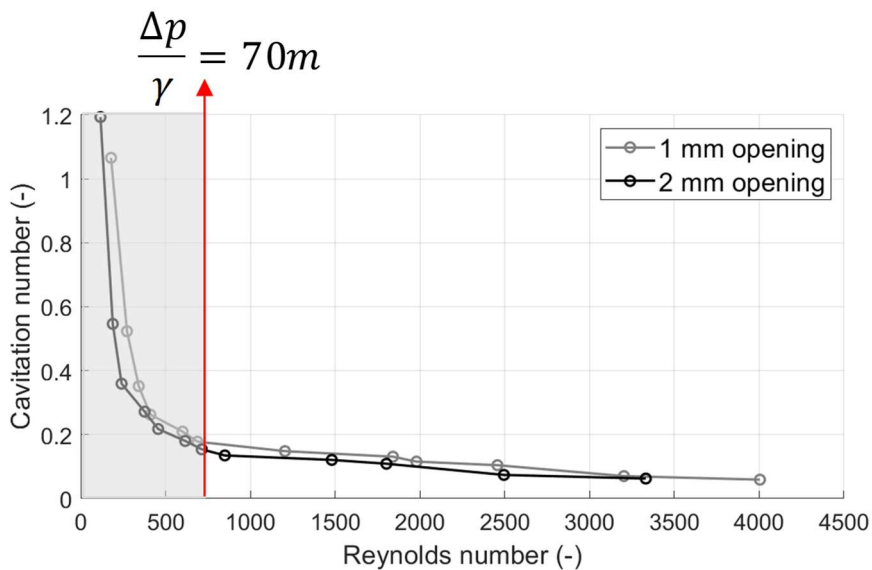In Figure 127, the cavitation number has been presented for both valve openings as a Reynolds number function.

Figure 127. The trend line of the Cavitation number versus the Reynolds number

161

Data presented in Figure 127 shows that the cavitation number becomes almost constant when the transition from non-cavitating to cavitating flow has been observed in tests 6 and 18. From these two tests, the inception of cavitation happens when the value of the lost energy ratio ($\Delta p/\gamma$) achieves 70m. During the transition, the cavitation number σ falls in the range 0.18-0.17 for both openings.

V.4 Numerical model description and results

The gaseous cavitation phenomenon, described in the previous paragraphs, has also been investigated using a numerical approach.

The approach used for three-dimensional CFD modeling has already been presented in this thesis. For this reason, the model description has not been described again.

For this model, in particular, it is necessary to provide a value for the fluid's dissolved and undissolved air. Average values have been set, known in the literature. In particular, the dissolved air value is 4% vol, while 0.1% of vol has been set for the undissolved air.

From the valve's geometry already shown in Figure 116, the fluid volume has been extracted; in Figure 128, the boundary condition and the fluid volumes of the valve are clearly distinguished by colors. Ports T and P are in blue and red (respectively of low and high pressure) while the spool fluid volume is gray. From the extracted fluid, volumes have been meshed using the grid generator of Simerics MP+® that is based on a body-fitted binary tree algorithm. The meshed volume has been shown in Figure 129).
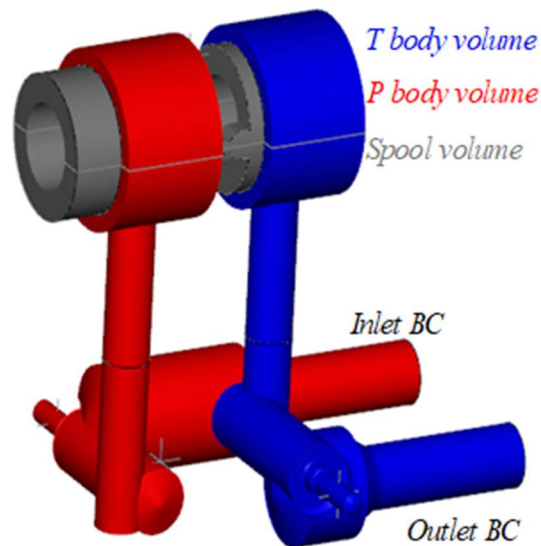
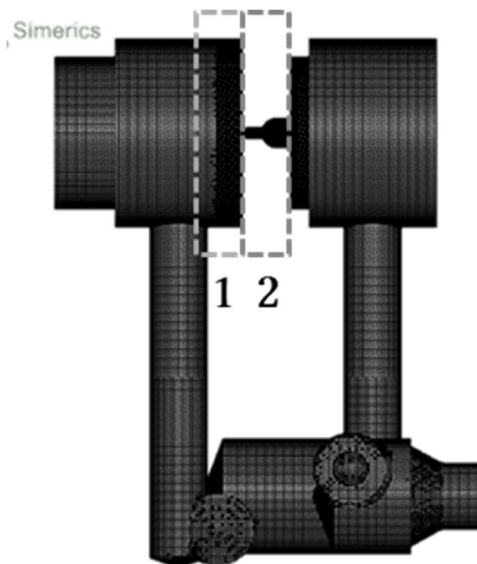**Figure 128.** Fluid volume: Valve extracted fluid volume

Figure 129. Fluid volume: Mesh of the extracted fluid volume

A mesh sensitivity analysis has been done increasing and decreasing the cells number in the AOI, which is the connection area between the fluid volumes of both port P and spool, called "1" and "2" in Figure 129. The grid has been varied to obtain the outlet volumetric flow rate independence from cell size. In Figure 130, a comparison of the grids has been presented with three different grids of 1.8M, 3M, and 7.8M of 3D Cells.
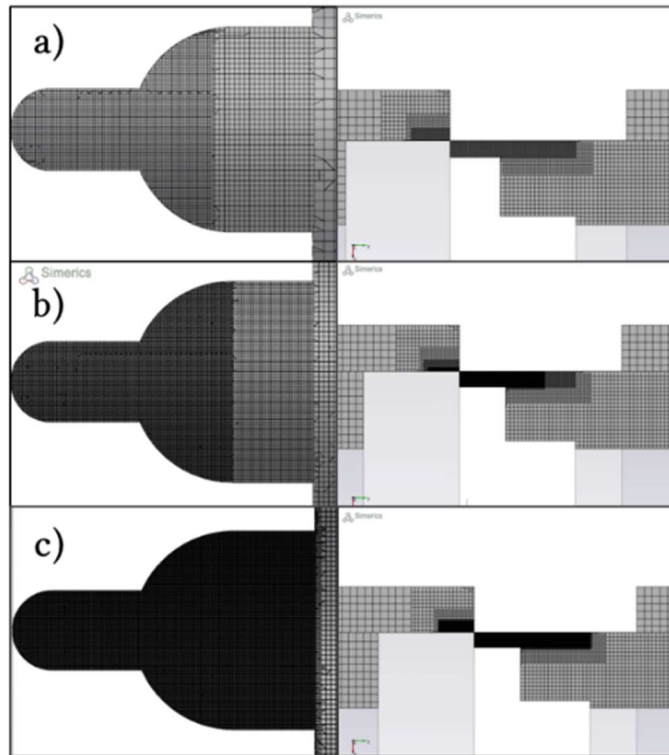
163

Figure 130. Mesh refinement in the U-notches: comparison among a model of 1.8M (a), 3M (b) and 7.8M cells (c)

Figure 131 and Figure 132 present the mesh sensitivity analysis; numerical models have been run at both valve openings' same working conditions. The analysis highlights that the capability of prediction of the volumetric flow (L/min) becomes the same for the models with 3.0M and 7.8M cells while it is unacceptable for the model of 1.8M cells; since the model with finer mesh requires extra computational time, the chosen model is the one with 3.0M 3D cells.
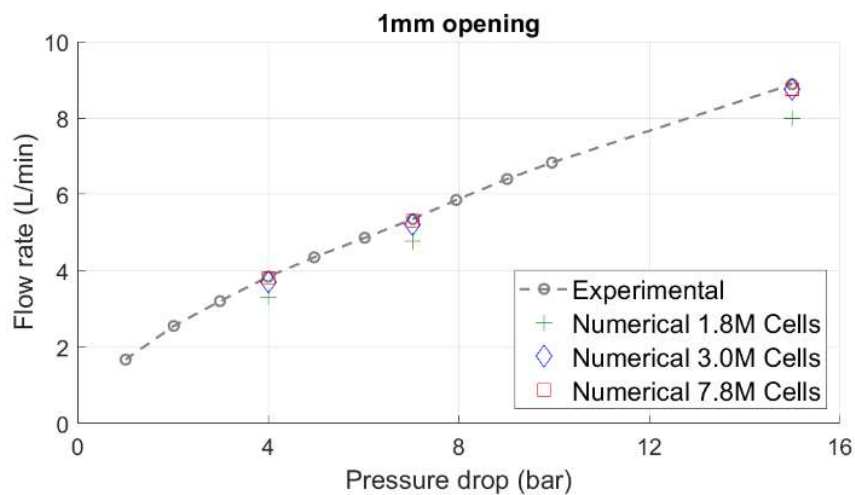

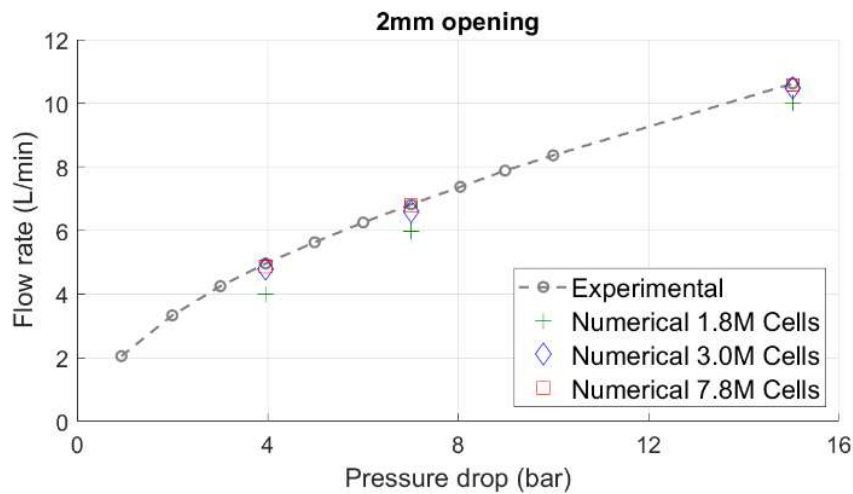**Figure 131.** Mesh sensitivity analysis for 1 mm opening

164

Figure 132. Mesh sensitivity analysis for 2 mm opening

The simulation has been set up at the same working condition of the experiments; therefore, for the two valve openings analyzed, the boundary conditions and fluid properties simulated are listed below:

- Total pressure at the inlet port that varies in the range [1-18] bar(a);

- Static pressure at the outlet port of 1 bar(a);

- The fluid is a hydraulic oil ISO VG46;

- Spool opening of 1 mm and 2 mm;

- Variable dynamic viscosity;

- Variable liquid bulk modulus (linearly dependent with pressure);

- Dissolved air 4% vol;

- Undissolved air 0.1% vol;

- Dissolved gas reference pressure of 0.47 bar(a);

- Oil vapor pressure 10 Pa.

The last two values presented in the previous list are values based on the experience, literature, and software developers' expertise. The model does not include heat transfer; however, the temperature has been assumed to affect the oil viscosity and density. An Intel® Core™ i7-7700HQ CPU 2.80 GHz, with a computational time of around 20 minutes per simulation, has been utilized for this purpose; it is significant to underline that the

165

convergence criteria for the flow are of 10-5 for the turbulence and 10-4 for the cavitation. A comparison between the experimental images and the simulated results has been shown in Figure 133 for both valve openings. Images related to the numerical results have been generated, visualizing the total gas volume fraction's iso-surface. The evaluated total gas volume fraction may vary in the range [0 – 1]; where the value of 0 identifies a fluid composed only by liquid (oil) and dissolved air/gas and 1 distinguishes a volume occupied only by undissolved air/gas or oil vapor; internal values are a mixture. Iso-surfaces presented in Figure 133 have been generated for the value of the total gas volume fraction above 0.3. Figure 133 shows the average accuracy of the model in predicting the cavitation. There are tests where images have a good overlap and others with some differences. As the difference between upstream and downstream pressure increases, the bubbles change their dimensions and shape along the axial direction for a given valve opening. Simulations have been run for both valve opening; in particular, in Figure 133, tests 4 to 11 are referred to a 1 mm opening while tests 14 to 23 to 2 mm opening. It is possible to observe more significant cavitation regions for lower valve openings, showing the flow field's symmetrical behavior due to the notch geometry. The onset of two swirl flow on the two gas tongues is evident at higher upstream pressure, which cannot be entirely numerically solved using a RANS approach. Figure 134presents, for test number 11, the streamlines colored as a function of the fluid velocity are combined with the iso-surface of the gas volume fraction. In this figure, it is possible to see, however, the macroscopic vorticity of the flow.
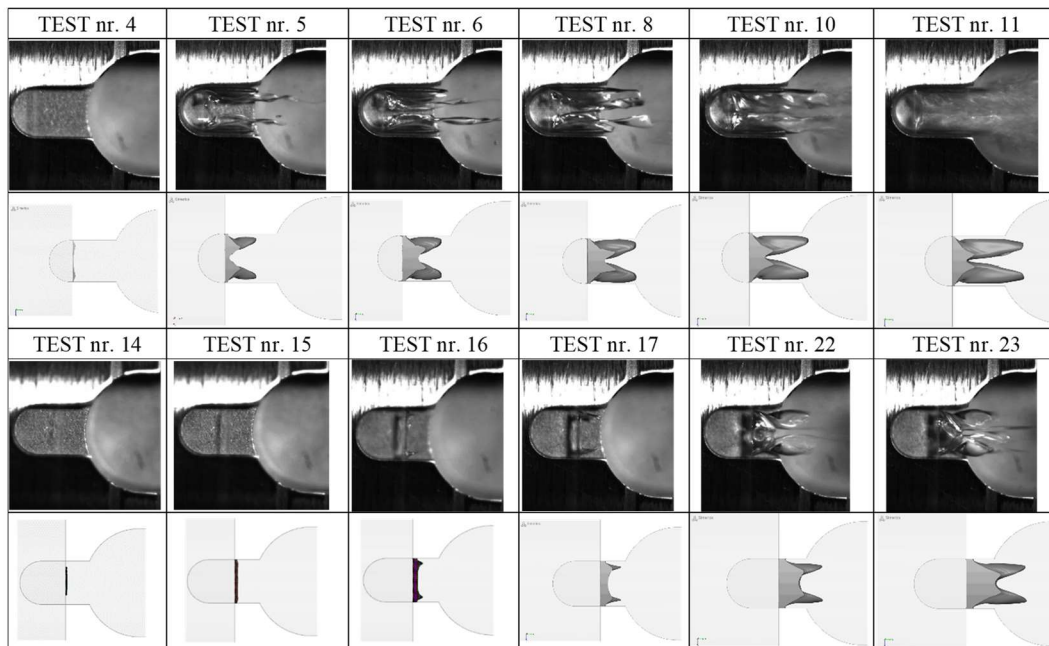
Figure 133. Comparison between the numerical model results and the experimental data for both openings
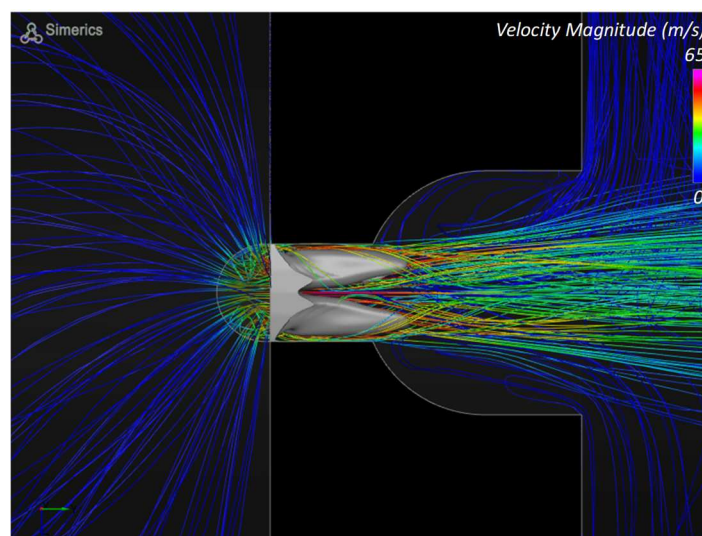

Figure 134. Numerical results, test nr. 11: Streamlines and iso-surface of the total gas volume fraction

The numerical model has been run in other operating conditions to understand better the influence on the valve opening's cavitation phenomenon. In particular, fixing the delta pressure at 6bar, the valve opening has been varied from 3mm to 0.1mm. For a better understanding, the numerical flow velocity profile and cross-sectional views have been presented in Figure 128, and Figure 129 present the numerical pressure distribution combined with the iso-surface of the total gas volume fraction
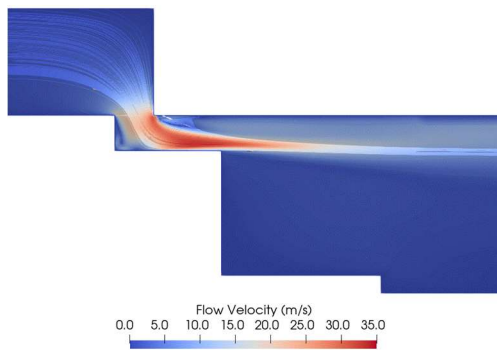
167

cross-sectional view. When the oil passes through the U-notch, it is accelerated on the curved edge instead of straight. The velocity of flow near the U-notch is more significant at its center, and its value is about 35 m/s.
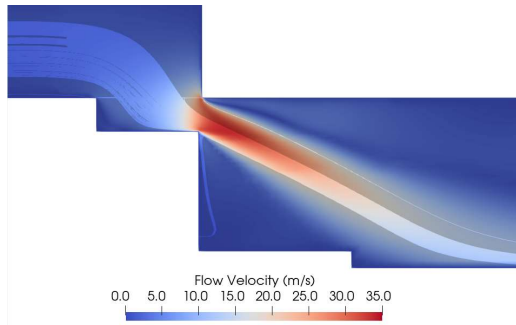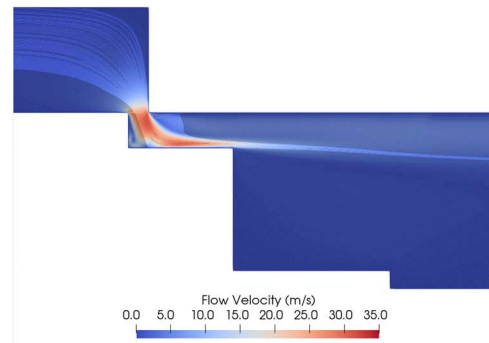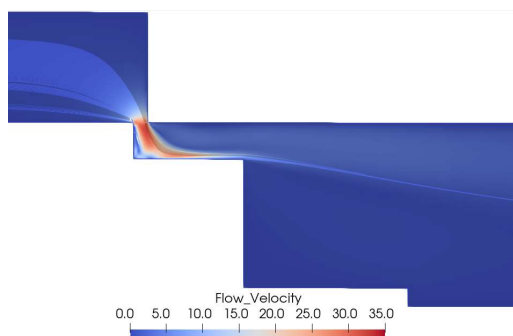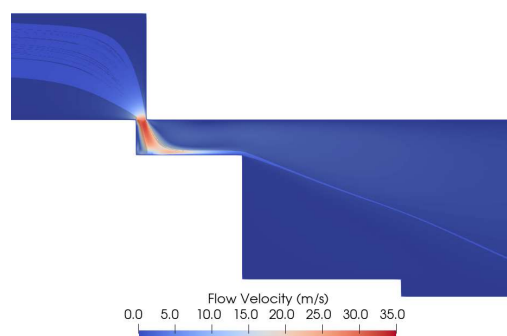

s=3mm
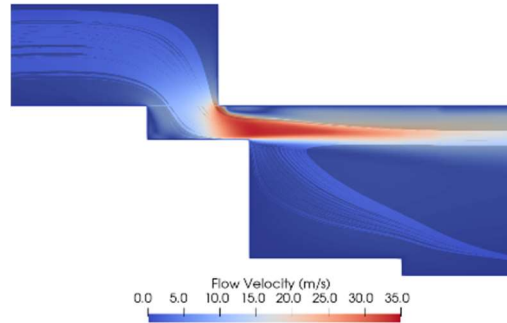
s=2mm

s=1mm

s=0.5mm

s=0.3mm

s=0.2mm
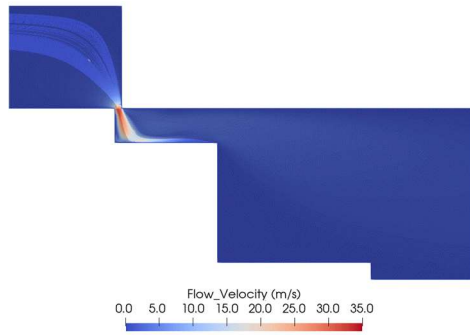
s=0.1mm

Figure 135. Numerical results: velocity contours different valve openings

Numerical results clearly show that the cavitation phenomenon is correlated with those valves' geometry and, in particular, with the notch shape. The existence of a corner causes a flow acceleration on the curved edge instead of going straight with an increment in those regions of the energy dissipation. In addition to the previous considerations, Figure 136 presents other interesting results obtained with the model and shows overlapping views of iso-surfaces of the total gas volume fraction and pressure for each size valve opening.

Since the cavitation regions are closely related to the pressure levels, iso-surfaces of the total gas volume fraction and pressure distributions have been overlapped. The pressure in those images varies in the range [0 – 1] barA. Regarding the iso-surfaces of the gas volume fraction, as already said, images have been generated for value above 0.3.

s=3mm   *s=2mm*

s=1mm

s=0.5mm

s=0.3mm

s=0.2mm
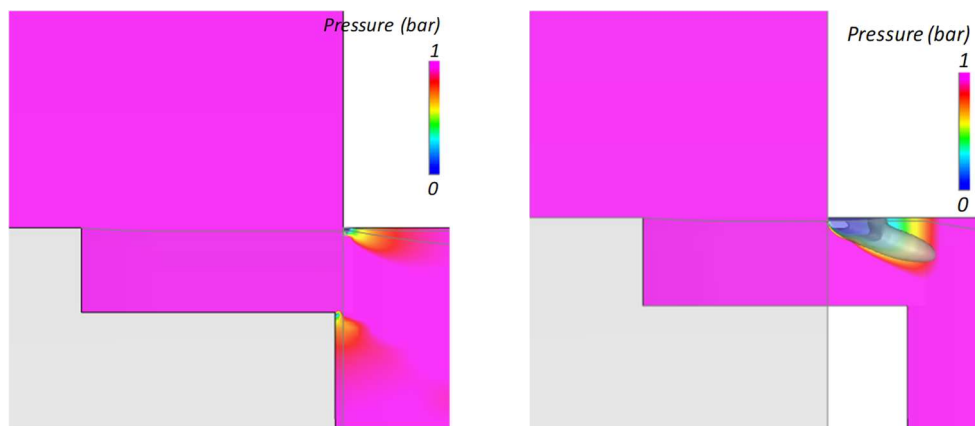
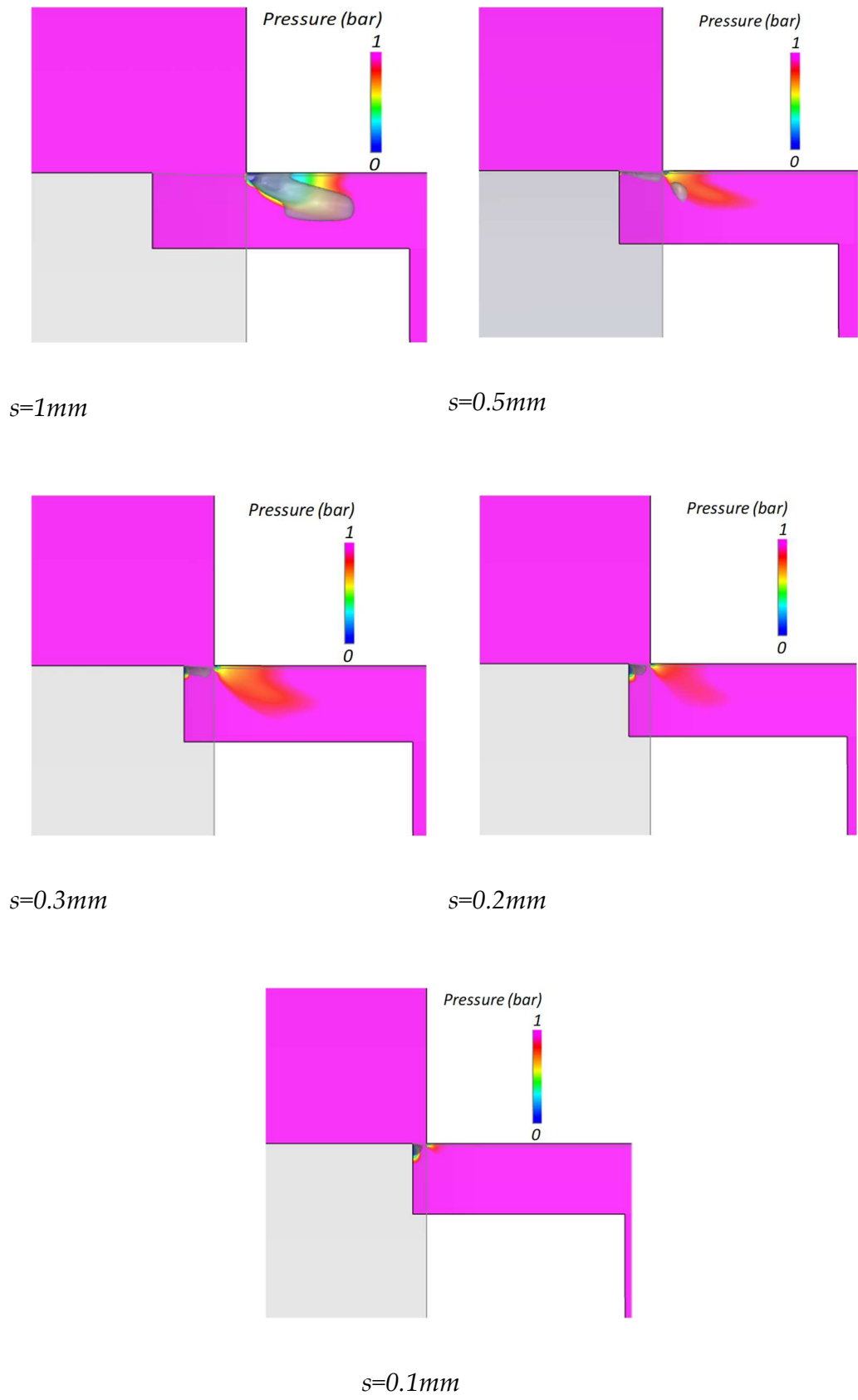*s=0.1mm*

Figure 136. Numerical results: pressure distribution and cavitation iso-surface for different valve openings

170

Iso-surfaces of the total gas volume fraction are always located in the cavitation region already described in paragraph three; therefore, bobbles to grooving up in the U – notches with a dimension that depends on the valve opening. Starting from the first image, which corresponds to an opening of 3mm, the iso-surface is absent since there are not the pressure conditions that promote the phenomenon; at 2 mm, the iso-surface is present, but it is less than for s = 1 mm; at that point, the cavitating phenomenon inverts the trends and bobbles become lower and lower. Further decrease of valve opening is effective in suppressing cavitation inception. Therefore, reducing s below the critical value of 1mm, the narrow passage areas almost suppress the cavitation inception, and, as a consequence, the cavitation intensity becomes slight.

V.5 Conclusions

This paper's results are only a part of ongoing research mainly focused on understanding the gaseous cavitation in spool valves, especially when it becomes a noise and vibration source. A better understanding of this phenomenon can help during the prototyping phase when a quiet valve is required for some application (i.e., aerospace and marine), where every onboard component's noise is critical. To capture the phenomenon, a plexiglass body of a 2 way – 2 position directional control valve has been designed and prototyped to indagate this kind of valve's behavior better when they work with small openings. The cavitating area has been identified during preliminary tests and subsequently studied with a high-speed camera placed directly in front of the transparent valve body. The post-processing of the acquired images has been based on recognizing progressive contour through a neural network method [77] [78]. This approach provides the most probable contours of a series of images, reducing errors due to parallax and shadows. The result of the post-processing showed different behaviors during the cavitating phase. Initially, with the increasing flow supply, the formation of a stable gas phase has been observed. The experimental analysis evidenced the difficulty to control the cavitation phenomenon in the flow when the valve opening is small since a sudden transition has been observed. Interesting results have been achieved by analyzing the variation of the flow coefficient, the Euler number, and the cavitation number as a function of

the lost energy ratio. It has been demonstrated that the rise of the cavitation phenomenon induces a sudden reduction of the contract vena. The Euler number has been evaluated to distinguish the non-cavitating and the cavitating areas clearly. This transition happens almost instantaneously when the lost energy ratio achieves 70 m that corresponds to a value of the cavitation number in the range of 0.17-0.18 for both analyzed openings. All the mentioned correlations can be used for studying cavitation inception.

A three-dimensional CFD numerical model has been built to simulate the flow field, pressure drop, velocity profiles, and gas volume fractions. To accurately predict the cavitation inception, the numerical model includes a full cavitation model able to predict the phenomenon, aeration, and liquid compressibility. The methodology proposed in this paper combines both the experimental and the numerical features to understand the cavitation location. Numerical results showed good accuracy with tests; therefore, the 3D CFD model can be used to find different geometries to reduce the cavitation, increasing the valve's whole performance.

The next steps will regard the redesign of the spool geometry, optimizing the notches for recovering static pressure with a relative reduction of the gas phase. New geometries are already under investigation combining the analysis showed in this paper with a novel automated DOE approach based on three-dimensional CFD simulations developed. The final goal will also be focused on developing a diagnostic technique to detect the onset of cavitation.

V.6 Nomenclature

Acronyms

Name	Descriptions
AOI	Area of Interest

Symbols

Name	Descriptions
C_d	Flow coefficient
D	Higher dimension of the U-notch (m)
D_G	Dimension of the contract vena due to cavitation (m)
D_T	Lower dimension of the U-notch (m)
Eu	Euler number
g	Gravitational acceleration (m/s^2)
H	Notch depth (m)
p_d	Downstream pressure (Pa)
p_u	Upstream Pressure (Pa)
p_v	Phase-change threshold pressure (Pa)
Re	Reynolds number
s	Valve opening (m)
S_1	Inlet valve section (m^2)
S_B	Section related to the contract vena (m^2)
v_B	Velocity in the section B (m/s)

Greek Symbols

Name	Descriptions
γ	Product of density and gravitational acceleration (kg s^{2}m^{-4})
Δp	Pressure drop (Pa)
μ_t	Turbulent viscosity (Pa*s)
σ	Cavitation number
τ	Time scale (s)

Conclusions

This thesis presented different works with systematic approaches for analyzing different displacement pumps. The scope was always acting on fluid-borne noise, reducing cavitation occurrence, and flow non-uniformity amplitude. The challenge was enormous; trying to create tools for such different pumps, where different physics was involved, could always fall into potential failures.

The piston pump project, the first approached during the program, created the next studies' fundamental basis. The primary purpose of an industrial Ph.D., where central characterization was to create high postgraduate formation and doctoral-level specialization consistently with the Italian productive system's needs, was centered since everything studied and optimized is standard production. The piston pump efficiency and noise reduction have had benefits from the developed tools. Starting from the pump's fundamentals, numerical modeling approaches have been presented, validated, and compared. Finally, the optimization process has been presented, and the best design is machined and tested, showing high accuracy of efficiency, flow-ripple and cavitation prediction.

During the last year, a comprehensive tool has been fully developed to simulate external gear machines. Different subroutines compose the tool; the main subroutine is composed of the Surface Tool©, which provides essential data for the hydraulic simulation, which has been done in 0D/1D environment. This modeling approach has been compared with 3D-CFD results, showing high robustness never seen in the literature. The tool developed by the author, in its first version, has high potential, and it is very user-friendly. With this tool, different designs have been investigated to reduce the flow ripple. An innovative methodology that acts on the reverse flow during the suction-to-pressure transition has been presented and

analyzed. The results are very promising, showing a drastic reduction of about 60% of the NUG, which means a significant reduction of the pump's fluid-borne noise.

Other studies have been carried out as well. A script to smoothly simulate the vane detachment from the stator ring has been presented. Its results showed the importance of considering vane detachment in three-dimensional CFD simulation; otherwise, numerical results of flow ripple and chamber pressurization will be with no-high confidence. The script can also qualitatively analyze the ring wear, studying the contact force between the vane tip and the ring itself.

Besides, a cavitation study of a valve with a plexiglass body has been conducted. Images of the cavitating flow have been acquired and post-processed. A particular value of the *lost energy ratio* has been identified for the transition from a non-cavitating to a cavitation regime, analyzing different valve openings.

A three-dimensional CFD numerical model of the valve has been done. The cavitation model considered, based on the "Full cavitation model", showed high predictivity of the phenomenon.

This cavitation model has also been used for the other studies presented in this thesis, showing high accuracy.

Unfortunately, the pandemic crisis that affected the globe during this tremendous year slowed the whole project down for what concerns the experimental support. This support is still scheduled, but the delays stretch every month. Vibrational and noise analysis are in the program on EGPs and the PMMA valve in the next year (2021).

All the studies presented have created potential tools that will be used for different future purposes, from the optimization of actual designs in terms of performance to investigate new methodologies for pump improvements and understand failure without explanation and for noise reduction.

Reference

[1]   J. Ivantysyn and M. Ivantysynova, Hydrostatic Pumps and Motors: Principles, Design, Performance, Modelling, Analysis, Control and Testing., Tech Books International, 2003.

[2]   J. D. N., Measurement and prediction of the fluid borne noise characteristics of hydraulic, University of Bath, 1987.

[3]   B. Xu, Y. Sun, J. Zhang, T. Sun and Z. Mao, "A new design method for the transition region of the valve plate for an axial piston pump," *Zhejiang Univ-Sci A (Appl Phys & Eng)*, vol. 16, no. 3, pp. 229-240, 2015.

[4]   S. G. Ye, J. H. Zhang and B. Xu, "Noise Reduction of an Axial Piston Pump by Valve Plate Optimization," *Chin. J. Mech. Eng.*, vol. 31, no. 57, 2018.

[5]   S. Wang, "The Analysis of Cavitation Problems in the Axial Piston Pump," *ASME J. Fluids Eng.*, vol. 132, no. 7, 2010.

[6]   H. Ding, F. C. Visser, Y. Jiang and M. Furmanczyk, "Demonstration and Validation of a 3D CFD Simulation Tool Predicting Pump Performance and Cavitation for Industrial Applications," *J. Fluids Eng.*, vol. 133, no. 1, p. 011101, 2011.

[7]   G. Changbin, J. Zongxia and H. Shouzhan, "Theoretical study of flow ripple for an aviation axial-piston pump with damping holes in the valve plate," *Chinese Journal of Aeronautics*, vol. 27, no. 1, pp. 169-181, 2014.

[8]   P. Casoli, M. Pastori, F. Scolari and M. Rundo, "Active Pressure Ripple Control in Axial Piston Pumps through High-Frequency Swash Plate Oscillations—A Theoretical Analysis," *Energies*, vol. 12, p. 1377, 2019.

[9] G. Berta, P. Casoli, A. Vacca and M. Guidetti, "Simulation model of axial piston pumps inclusive of cavitation," in *ASME International Mechanical Engineering Congress and Exposition*, New Orleans, Louisiana, USA, 2002.

[10] X. Wu, C. Chen, C. Hong and Y. He, "Flow ripple analysis and structural parametric design of a piston pump," *Journal of Mechanical Science and Technology,* vol. 31, no. 9, pp. 4245-4254, 2017.

[11] N. D. Manring and Y. Zhang, "The Improved Volumetric- Efficiency of an Axial-Piston Pump Utilizing a Trapped-Volume Design," *J. Dyn. Sys., Meas., Control.,* vol. 123, no. 3, pp. 479-487, 2001.

[12] *Simcenter Amesim®, Rev 2020.1, Technical bulletin 118.*

[13] C. Canudas de Wit, H. Olsson, K. Astrom and P. Lichinsky, "A new model for control of systems with friction," vol. 40, no. 3, 1995.

[14] C. Canudas de Wit, P. Tsiotras, E. Velenise and M. Basset, "Dynamic Friction Models for Road/Tire Longitudinal Interaction," *Vehicle System Dynamics,* vol. Draft article, 2001.

[15] C. Canudas de Wit, P. Tsiotras, T. Yi and R. Horowitz, "Friction Tire/Road modeling, Estimation and Optimal Braking Control," *Lund NACO2 Workshop,* vol. Draft article, 2001.

[16] H. Olsson, Control Systems with Friction, Lund Institute of Technology, University of Lund: Ph.D. thesis, 1996.

[17] H. Olsson, K. Astrom, C. Canudas de Wit, M. Gafvert and P. Lichinsky, "Friction models and Friction Compensation," 1997.

[18] B. Armstrong-Helouvry, "Control of Machines with Friction," *Kluwer Academic Publishers,* 1991.

[19] H. D.A. and F. B., "On the modeling and Simulation of Friction," *Transactions ASME, Journal of Dynamic Systems, Measurement and Control,* vol. 113, pp. 354-362, 1991.

[20] P. Dahl, "A solid friction model," in *Technical report TOR-0158(3107-18)-1*, The Aerospace Corporation, El Segundo, CA, 1968.

[21] P. Dahl, "Solid Friction Damping of Mechanical Vibrations," *AIAA Journal* , vol. 14, no. 12, pp. 1675-82, 1976.

[22] P. Dahl, "Solid friction damping of spacecraft oscillations," in *AIAA Guidance and Control Conference*, Boston Mass, 1975.

[23] R. Stribeck, "Zeitschrift des Vereines Seutcher Ingenieure," Vols. 46(38,39), pp. 1342-48, 1432-37.

[24] A. Singhal, M. Athavale, H. Li and Y. Jiang, "Mathematical basis and validation of the full cavitation model," *J. Fluids Eng.* , vol. 124, pp. 617-624, 2002.

[25] *Inc. S. Simerics MP+'s User Manual – v 5.0.11..*

[26] T. Nykänen, S. Esque and A. Ellman, "Comparison of different fluid models," in *Bath Workshop on Power Transmission and Motion Control*, Bath, 2000.

[27] M. Pettersson, "Design of fluid power piston pumps with special reference to noise reduction," Linkoping University, Linkoping, Sweden, 1995.

[28] M. Rundo, "Models for Flow Rate Simulation in Gear Pumps: A Review," *Energies,* vol. 10, no. 9, p. 1261, 2017.

[29] N. Manring and S. Kasaragadda, "The theoretical flow ripple of an external gear pump," *J. Dyn. Syst. Meas. Control* , vol. 125, no. 396, 2003.

[30] A. Vacca and M. Guidetti, "Modelling and experimental validation of external spur gear machines for fluid power applications," *Simul. Model. Pract. Theory*, vol. 19, pp. 2007-2031, 2011.

[31] X. Zhao and A. Vacca, "Formulation and optimization of involute spur gear in external gear pump," *Mech. Mach. Theory*, vol. 117, p. 114–132, 2017.

[32] F. Rituraj, A. Vacca and M. Morselli, "Modeling of manufacturing errors in external gear machines and experimental validation," *Mech. Mach. Theory,* vol. 140, p. 457–478, 2019.

[33] R. Rituraj, A. Vacca and M. A. Morselli, "Thermal Modelling of External Gear Machines and Experimental Validation," *Energies,* vol. 13, no. 11, p. 2920, 2020.

[34] X. Zhao, A. Vacca and D. Sujan, "Numerical modeling of a helical external gear pump with continuous-contact gear profile: a comparison between a lumped-parameter and a 3D CFD approach of simulation," in *Proceeding of BATH/ASME 2018 Symposium on Fluid Power and Motion Control*, 2018.

[35] M. Borghi, B. Zardin and E. Specchia, "External gear pump volumetric efficiency: Numerical and experimental analysis," in *Proceedings of SAE 2014 World Congress and Exhibition*, Detroit, MI, USA, 8–10 April 2009.

[36] B. Zardin, E. Natali and M. Borghi, "Evaluation of the Hydro—Mechanical Efficiency of External Gear Pumps," *Energies,* vol. 12, p. 2468, 2019.

[37] S. Mancò and N. Nervegna, "Simulation of an external gear pump and experimental verification," in *Proceedings of the JHPS International Symposium on Fluid Power*, Tokyo, Japan, 13–16 March 1989.

[38] J. Zhou, A. Vacca and P. Casoli, "A novel approach for predicting the operation of external gear pumps under cavitating conditions," *Simul. Model. Pract. Theory*, vol. 45, pp. 35-49, 2014.

[39] B. Zardin and M. Borghi, "Modeling and simulation of external gear pumps and motors," in *Proceedings of the 5th FPNI—PhD Symposium on Fluid Power*, Krakow, Poland, 1 January 2008.

[40] S. Falfari and P. Pelloni, "Setup of a 1D model for simulating dynamic behaviour of external gear pumps," in *Proceedings of the SAE 2007 Commercial Vehicle Engineering Congress & Exhibition*, Rosemont, IL, USA, 30 October 2007.

[41] E. Mucchi, G. Dalpiaz and A. Fernandez Del Rincon, "Elastodynamic analysis of a gear pump. Part I: Pressure distribution and gear eccentricity," *Mech. Syst. Signal Process,* vol. 24, p. 2160–2179, 2010.

[42] W. Strasser, "CFD investigation of gear pump mixing using deforming/agglomerating mesh," *J. Fluids Eng,* vol. 129, p. 476–484, 2007.

[43] F. Qi, S. Dhar, V. Nichani, C. Srinivasan, D. Wang, L. Yang, Z. Bing and J. Yang, "A CFD study of an electronic hydraulic power steering helical external gear pump: Model development, validation and application," *SAE Int. J. Passeng. Cars Mech. Syst.,* vol. 9, p. 346–352, 2016.

[44] A. Corvaglia, A. Ferrari, M. Rundo and O. Vento, "Three-dimensional model of an external gear pump with an experimental evaluation of the flow ripple," *Proc IMechE Part C: J Mechanical Engineering Science,* p. 1–9, 2020.

[45] R. Castilla, P. Gamez-Montero, N. Ert€urk, A. Vernet, M. Coussirat and E. and Codina, "Numerical Simulation of Turbulent Flow in the Suction Chamber of a Gearpump Using Deforming Mesh and Mesh Replacement," *Int. J. Mech. Sci.,* vol. 52, no. 10, p. 1334–1342, 2010.

[46] R. Castilla, P. Gamez-Montero, D. Del Campo, G. Raush, M. Garcia-Vilchez and E. Codina, "Three-dimensional numerical simulation of an external gear pump with decompression slot and meshing contact point," *J. Fluids Eng.,* vol. 137, p. 041105, 2015.

[47] M. Borghi, M. Milani, F. Paltrinieri and B. Zardin, "Pressure transients in external gear pumps and motors meshing volumes," in *Proceedings of the SAE Commercial Vehicle Engineering Congress,* Chicago, IL, USA.

[48] E. Frosina, A. Senatore and M. Rigosi, "Study of a high-pressure external gear pump with a computational fluid dynamic modeling approach," *Energies ,* vol. 10, no. 8, p. 1113, 2017.

[49] B. Geist and W. Resh, "Dynamic Modeling of a Variable Displacement Vane Pump Within an Engine Oil Circuit," in *Proceedings of the ASME 2011 Internal Combustion Engine Division Fall Technical Conference ICEF2011,* Morgantown, West Virginia, USA, October 2-5, 2011.

[50] P. Sullivan and M. Sehmby, "Internal Force Analysis of a Variable Displacement Vane Pump," *SAE Technical Paper,* vol. 01, no. 0409, 2012.

[51] M. Rundo and P. M. A., "Comprehensive Simulation Model of a High Pressure Variable Displacement Vane Pump for Industrial Applications," in *Proceedings of the ASME 2018 International Design Engineering Technical Conferences and Computers and Information in Engineering Conference IDETC/CIE 2018*, Quebec City, Quebec, Canada, August 26-29, 2018.

[52] M. Rundo and G. Altare, "Lumped Parameter and Three-Dimensional CFD Simulation of a Variable Displacement Vane Pump for Engine Lubrication," in *Proceedings of the ASME 2017 Fluids Engineering Division Summer Meeting FEDSM2017*, Waikoloa, Hawaii, USA, July 30-August 3, 2017.

[53] F. Fornarelli, A. Lippolis, P. Oresta and P. A., " Investigation of a pressure compensated vane pump," in *Proceeding of the 73rd Conference of the Italian Thermal Machines Engineering Association (ATI 2018)*, Pisa, Italy, 12–14 September 2018.

[54] E. Frosina, A. Senatore, D. Buono, K. Stelson, F. Wang, B. Mohanty and M. Gust, "Vane pump power split transmission: three dimensional computational fluid dynamic modeling," in *Proceedings of the ASME/BATH 2015 Symposium on Fluid Power and Motion Control, FPMC2015*, Chicago, Illinois, USA, 2015.

[55] E. Frosina, A. Senatore, D. Buono, K. Stelson, F. Wang and H. Gao, "A Three-Dimensional CFD Methodology to Study Vane-Ring and Vane-Under-Vane Interactions of a Vane Pump Power Split Transmission," in *9th FPNI Ph.D. Symposium on Fluid Power (FPNI2016)*, Florianópolis, Brazil, 2016.

[56] X. Fu, L. Lu, X. Ruan, J. Zou and X. Du, "Noise Properties in Spool Valves with Cavitating Flow," in *International Conference on Intelligent Robotics and Applications ICIRA 2008: Intelligent Robotics and Applications*, 2008.

[57] P. A. and T. C., "Proactive fault finding in a 4/3-way direction control valve of a high pressure hydraulic system using the bond graph method with digital simulation," *Mechanism and Machine Theory*, vol. 50, pp. 64-89.

[58] C. Martin, H. Medlarz and W. D.C., "Cavitation inception in spool valves," *J. Fluids Eng.,* vol. 103, no. 4, pp. 564-575.

[59] S. Oshima and T. Ichikawa, "Cavitation Phenomena and Performance of Oil Hydraulic Poppet Valve: 1st report mechanism of generation of cavitation and flow performance," *Bulletin of JSME,* vol. 28, no. 244, pp. 2264-2271, 1985.

[60] S. Oshima and T. Ichikawa, "Cavitation Phenomena and Performance of Oil Hydraulic Poppet Valve: 2nd Report, Influence of the Chamfer Length of the Seat and the Flow Performance," *Bulletin of JSME,* vol. 28, no. 244, pp. 2272-2279, 1985.

[61] S. Oshima and T. Ichikawa, "Cavitation Phenomena and Performance of Oil Hydraulic Poppet Valve: 3rd report, influence of the poppet angle and oil temperature on the flow performance," *Bulletin of JSME,* vol. 29, no. 249, pp. 743-750, 1986.

[62] S. Oshima, T. Leino, M. Linjama, K. T. Koskinen and M. J. Vilenius, "Effect of cavitation in water hydraulic poppet valves," *International Journal of Fluid Power,* vol. 2, no. 3, p. 5–13, 2001.

[63] Y. S. Liu, Y. Huang and Z. Y. Li, "Experimental investigation of flow and cavitation characteristics of a two-step throttle in water hydraulic valves," in *Proceedings of the Institution of Mechanical Engineers, Part A: Journal of Power and Energy,* 2002.

[64] L. Lu, J. Zou and X. Fu, "The acoustics of cavitation in spool valve with U-notches," in *Proc IMechE, Part G: J Aerospace Engineering,* 2011.

[65] L. Yinshui, Y. Yousheng and L. & Zhuangyun, "Research on the flow and cavitation characteristics of multi-stage throttle in water-hydraulics," *Journal of Process Mechanical Engineering,* vol. 220, no. 2, pp. 99-108, 2006.

[66] X. Liu, H. Jie, J. Zhao, Z. Long, W. Li and B. Li, "Biofluid flow through a throttle valve: a computational fluid dynamics study of cavitation," *J Mech Med Biol,* vol. 16, p. 1650034, 2015.

[67] J. He, B. Li and X. Liu, "investigation of flow characteristics in the U-shaped throttle valve," *Advances in Mechanical Engineering,* vol. 11, no. 3, p. 1–10, 2019.

[68] E. Brujan, T. Ikeda and M. Y., "On the pressure of cavitation bubbles," *Experimental Thermal and Fluid Science,* vol. 32, no. 5, pp. 1188-1191, 2008.

[69] H. Liu, C. Kang, W. Zhang and T. Zhang, "Flow structures and cavitation in submerged waterjet at high jet pressure," *Experimental Thermal and Fluid Science,* vol. 88, pp. 504-512, 2017.

[70] M. Perpar, E. Polutnik, M. Pečar and I. Žun, "Bubbly structures in a cavitating slot orifice," *Experimental Thermal and Fluid Science,* vol. 53, pp. 57-69, 2014.

[71] A. Osterman, M. Hočevar, B. Širok and M. Dular, "Characterization of incipient cavitation in axial valve by hydrophone and visualization," *Experimental Thermal and Fluid Science,* vol. 33, no. 4, pp. 620-629, 2009.

[72] R. Payri, F. J. Salvador, J. Gimeno and O. Venegas, "Study of cavitation phenomenon using different fuels in a transparent nozzle by hydraulic characterization and visualization," *Experimental Thermal and Fluid Science,* vol. 44, pp. 235-244, 2013.

[73] X. Wu, E. Maheux and G. Chahine, "An experimental study of sheet to cloud cavitation," *Experimental Thermal and Fluid Science,* vol. 83, pp. 129-140.

[74] A. Amoresano, C. Allouis, M. Di Santo, P. Iodice and V. Niola, "Experimental characterization of a pressure swirl spray by analyzing the half cone angle fluctuation," *Experimental Thermal and Fluid Science,* vol. 94, pp. 122-133, 2018.

[75] A. Corvaglia, G. Altare, R. Finesso and M. Rundo, "Computational fluid dynamics modelling of a load sensing proportional valve," in *proceeding of ASME-JSME-KSME 2019 8th Joint Fluids Engineering Conference*, San Francisco, CA, USA, 2019.

[76] G. Altare, M. Rundo and O. M., "3D Dynamic Simulation of a Flow Force Compensated Pressure Relief Valve," in *Proceedings of the ASME*

2016 International Mechanical Engineering Congress and Exposition IMECE2016, Phoenix, Arizona, USA, 2016.

[77] D. ChenJean, M. Odobez and H. Bourlard, "Text detection and recognition in images and video frames," *Pattern Recognition,* vol. 37, no. 3, pp. 595-608, 2004.

[78] W. D. Silva, M. Habermann, E. H. Shiguemori, L. D. L. Andrade and R. M. D. Castro, "Multispectral Image Classification Using Multilayer Perceptron and Principal Components Analysis," in *2013 BRICS Congress on Computational Intelligence and 11th Brazilian Congress on Computational Intelligence*, Ipojuca, 2013.

[79] M. Vadivukkarasan, Mahesh and V. Panchagnula, "Rayleigh-Taylor Instability Induced Liquid Atomization," pp. 135-144, 2016.

[80] E. Frosina, A. Senatore, D. Buono and S. K. A., "A Mathematical Model to Analyze the Torque Caused by Fluid–Solid Interaction on a Hydraulic Valve," *J. Fluids Eng.,* vol. 138, no. 6, p. 061103, 2016.

Ringraziamenti